



Universiteit  
Leiden  
The Netherlands

## **Imaging of alkyne-functionalized ruthenium complexes for photoactivated chemotherapy**

Busemann, A.

### **Citation**

Busemann, A. (2019, October 1). *Imaging of alkyne-functionalized ruthenium complexes for photoactivated chemotherapy*. Retrieved from <https://hdl.handle.net/1887/78473>

Version: Publisher's Version

License: [Licence agreement concerning inclusion of doctoral thesis in the Institutional Repository of the University of Leiden](#)

Downloaded from: <https://hdl.handle.net/1887/78473>

**Note:** To cite this publication please use the final published version (if applicable).

Cover Page



Universiteit Leiden



The following handle holds various files of this Leiden University dissertation:  
<http://hdl.handle.net/1887/78473>

**Author:** Busemann, A.

**Title:** Imaging of alkyne-functionalized ruthenium complexes for photoactivated chemotherapy

**Issue Date:** 2019-10-01

# Imaging of alkyne-functionalized ruthenium complexes for photoactivated chemotherapy

PROEFSCHRIFT

ter verkrijging van  
de graad van Doctor aan de Universiteit Leiden,  
op gezag van Rector Magnificus Prof. mr. C. J. J. M. Stolker  
volgens besluit van het College voor Promoties  
te verdedigen op dinsdag 1 oktober 2019  
klokke 10:00 uur

door

Anja Busemann  
Geboren te Naumburg (Saale), Duitsland  
in 1988

## **Samenstelling Promotiecommissie**

### **Promotor**

Dr. S. Bonnet

Prof. dr. E. Bouwman

### **Overige Leden**

Prof. dr. H. S. Overkleeft

Prof. dr. M. van der Stelt

Prof. dr. S. Rau (Universitat Ulm)

Dr. S. Oliveira (Universiteit Utrecht)

ISBN 987-94-6375-523-8

Printed by Ridderprint BV

*Was mich nicht umbringt, macht mich stärker.*

*What does not kill me, makes me stronger.*

Friedrich Nietzsche

To my family and friends.

Thank you!



# Table of contents

---

## CHAPTER 1

Introduction	7
--------------	---

## CHAPTER 2

Alkyne functionalization of photoactivated ruthenium complex [Ru(tpy)(bpy)(Hmte)](PF <sub>6</sub> ) <sub>2</sub> for protein interaction studies	29
---	----

## CHAPTER 3

Ruthenium-based PACT agents: synthesis, photochemistry, and cytotoxicity studies	49
---	----

## CHAPTER 4

Visualizing the invisible: Imaging of ruthenium-based PACT agents in fixed cancer cells	67
--	----

## CHAPTER 5

Synthesis of other alkyne-functionalized ruthenium polypyridyl complexes	89
---	----

## CHAPTER 6

Summary, Discussion, and Conclusion	105
-------------------------------------	-----

Appendix I: General experimental methods	123
--	-----

Appendix II: Supporting information for Chapter 2	129
---	-----

Appendix III: Supporting information for Chapter 3	137
--	-----

Appendix IV: Supporting information for Chapter 4	147
---	-----

Appendix V: Supporting information for Chapter 5	159
--	-----

Samenvatting	165
--------------	-----

Zusammenfassung	169
-----------------	-----

List of Publications	175
----------------------	-----

Curriculum Vitae	177
------------------	-----

Acknowledgements	178
------------------	-----





# 1

## INTRODUCTION

## 1.1 DNA as target of anticancer metallodrugs

In 1965, Barnett Rosenberg unexpectedly discovered the anticancer property of cis-dichlorodiammineplatinum(II), better known as cisplatin.<sup>1</sup> Since 1978, cisplatin is available for clinical practice and is used as chemotherapeutic agent for a wide range of tumors, and notably for metastatic testicular and ovarian cancer.<sup>2</sup> Cisplatin becomes cytotoxic upon hydrolysis, leading to the binding of the complex to the purine bases of DNA (N7 of guanine and adenine). This interaction results in cross-linked DNA.<sup>3</sup> Subsequently, repair, replication, and transcription of the nucleic acid is no longer possible, causing apoptosis of the cell. The main drawbacks of cisplatin are the inherent or acquired resistance of cells and side effects like nephrotoxicity, ototoxicity, and neurotoxicity caused by non-specific binding of the complex to other biomolecules.<sup>2</sup> New derivatives of the platinum drug were synthesized (carboplatin and oxaliplatin, Figure 1.1) to improve on those side effects, but these drugs require higher dosages and are effective against a smaller range of tumors.<sup>4</sup>

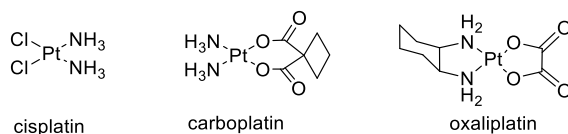


**Figure 1.1.** Chemical structures of cisplatin and its derivatives carboplatin and oxaliplatin.

Other transition metal-based anticancer compounds were investigated to find complexes with a higher selectivity towards cancer cells and to keep side effects to a minimum. Inspired by the mode of action of cisplatin, these metallodrugs were designed to interact with DNA and to induce apoptosis. Ruthenium-based anticancer agents contain chloride ligands as leaving groups for effective hydrolysis, which enables covalent binding to DNA.<sup>5</sup> In addition, polyaminocarboxylate, arylazopyridine, polypyridyl, or arene ligands were used to induce  $\pi$ - $\pi$  stacking with the DNA base pairs, and to intercalate with DNA.<sup>6</sup>

In the complex [Ru(II)( $\eta^6$ -biphenyl)(ethylenediamine)(Cl)]<sup>+</sup> (RM175) for example, the hydrophobic arene ligand is used to stabilize the oxidation state of ruthenium and to facilitate drug uptake by passive transport (Figure 1.2).<sup>7</sup> In addition, the biphenyl ligand can intercalate between DNA base pairs. The *in vitro* cytotoxicity of RM175 is similar to that of carboplatin (in A2780 human ovarian cancer cells: 5, 6, and 0.6  $\mu$ M for RM175, carboplatin, and cisplatin, respectively),<sup>8</sup> and the level of DNA-Ru adduct formation is similar to DNA platination by cisplatin.<sup>9</sup> Studies on

single-strand DNA as well as on duplex DNA, analyzed by NMR spectroscopy, revealed an efficient binding of the ruthenium center with N7 of guanine.<sup>9, 10</sup> Competition reactions in the presence of proteins did not affect the binding, pointing towards DNA as primary target of RM175.<sup>11</sup> *In vitro* studies in wild type HCT116 colorectal cancer cells showed that the treatment of cancer cells with RM175 results in the accumulation of the suppressor proteins p53, p21, and BAX.<sup>12</sup> Those proteins induce cell cycle arrest (in G1 and G2 phase) and apoptosis in case of damaged DNA.

Another example is indazolium *trans*-[tetrachlorobis(1H-indazole)ruthenate(III)], better known as KP1019. Developed by Keppler and coworker (Figure 1.2),<sup>13</sup> KP1019 acts against colon cancer and is one of the most famous and successful examples of ruthenium-based anticancer drugs since it reached clinical trial.<sup>13</sup> Activation by reduction of KP1019 in cells leads to the formation of the Ru(II) species with more labile Ru-Cl bonds.<sup>14</sup> The drug binds in a non-covalent manner to human serum albumin (HSA),<sup>15</sup> and it is assumed that specific transport *via* plasma protein transferrin (Tf) leads to the accumulation of the drug in cancer cells. In the cells, KP1019 interacts with DNA *via* monofunctional N7 coordination of the purines of guanosine 5'-monophosphate (GMP) and adenosine 5'-monophosphate (AMP).<sup>14</sup> The drug causes DNA unwinding, resulting in weak bending. KP1019 induces apoptosis *via* the intrinsic (mitochondrial) pathway.<sup>13</sup> The drug finished Phase I of clinical trials successfully without severe side effects. Due to its low solubility, the clinical testing proceeded with the water-soluble sodium salt analogue NKP1339.<sup>16</sup>

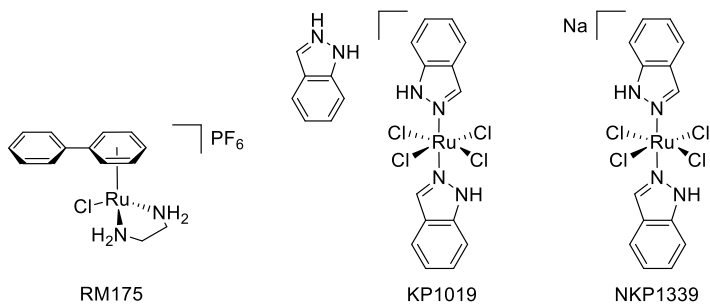


**Figure 1.2.** Chemical structure of the anticancer compounds RM175, KP1019, and NKP1339.

## 1.2 Cytotoxicity beyond DNA interaction

The RAPTA family consists of ruthenium-based anticancer complexes with the monodentate ligand 1,3,5-triaza-7-phosphatricyclo[3.3.1.1]decane (pta) and  $\eta^6$ -arene. The two remaining coordination sites are occupied by chloride or bridging carboxylate ligands, inspired by cisplatin and its derivatives (Figure 1.3). The

complexes are air-stable and are soluble in polar organic solvents and water.<sup>6</sup> RAPTA-C is the prototype compound of the RAPTA family. It has a high *in vitro* EC<sub>50</sub> value (507  $\mu$ M for TS/A mouse adenocarcinoma), but shows selectivity for cancerous over healthy cells (EC<sub>50</sub> >1000  $\mu$ M for non-tumorigenic HBL-100 human mammary cell line).<sup>6</sup> In addition, *in vivo* studies showed the reduction of the number of lung metastases from mammary carcinoma in mice after administration of the metallodrug.<sup>17</sup> The interaction of RAPTA-C with 2'-deoxyguanosine 5'-monophosphate (dGMP) was investigated and compared to that of KP1019.<sup>18</sup> RAPTA-C hydrolyzes rapidly to form the corresponding aqua complex and therefore, the complex is more reactive towards dGMP than KP1019. However, since no direct correlation between the binding to dGMP and its cytotoxicity could be found, it was hypothesized that proteins are the major target of RAPTA-C rather than DNA. It is assumed that the bulky pta ligand causes unfavorable steric interaction with DNA, leading to a preferred protein binding.<sup>19</sup> This hypothesis was confirmed by studies of the ruthenium complex in the presence of critical intracellular proteins (such as ubiquitin, cytochrome c, and superoxide dismutase) in which the interaction of RAPTA-C with these proteins was shown.<sup>20</sup>

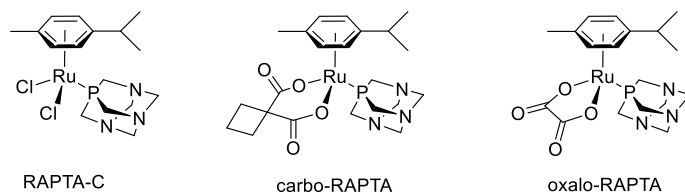


**Figure 1.3.** Chemical structures of anticancer drugs of the RAPTA family, derived from cisplatin and its derivatives.

Nowadays, the “DNA paradigm” that metallodrugs only cause cytotoxicity by direct damage of the DNA,<sup>21</sup> is not valid anymore. Even for cisplatin, protein interactions are reported in the literature *e.g.* with HSA and Tf.<sup>22, 23</sup> Therefore, the interaction of metallodrugs with proteins should not be neglected. Metallodrug-protein adducts can be the cause of drug cytotoxicity, side effects (*in vivo*), or be responsible for resistance mechanisms.<sup>24</sup> The interaction between the drug and a protein can be covalent (direct binding of an amino acid residue to the metal center) or non-covalent (*e.g. via*  $\pi$ - $\pi$  stacking, hydrophobic, or electrostatic interactions). In addition, the drug can act as specific protein inhibitor. Typical proteins that have been shown to be inhibited by metallodrugs are kinases, estrogen receptors, cysteine-containing proteins, or glutathione S-transferase. A detailed overview can be found in reviews by Hartinger and Meggers.<sup>25, 26</sup>

Targeting a protein that is involved in cancer-correlated pathways increases the chances to obtain a drug which is usually more toxic for cancerous cells than for healthy cells. This selectivity is essential in anticancer therapy as it increases the effect of the drug while lowering the probability of side effects.<sup>6</sup> According to Bergamo, targeted metallodrugs interfere with the specific target and thus control metastasis rather than having a general/unspecific antitumor activity caused by interaction with nucleic acids, mitochondria or proteins commonly expressed and used by all kinds of cells.<sup>27</sup> However, Dyson points out that with this approach targeted chemotherapeutics are so specific, that only certain cancer types are treated. In contrast to targeted chemotherapy, “classical” non-targeted drugs such as cisplatin can be used widely.<sup>6</sup> Instead of looking for specific biological targets, selectivity can also be triggered by physical factors. KP1019 and RAPTA-C are thought to be activated by reduction.<sup>14, 17, 28</sup> Since cancerous cells are generally more acidic than healthy cells, reduction of *e.g.* Pt(IV) or Co(III) complexes is more efficient in cancer cells. More details about “activation by reduction” of metal complexes can be found in reviews by Lippard and Heffeter.<sup>29, 30</sup>

### 1.3 Phototherapy - selectivity based on light activation

Another type of selectivity can be acquired using photoactivation. In this physical approach, light triggers the activation of a biologically inactive but photoreactive compound, called a photoactivatable prodrug (Scheme 1.1). Upon injection, the prodrug distributes throughout the body, and later, local irradiation with visible light induces an increased biological activity of the drug at the tumor site. With this method, undesired interactions of the drug with healthy cells, in particular in non-irradiated organs, are minimized.



**Scheme 1.1.** A non-toxic prodrug (orange) is administered to the patient with a tumor (grey) and activated in a spatially and temporally controlled way by visible light. The activated drug (red) selectively acts only at the irradiated area.

There are two main types of phototherapy in cancer treatment: photodynamic therapy (PDT) and photoactivated chemotherapy (PACT). In PDT, a photosensitizer (PS) absorbs a photon and is thereby excited to a singlet state (Scheme 1.2). *Via* intersystem crossing (ISC), an excited triplet state is reached. In PDT type 2, this excited triplet state is quenched by molecular oxygen ( $^3\text{O}_2$ ) and energy transfer leads to the formation of singlet oxygen ( $^1\text{O}_2$ ). The highly reactive  $^1\text{O}_2$  oxidizes biomolecules, which produces an excess of reactive oxygen species (ROS) that may cause cell death. In PDT type 1, the excited triplet state reacts directly with biomolecules; electron transfer produces free radicals that may also react with  $^3\text{O}_2$  to produce superoxide. Here as well, increased ROS level lead to cell death. Phototoxicity in PDT may occur through three pathways: direct tumor cell killing, vascular damage (causing nutrient depletion), and/or an immune response.<sup>31</sup> In PDT  $^1\text{O}_2$  production is a catalytic process, meaning that the PS is not consumed but it can turnover. Eosin was the first photosensitizer used in PDT to treat skin cancer.<sup>32</sup> Hereafter, the first porphyrin-based PDT agent, haematoporphyrin, was introduced. Its derivative, Photofrin, has become the first PDT drug approved for clinical use and is still the most widely used PS in cancer treatment.<sup>32</sup> Other examples of PDT agents approved by the FDA are Foscan (Figure 1.4), Levulan, Metvix, and Padeliporfin (WST11). Metal complexes can also act as PDT agents. The ruthenium-based photosensitizer TLD1433 was developed by McFarland and co-workers (Figure 1.4). TLD1433 is non-toxic in the dark, but upon red light activation it shows promising cytotoxicity against promyelocytic leukemia cells (HL-60).<sup>33</sup> This photosensitizer entered clinical trials for the treatment of bladder cancer and finished Phase I successfully.<sup>34</sup> For now, harmful side effects such as long lasting photosensitivity still affect patients receiving currently approved PDT treatment.<sup>35</sup> In addition, because PDT requires the presence of cellular oxygen to create ROS, it is less effective when oxygen concentration at the irradiated tumor site is low. This limits the effectiveness when treating tumors with large hypoxic regions. These tumors tend to be harder to treat with traditional chemotherapy methods, as indicated by the lower survival of patients with such tumors.<sup>36, 37</sup>

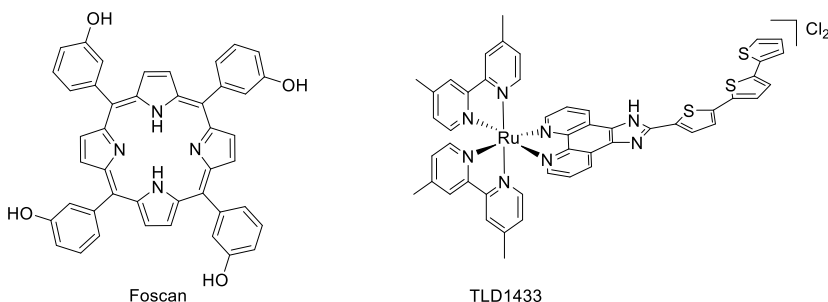
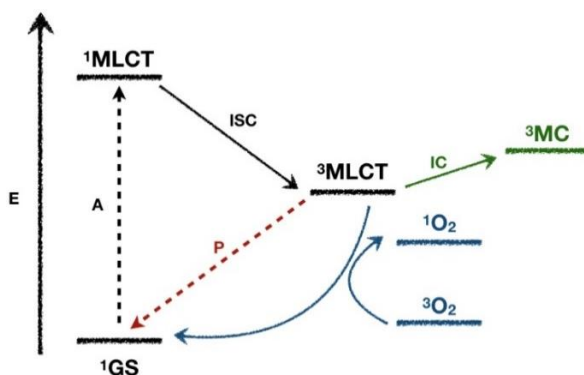


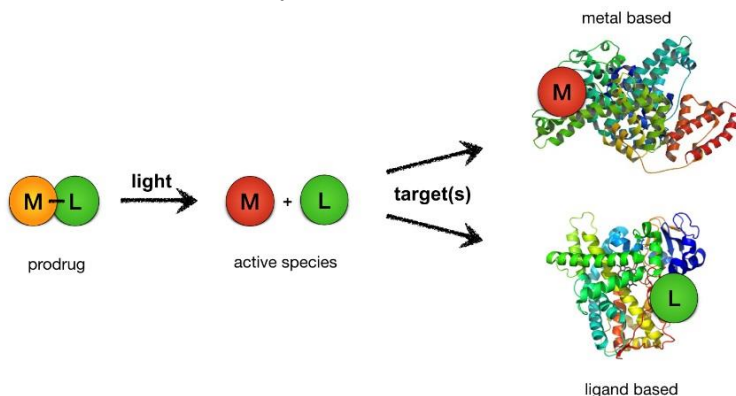
**Figure 1.4.** Chemical structure of the PDT photosensitizers Foscan and TLD1433.



**Scheme 1.2.** Jablonski diagram of the photoactivation of  $d^6$  transition metal complexes and their physical relaxation pathways in phototherapy. In the presence of molecular oxygen, photodynamic therapy (PDT) can lead to the production of reactive oxygen species (ROS) such as  $^1O_2$  (in blue). In photoactivated chemotherapy (PACT), population of the  $^3MC$  state leads to ligand substitution (in green). Dashed lines indicate processes involving photons. Non-radiative decay from the  $^3MLCT$  and  $^3MC$  state are omitted for clarity. Abbreviations: A = absorption, ISC = Intersystem crossing, IC = internal conversion, P = phosphorescence.

PACT agents, in contrast, can be utilized in low oxygen conditions, making them suitable for treating hypoxic tumors. The term PACT was introduced by Sadler and describes an inorganic photocaging strategy in oncology.<sup>38</sup> PACT utilizes the photochemical properties of  $d^6$  transition metals like Rh(III), Pt(IV), Ru(II), and Co(III) to create metallodrugs that are non-toxic until light irradiation triggers activation.<sup>38, 39</sup> Exposure of the PACT agent to light causes an irreversible chemical change of the metal complex leading to the formation of a biologically active species (Scheme 1.3). In the case of ruthenium-based PACT agents, this activation is based on photosubstitution. Light irradiation creates a singlet metal-to-ligand charge transfer state ( $^1MLCT$ ) and *via* ISC a triplet metal-to-ligand charge transfer state ( $^3MLCT$ ) is reached. Due to the distorted coordination spheres of PACT agents, a low-lying triplet metal-centered state ( $^3MC$ ) is available that can thermally be

populated from the photochemically generated  $^3\text{MLCT}$  state. The  $^3\text{MC}$  state has a dissociative character due to an electron being promoted in an antibonding  $d\sigma^*$  orbital, which leads to the dissociation of a ligand and its substitution by a solvent molecule (Scheme 1.2). Quenching of the  $^3\text{MLCT}$  state by the  $^3\text{MC}$  state causes PACT agents to be usually non-emissive, and to show low  $^1\text{O}_2$  quantum yields.<sup>40, 41</sup> The light-induced cytotoxicity can be caused by the interaction of cellular targets such as proteins or DNA with either the released ligand,<sup>42-46</sup> the metal species,<sup>40, 47</sup> or both. Almost any mode of action can be foreseen for a metal-based PACT compound, which opened a new field of research to identify the active species and its targets. PACT has not reached the clinics yet.



**Scheme 1.3.** General mechanism of PACT. A non-toxic prodrug is activated by light to generate the active species, which can be either the metal ion (M), the ligand (L), or both. The interaction with biomolecules such as proteins or DNA leads to the cytotoxicity at the irradiated tumor site.

## 1.4 Studying metal-protein interactions

### 1.4.1 Traditional methods to study interactions

In order to acquire insight on the mode of action of new metallodrugs, a variety of analytical methods has been used that allow for studying the interaction between the drugs and model proteins. The most frequently used proteins in this context are: bovine serum albumin (BSA), a model for human serum albumin (HSA), which is one of the main transport proteins in the blood; hen egg white lysozyme (HEWL), which is a histidine-rich protein and has been used a lot to model the interaction of metal compounds with this amino acid; and cytochrome c (cyt c), which is localized in the mitochondria and plays a crucial role in apoptotic pathways. Furthermore, ubiquitin (regulatory protein) and metallothionein-2 (MT-2, a cysteine-rich protein responsible for metallodrug resistance) have also been utilized. The most frequently



used experimental techniques to study metallodrug-protein interactions are introduced below.

X-ray diffraction (XRD) analysis allows for structure elucidation of metal-protein adducts. Information about possible ligand dissociation, the oxidation state of the metal center, as well as the binding sites on the biomolecule, can be obtained with atomic accuracy. For example, the XRD analysis of a KP1019-HSA adduct revealed that two ruthenium centers bind to histidine residues His146 and His242 in the hydrophobic core of albumin.<sup>48</sup> In addition, the crystal structure showed that all ligands dissociated from the ruthenium center before the metal ion bound covalently to HSA (Figure 1.5). The disadvantage of this method is the challenging preparation of single crystals of metal-biomolecule adducts and the non-biological conditions that are enforced during crystal growth (*e.g.* high metal complex and/or protein concentration are used, or protein crystals are soaked with the metallodrug). In addition, the structure only shows a final state, and no dynamics. The processes of ligand dissociation in solution are difficult to study.<sup>49</sup>

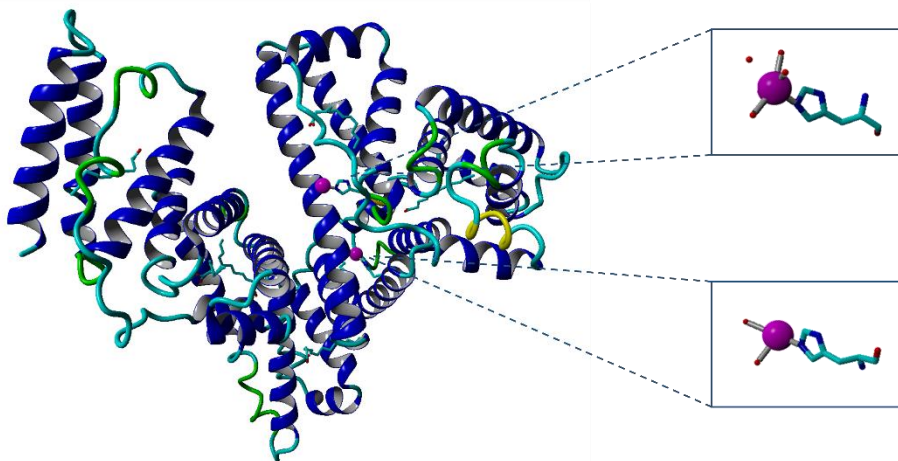


**Figure 1.5.** XRD structure of the KP1019-HSA adduct. All ligands are dissociated before binding of the ruthenium ion occurred at the histidine residues.<sup>48</sup>

Circular Dichroism (CD) spectroscopy enables the study of conformational changes in the secondary structures of DNA and proteins caused by metalation. The alteration of the absorption of circularly polarized light is a measurement of the interaction between the metal complex and the biomolecule. Often, CD measurements are performed in combination with fluorescence spectroscopy. The group of Keppler used CD to investigate the interaction of KP1019 with HSA.<sup>50</sup> KP1019 interactions with HSA lead to the loss of helical stability of the protein. The

relative fluorescence intensity of HSA decreased in the presence of the ruthenium complex, implying that conformational changes occurred close to the fluorescent tryptophan residue.

Electron spray ionization mass spectrometry (ESI-MS) is one of the most frequently used methods for the analysis of metal-bound proteins reported in literature. The soft ionization technique preserves most metal-protein interaction,<sup>51</sup> revealing the composition of the ligand-metal adducts, and enabling the quantification of metal centers bound to one protein. Casini performed ESI-MS experiments to study the interaction of RAPTA-C, carbo-RAPTA, and oxalate-RAPTA complexes with cyt c and HEWL.<sup>52</sup> The highest cyt c metalation was achieved with RAPTA-C, probably due to the good leaving group (chloride). A lower reactivity of the RAPTA complexes was observed for HEWL. RAPTA-C showed a preferred interaction with histidine residues at the protein surface of HEWL. The reactivity of RAPTA-C with MT-2 compared to cisplatin was also investigated by Casini.<sup>53</sup> The study showed that the affinity of RAPTA-C to MT-2 is lower than that of cisplatin, probably due to the presence of the arene ligand. Cysteine residues are the favorite binding site of the ruthenium center, and MT-2 can abstract RAPTA-C from competitive proteins in solution, giving insight in possible resistance mechanism and detoxifications of the drug. Glutathione (GSH, an abundant antioxidant) might also be involved in the detoxification of RAPTA-C. Their interaction was investigated by ESI-MS and the binding was confirmed.<sup>54</sup> In addition, GSH is able to disrupt an existing protein adduct of RAPTA-C and ubiquitin.

All these studies of metallodrug-protein adduct formations are usually performed with an isolated protein, sometimes in the presence of a few competitive targets. They provide chemical information about the reactivity of the tested metal complex. However, such controlled experiments do not resemble the complex environment of a cell since the conditions of the investigations are oversimplified and concentrations and protein-metal ratios are optimized for the analysis technique, rather than mimicking concentrations found in a cell. Therefore, techniques that identify the drug target in the cell and/or cell lysate are also necessary, in order to obtain a better insight on the mode of action of metallodrugs under physiological conditions.

#### **1.4.2 Metalloproteomics**

The observed cytotoxicity of a metal complex is often correlated to its cellular uptake. Inductively coupled plasma – mass spectrometry (ICP-MS) allows for quantitative analysis of the metal content in cell lysate after cell uptake or

fractionation experiments. The technique is element specific and allows for the analysis of *in vivo* samples as well.<sup>51</sup> Dyson *et al.* studied the differences in cellular uptake and subcellular distribution of NAMI-A, KP1019, and cisplatin, to be able to explain their different behavior in cisplatin-resistant and sensitive cells.<sup>55</sup> Ho and coworkers showed that outer membrane protein (OmpF), a cation-selective pore for small hydrophilic molecules in *E.coli*, plays a key role in the transportation of [Ru(tpy)(bpy)(Cl)]Cl (where tpy = 2,2':6',2''-terpyridine and bpy = 2,2'-bipyridine) into the cell.<sup>56</sup> The amount of ruthenium-based drug in the cell was quantified by ICP-MS measurements and a direct correlation between drug uptake and the presence of transport protein OmpF was indicated.

The combination of ICP-MS with separation techniques such as chromatographic columns (liquid chromatography, LC; high-performance liquid chromatography, HPLC; size exclusion chromatography, SEC; capillary electrophoresis, CE) enables the protein profiling of complex biological mixtures and can help to identify drug binding partners. The different types of MS hyphenation were reviewed several times.<sup>51, 57-59</sup> In addition, gel electrophoresis (GE) is also used for the separation of complex samples prior to MS analysis. In 2D GE, the biological sample is first separated based on isoelectric properties, followed by separation based on molecular weight. Dyson and co-workers investigated the difference in protein binding of NAMI-A and cisplatin with 2D GE and MS.<sup>60</sup> The quantification of the binding level of the two drugs to HSA, transferrin (Tf), and BSA were investigated, and the results demonstrated that NAMI-A is significantly less toxic than cisplatin, probably due to a different binding mode to the proteins (weaker interactions). Cheng *et al.* used 2D GE to compare the proteomic profiles of *E.coli* after treatment with different ruthenium complexes (Figure 1.6a).<sup>61</sup> After treatment, major effects were observed on transport proteins and oxidoreductases but also on hydrolases, stress-regulated proteins, and carbohydrate-related reactions compared to non-treated *E.coli* (Figure 1.6b and c). In addition, comparison of the different protein expressions after treatment demonstrated that an alteration of the bidentate ligand results in a change of the mode of action of the metallodrug.

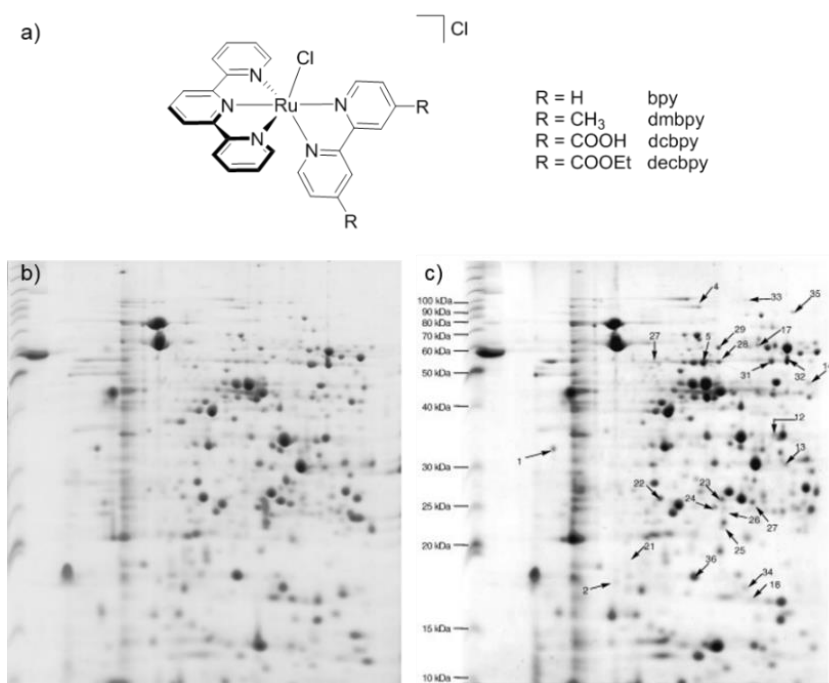


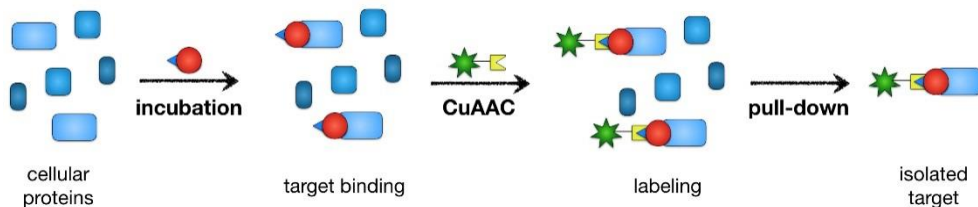
**Figure 1.6.** Ruthenium-based complexes with modified bpy ligands used by Cheng (a), 2D gel containing proteins of *E. coli* after control reaction without ruthenium complex (b), and 2D gel containing proteins of *E. coli* affected by ruthenium complex  $[\text{Ru}(\text{tpy})(\text{bpy})(\text{Cl})]\text{Cl}$  at  $160 \mu\text{M}$  (c).<sup>61</sup>

Other methods used for the analysis of biological samples are multidimensional protein identification technology (MudPIT),<sup>62, 63</sup> functional identification of target by expression proteomics (FITeXP),<sup>64</sup> isotope-coded affinity tag (ICAT),<sup>65</sup> and surface enhanced laser desorption ionization time-of-flight mass spectrometry (SELDI-TOF MS).<sup>66</sup> They are not discussed in further details in this introduction.

### 1.4.3 Drug pull-down

The techniques mentioned above provide information regarding the effect of a drug on the proteasome of a cell. To identify the actual target of a drug, its binding partners need to be isolated and analyzed. This can be achieved in a so-called pull-down assay (Scheme 1.4). Such assays are used in chemical biology for the identification of protein-protein interactions, but they can also be applied to study metal-protein interactions. In order to perform a pull-down assay, the drug (in red) is functionalized with a handle (in blue, *e.g.* a biotin, azide, or alkyne moiety). After incubation of this drug derivative with lysate or cells, a reporter tag (in green) binds to the handle. This tag allows for the separation of the metallated proteins from the

unbound proteins. Depending on the reporter tag, this separation can be achieved *e.g. via* gel electrophoresis or affinity purification. After the enrichment of the metallated proteins, the targets are analyzed by MS and identified.



**Scheme 1.4.** Drug pull-down experiments allow for the identification of the drug binding partners. The drug (in red), functionalized with a handle (in blue), is incubated and labeled with a reporter tag (in green, here *via* CuAAC). This method allows for the separation of the metallated proteins. The isolated protein targets can be further analyzed and identified by MS.

In recent years, several groups performed pull-down assays to study the interaction of their metal-based drug with proteins. The first example of a drug pull-down experiment involving metallodrugs was reported by Hartinger and co-workers, investigating the targets of RAPTA-C. The complex was functionalized with a biotin handle that allowed for the immobilization of the drug *via* streptavidin-modified beads (Figure 1.7).<sup>67</sup> The drug derivative was exposed to human cancer cell lysates of ovarian cancer (CH1), and the metal-protein adducts were separated from unbound proteins by centrifugation. 15 cancer-related target proteins were identified with high resolution MS. The researchers were able to correlate the isolated proteins to the antimetastatic properties of the drug. A similar approach was used more recently by Meier *et al.* to profile the targets of another ruthenium(arene) complex.<sup>68</sup> After incubation of the biotin-functionalized derivative of the drug with the cell lysate of HCT116 colon carcinoma cells, the isolated adducts were analyzed by MS. In addition, the effect of the drug on the protein expression of HCT116 colon carcinoma cells after drug treatment was determined (response profiling) and correlated to the proteins isolated earlier *via* the pull-down assay. Bioinformatic analysis enabled the researcher to identify and also justify the structural protein plectin as possible target. The biotin handle used in these examples leads to drastic modifications of the chemical properties of the drug, which may in turn change its biological properties, such as cellular uptake and intracellular distribution. The use of such large handles is limited to fishing protein

targets in a cell lysate, while protein target identification in living systems may require the development of smaller handles.

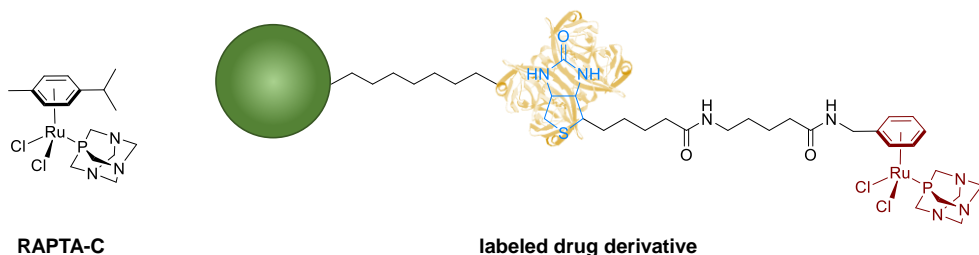


**Figure 1.7.** Structure of RAPTA-C and the drug derivative used in drug pull-down by the Hartinger group, bound to streptavidin-modified beads.

Indeed, if treating living cells with a handle-functionalized drug to deliver information on the mode of action of the drug without the handle, then such handle must be as small as possible, so that its presence only minimally interferes with the biological activity of the drug. Very small handles such as azide or terminal alkyne groups represent attractive alternatives. DeRose and co-workers synthesized azide-functionalized cisplatin derivatives and incubated *Saccharomyces cerevisiae* with these drug derivatives. After isolation of the DNA and RNA, fluorophore labeling *via* Cu(I)-catalyzed azide-alkyne cycloaddition (CuAAC, explained in section 1.5) in gel electrophoresis confirmed the interaction of the complexes with these biomolecules, as expected for cisplatin derivatives.<sup>69, 70</sup> In addition, Cunningham *et al.* investigated additional protein targets in drug-treated *S. cerevisiae*, by labeling the azide-functionalized platinum complex with biotin *via* CuAAC. This tag allowed for affinity purification and isolation of the Pt-protein adducts (Figure 1.8a).<sup>71</sup> They found several protein targets involved in the endoplasmic reticulum stress response. Che and co-workers also used click handles, but instead of azides, they functionalize their gold-based anticancer complexes with an alkyne click handle and a photoaffinity moiety (Figure 1.8b).<sup>72, 73</sup> Irradiation with UV light led to the covalent binding of the complex to the protein. Biotin labeling *via* CuAAC allowed for pull-down experiments. The studies revealed that some of their complexes interact with mitochondrial chaperons in HeLa cells,<sup>72</sup> while others show an affinity to several molecular targets.<sup>73</sup>

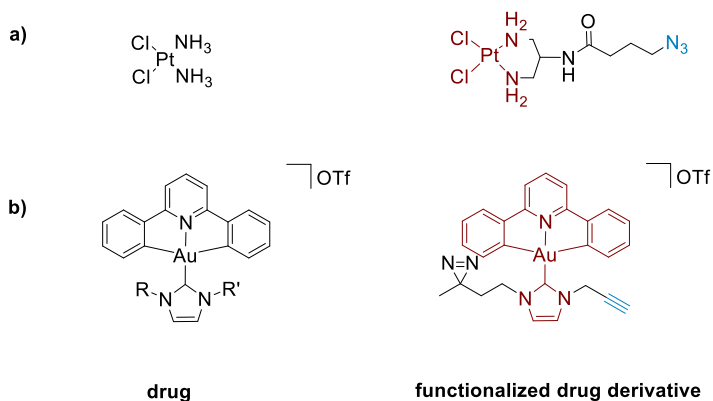
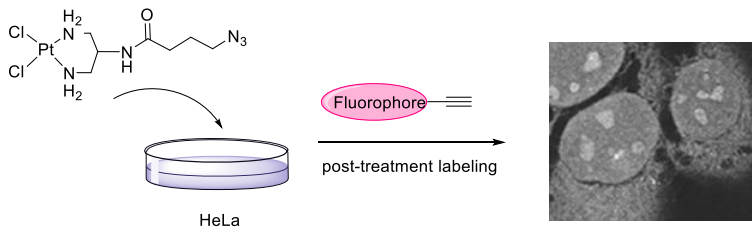


**Figure 1.8.** Complexes and corresponding probes of drug pull-down experiments of a) the DeRose group and b) the Che group. The enrichment is achieved *via* Cu(I)-catalyzed azide-alkyne cycloaddition.

In addition to pull-down experiments, small click handles also open new opportunities to perform localization experiments in fixed cells. Instead of a label for drug enrichment, a fluorophore moiety can be attached to the complex. This post-treatment labeling allows for the preservation of the biological activity compared to previous methods involving fluorophore-drug derivatives. Introduced by Bierbach and co-workers,<sup>74</sup> the technique was also applied by the groups of DeRose (Scheme 1.5) and Che to localize their drugs in nucleoli and mitochondria of HeLa cells, respectively.<sup>73, 75</sup>



**Scheme 1.5.** DeRose and co-workers imaged their platinum-based drug in fixed HeLa cells *via* CuAAC after drug treatment. The compound accumulates in the nucleoli of the nucleus.<sup>75</sup>

To conclude, investigations of protein-target interactions and the mode of action of metallodrugs have expanded from controlled reactions with protein models to proteomic studies that revealed the effect of the metallodrug, and even to the analysis of *in vivo* samples. The combination of these approaches allows for a more realistic insight in the fate of the metallodrug in cells. The enrichment of metal-bound proteins by affinity purification or click chemistry allows for the detection of even low abundant binding partners in complex biological samples by MS.

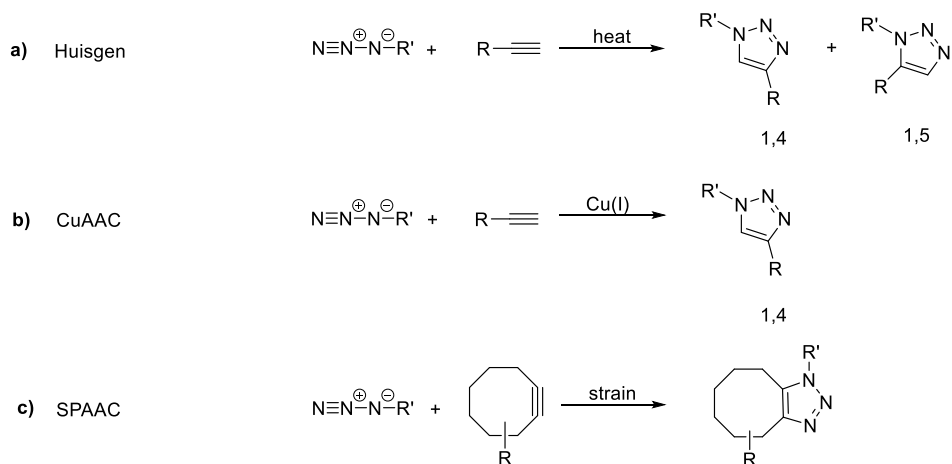
However, so far this approach was associated with rather drastic modifications of the metallodrug (Figure 1.7), which might influence its mode of action and localization.

## 1.5 Click chemistry for studying metal-protein interactions

### 1.5.1 Click chemistry as bioorthogonal reaction

The term “click chemistry” was introduced by Sharpless *et al.* in 2001 to describe reactions of a set of modular small building blocks for the easy, reliable, and fast production of larger desired compounds.<sup>76</sup> The reactions need to fulfill the following criteria: “*modular, wide in scope, give very high yields, generate only inoffensive byproducts that can be removed by nonchromatographic methods, and be stereospecific [...], simple reaction conditions (ideally, the process should be insensitive to oxygen and water), readily available starting materials and reagents, the use of no solvent or a solvent that is benign (such as water) or easily removed, and simple product isolation.*”<sup>76</sup> Typical examples of such reactions are nucleophilic substitution reactions such as the ring opening of strained heterocyclic electrophiles like epoxides or aziridines, and cycloaddition reactions such as the Diels-Alder reaction and the 1,3-dipolar cycloaddition. The latter is the reaction of two unsaturated molecules to give a five-membered heterocycle, *e.g.* the reaction of an azide and an alkyne resulting in the formation of a triazole (Huisgen 1,3-dipolar cycloaddition, Scheme 1.6a). The non-catalyzed Huisgen 1,3-dipolar cycloaddition requires high temperatures, proceeds with moderate speed and yields a mixture of regioisomers. In 2002, the groups of Sharpless and Meldal independently reported on an improved Huisgen 1,3-dipolar cycloaddition, the copper-catalyzed azide-alkyne cycloaddition (CuAAC, Scheme 1.6b).<sup>77, 78</sup> Depending on the amount of catalytic Cu(I), reaction rates between  $10 - 200 \text{ M}^{-1} \cdot \text{s}^{-1}$  can be achieved for the reaction between an azide and a terminal alkyne.<sup>79</sup> The CuAAC is a biorthogonal reaction: the reagents are not abundant in biological systems and react selectively, their small size minimizes the possibility of perturbations with other biological structures, and the reaction conditions are essentially biocompatible. However, Cu(I) is toxic to cells, which limits the application of this reaction in living systems. To overcome this drawback, Bertozzi *et al.* introduced the strain-promoted [3+2] azide-alkyne cycloaddition (SPAAC, Scheme 1.6c) utilizing cyclooctynes.<sup>80</sup> This reaction is faster than the Huisgen 1,3-dipolar cycloaddition ( $10^{-2} - 1 \text{ M}^{-1} \cdot \text{s}^{-1}$ ), and efficient protein labeling in living systems is reported.<sup>79, 81</sup> However, background fluorescence can occur due to reactions of cyclooctynes with cellular nucleophiles such as glutathione.<sup>82</sup>





**Scheme 1.6.** Overview of azide-alkyne reactions.

### 1.5.2 The CuAAC reaction

The CuAAC can be applied to a wide range of substituted azides and alkynes in high yield (82-94%).<sup>77</sup> The usage of the Cu(I) catalyst leads to an improved regioselectivity since only the 1,4 isomer is formed, to mild reaction conditions (reaction proceeds at room temperature), and to an enhanced reaction rate.<sup>83</sup> Different Cu(I) sources can be used, but the best results are usually obtained when preparing the catalyst *in situ* from Cu(II) salts (like CuSO<sub>4</sub>) and sodium ascorbate as reductant. The CuAAC reaction can be performed in almost every solvent: non-coordinating, weakly coordinating, polar solvents, as well as in aqueous solutions.<sup>84</sup> The reaction mechanism of the CuAAC is still discussed, and in particular the involvement of one or two Cu(I) centers in catalysis is debated.<sup>85-87</sup> Ligands such as TBTA (tris(benzyltriazolylmethyl)amine), BTES (bis(tert-butyltriazolmethyl)amine-triazoethyl hydrogen sulfate), THPTA (tris(3-hydroxypropyltriazolylmethyl)amine), have been reported to further decrease the reaction time (Figure 1.9).<sup>88</sup> Those polydentate nitrogen donors bind Cu(I), and stabilize its +1 oxidation state. Therefore, less Cu(I) is required and thus, the reaction is less toxic to cells.<sup>88, 89</sup> Due to the tolerant reaction conditions (wide range of functional groups, solvents, and Cu(I) sources), the CuAAC is used for many applications. It is used in organic synthesis, pharmaceutical science, polymer chemistry, in the synthesis of dendrimers, in material science for surface functionalization,<sup>84, 90</sup> as well as in bioconjugation (like activity-based protein profiling (ABPP) and pull-down assays), as has been summarized in many reviews.<sup>79, 83, 91-93</sup>

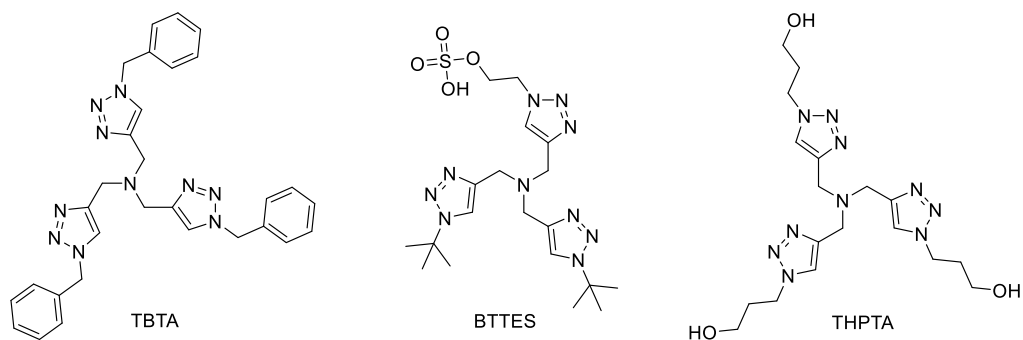


**Figure 1.9.** Tris(triazolylmethyl)amine ligands for CuAAC applications.

## 1.6 Aim and outline of this thesis

The goal of the research described in this thesis was to develop a method to functionalize ruthenium polypyridyl complexes suitable for PACT with an alkyne handle. This handle can be utilized in CuAAC to study the localization and mode of action of the PACT compound within cancer cells. Alkyne functionalization is the smallest handle modification possible, and we investigated whether this minimal modification influences the chemical and biological properties of the (pro)drug. The handle enables CuAAC on the complex, and therefore, the labeling of the complex with a reporter tag. The presence of Cu(I) prevents the application in living cells, however, the efficient labeling *via* CuAAC of the ruthenium-based compound would enable localization of the drug in fixed cells with low background fluorescence.

In Chapter 2, the challenging synthesis of an alkyne-functionalized ruthenium polypyridyl complex is described. In addition, fluorophore labeling of the complex *via* CuAAC click chemistry demonstrated that the ruthenium complex interacts with the model protein BSA after light activation. Furthermore, the results showed that fluorescence labeling is a promising method to identify weak non-covalent metal-protein interactions in gel.

In Chapter 3, two new ruthenium-based phototoxic complexes with lipophilic bidentate ligands are introduced. Their light activation, cellular uptake, and singlet oxygen quantum yield were determined and compared to that of [Ru(tpy)(bpy)(Hmte)](PF<sub>6</sub>)<sub>2</sub>. Depending on the bidentate ligand, the photosubstitution quantum yield can be tuned. In addition, it is shown that the two new complexes are more cytotoxic than their bipyridine analogue due to their

improved cellular uptake. Low singlet oxygen production and light activation in cancer cells supports the true PACT character of these compounds.

In Chapter 4, alkyne-functionalized analogues of the PACT agents introduced in Chapter 3 are reported. Their chemical and biological properties were compared. CuAAC in fixed lung cancer cells allowed for the labeling of the non-emissive ruthenium complexes with a fluorophore. The subcellular location of the labeled complexes was analyzed *via* confocal microscopy imaging and revealed a different mode of action compared to cisplatin.

In Chapter 5, the alkyne functionalization introduced in Chapter 2 was expanded to other polypyridyl ligands coordinated to ruthenium. The known syntheses of the non-functionalized complexes were adjusted to obtain the alkyne analogue complexes. The wide application range of the alkyne functionalization as well as the limitations of this synthesis method are described.

Finally, in Chapter 6, a summary is presented of the main findings described in this thesis, followed by a discussion, and suggestions for further research in this field.

## 1.7 References

- 1 B. Rosenberg, L. Van Camp, and T. Krigas, *Nature* **1965**, 205 (4972), 698-699.
- 2 G. Ciarimboli, *Scientifica* **2012**, 2012 (-), 1-18.
- 3 J. Reedijk, *Platin. Met. Rev.* **2008**, 52 (1), 2-11.
- 4 L. Kelland, *Nat. Rev. Cancer* **2007**, 7 (8), 573-584.
- 5 A. C. Komor and J. K. Barton, *Chem. Commun.* **2013**, 49 (35), 3617-3630.
- 6 W. Han Ang and P. J. Dyson, *Eur. J. Inorg. Chem.* **2006**, 2006 (20), 4003-4018.
- 7 A. Bergamo, A. Masi, A. F. A. Peacock, A. Habtemariam, P. J. Sadler, and G. Sava, *J. Inorg. Biochem.* **2010**, 104 (1), 79-86.
- 8 R. E. Aird, J. Cummings, A. A. Ritchie, M. Muir, R. E. Morris, H. Chen, P. J. Sadler, and D. I. Jodrell, *Br. J. Cancer* **2002**, 86 (10), 1652-1657.
- 9 H.-K. Liu, S. J. Berners-Price, F. Wang, J. A. Parkinson, J. Xu, J. Bella, and P. J. Sadler, *Angew. Chem.* **2006**, 118 (48), 8333-8336.
- 10 H. Chen, J. A. Parkinson, R. E. Morris, and P. J. Sadler, *J. Am. Chem. Soc.* **2003**, 125 (1), 173-186.
- 11 F. Wang, J. Bella, J. A. Parkinson, and P. J. Sadler, *J. Biol. Inorg. Chem.* **2005**, 10 (2), 147-155.
- 12 R. L. Hayward, Q. C. Schornagel, R. Tente, J. S. Macpherson, R. E. Aird, S. Guichard, A. Habtemariam, P. Sadler, and D. I. Jodrell, *Cancer Chemother Pharmacol* **2005**, 55 (6), 577-583.
- 13 C. G. Hartinger, S. Zorbas-Seifried, M. A. Jakupec, B. Kynast, H. Zorbas, and B. K. Keppler, *J. Inorg. Biochem.* **2006**, 100 (5), 891-904.
- 14 C. G. Hartinger, M. A. Jakupec, S. Zorbas-Seifried, M. Groessl, A. Egger, W. Berger, H. Zorbas, P. J. Dyson, and B. K. Keppler, *Chem. Biodiversity* **2008**, 5 (10), 2140-2155.
- 15 O. Dömötör, C. G. Hartinger, A. K. Bytcek, T. Kiss, B. K. Keppler, and E. A. Enyedy, *J. Biol. Inorg. Chem.* **2013**, 18 (1), 9-17.

- 16 R. Trondl, P. Heffeter, C. R. Kowol, M. A. Jakupec, W. Berger, and B. K. Keppler, *Chem. Sci.* **2014**, 5 (8), 2925-2932.
- 17 C. Scolaro, A. Bergamo, L. Brescacin, R. Delfino, M. Cocchietto, G. Laurenczy, T. J. Geldbach, G. Sava, and P. J. Dyson, *J. Med. Chem.* **2005**, 48 (12), 4161-4171.
- 18 M. Groessler, C. G. Hartinger, P. J. Dyson, and B. K. Keppler, *J. Inorg. Biochem.* **2008**, 102 (5-6), 1060-1065.
- 19 B. Wu, M. S. Ong, M. Groessler, Z. Adhireksan, C. G. Hartinger, P. J. Dyson, and C. A. Davey, *Chem. Eur. J.* **2011**, 17 (13), 3562-3566.
- 20 A. Casini, C. Gabbiani, E. Michelucci, G. Pieraccini, G. Moneti, P. Dyson, and L. Messori, *J. Biol. Inorg. Chem.* **2009**, 14 (5), 761-770.
- 21 A. Casini, C. Gabbiani, F. Sorrentino, M. P. Rigobello, A. Bindoli, T. J. Geldbach, A. Marrone, N. Re, C. G. Hartinger, P. J. Dyson, and L. Messori, *J. Med. Chem.* **2008**, 51 (21), 6773-6781.
- 22 A. R. Timerbaev, C. G. Hartinger, S. S. Aleksenko, and B. K. Keppler, *Chem. Rev.* **2006**, 106 (6), 2224-2248.
- 23 A. V. Rudnev, S. S. Aleksenko, O. Semenova, C. G. Hartinger, A. R. Timerbaev, and B. K. Keppler, *J. Sep. Sci.* **2005**, 28 (2), 121-127.
- 24 A. Casini and J. Reedijk, *Chem. Sci.* **2012**, 3 (11), 3135-3144.
- 25 M. P. Sullivan, H. U. Holtkamp, and C. G. Hartinger, Antitumor Metallo-drugs that Target Proteins in *Metallo-Drugs: Development and Action of Anticancer Agents* **2018**, 351-386.
- 26 E. Meggers, *Chem. Commun.* **2009**, - (9), 1001-1010.
- 27 G. Sava, G. Jaouen, E. A. Hillard, and A. Bergamo, *Dalton Trans.* **2012**, 41 (27), 8226-8234.
- 28 A. K. Renfrew, A. D. Phillips, E. Tapavicza, R. Scopelliti, U. Rothlisberger, and P. J. Dyson, *Organometallics* **2009**, 28 (17), 5061-5071.
- 29 N. Graf and S. J. Lippard, *Adv. Drug Delivery Rev.* **2012**, 64 (11), 993-1004.
- 30 U. Jungwirth, C. R. Kowol, B. K. Keppler, C. G. Hartinger, W. Berger, and P. Heffeter, *Antioxid. Redox Signaling* **2011**, 15 (4), 1085-1127.
- 31 M. D. Daniell and J. S. Hill, *ANZ J Surg* **1991**, 61 (5), 340-348.
- 32 D. E. J. G. J. Dolmans, D. Fukumura, and R. K. Jain, *Nat. Rev. Cancer* **2003**, 3 (-), 380-387.
- 33 G. Shi, S. Monro, R. Hennigar, J. Colpitts, J. Fong, K. Kasimova, H. Yin, R. DeCoste, C. Spencer, L. Chamberlain, A. Mandel, L. Lilge, and S. A. McFarland, *Coord. Chem. Rev.* **2015**, 282-283 127-138.
- 34 Y. Arenas, S. Monro, G. Shi, A. Mandel, S. McFarland, and L. Lilge, *Photodiagnosis Photodyn. Ther.* **2013**, 10 (4), 615-625.
- 35 P. Agostinis, K. Berg, K. A. Cengel, T. H. Foster, A. W. Girotti, S. O. Gollnick, S. M. Hahn, M. R. Hamblin, A. Juzeniene, D. Kessel, M. Korbelik, J. Moan, P. Mroz, D. Nowis, J. Piette, B. C. Wilson, and J. Golab, *CA: Cancer J. Clin.* **2011**, 61 (4), 250-281.
- 36 B. Muz, P. de la Puente, F. Azab, and A. K. Azab, *Hypoxia (Auckland, N.Z.)* **2015**, 3 (-), 83-92.
- 37 P. Stadler, A. Becker, H. Jürgen Feldmann, G. Hänsgen, J. Dunst, F. Würschmidt, and M. Molls, *Int. J. Radiat. Oncol., Biol., Phys.* **1999**, 44 (4), 749-754.
- 38 N. J. Farrer, L. Salassa, and P. J. Sadler, *Dalton Trans.* **2009**, - (48), 10690-10701.
- 39 S. Bonnet, *Dalton Trans.* **2018**, 47 (31), 10330-10343.
- 40 V. H. S. van Rixel, B. Siewert, S. L. Hopkins, S. H. C. Askes, A. Busemann, M. A. Siegler, and S. Bonnet, *Chem. Sci.* **2016**, 7 (8), 4922-4929.
- 41 L. N. Lameijer, T. G. Brevé, V. H. S. van Rixel, S. H. C. Askes, M. A. Siegler, and S. Bonnet, *Chem. Eur. J.* **2018**, 24 (11), 2709-2717.
- 42 A. Li, C. Turro, and J. J. Kodanko, *Chem. Commun.* **2018**, 54 (11), 1280-1290.

- 43 M. Huisman, J. K. White, V. G. Lewalski, I. Podgorski, C. Turro, and J. J. Kodanko, *Chem. Commun.* **2016**, 52 (85), 12590-12593.
- 44 T. N. Rohrabough, A. M. Rohrabough, J. J. Kodanko, J. K. White, and C. Turro, *Chem. Commun.* **2018**, 54 (41), 5193-5196.
- 45 J.-A. Cuello-Garibo, M. S. Meijer, and S. Bonnet, *Chem. Commun.* **2017**, 53 (50), 6768-6771.
- 46 L. N. Lameijer, D. Ernst, S. L. Hopkins, M. S. Meijer, S. H. Askes, S. E. Le Dévédec, and S. Bonnet, *Angew. Chem., Int. Ed.* **2017**, 56 (38), 11549-11553.
- 47 J.-A. Cuello-Garibo, C. C. James, M. A. Siegler, and S. Bonnet, *Chem. Sq* **2017**, 1 (2), 1-19.
- 48 A. Bijelic, S. Theiner, B. K. Keppler, and A. Rompel, *J. Med. Chem.* **2016**, 59 (12), 5894-5903.
- 49 A. Casini, A. Guerri, C. Gabbiani, and L. Messori, *J. Inorg. Biochem.* **2008**, 102 (5), 995-1006.
- 50 L. Trynda-Lemiesz, A. Karaczyn, B. K. Keppler, and H. Kozlowski, *J. Inorg. Biochem.* **2000**, 78 (4), 341-346.
- 51 M. Groessl and P. J. Dyson, *Curr. Top. Med. Chem.* **2011**, 11 (21), 2632-2646.
- 52 A. Casini, G. Mastrobuoni, W. H. Ang, C. Gabbiani, G. Pieraccini, G. Moneti, P. J. Dyson, and L. Messori, *ChemMedChem* **2007**, 2 (5), 631-635.
- 53 A. Casini, A. Karotki, C. Gabbiani, F. Rugi, M. Vasak, L. Messori, and P. J. Dyson, *Metallomics* **2009**, 1 (5), 434-441.
- 54 C. G. Hartinger, A. Casini, C. Duhot, Y. O. Tsybin, L. Messori, and P. J. Dyson, *J. Inorg. Biochem.* **2008**, 102 (12), 2136-2141.
- 55 M. Groessl, O. Zava, and P. J. Dyson, *Metallomics* **2011**, 3 (6), 591-599.
- 56 M.-Y. Ho, M.-L. Chiou, R.-C. Chang, Y.-H. Chen, and C.-C. Cheng, *J. Inorg. Biochem.* **2010**, 104 (5), 614-617.
- 57 C. G. Hartinger, M. Groessl, S. M. Meier, A. Casini, and P. J. Dyson, *Chem. Soc. Rev.* **2013**, 42 (14), 6186-6199.
- 58 H. U. Holtkamp and C. G. Hartinger, *Trends Anal. Chem.* **2018**, 104 (-), 110-117.
- 59 C. Artner, H. U. Holtkamp, W. Kandioller, C. G. Hartinger, S. M. Meier-Menches, and B. K. Keppler, *Chem. Commun.* **2017**, 53 (57), 8002-8005.
- 60 I. Khalaila, A. Bergamo, F. Bussy, G. Sava, and P. J. Dyson, *Int. J. Oncol.* **2006**, 29 (1), 261-268.
- 61 M.-Y. Ho, M.-L. Chiou, W.-S. Du, F. Y. Chang, Y.-H. Chen, Y.-J. Weng, and C.-C. Cheng, *J. Inorg. Biochem.* **2011**, 105 (6), 902-910.
- 62 M. P. Washburn, D. Wolters, and J. R. Yates, *Nat Biotech* **2001**, 19 (3), 242-247.
- 63 J. Will, A. Kyas, W. Sheldrick, and D. Wolters, *J. Biol. Inorg. Chem.* **2007**, 12 (6), 883-894.
- 64 R. F. S. Lee, A. Chernobrovkin, D. Rutishauser, C. S. Allardyce, D. Hacker, K. Johnsson, R. A. Zubarev, and P. J. Dyson, *Scientific Reports* **2017**, 7 (1), 1590-1600.
- 65 S. P. Gygi, B. Rist, S. A. Gerber, F. Turecek, M. H. Gelb, and R. Aebersold, *Nat. Biotech.* **1999**, 17 (10), 994-999.
- 66 T. W. Hutchens and T.-T. Yip, *Rapid Commun. Mass Spectrom.* **1993**, 7 (7), 576-580.
- 67 M. V. Babak, S. M. Meier, K. V. M. Huber, J. Reynisson, A. A. Legin, M. A. Jakupec, A. Roller, A. Stukalov, M. Gridling, K. L. Bennett, J. Colinge, W. Berger, P. J. Dyson, G. Superti-Furga, B. K. Keppler, and C. G. Hartinger, *Chem. Sci.* **2015**, 6 (4), 2449-2456.
- 68 S. M. Meier, D. Kreutz, L. Winter, M. H. M. Klose, K. Cseh, T. Weiss, A. Bileck, B. Alte, J. C. Mader, S. Jana, A. Chatterjee, A. Bhattacharyya, M. Hejl, M. A. Jakupec, P. Heffeter, W. Berger, C. G. Hartinger, B. K. Keppler, G. Wiche, and C. Gerner, *Angew. Chem., Int. Ed.* **2017**, 56 (28), 8267-8271.
- 69 J. D. White, M. F. Osborn, A. D. Moghaddam, L. E. Guzman, M. M. Haley, and V. J. DeRose, *J. Am. Chem. Soc.* **2013**, 135 (32), 11680-11683.

- 70 M. F. Osborn, J. D. White, M. M. Haley, and V. J. DeRose, *ACS Chem. Biol.* **2014**, 9 (10), 2404-2411.
- 71 R. M. Cunningham and V. J. DeRose, *ACS Chem. Biol.* **2017**, 12 (11), 2737-2745.
- 72 D. Hu, Y. Liu, Y.-T. Lai, K.-C. Tong, Y.-M. Fung, C.-N. Lok, and C.-M. Che, *Angew. Chem., Int. Ed.* **2016**, 55 (4), 1387-1391.
- 73 S. K. Fung, T. Zou, B. Cao, P.-Y. Lee, Y. M. E. Fung, D. Hu, C.-N. Lok, and C.-M. Che, *Angew. Chem.* **2017**, 129 (14), 3950-3954.
- 74 S. Ding, X. Qiao, J. Suryadi, G. S. Marrs, G. L. Kucera, and U. Bierbach, *Angew. Chem.* **2013**, 125 (12), 3434-3438.
- 75 R. Wirth, J. D. White, A. D. Moghaddam, A. L. Ginzburg, L. N. Zakharov, M. M. Haley, and V. J. DeRose, *J. Am. Chem. Soc.* **2015**, 137 (48), 15169-15175.
- 76 H. C. Kolb, M. G. Finn, and K. B. Sharpless, *Angew. Chem., Int. Ed.* **2001**, 40 (11), 2004-2021.
- 77 V. V. Rostovtsev, L. G. Green, V. V. Fokin, and K. B. Sharpless, *Angew. Chem., Int. Ed.* **2002**, 41 (14), 2596-2599.
- 78 C. W. Tornøe, C. Christensen, and M. Meldal, *J. Org. Chem.* **2002**, 67 (9), 3057-3064.
- 79 K. Lang and J. W. Chin, *ACS Chem. Biol.* **2014**, 9 (1), 16-20.
- 80 N. J. Agard, J. A. Prescher, and C. R. Bertozzi, *J. Am. Chem. Soc.* **2004**, 126 (46), 15046-15047.
- 81 N. J. Agard, J. M. Baskin, J. A. Prescher, A. Lo, and C. R. Bertozzi, *ACS Chem. Biol.* **2006**, 1 (10), 644-648.
- 82 C. S. McKay and M. G. Finn, *Chem. Biol.* **2014**, 21 (9), 1075-1101.
- 83 M. D. Best, *Biochemistry* **2009**, 48 (28), 6571-6584.
- 84 L. Liang and D. Astruc, *Coord. Chem. Rev.* **2011**, 255 (23), 2933-2945.
- 85 V. O. Rodionov, V. V. Fokin, and M. G. Finn, *Angew. Chem.* **2005**, 117 (15), 2250-2255.
- 86 M. Meldal and C. W. Tornøe, *Chem. Rev.* **2008**, 108 (8), 2952-3015.
- 87 B. T. Worrell, J. A. Malik, and V. V. Fokin, *Science* **2013**, 340 (6131), 457-460.
- 88 C. Besanceney-Webler, H. Jiang, T. Zheng, L. Feng, D. Soriano del Amo, W. Wang, L. M. Klivansky, F. L. Marlow, Y. Liu, and P. Wu, *Angew. Chem., Int. Ed.* **2011**, 50 (35), 8051-8056.
- 89 V. Hong, N. F. Steinmetz, M. Manchester, and M. G. Finn, *Bioconjugate Chem.* **2010**, 21 (10), 1912-1916.
- 90 C. D. Hein, X.-M. Liu, and D. Wang, *Pharm. Res.* **2008**, 25 (10), 2216-2230.
- 91 C. P. Ramil and Q. Lin, *Chem. Commun.* **2013**, 49 (94), 11007-11022.
- 92 D. M. Patterson, L. A. Nazarova, and J. A. Prescher, *ACS Chem. Biol.* **2014**, 9 (3), 592-605.
- 93 E. M. Sletten and C. R. Bertozzi, *Angew. Chem., Int. Ed.* **2009**, 48 (38), 6974-6998.

# 2

## ALKYNE FUNCTIONALIZATION OF PHOTOACTIVATED RUTHENIUM COMPLEX [RU(TPY)(BPY)(HMTE)](PF<sub>6</sub>)<sub>2</sub> FOR PROTEIN INTERACTION STUDIES

*A synthetic procedure for the generation of the alkyne-functionalized ruthenium polypyridyl complex [Ru(HCC-tpy)(bpy)(Hmte)](PF<sub>6</sub>)<sub>2</sub>, where HCC-tpy = 4'-ethynyl-2,2':6',2''-terpyridine, bpy = 2,2'-bipyridine, and Hmte = 2-(methylthio)ethanol was developed. The alkyne group allows for the detection of the interaction between the metal complex and bovine serum albumin (BSA) using copper-catalyzed click chemistry with an azide-labelled fluorophore and gel electrophoresis. This method demonstrates that a) the interaction between the ruthenium complex and BSA is strictly controlled by light irradiation and b) visualization is possible of weak complex-protein interactions that are difficult to study using traditional methods such as UV-vis spectroscopy or ESI MS. Overall, these results indicate that the combination of photoactivation and fluorophore post-labelling is an elegant method to study weak interactions.*

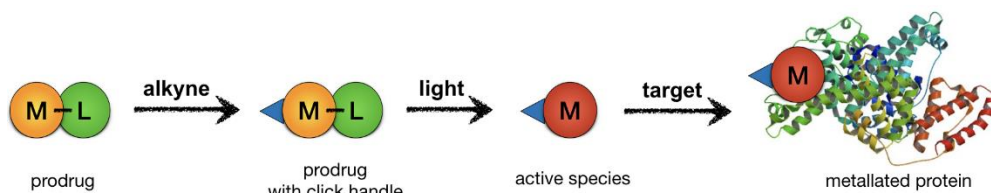
## 2.1 Introduction

Cytotoxicity assays, cell uptake studies, and cell fractionation experiments are typically performed to study the biological effects and the intracellular fate of metal-based anticancer compounds.<sup>1-4</sup> In addition, experiments regarding the interaction of the metallodrug with isolated biomolecules provide insights about possible targets and binding sites. A frequently studied protein in bioinorganic chemistry is serum albumin. It is the most abundant protein in the blood stream (35 – 50 g/L) and thus a highly likely binding partner for injected metallodrugs. Serum albumin is responsible for the transport of biomolecules,<sup>5</sup> it can act as drug carrier and reservoir,<sup>6-10</sup> and might support drug accumulation in tumor cells.<sup>6</sup> It has, however, been demonstrated that interaction of anticancer drugs with serum albumin can cause undesired side effects,<sup>6, 11</sup> and can hinder the interaction with the actual targets of the drug.<sup>12</sup> Bovine serum albumin (BSA) is a model protein for human serum albumin (HSA),<sup>10</sup> with which it shares 76% of sequence homology,<sup>13</sup> and it is a major component of cell-growth medium.

Common methods to investigate metallodrug-protein interactions are X-ray diffraction analysis,<sup>11, 14, 15</sup> electrospray ionization mass spectrometry (ESI),<sup>16</sup> UV-vis spectroscopy,<sup>17</sup> and circular dichroism (CD) spectroscopy.<sup>18</sup> For emissive metallodrugs, the complex and its interaction with biomolecules can be imaged in gel electrophoresis or in cells by emission microscopy.<sup>19, 20</sup> An effective approach to visualize non-emissive complexes is fluorophore labeling of the metallodrug *via* Cu(I)-catalyzed azide-alkyne cycloaddition (CuAAC).<sup>21, 22</sup> However, this method requires the modification of the complex with an azide or alkyne click handle. The synthesis of those functionalized polypyridyl complexes is challenging: Azide-functionalized ruthenium complexes are known to be unstable,<sup>23, 24</sup> and alkynes can act as ligands for ruthenium and cobalt centers,<sup>25</sup> leading to formation of byproducts.<sup>26</sup> So far, higher yields for the synthesis of alkyne-functionalized ruthenium complexes are only achieved by utilization of silver(I) ions. These are used to either enhance the ligand exchange process,<sup>23</sup> or to remove the protecting group that was used to prevent alkyne coordination to the metal center.<sup>27</sup> Silver ions, however, are toxic and thus, the complexes synthesized according to these reaction procedures may contain traces of the heavy metal and thus cannot be used in living systems.<sup>28</sup>



The ruthenium polypyridyl complex  $[\text{Ru}(\text{tpy})(\text{bpy})(\text{Hmte})](\text{PF}_6)_2$  ( $[\mathbf{1}](\text{PF}_6)_2$ , where  $\text{tpy} = 2,2':6',2''$ -terpyridine,  $\text{bpy} = 2,2'$ -bipyridine, and  $\text{Hmte} = 2$ -(methylthio)ethanol) is such a non-emissive complex that cannot be easily followed in cells.<sup>29</sup> In the dark, the interaction of  $[\mathbf{1}](\text{PF}_6)_2$  with proteins is prevented by the protecting monodentate  $\text{Hmte}$  ligand. Only after controlled photosubstitution of the thioether ligand by a solvent molecule, coordination of the activated drug to proteins or DNA is possible, an idea that is central in ruthenium-based photoactivated chemotherapy (PACT).<sup>30, 31</sup> By doing so, the biological activity of the metal complex can be controlled, in contrast to thermally unstable complexes such as  $[\text{Ru}(\text{tpy})(\text{bpy})(\text{Cl})]\text{Cl}$  or  $\text{RAPTA-C}$ , which hydrolyze quickly in aqueous solution.<sup>32-34</sup> However, this light-controlled protein interaction has never been demonstrated experimentally. Here, an alkyne-functionalized analogue of photoactivatable ruthenium complex  $[\mathbf{1}](\text{PF}_6)_2$  was synthesized,  $[\text{Ru}(\text{HCC-tpy})(\text{bpy})(\text{Hmte})](\text{PF}_6)_2$  ( $[\mathbf{2}](\text{PF}_6)_2$ , where  $\text{HCC-tpy} = 4'$ -ethynyl- $2,2':6',2''$ -terpyridine). The synthesis procedure of the complex with a simple CCH group was developed, and the light-controlled interaction of  $[\mathbf{2}](\text{PF}_6)_2$  with BSA was studied by fluorophore labeling *via* CuAAC (Scheme 2.1). This method is compared with two known methods for studying BSA-metallodrug interaction, *i.e.* UV-vis spectroscopy and ESI MS.



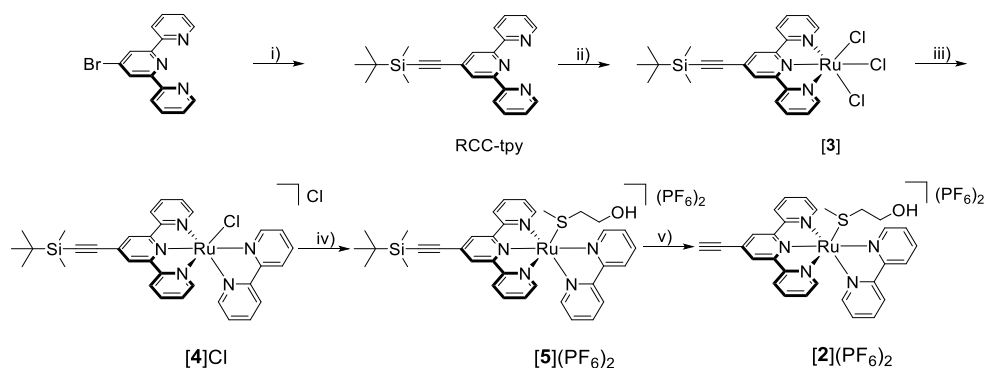
**Scheme 2.1.** Schematic overview of the interaction of an alkyne-functionalized ruthenium-based drug with its biological target after visible light activation.

## 2.2 Results and Discussion

### 2.2.1 Synthesis and characterization

An alkyne-functionalized analogue of the ruthenium polypyridyl complex  $[\mathbf{1}](\text{PF}_6)_2$  was synthesized by placing an alkyne moiety in the  $4'$ -position of the  $\text{tpy}$  ligand. By doing so, the symmetry of the resulting complex is preserved, while monosubstitution of the ligands on any other position would lead to the formation of stereoisomers. Since the alkyne-protecting triisopropylsilyl (TIPS) group was reported to be difficult to remove,<sup>35</sup> the use of trimethylsilyl (TMS) and *tert*-butyldimethylsilyl (TBDMS) was investigated. Both are known protecting

groups for terminal alkynes, but they are more readily removed compared to TIPS. In our hands, the TMS protecting group was not stable enough to withstand subsequent reaction steps, leading to the formation of undesired byproducts. Therefore, the synthesis of the alkyne-functionalized ruthenium complex  $[2](PF_6)_2$  was finally realized using the TBDMS group (Scheme 2.2). The alkyne-functionalized tpy ligand (RCC-tpy, where R = TBDMS) was synthesized using a Sonogashira coupling,<sup>26</sup> purified by column chromatography, and the desired product RCC-tpy was obtained with a yield of 95%. Instead of using a ruthenium(II) precursor, as reported elsewhere,<sup>27, 36</sup> RCC-tpy was reacted with ruthenium(III) chloride, to obtain  $[Ru(RCC-tpy)(Cl)_3]$  (**[3]**). The reaction with bpy in ethanol/water (3:1) yielded the desired ruthenium(II) product  $[Ru(RCC-tpy)(bpy)(Cl)Cl]$  (**[4]Cl**) in a yield of 83%. The chloride ligand was then substituted in a reaction with Hmte in pure water at 60 °C for 16 h. Precipitation of the product after the reaction was achieved by addition of saturated aqueous potassium hexafluoridophosphate. Two singlets at 1.10 and 0.32 ppm in the  $^1H$  NMR spectrum in acetone- $d_6$  (Figure AII.1) integrating for nine and six protons, respectively, and the major peak in the MS spectrum at  $m/z = 360.9$  confirmed the stability of the TBDMS protecting group during ligand exchange and the nature of  $[Ru(RCC-tpy)(bpy)(Hmte)]^{2+}$  (calc.  $m/z = 360.6$  for **[5]<sup>2+</sup>**). Noteworthy, when coordination of Hmte was performed at 80 °C, TBDMS protection was not fully retained, resulting in the formation of byproducts. Analysis of these byproducts showed that the ruthenium center can act as a catalyst in the reaction of a terminal alkyne with alcohol groups (ethanol or Hmte), leading to formation of enol esters (see Scheme AII.1).<sup>37</sup> These findings emphasized that the TBDMS protecting group was necessary to protect the alkyne as long as the ruthenium center bears labile ligands or goes through ligand exchange. Controlled deprotection of the alkyne in **[5](PF<sub>6</sub>)<sub>2</sub>** was performed using five equivalents of potassium fluoride in methanol at 30 °C.  $^1H$  NMR in acetone- $d_6$  shows the disappearance of the two singlets of the protecting TBDMS group concomitant with the appearance of a new singlet at 4.55 ppm integrating for one proton, characteristic for the free alkyne (Figure AII.2). In combination with mass spectrometry, the successful synthesis of  $[Ru(HCC-tpy)(bpy)(Hmte)](PF_6)_2$  (**[2](PF<sub>6</sub>)<sub>2</sub>**,  $m/z = 303.5$ ; calc.  $m/z = 303.6$  for **[2]<sup>2+</sup>**), was confirmed.



**Scheme 2.2.** Reaction scheme of the stepwise synthesis of  $[\mathbf{2}](\text{PF}_6)_2$ . Conditions: i) CuI, Pd(PPh<sub>3</sub>)<sub>2</sub>Cl<sub>2</sub>, TBDMS-ethyne, Et<sub>3</sub>N, 80 °C, N<sub>2</sub>, 7 h; 95% ii) RuCl<sub>3</sub>, ethanol, 80 °C, 16 h; 75% iii) bpy, LiCl, Et<sub>3</sub>N, ethanol/water (3:1), 60 °C, 16 h; 83% iv) Hmte, water, 60 °C, N<sub>2</sub>, 16 h, aq. KPF<sub>6</sub>; 85% v) KF, methanol, 30 °C, 16 h, aq. KPF<sub>6</sub>; 76%.

Dark red rhombic single crystals of  $[\mathbf{2}](\text{PF}_6)_2$  suitable for X-ray structure determination were obtained through slow vapor diffusion of diisopropyl ether into a solution of  $[\mathbf{2}](\text{PF}_6)_2$  in acetonitrile (Figure 2.1). Selected bond lengths and angles are summarized in Table 2.1, together with those reported for the structure of  $[\mathbf{1}](\text{PF}_6)_2$ .<sup>29</sup> The alkyne bond length (C17≡C16 = 1.180(4) Å) is comparable with that of published data.<sup>27</sup> The Ru-N bond distances of the tpy as well as of the bpy ligand in  $[\mathbf{2}](\text{PF}_6)_2$  are not significantly different from those in the non-functionalized analogue  $[\mathbf{1}](\text{PF}_6)_2$ . Hmte is bound *via* the sulfur atom with a Ru-S bond distance of 2.3764(6) Å, which is slightly longer than in  $[\mathbf{1}](\text{PF}_6)_2$ .<sup>38</sup> Therefore, it can be concluded that the alkyne moiety has no significant effect on the geometry of  $[\mathbf{2}](\text{PF}_6)_2$  compared to  $[\mathbf{1}](\text{PF}_6)_2$ .

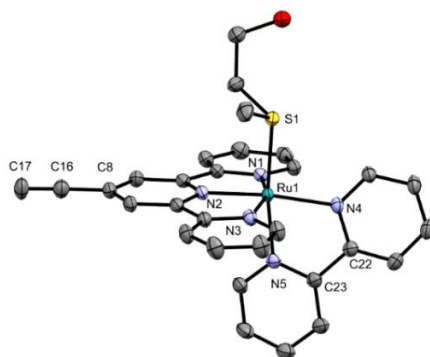


**Figure 2.1.** Displacement ellipsoid (50% probability level) of the cationic part of  $[\mathbf{2}](\text{PF}_6)_2$  as observed in the crystal structure. Counter ions and H atoms have been omitted for clarity.

**Table 2.1.** Selected bond lengths (Å) and angles (°) for [2](PF<sub>6</sub>)<sub>2</sub> and [1](PF<sub>6</sub>)<sub>2</sub>.

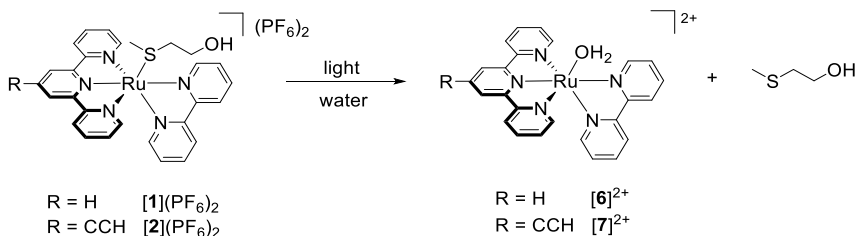
	[2](PF <sub>6</sub> ) <sub>2</sub>	[1](PF <sub>6</sub> ) <sub>2</sub> <sup>a</sup>
Ru-N1	2.0566(19)	2.061(1)
Ru-N2	1.9568(19)	1.961(1)
Ru-N3	2.0709(19)	2.066(1)
Ru-N4	2.0948(18)	2.092(1)
Ru-N5	2.0676(19)	2.064(1)
Ru-S1	2.3764(6)	2.3690(5)
C17-C16	1.180(4)	-
C16-C8	1.440(3)	-
N1-Ru1-N2	79.90(8)	80.08(6)
N2-Ru1-N3	79.92(8)	79.39(6)
N1-Ru1-N3	159.55(8)	159.31(6)
N4-Ru1-N5	78.12(7)	78.12(6)

<sup>a</sup> Data taken from Bahreman *et al.*<sup>29</sup>

### 2.2.2 Photochemistry of [2](PF<sub>6</sub>)<sub>2</sub>

[1](PF<sub>6</sub>)<sub>2</sub> is known to be stable in the dark while light irradiation initiates the substitution of the thioether ligand by a water molecule ([6]<sup>2+</sup>, Scheme 2.3).<sup>29</sup> To test whether alkyne-functionalized [2](PF<sub>6</sub>)<sub>2</sub> possesses the same photochemical properties, UV-vis spectra of a solution of [2](PF<sub>6</sub>)<sub>2</sub> in water were recorded. The absorbance spectrum of [2](PF<sub>6</sub>)<sub>2</sub> in aqueous solution is characterized by an absorption maximum at 470 nm, and when kept in the dark, the complex is stable at 37 °C for 16 h (see Figure AII.3 and AII.4). However, when irradiated with a green LED (517 nm) at 37 °C in water, the UV-vis spectrum of [2](PF<sub>6</sub>)<sub>2</sub> showed a bathochromic shift of the maximum to 491 nm (Figure 2.2). This change was accompanied by a change of the major peaks in MS spectra from *m/z* = 303.2 ([2]<sup>2+</sup>, calc. *m/z* = 303.6) to *m/z* = 266.2, indicating the formation of the aqua complex [Ru(HCC-tpy)(bpy)(OH<sub>2</sub>)]<sup>2+</sup> ([7]<sup>2+</sup>, calc. *m/z* = 266.5, Figure AII.5). The photosubstitution was completed after approximately 30 min of irradiation, corresponding to a photosubstitution quantum yield Φ<sub>470</sub> of 0.021 in water (Table 2.2). These results are comparable to those found for the non-functionalized analogue [1](PF<sub>6</sub>)<sub>2</sub>, which under blue light irradiation (452 nm) showed a quantum yield Φ<sub>450</sub> of 0.022.<sup>29</sup> In addition, [1](PF<sub>6</sub>)<sub>2</sub> and [2](PF<sub>6</sub>)<sub>2</sub> show similar low singlet oxygen generation quantum yields (Φ<sub>Δ</sub>) and phosphorescence quantum yields (Φ<sub>P</sub>)

(Table 2.2, Figure AII.6). These results demonstrated that the alkyne moiety in  $[2]^{2+}$  does not have a significant effect on the photochemical properties of the complex compared to  $[1]^{2+}$ .



**Scheme 2.3.** Photosubstitution reaction of  $[1](\text{PF}_6)_2$  and  $[2](\text{PF}_6)_2$  in aqueous solution.

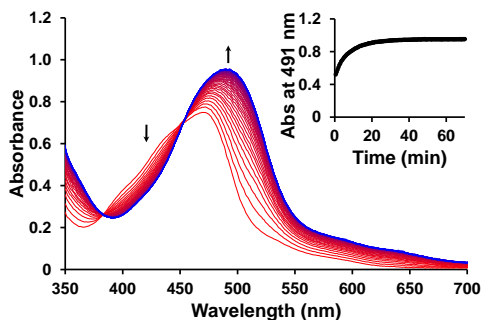


**Figure 2.2.** Evolution of the UV-vis absorption spectra (region 350 – 700 nm) of a solution of  $[2](\text{PF}_6)_2$  in water upon green light irradiation. Conditions:  $[\text{Ru}] = 0.074 \text{ mM}$ ,  $T = 37 \text{ }^\circ\text{C}$ , light source:  $\lambda = 517 \text{ nm}$ ,  $\Delta\lambda_{1/2} = 23 \text{ nm}$ ,  $5.42 \text{ mW}$ , photon flux  $\Phi = 5.4 \cdot 10^{-8} \text{ mol} \cdot \text{s}^{-1}$ ,  $V = 3 \text{ mL}$ , under air atmosphere. Inset: Time evolution of absorbance at wavelength 491 nm.

**Table 2.2** Maximum absorption wavelengths ( $\lambda_{\text{max}}$  in nm), molar absorption coefficient ( $\epsilon$  in  $\text{M}^{-1} \cdot \text{cm}^{-1}$ ), phosphorescence quantum yield ( $\Phi_{\text{P}}$ ) in methanol- $\text{d}_6$ , singlet oxygen generation quantum yield ( $\Phi_{\Delta}$ ) in methanol- $\text{d}_6$ , and photosubstitution quantum yields ( $\Phi_{\text{max}}$ ) in water at  $25 \text{ }^\circ\text{C}$  for complexes  $[2](\text{PF}_6)_2$  and  $[1](\text{PF}_6)_2$ .

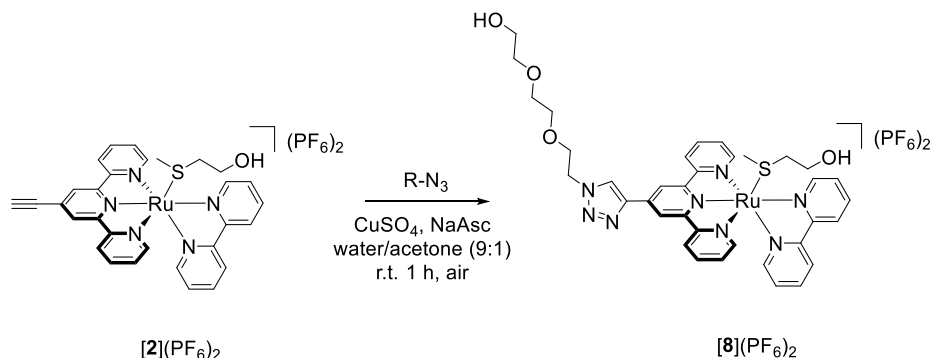
	$\lambda_{\text{max}}^{\text{a)}$	$\epsilon_{\lambda_{\text{max}}}^{\text{a)}$	$\Phi_{\text{P}}^{\text{b)}$	$\Phi_{\Delta}^{\text{b)}$	$\Phi_{\text{max}}^{\text{a)}$
$[2](\text{PF}_6)_2$	470	$9.54 \cdot 10^3$	$< 1.0 \cdot 10^{-4}$	0.007	0.021 <sup>d)</sup>
$[1](\text{PF}_6)_2$	450 <sup>c)</sup>	$6.60 \cdot 10^3$ <sup>c)</sup>	$< 1.0 \cdot 10^{-4}$	$< 0.005$	0.022 <sup>c), e)</sup>

<sup>a)</sup> in MiliQ water, <sup>b)</sup> in methanol- $\text{d}_6$ , <sup>c)</sup> Data from Bahreman *et al.*<sup>29</sup>, <sup>d)</sup> at 470 nm, <sup>e)</sup> at 450 nm

### 2.2.3 CuAAC reaction on ruthenium complex

To test whether the alkyne-functionalization allows for the CuAAC reaction on the ruthenium complex,  $[2](\text{PF}_6)_2$  was reacted with an excess of 2-(2-(2-azidoethoxy)ethoxy)ethanol in the presence of catalytic amounts of Cu(II)

and sodium ascorbate in a water/acetone mixture (9:1) at 25 °C for 1 h (Scheme 2.4). MS analysis of the reaction mixture showed peaks centered at  $m/z = 391.2$  corresponding to the click product  $[8]^{2+}$  (calc.  $m/z = 391.1$ ). The signal of the starting material  $[2]^{2+}$  at calc.  $m/z = 303.6$  had disappeared. After liquid-liquid extraction from dichloromethane, the  $^1\text{H}$  NMR spectrum in acetone- $d_6$  showed no singlet peak at 4.56 ppm corresponding to the terminal alkyne, but a new singlet at 9.04 ppm for the triazole formation (Figure AII.7). Overall, the CuAAC reaction on  $[2](\text{PF}_6)_2$  was successful and full conversion after 1 h reaction time was demonstrated.



**Scheme 2.4.** Reaction procedure of the CuAAC reaction of  $[2](\text{PF}_6)_2$  with  $\text{R-N}_3$  (2-(2-(2-azidoethoxy)ethoxy)ethanol).

### 2.2.4 Investigation of the interaction between $[2]^{2+}$ and BSA

The interaction of  $[2](\text{PF}_6)_2$  and BSA was investigated by fluorophore-labeling *via* CuAAC reaction on the alkyne-functionalized complex-BSA adduct with an azide-fluorophore (Alexa Fluor™ 647 azide, A647), and analyzed by gel electrophoresis (Figure 2.3). Incubation of Hmte-protected  $[2](\text{PF}_6)_2$  (75  $\mu\text{M}$ ) with BSA (15  $\mu\text{M}$ ) for 24 h at 37 °C in the dark did not result in a fluorescent signal after the CuAAC reaction (Figure 2.3, lane 1), indicating that the protected complex could not bind to BSA. However, when the mixture was irradiated with green light ( $\lambda = 520$  nm) for 1 h, and then further incubated with BSA in the dark for 6 or 24 h, a fluorescent band appeared between 55 and 70 kDa (Figure 2.3, lane 6 for 6 h and lane 12 for 24 h). This result indicated that i) light-activation of the complex was successful and allowed for controlling the interaction of the complex with BSA, ii) the complex-BSA adduct can be labelled with a fluorophore by CuAAC, and iii) adduct formation between the ruthenium complex and BSA increases over time (quantitatively shown by elevated levels of fluorescence intensity of the band when going from 6 to 24 h incubation time). Several negative controls were performed *e.g.* samples with non-functionalized complex  $[1](\text{PF}_6)_2$  (Figure 2.3, lane 3 and 8) or without any complex (Figure 2.3, lane 5). These samples did not result in any

significant labelling. A low background fluorescence in lane 5 was observed due to unspecific binding of the fluorophore A647 to BSA. Indeed, this was confirmed by BSA-free controls (lane 4) and fluorophore-free controls (lane 2, 7, and 10 in Figure 2.3), as these did not exhibit any fluorescence. If not activated, [2](PF<sub>6</sub>)<sub>2</sub> remained thermally stable for the entire incubation time (lane 13 in Figure 2.3 and Figure AII.4). Upon increased BSA concentrations, the intensity of the fluorescent band increased as well (BSA concentrations vary from 5 to 20 μM, Ru:BSA 5:1, 5:3, and 5:5, Figure AII.8 and AII.9). These experiments showed that the fluorescence intensity of the bands is correlated to the increased BSA concentration. Thus, the interaction between [2]<sup>2+</sup> and BSA appears to be dose-dependent.

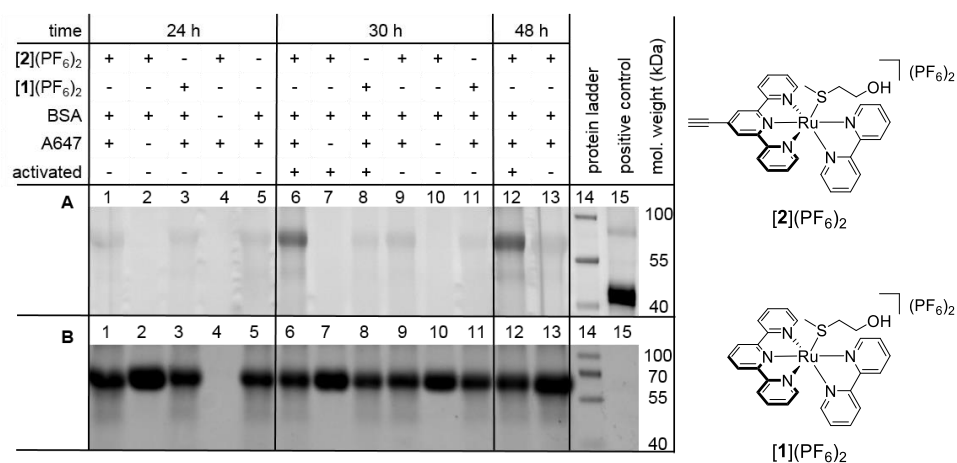


**Figure 2.3.** Polyacrylamide gel electrophoresis (PAGE) showing post-labeled Ru-bound BSA (A). Fluorescence labeling is achieved *via* CuAAC reaction with A647. The protecting Hmte ligand of [2](PF<sub>6</sub>)<sub>2</sub> prevents interaction with BSA, resulting in the absence of fluorescence labeling (lane 1, 9, and 13). Light irradiation after 24 h generates the aqua complex [7]<sup>2+</sup> that interacts with BSA after 6 and 24 h incubation in the dark (lane 6 and 12, respectively). Control reactions with alkyne-free [1](PF<sub>6</sub>)<sub>2</sub> (lane 3 and 8), without A647 (lane 2, 7, and 10), and without BSA (lane 4) show no fluorescent labeling. Coomassie staining (B). Conditions: [Ru] = 75 μM, [BSA] = 15 μM. Green light activation: λ = 520 nm, light dosage: 76 J/cm<sup>2</sup>, t = 1 h, T = 37 °C. Click conditions: 2.5 μM A647, 3.2 mM CuSO<sub>4</sub>, 18.8 mM NaAsc, 0.7 mM THPTA, 46.3 mM Tris-HCl, t = 1h, T = 25 °C. Lane 14: prestained protein ladder, lane 15: positive control: alkyne-substituted vinculin, Homopropargylglycine-Vin.

To further explore the added value of this method to study the BSA-Ru interaction, the interaction between the ruthenium complex and BSA was investigated with UV-vis spectroscopy. First, the absorbance spectra of solutions of only the complexes (15 μM) or BSA (15 μM) were recorded separately in PBS for 24 h at 37 °C (Figure AII.10 and AII.11). The unchanged UV-vis spectra indicated the thermal stability of

both individual species. Thereafter, the absorbance spectra of mixtures of the ruthenium complexes (15  $\mu\text{M}$ ) and BSA (15  $\mu\text{M}$ ) were recorded under the same conditions. The spectrum of the solution of  $[\mathbf{1}](\text{PF}_6)_2$  and BSA did not change during 24 h, as expected for the Hmte-protected complex (Figure 2.4a). However, when using  $[\mathbf{6}]^{2+}$ , the UV-vis spectrum also did not show a change (Figure 2.4b). Similar results were obtained when using alkyne-functionalized complexes  $[\mathbf{2}](\text{PF}_6)_2$  and  $[\mathbf{7}]^{2+}$  in the presence of BSA (Figure 2.4c and d). Therefore, it appeared that the interaction between ruthenium complexes and BSA after light activation cannot be monitored using UV-vis spectroscopy under the conditions reported.

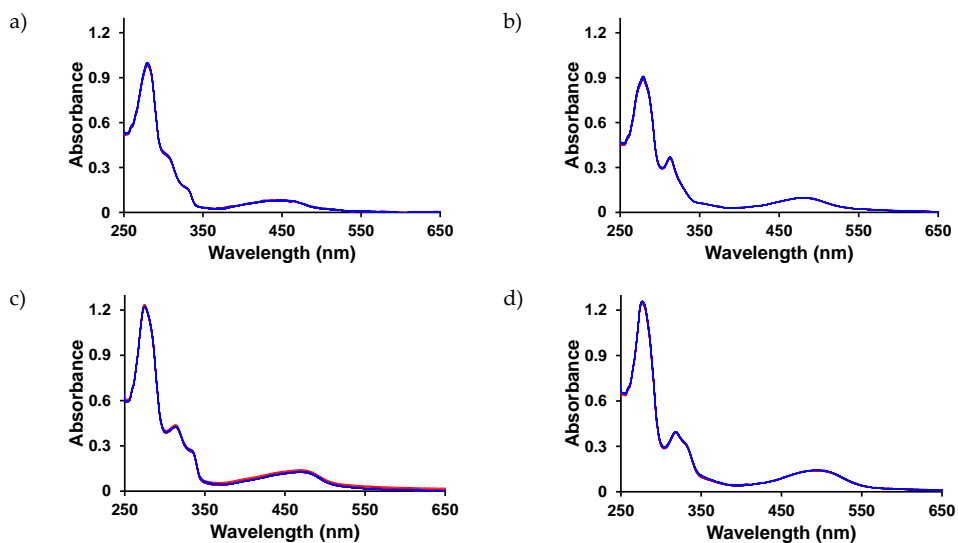


**Figure 2.4.** Evolution of the UV-vis spectra (region 250 – 650 nm) of a solution of ruthenium complex (0.015 mM) with BSA (0.015 mM) in PBS under air atmosphere for 24 h at 37 °C. a)  $[\mathbf{1}](\text{PF}_6)_2$ , b)  $[\mathbf{6}]^{2+}$ , c)  $[\mathbf{2}](\text{PF}_6)_2$ , d)  $[\mathbf{7}]^{2+}$ .

Mass spectrometry is also a very powerful method to study protein-metallodrug interactions.<sup>39-41</sup> ESI MS spectra were recorded to quantify the amount of ruthenium complexes interacting with BSA. Different mixtures of  $[\mathbf{1}](\text{PF}_6)_2$  (100, 300, or 500  $\mu\text{M}$ ) and BSA (100  $\mu\text{M}$ ) in aqueous solution were incubated at 37 °C for 24 h in the dark and were activated thereafter with green light (517 nm) for 1 h. 24 h After light activation, samples were subjected to ESI-MS analysis. The presence of the activated ruthenium species led to a signal broadening and loss of spectral resolution compared to BSA only (66429 Da). However, no evident signals that can be ascribed to Ru-BSA adducts were detected. To improve the signal, ultrafiltration with a 10 kDa cut-off was performed, followed by extensive washing steps. Upon this



treatment, spectra showed a better resolution, but the signal showed only unreacted BSA. Analysis of the ultrafiltered fraction by ICP-AES revealed that indeed very little ruthenium was present in the BSA samples (see Table AII.1). These results suggest that the interaction between the ruthenium species and BSA is of non-covalent nature and too weak to be detected by mass spectrometry after ultrafiltration. Control experiments with [2](PF<sub>6</sub>)<sub>2</sub> were performed and resulted in similar spectra, indicating that the alkyne-functionalization did not cause an enhanced interaction of the ruthenium center with BSA.

Fluorescent labeling clearly showed that the activated ruthenium complex interacts with BSA, and that this interaction is concentration dependent. On the other hand, the results from ESI MS and UV-vis spectroscopy suggest that the binding is weak, since no signal of a ruthenated protein was observed after sample preparation. Strong covalent binding of the ruthenium complex to methionine and histidine residues, as seen with other ruthenium complexes,<sup>17, 32, 42-45</sup> can therefore be excluded. In addition, BSA contains 35 cysteine residues, forming 17 disulfide bridges. Therefore, only one thiol group is available for binding, Cys34.<sup>46</sup> However, the bond between cysteine and ruthenium(II) is oxygen-sensitive. Once coordinated to ruthenium, cysteine is easily oxidized, which leads to the formation of unstable sulfenato and sulfinato ruthenium complexes, that ultimately release the hydrolyzed ruthenium complexes [6]<sup>2+</sup> and [7]<sup>2+</sup>.<sup>47</sup> Another possibility is that the activated ruthenium complex might interact non-covalently with the hydrophobic core of BSA, similar to what has been described for KP1019 with HSA.<sup>48, 49</sup> Therefore, it is reasonable to hypothesize that the weak interaction between the aqua complexes and BSA occurs either *via* coordination to Cys34 followed by oxidation, or *via* non-covalent interactions with the hydrophobic pockets of BSA. Since in gel fluorescence showed that the intensity of the fluorescent band corresponding to the ruthenated BSA increased with incubation time, the interaction *via* Cys34 coordination can be excluded due to its instability over time. Overall, our data indicate that after light activation the corresponding aqua complex interacts non-covalently with BSA *via* weak interactions, rather than *via* coordination to Cys34 or other protein residues.

## 2.3 Conclusion

To conclude, a synthetic route was developed for the functionalization of a photolabile ruthenium complex with an alkyne handle. The TBDMS group appears

to be the best alkyne protecting group during ligand introduction and exchange, preventing the formation of side products. In addition, this protecting group is easily removed with a small excess of potassium fluoride, without the need for toxic silver ions. The small alkyne handle allowed for fluorophore post-labeling *via* CuAAC to study the non-covalent interactions between the ruthenium complex and BSA, which were very difficult to detect with state-of-art methods such as UV-vis spectroscopy and mass spectrometry. In addition, fluorophore post-labeling also demonstrate the protective character of the thioether ligand regarding the interaction of [1]<sup>2+</sup> or [2]<sup>2+</sup> with the protein, which lies at the core of photoactivated chemotherapy. As an interaction between the metal complex and BSA was only detected after light activation, it can be hypothesized that PACT prodrugs have little interaction with blood proteins before light activation, which may result in poor systemic toxicity, compared to drugs that activate spontaneously by thermal hydrolysis or reduction. Overall, fluorophore labeling *via* CuAAC on alkyne-functionalized prodrugs appears to be an excellent way to visualize even weak interactions between metallodrugs and proteins.

## 2.4 Experimental

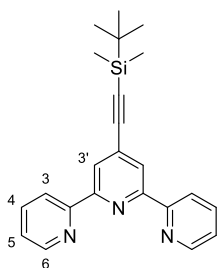
### 2.4.1 Materials and Methods

4'-Bromo-2,2':6',2''-terpyridine and 2,2'-bipyridine were purchased from TCI Europe, RuCl<sub>3</sub> from Alfa Aesar, 2-(methylthio)ethanol, and *tert*-butyldimethylsilylethyne from Sigma Aldrich. [1](PF<sub>6</sub>)<sub>2</sub> was synthesized according to literature.<sup>29</sup> All metal complexes were synthesized in dim light and stored in darkness. All commercial reactants and solvents were used without further purification. <sup>1</sup>H NMR spectra were recorded on a Bruker AV-300 spectrometer. Chemical shifts are indicated in ppm. Mass spectra were recorded by using an MSQ Plus Spectrometer.

### 2.4.2 Synthesis

#### RCC-tpy (R = TBDMS)

RCC-tpy was synthesized using an adapted literature procedure.<sup>26</sup> To dry and degassed triethylamine (12 mL), 4'-bromo-2,2':6',2''-terpyridine (1.0 g, 3.2 mmol), copper(I) iodide (38 mg, 0.20 mmol), dichlorobis(triphenylphosphine)palladium (70 mg, 0.10 mmol), and *tert*-butyldimethylsilylethyne (1.0 mL, 5.3 mmol) were added under dinitrogen atmosphere. The reaction mixture was stirred and refluxed for 7 h at 80 °C under dinitrogen atmosphere. During reflux the same amounts of triethylamine and *tert*-butyldimethylsilylethyne were added twice (after 2 h 20 min and 4 h 40 min). The solvent was evaporated with a rotary evaporator at 40 °C, the solid was dissolved in *n*-hexane and filtered. The filtrate was purified by column chromatography on silica with *n*-hexane/ethyl acetate 9:1 as eluent (*R<sub>f</sub>* = 0.34), yielding a white solid (94%, 1.1 g, 3.0 mmol).



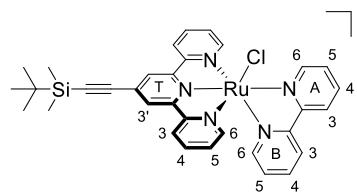
$^1\text{H NMR}$  (300 MHz, chloroform-*d*, 298 K)  $\delta$  8.70 (ddd,  $J = 4.8, 1.8, 0.9$  Hz, 1H, T6), 8.59 (dt,  $J = 8.0, 1.1$  Hz, 1H, T3), 8.49 (s, 1H, T3'), 7.85 (td,  $J = 7.7, 1.8$  Hz, 1H, T4), 7.34 (ddd,  $J = 7.5, 4.8, 1.2$  Hz, 1H, T5), 1.01 (s, 5H), 0.21 (s, 3H).  $^{13}\text{C NMR}$  (75 MHz, chloroform-*d*, 298 K)  $\delta$  155.6 + 155.4 (T2 + T2'), 149.1 (T6), 136.9 (T4), 133.3 (T4'), 124.0 (T5), 123.2 (T3'), 121.2 (T4), 103.3 (C-C-Si), 98.03 (Ar-C-C), 26.2 (Si-C-(CH<sub>3</sub>)<sub>3</sub>), 16.7 (Si-C-(CH<sub>3</sub>)<sub>3</sub>), -4.7 (Si-(CH<sub>3</sub>)<sub>2</sub>). *ES MS m/z (calc.)*: 372.5 (372.2 [M + H]<sup>+</sup>).

### [Ru(RCC-tpy)(Cl)<sub>3</sub>] (R = TBDMS), [3]

RuCl<sub>3</sub> · H<sub>2</sub>O (500 mg, 2.41 mmol) and RCC-tpy (895 mg, 2.41 mmol) were dissolved in ethanol (250 mL) and refluxed overnight while stirring. The reaction was cooled down to room temperature and chilled in the freezer overnight. The precipitate was filtered from the red solution and washed with cold ethanol and diethyl ether. Drying *in vacuo* yielded a brownish red solid that was used without further purification (75%, 1.05 g, 1.82 mmol).

### [Ru(RCC-tpy)(bpy)(Cl)]Cl (R = TBDMS), [4]Cl

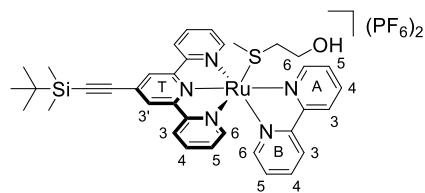
[Ru(RCC-tpy)(Cl)<sub>3</sub>] (100 mg, 0.18 mmol), 2,2'-bipyridine (28 mg, 0.18 mmol), and lithium chloride (41 mg, 0.98 mmol) were dissolved in degassed ethanol/water mixture (20 mL, 3:1). Triethylamine (62  $\mu\text{L}$ , 0.45 mmol) was added and the reaction mixture was stirred at 60 °C under dinitrogen atmosphere overnight. The reaction mixture was filtered hot over *Celite* and the cake was washed with ethanol. After evaporation of the combined solvents, the crude was purified by column chromatography on silica with dichloromethane/methanol (9:1, R<sub>f</sub> = 0.42) as eluent. Evaporation of the solvent yielded [4]Cl as a dark purple solid (82%, 103 mg, 0.15 mmol).



$^1\text{H NMR}$  (300 MHz, methanol-*d*<sub>4</sub>, 298 K)  $\delta$  10.19 (dd,  $J = 5.6, 1.6, 0.7$  Hz, 1H, A6), 8.79 (dt,  $J = 8.2, 1.1$  Hz, 1H, A3), 8.71 (s, 2H, T3'), 8.61 (dt,  $J = 8.0, 1.1$  Hz, 2H, T3), 8.49 (dd,  $J = 8.1, 1.2$  Hz, 1H, B3), 8.34 (td,  $J = 7.8, 1.5$  Hz, 1H, A4), 8.02 (ddd,  $J = 7.4, 5.7, 1.3$  Hz, 1H, A5), 7.93 (td,  $J = 7.9, 1.5$  Hz, 2H, T4), 7.75 (td,  $J = 7.8, 1.4$  Hz, 1H, B4), 7.69 (ddd,  $J = 5.5, 1.6, 0.8$  Hz, 2H, T6), 7.43–7.28 (m, 3H, T5+B6), 7.05 (ddd,  $J = 7.3, 5.7, 1.4$  Hz, 1H, B5), 1.12 (s, 9H, Si-C-(CH<sub>3</sub>)<sub>3</sub>), 0.32 (s, 6H, Si-(CH<sub>3</sub>)<sub>2</sub>).  $^{13}\text{C NMR}$  (75 MHz, methanol-*d*<sub>4</sub>, 298 K)  $\delta$  160.1 + 157.5 (A2 + B2), 159.8 + 159.6 (T2 + T2'), 153.6 (A6), 153.2 (T6), 153.0 (B6), 138.5 (T4), 138.3 (A4), 137.1 (B4), 129.6 (T4'), 128.8 (T5), 128.2 (A5), 127.6 (B5), 125.6 (T3'), 125.3 (T3), 124.8 (A3), 124.6 (B3), 103.7+101.8 (Ar-C-C + C-C-Si), 26.6 (Si-C-(CH<sub>3</sub>)<sub>3</sub>), 17.6 (Si-C-(CH<sub>3</sub>)<sub>3</sub>), -4.6 (Si-(CH<sub>3</sub>)<sub>2</sub>). *ES MS m/z (calc.)*: 664.6 (664.1, [M - Cl]<sup>+</sup>).

### [Ru(RCC-tpy)(bpy)(Hmte)](PF<sub>6</sub>)<sub>2</sub> (R = TBDMS), [5](PF<sub>6</sub>)<sub>2</sub>

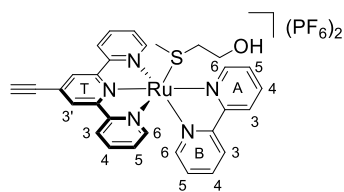
[Ru(RCC-tpy)(bpy)(Cl)]Cl (200 mg, 0.290 mmol) and 2-(methylthio)ethanol (1.26 mL, 14.5 mmol) were dissolved in degassed water (40 mL) and reacted at 60 °C under dinitrogen atmosphere overnight. After confirmation of reaction completion by TLC (silica, dichloromethane/methanol 9:1, R<sub>f</sub> = 0.28), saturated aqueous potassium hexafluoridophosphate solution was added. The precipitate was filtered and rinsed carefully with ice-cold water (10 mL) and diethyl ether (25 mL). Drying *in vacuo* yielded [5](PF<sub>6</sub>)<sub>2</sub> as an orange-brown solid (85%, 250 mg, 0.25 mmol).



$^1\text{H NMR}$  (300 MHz, *acetone-d*<sub>6</sub>, 298 K)  $\delta$  9.98 (d,  $J$  = 5.4 Hz, 1H, A6), 8.99 (s, 2H, T3'), 8.96 (d,  $J$  = 8.1 Hz, 1H, A3), 8.89 (d,  $J$  = 8.1 Hz, 2H, T3), 8.72 (d,  $J$  = 8.2 Hz, 1H, B3), 8.50 (td,  $J$  = 7.9, 1.4 Hz, 1H, A4), 8.28 – 8.12 (m, 3H, T4 + A5), 8.09 – 7.98 (m, 3H, T6 + B4), 7.66 (dd,  $J$  = 6.0, 1.0 Hz, 1H, B6), 7.57 (ddd,  $J$  = 7.4, 5.6, 1.3 Hz, 2H, T5), 7.31 (ddd,  $J$  = 7.3, 5.6, 1.3 Hz, 1H, B5), 4.07 (t,  $J$  = 5.1 Hz, 1H, OH), 3.56 (dt,  $J$  = 5.1, 5.6 Hz, 2H, S-CH<sub>2</sub>-CH<sub>2</sub>), 2.05 – 1.99 (m, 2H, S-CH<sub>2</sub>), 1.56 (s, 3H, S-CH<sub>3</sub>), 1.11 (s, 9H, Si-C-(CH<sub>3</sub>)<sub>3</sub>), 0.33 (s, 6H, Si-(CH<sub>3</sub>)<sub>2</sub>).  $^{13}\text{C NMR}$  (75 MHz, *acetone-d*<sub>6</sub>, 298 K)  $\delta$  158.7 + 158.6 (T2 + T2'), 157.7 + 157.6 (A2 + B2), 154.4 (T6), 153.1 (A6), 151.2 (B6), 139.9 (T4), 139.4 (A4), 139.3 (B4), 131.7 (T4'), 129.9 (T5), 129.0 (A5), 128.3 (B5), 127.1 (T3'), 126.4 (T3), 125.8 (A3), 124.9 (B3), 103.1 + 58.93 (Ar-C-C + C-C-Si), 59.04 (S-CH<sub>2</sub>-CH<sub>2</sub>), 37.6 (S-CH<sub>2</sub>), 26.5 (Si-C-(CH<sub>3</sub>)<sub>3</sub>), 17.3 (Si-C-(CH<sub>3</sub>)<sub>3</sub>), 14.9 (S-CH<sub>3</sub>), -4.6 (Si-(CH<sub>3</sub>)<sub>2</sub>). *ES MS m/z (calc.)*: 360.9 (360.6, [M - 2PF<sub>6</sub>]<sup>2+</sup>).

### [Ru(HCC-tpy)(bpy)(Hmte)](PF<sub>6</sub>)<sub>2</sub>, [2](PF<sub>6</sub>)<sub>2</sub>

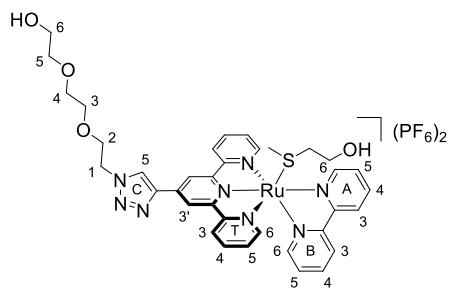
[Ru(RCC-tpy)(bpy)(Hmte)](PF<sub>6</sub>)<sub>2</sub> (250 mg, 0.247 mmol) and potassium fluoride (72 mg, 1.2 mmol) were dissolved in methanol (6 mL) and stirred at 30 °C overnight. The solvent was reduced in volume and saturated aqueous potassium hexafluoridophosphate solution was added till a precipitate was formed. The precipitate was filtered and rinsed carefully with ice-cold water (10 mL) and diethyl ether (25 mL). Drying *in vacuo* yielded [2](PF<sub>6</sub>)<sub>2</sub> an orange solid (76%, 168 mg, 0.187 mmol).



$^1\text{H NMR}$  (300 MHz, *acetone-d*<sub>6</sub>, 298 K)  $\delta$  9.97 (ddd,  $J$  = 5.6, 1.6, 0.8 Hz, 1H, A6), 8.99 (s, 2H, T3'), 8.96 (dt,  $J$  = 8.1, 1.1 Hz, 1H, A3), 8.88 (ddd,  $J$  = 7.8, 1.2, 0.6 Hz, 2H, T3), 8.72 (dt,  $J$  = 8.1, 1.1 Hz, 1H, B3), 8.50 (td,  $J$  = 7.9, 1.5 Hz, 1H, A4), 8.22 (td,  $J$  = 7.9, 1.5 Hz, 2H, T4), 8.19 – 8.13 (m, 1H, A5), 8.06 (ddd,  $J$  = 5.5, 1.5, 0.7 Hz, 2H, T6), 8.06 – 7.97 (m, 1H, B4), 7.63 (ddd,  $J$  = 5.7, 1.5, 0.7 Hz, 1H, B6), 7.58 (ddd,  $J$  = 7.7, 5.5, 1.3 Hz, 2H, T5), 7.30 (ddd,  $J$  = 7.2, 5.7, 1.3 Hz, 1H, B5), 4.55 (s, 1H, CCH), 4.06 (t,  $J$  = 5.1 Hz, 1H, OH), 3.56 (dt,  $J$  = 5.1, 5.7 Hz, 2H, S-CH<sub>2</sub>-CH<sub>2</sub>), 2.06 – 1.97 (m, 2H, S-CH<sub>2</sub>), 1.56 (s, 3H, S-CH<sub>3</sub>).  $^{13}\text{C NMR}$  (75 MHz, *acetone-d*<sub>6</sub>, 298 K)  $\delta$  158.8 + 158.6 (T2 + T2'), 157.7 + 157.6 (A2 + B2), 154.5 (T6), 153.1 (A6), 151.2 (B6), 140.0 (T4), 139.5 (A4), 139.3 (B4), 131.3 (T4'), 129.9 (T5), 129.0 (A5), 128.3 (B5), 127.4 (T3'), 126.4 (T3), 125.8 (A3), 124.9 (B3), 87.9 (CCH), 81.1 (CCH), 59.1 (S-CH<sub>2</sub>-CH<sub>2</sub>), 37.6 (S-CH<sub>2</sub>), 15.0 (S-CH<sub>3</sub>). *ES MS m/z (calc.)*: 303.5 (303.6, [M - 2PF<sub>6</sub>]<sup>2+</sup>). *High resolution ES MS m/z (calc.)*: 303.54874 (303.54881, [M - 2PF<sub>6</sub>]<sup>2+</sup>). *Elem. Anal. Calc.* for C<sub>30</sub>H<sub>27</sub>F<sub>12</sub>N<sub>5</sub>OP<sub>2</sub>RuS: C, 40.19; H, 3.04; N, 7.81. *Found*: C, 40.21; H, 3.06; N, 7.79.

### CuAAC reaction on [2](PF<sub>6</sub>)<sub>2</sub>

[Ru(HCC-tpy)(bpy)(Hmte)](PF<sub>6</sub>)<sub>2</sub> (41 mg, 0.046 mmol), 2-(2-(2-azidoethoxy)ethoxy)ethanol (110 mg, 0.63 mmol), CuSO<sub>4</sub>·5H<sub>2</sub>O (2.9 mg, 0.012 mmol), and ascorbic acid (8.4 mg, 0.042 mmol) were added to a water/acetone mixture (9:1, 4.6 mL). The mixture was left stirring at room temperature for 1 h under air atmosphere. Acetone was removed by rotary evaporation and saturated aqueous solution of potassium hexafluoridophosphate (50 mL) was added. The product was extracted with three times with dichloromethane. After evaporation, a red-colored sticky product was obtained that was not further purified (unreacted azide still present).



<sup>1</sup>H NMR (300 MHz, acetone-*d*<sub>6</sub>, 298 K) δ 9.95 (dd, *J* = 5.7, 1.4 Hz, 1H, A6), 9.31 (s, 2H, T3'), 9.04 (s, 1H, 5C), 9.00 – 8.86 (m, 3H, T3 + A3), 8.70 (d, *J* = 8.1 Hz, 1H, B3), 8.47 (td, *J* = 7.9, 1.5 Hz, 1H, A4), 8.20 (td, *J* = 7.9, 1.5 Hz, 2H, T4), 8.14 (ddd, *J* = 7.3, 5.6, 1.3 Hz, 1H, A5), 8.04 (d, *J* = 4.9 Hz, 2H, T6), 7.99 (dd, *J* = 7.9, 1.5 Hz, 1H, B4), 7.69 (dd, *J* = 5.7, 1.4 Hz, 1H, B6), 7.55 (ddd, *J* = 7.7, 5.5, 1.3 Hz, 2H, T5), 7.30 (ddd, *J* = 7.3, 5.7, 1.3 Hz, 1H, B5), 4.81 (t, *J* = 4.9 Hz, 2H, D1), 4.04 (t, *J* = 4.9 Hz, 2H, D2), 3.75 – 3.32 (m, D3 – D6, S-CH<sub>2</sub>-CH<sub>2</sub>; excess R-N<sub>3</sub>), 2.01 (m, 2H, S-CH<sub>2</sub>), 1.57 (s, 3H, S-CH<sub>3</sub>). <sup>13</sup>C NMR (75 MHz, acetone-*d*<sub>6</sub>, 298 K) δ 158.9 + 158.5 (T2 + T2'), 157.7 + 157.6 (A2 + B2), 154.4 (T6), 153.0 (A6), 151.0 (B6), 144.4 (C1), 140.8 (T4'), 139.8 (T4), 139.1 (A4), 139.0 (B4), 129.6 (T5), 128.8 (A5), 128.2 (B5), 126.0 (T3), 126.0 (A3), 125.6 (C5), 124.7 (B3), 120.6 (T3'), 73.4 + 71.0 + 70.9 (D3 + D4 + D5), 69.8 (D2), 62.0 (D6), 59.0 (S-CH<sub>2</sub>-CH<sub>2</sub>), 51.5 (D1), 37.6 (S-CH<sub>2</sub>), 14.9 (S-CH<sub>3</sub>). *ES MS m/z (calc.)*: 391.2 (391.1 [M – 2PF<sub>6</sub>]<sup>2+</sup>).

### 2.4.3 Single Crystal X-Ray crystallography

Single crystals of [2](PF<sub>6</sub>)<sub>2</sub> were obtained by recrystallization through liquid-vapor diffusion using acetonitrile as solvent and diisopropyl ether as counter-solvent. In short, 1 mg of [2](PF<sub>6</sub>)<sub>2</sub> was dissolved in 1 mL of acetonitrile and placed in a small vial. This vial was placed in a larger vial containing 2.8 mL diisopropyl ether. The large vial was closed, and vapor diffusion occurred within a few days to afford X-ray quality dark red rhombic crystals.

All reflection intensities were measured at 110(2) K using a SuperNova diffractometer (equipped with Atlas detector) with Cu *K*α radiation ( $\lambda = 1.54178 \text{ \AA}$ ) under the program CrysAlisPro (Version CrysAlisPro 1.171.39.29c, Rigaku OD, 2017). The same program was used to refine the cell dimensions and for data reduction. The structure was solved with the program SHELXS-2014/7 (Sheldrick, 2015) and was refined on *F*<sup>2</sup> with SHELXL-2014/7 (Sheldrick, 2015). Analytical numeric absorption correction using a multifaceted crystal model was applied using CrysAlisPro. The temperature of the data collection was controlled using the system Cryojet (manufactured by Oxford Instruments). The H atoms were placed at calculated positions using the instructions AFIX 23, AFIX 43, AFIX 137, AFIX 147 or AFIX 163 with isotropic displacement parameters having values 1.2 or 1.5 *U*<sub>eq</sub> of the attached C or O atoms.

The structure of [2](PF<sub>6</sub>)<sub>2</sub> is ordered.

[2](PF<sub>6</sub>)<sub>2</sub>: 0.15 × 0.13 × 0.02 mm<sup>3</sup>, triclinic, *P*-1, *a* = 9.9395 (3), *b* = 11.2670 (3), *c* = 16.2664 (4) Å,  $\alpha = 96.662$  (2),  $\beta = 91.650$  (2),  $\gamma = 111.580$  (2)°, *V* = 1677.48 (8) Å<sup>3</sup>, *Z* = 2,  $\mu = 6.21 \text{ mm}^{-1}$ , transmission factor range: 0.485–0.882. 21777 Reflections were measured up to a resolution of  $(\sin \theta/\lambda)_{\text{max}} = 0.616 \text{ \AA}^{-1}$ . 6568 Reflections were unique (*R*<sub>int</sub> = 0.027), of which 6083 were observed [*I* > 2σ(*I*)]. 471 Parameters were refined. *R*<sub>1</sub>/*wR*<sub>2</sub> [*I* > 2σ(*I*)]: 0.0273/0.0674. *R*<sub>1</sub>/*wR*<sub>2</sub> [all refl.]: 0.0305/0.0699. *S* = 1.026. Residual electron density found between –0.49 and 0.90 e Å<sup>–3</sup>.

## 2.4.4 Photochemistry

### Materials

Photoreactions monitored with UV-vis were performed using a Cary 50 Varian spectrometer equipped with temperature control and a magnetic stirrer. The measurements were performed in a quartz cuvette, containing 3 mL of solution. Irradiations were carried out under air atmosphere. Irradiation was performed from the top of the cuvette perpendicularly to the optical axis of the spectrometer using a custom-build LED irradiation setup, consisting of a high-power LED driven by a LED driver operating at 350 mA.

### Photoactivation

For photoactivation with green light, a LED light source ( $\lambda = 517$  nm,  $\Delta\lambda_{1/2} = 23$  nm, 5.42 mW,  $5.4 \cdot 10^{-8}$  mol  $\cdot$  s $^{-1}$ ) was used, and absorption spectrum was measured for 70 min at  $T = 25$  °C. [Ru] = 0.130 mM for [1](PF<sub>6</sub>)<sub>2</sub> and 0.074 mM for [2](PF<sub>6</sub>)<sub>2</sub>. Data was analyzed using Microsoft Excel 2010.

### Photosubstitution quantum yield

For photosubstitution quantum yield determination for [2](PF<sub>6</sub>)<sub>2</sub> (0.074 mM), a LED light source ( $\lambda = 466$  nm,  $\Delta\lambda_{1/2} = 36$  nm, 15.4 mW,  $1.11 \cdot 10^{-7}$  mol  $\cdot$  s $^{-1}$ ) was used and UV-vis absorption spectra were recorded every 12 sec for 30 min at  $T = 37$  °C. Data was analyzed using Microsoft Excel 2010. The rate constants of the photosubstitution reaction ( $k_{\Phi}$ ) was derived by fitting the time evolution of the UV-vis absorption at 450 nm to a mono-exponential decay function using Origin Pro 9.1. As the irradiation wavelength was chosen close to the isosbestic point in the photosubstitution reactions,  $A_{466}$  was assumed to be constant in time, so that the obtained rate constants could be converted into quantum yields for the photosubstitution reactions ( $\Phi_{466}$ ) using Equation 2.1.

$$\Phi_{466} = \frac{k_{\Phi} \cdot n_{\text{Ru}}}{q_{\text{p}} \cdot (1 - 10^{-A_{466}})} \quad \text{Equation 2.1}$$

Here,  $k_{\Phi}$  is the found photochemical rate constant,  $n_{\text{Ru}}$  is the total amount of ruthenium ions,  $q_{\text{p}}$  is the incoming photon flux, and  $A_{466}$  is the absorbance at the irradiation wavelength.

## 2.4.5 Mass spectrometry for Ru-BSA interaction

### Sample preparation

Interactions between the photoactivable ruthenium compounds and Bovine Serum Albumin were assessed by high-resolution ESI-MS with slight modifications of the general method described in literature.<sup>41, 50, 51</sup> Two stock solutions of [1](PF<sub>6</sub>)<sub>2</sub> and [2](PF<sub>6</sub>)<sub>2</sub> were prepared in LC-MS grade water to a final concentration of  $10^{-3}$  M. Another stock solution of Bovine Serum Albumin (fatty free, from Sigma-Aldrich) was prepared in LC-MS grade water at  $10^{-3}$  M. Appropriate aliquots of these stock solutions were mixed and diluted with water to a final protein concentration of 100  $\mu$ M and complex concentrations of 100, 300, or 500  $\mu$ M. The reaction mixtures were prepared in duplicate for both ruthenium compounds, one sample was completely protected from light exposure and incubated up to 24 h at 37 °C. The other sample was irradiated for 1 h at 515 nm shaking at 400 rpm and then incubated for up to 24 h at 37 °C.

## ESI-MS

Aliquots were sampled after 2 and 24 h and diluted with LC-MS water at  $10^{-5}$  M protein final concentration with the addition of 0.1% formic acid. Respective ESI-MS spectra were acquired through direct infusion at  $10 \mu\text{L min}^{-1}$  flow rate in a TripleTOF® 5600+ high-resolution mass spectrometer (Sciex, Framingham, MA, U.S.A.), equipped with a DuoSpray® interface operating with an ESI probe. The ESI source parameters were optimized and were as follows: positive polarity, Ionspray Voltage Floating 5400 V, Temperature 50 °C, Ion source Gas 1 (GS1) 40; Ion source Gas 2 (GS2) 0; Curtain Gas (CUR) 15, Declustering Potential (DP) 250 V, Collision Energy (CE) 10 V. For acquisition, Analyst TF software 1.7.1 (Sciex) was used and deconvoluted spectra were obtained by using the Bio Tool Kit micro-application v.2.2 embedded in PeakView™ software v.2.2 (Sciex).

## ICP-AES

The residual fractions of the reaction mixtures prepared for the MS analysis (about 0.9 mL) were used for the ICP-AES determination of the ruthenium bound to the protein, following a well-established protocol.<sup>52, 53</sup> The metallated proteins were isolated using a centrifugal filter device with a cut-off membrane of 10 kDa and washed several times with LC-MS grade water. The final metal/protein adducts were recovered by spinning the filters upside-down at 3500 rpm for 3 min with 200  $\mu\text{L}$  of water. The samples were mineralized in a thermoreactor at 90 °C for 8 h with 1.0 mL of HCl 30% Suprapur grade (Merck Millipore). After that, the samples were diluted exactly to 6.0 mL with MilliQ water ( $\leq 18 \text{ M}\Omega$ ). The determination of ruthenium content in these solutions was performed using a Varian 720-ES Inductively Coupled Plasma Atomic Emission Spectrometer (ICP-AES). The calibration curve of ruthenium was obtained using known concentrations of a Ru ICP standard solution purchased from Sigma-Aldrich. Moreover, each sample was spiked with 1 ppm of Ge used as an internal standard. The wavelength used for Ru determination was 267.876 nm whereas for Ge the line at 209.426 nm was used. The operating conditions were optimized to obtain maximum signal intensity and, between each sample, a rinse solution containing 1.0 mL of HCl 30% Suprapur grade and 5.0 mL of ultrapure water was used to avoid any “memory effect”.

### 2.4.6 Fluorophore labeling

#### Materials

BSA and tris(3-hydroxypropyltriazolylmethyl)amine were purchased from Sigma Aldrich, Alexa Fluor™ 647 azide as triethylammonium salt from Thermo Fisher.

#### Click reaction

BSA (in 1X PBS, 15  $\mu\text{M}$ ) was incubated with [2](PF<sub>6</sub>)<sub>2</sub> (in DMSO, 75  $\mu\text{M}$ ) at 37 °C in the dark for 24 h under constant shaking. After activation with green light (520 nm, 76 J · cm<sup>2</sup>) for 1 h, the solution was incubated at 37 °C in the dark for an additional 24 h. Samples (50  $\mu\text{L}$ ) were taken before and after light activation (6 and 24 h after activation). Dark control samples as well as negative controls (without complex, without BSA or without fluorophore) which were not activated were collected at the same time points. Samples were stored at -20 °C if not used directly. For the click reaction, each sample was incubated with an equivalent amount of click cocktail (50  $\mu\text{L}$ , copper sulfate (6.4 mM), sodium ascorbate (37.5 mM), tris(3-hydroxypropyltriazolylmethyl)amine (THPTA) (in DMSO, 1.3 mM), Tris-HCl (100 mM, pH 8.0), and Alexa Fluor 647 azide (in DMSO, 5  $\mu\text{M}$ ) at r.t under gentle shaking for 1 h in the dark. The click reaction was quenched with SDS loading Buffer (50  $\mu\text{L}$ ) and used immediately for in-gel fluorescence.

Alkyne-substituted vinculin, Homopropargylglycine-Vin (Hpg-Vin), was used as positive control and prepared by Dr. Can Araman according to a published procedure.<sup>54</sup>

Note that electrophoresis was performed in the dark. 2 µg of protein was added to each well of a 15 well 1.5 mm SDS gel at 200 V for 1 h. Protein concentration of each sample was measured using a Qubit reader (Thermo Fisher). Fluorescent bands of the SDS gels were visualized using a BioRad ChemiDoc™ Touch Imaging System with Alexa647 filter. Coomassie staining was applied overnight and de-stained with the destaining solution (MeOH:water:AcOH; 5:4:1).

### 2.4.7 Supporting Information

<sup>1</sup>H NMR spectra of [5](PF<sub>6</sub>)<sub>2</sub>, [2](PF<sub>6</sub>)<sub>2</sub>, and the click product, dark stability measurements, singlet oxygen production and phosphorescence spectra, UV-vis spectra of BSA interaction, and images of SDS PAGE gel electrophoresis are provided in Appendix AII.

## 2.5 Contribution

Dr. Can Araman supervised the Ru-BSA interaction SDS gel experiments performed by Ingrid Flashpohler. Dr. Alessandro Pratesi and Prof. Luigi Messori performed ESI MS measurements. Dr. Vincent van Rixel grew single crystals, and Dr. Maxime Siegler performed X-ray diffraction experiments and crystal structure determination. Dr. Sylvestre Bonnet, Dr. Can Araman, and Prof. Lies Bouwman provided experimental guidance and significant editorial feedback.

## 2.6 References

- 1 M. Groessl, O. Zava, and P. J. Dyson, *Metallomics* **2011**, 3 (6), 591-599.
- 2 A. Frei, R. Rubbiani, S. Tubafard, O. Blacque, P. Anstaett, A. Felgenträger, T. Maisch, L. Spiccia, and G. Gasser, *J. Med. Chem.* **2014**, 57 (17), 7280-7292.
- 3 T. S. Morais, F. C. Santos, T. F. Jorge, L. Côte-Real, P. J. A. Madeira, F. Marques, M. P. Robalo, A. Matos, I. Santos, and M. H. Garcia, *J. Inorg. Biochem.* **2014**, 130 1-14.
- 4 L. Côte-Real, F. Mendes, J. Coimbra, T. S. Morais, A. I. Tomaz, A. Valente, M. H. Garcia, I. Santos, M. Bicho, and F. Marques, *J. Biol. Inorg. Chem.* **2014**, 19 (6), 853-867.
- 5 Walker Henry K, Hall Wilbur D, and H. J. W, *Clinical Methods: The History, Physical, and Laboratory Examinations.* **1990**, 3rd.
- 6 M. P. Sullivan, H. U. Holtkamp, and C. G. Hartinger, Antitumor Metalloodrugs that Target Proteins in *Metallo-Drugs: Development and Action of Anticancer Agents* **2018**, 351-386.
- 7 Y. Zhang, A. Ho, J. Yue, L. Kong, Z. Zhou, X. Wu, F. Yang, and H. Liang, *Eur. J. Med. Chem.* **2014**, 86 449-455.
- 8 J. Mayr, P. Heffeter, D. Groza, L. Galvez, G. Koellensperger, A. Roller, B. Alte, M. Haider, W. Berger, C. R. Kowol, and B. K. Keppler, *Chem. Sci.* **2017**, 8 (3), 2241-2250.
- 9 A. Bergamo, A. Masi, A. F. A. Peacock, A. Habtemariam, P. J. Sadler, and G. Sava, *J. Inorg. Biochem.* **2010**, 104 (1), 79-86.
- 10 A. R. Timerbaev, C. G. Hartinger, S. S. Aleksenko, and B. K. Keppler, *Chem. Rev.* **2006**, 106 (6), 2224-2248.
- 11 G. Ferraro, L. Massai, L. Messori, and A. Merlino, *Chem. Commun.* **2015**, 51 (46), 9436-9439.



- 12 A. Wragg, M. R. Gill, L. McKenzie, C. Glover, R. Mowll, J. A. Weinstein, X. Su, C. Smythe, and  
J. A. Thomas, *Chem. Eur. J.* **2015**, 21 (33), 11865-11871.
- 13 B. X. Huang, H.-Y. Kim, and C. Dass, *J. Am. Soc. Mass Spectrom.* **2004**, 15 (8), 1237-1247.
- 14 A. Bijelic, S. Theiner, B. K. Keppler, and A. Rompel, *J. Med. Chem.* **2016**, 59 (12), 5894-5903.
- 15 A. Merlini, *Coord. Chem. Rev.* **2016**, 326 111-134.
- 16 A. Casini, A. Karotki, C. Gabbiani, F. Rugi, M. Vasak, L. Messori, and P. J. Dyson, *Metallomics*  
**2009**, 1 (5), 434-441.
- 17 F. Piccioli, S. Sabatini, L. Messori, P. Orioli, C. G. Hartinger, and B. K. Keppler, *J. Inorg. Biochem.*  
**2004**, 98 (6), 1135-1142.
- 18 L. Trynda-Lemiesz, A. Karaczyn, B. K. Keppler, and H. Kozlowski, *J. Inorg. Biochem.* **2000**, 78  
(4), 341-346.
- 19 J. D. White, M. F. Osborn, A. D. Moghaddam, L. E. Guzman, M. M. Haley, and V. J. DeRose, *J.*  
*Am. Chem. Soc.* **2013**, 135 (32), 11680-11683.
- 20 S. Ding, X. Qiao, J. Suryadi, G. S. Marrs, G. L. Kucera, and U. Bierbach, *Angew. Chem.* **2013**, 125  
(12), 3434-3438.
- 21 H. C. Kolb, M. G. Finn, and K. B. Sharpless, *Angew. Chem., Int. Ed.* **2001**, 40 (11), 2004-2021.
- 22 V. V. Rostovtsev, L. G. Green, V. V. Fokin, and K. B. Sharpless, *Angew. Chem., Int. Ed.* **2002**, 41  
(14), 2596-2599.
- 23 A. Baron, C. Herrero, A. Quaranta, M.-F. Charlot, W. Leibl, B. Vauzeilles, and A. Aukauloo,  
*Inorg. Chem.* **2012**, 51 (11), 5985-5987.
- 24 K. P. Chitre, E. Guillén, A. S. Yoon, and E. Galoppini, *Eur. J. Inorg. Chem.* **2012**, 2012 (33), 5461-  
5464.
- 25 I. Ott, K. Schmidt, B. Kircher, P. Schumacher, T. Wiglenda, and R. Gust, *J. Med. Chem.* **2005**, 48  
(2), 622-629.
- 26 N. Zabarska, D. Sorsche, F. W. Heinemann, S. Glump, and S. Rau, *Eur. J. Inorg. Chem.* **2015**, 2015  
(29), 4869-4877.
- 27 J. B. Gerken, M. L. Rigsby, R. E. Ruther, R. J. Pérez-Rodríguez, I. A. Guzei, R. J. Hamers, and S.  
S. Stahl, *Inorg. Chem.* **2013**, 52 (6), 2796-2798.
- 28 H. T. Ratte, *Environ. Toxicol. Chem.* **1999**, 18 (1), 89-108.
- 29 A. Bahreman, B. Limburg, M. A. Siegler, E. Bouwman, and S. Bonnet, *Inorg. Chem.* **2013**, 52 (16),  
9456-69.
- 30 N. J. Farrer, L. Salassa, and P. J. Sadler, *Dalton Trans.* **2009**, - (48), 10690-10701.
- 31 S. Bonnet, *Dalton Trans.* **2018**, 47 (31), 10330-10343.
- 32 R. E. Goldbach, I. Rodriguez-Garcia, J. H. van Lenthe, M. A. Siegler, and S. Bonnet, *Chem. Eur. J.*  
**2011**, 17 (36), 9924-9929.
- 33 J. Rodríguez, J. Mosquera, J. R. Couceiro, M. E. Vázquez, and J. L. Mascareñas, *Angew. Chem.*  
**2016**, 128 (50), 15844-15847.
- 34 C. Sclaro, C. G. Hartinger, C. S. Allardyce, B. K. Keppler, and P. J. Dyson, *J. Inorg. Biochem.*  
**2008**, 102 (9), 1743-1748.
- 35 P. G. M. Wuts and T. W. Greene, Protection for the Alkyne-CH in *Greene's Protective Groups in*  
*Organic Synthesis* **2007**, 927-933.
- 36 R. Ziesse, V. Grosshenny, M. Hissler, and C. Stroh, *Inorg. Chem.* **2004**, 43 (14), 4262-4271.
- 37 C. Ruppin and P. H. Dixneuf, *Tetrahedron Lett.* **1986**, 27 (52), 6323-6324.
- 38 V. H. S. van Rixel, G. F. Moolenaar, M. A. Siegler, L. Messori, and S. Bonnet, *Dalton Trans.* **2018**,  
47 (2), 507-516.

- 39 A. Casini, G. Mastrobuoni, W. H. Ang, C. Gabbiani, G. Pieraccini, G. Moneti, P. J. Dyson, and L. Messori, *ChemMedChem* **2007**, 2 (5), 631-635.
- 40 C. G. Hartinger, M. Groessl, S. M. Meier, A. Casini, and P. J. Dyson, *Chem. Soc. Rev.* **2013**, 42 (14), 6186-6199.
- 41 E. Michelucci, G. Pieraccini, G. Moneti, C. Gabbiani, A. Pratesi, and L. Messori, *Talanta* **2017**, 167 30-38.
- 42 J. R. Brown, Serum Albumin: Amino Acid Sequence in *Albumin: Structure, Function and Uses* **1977**, 27-52.
- 43 F. Wang, H. Chen, J. A. Parkinson, P. d. S. Murdoch, and P. J. Sadler, *Inorg. Chem.* **2002**, 41 (17), 4509-4523.
- 44 D. Lazić, A. Arsenijević, R. Puchta, Ž. D. Bugarčić, and A. Rilak, *Dalton Trans.* **2016**, 45 (11), 4633-4646.
- 45 F. Wang, J. Bella, J. A. Parkinson, and P. J. Sadler, *J. Biol. Inorg. Chem.* **2005**, 10 (2), 147-155.
- 46 G. J. Quinlan, G. S. Martin, and T. W. Evans, *Hepatology* **2005**, 41 (6), 1211-1219.
- 47 V. H. S. van Rixel, A. Busemann, A. J. Göttle, and S. Bonnet, *J. Inorg. Biochem.* **2015**, 150 174-181.
- 48 M. I. Webb, R. A. Chard, Y. M. Al-Jobory, M. R. Jones, E. W. Y. Wong, and C. J. Walsby, *Inorg. Chem.* **2012**, 51 (2), 954-966.
- 49 Y.-R. Zheng, K. Suntharalingam, T. C. Johnstone, H. Yoo, W. Lin, J. G. Brooks, and S. J. Lippard, *J. Am. Chem. Soc.* **2014**, 136 (24), 8790-8798.
- 50 T. Marzo, S. A. De Pascali, C. Gabbiani, F. P. Fanizzi, L. Messori, and A. Pratesi, *BioMetals* **2017**, 30 (4), 609-614.
- 51 A. Pratesi, D. Cirri, L. Ciofi, and L. Messori, *Inorg. Chem.* **2018**, 57 (17), 10507-10510.
- 52 I. Landini, A. Lapucci, A. Pratesi, L. Massai, C. Napoli, G. Perrone, P. Pinzani, L. Messori, E. Mini, and S. Nobili, *Oncotarget* **2017**, 8 (56), 96062-96078.
- 53 S. Ciambellotti, A. Pratesi, M. Severi, G. Ferraro, E. Alessio, A. Merlino, and L. Messori, *Dalton Trans.* **2018**, 47 (33), 11429-11437.
- 54 C. M. C. Araman, L. Pieper-Pournara, A. S. B. Kampstra, M. H. S. Marqvorsen, C. Nascimento, W. van der Wulp, M. G. J. M. Groenewold, M. G. M. Camps, F. Ossendorp, R. Toes, and S. I. van Kasteren, *bioRxiv* **2018**, 439323.

# 3

## RUTHENIUM-BASED PACT AGENTS: SYNTHESIS, PHOTOCHEMISTRY, AND CYTOTOXICITY STUDIES

*The series of complexes  $[Ru(tpy)(NN)(Hmte)](PF_6)_2$ , where  $tpy = 2,2':6',2''$ -terpyridine,  $NN = 2,2'$ -bipyridine (**1**)( $PF_6$ )<sub>2</sub>, 3,3'-biisoquinoline (*i*-biq, **2**)( $PF_6$ )<sub>2</sub>, or di(isoquinolin-3-yl)amine (*i*-Hdiqa, **3**)( $PF_6$ )<sub>2</sub>, and  $Hmte = 2$ -(methylthio)ethanol, were synthesized and their photochemical and (photo)cytotoxic properties were investigated in order to assess their suitability as photoactivated chemotherapy (PACT) agents. The increase of the aromatic surface of **2**( $PF_6$ )<sub>2</sub> and **3**( $PF_6$ )<sub>2</sub>, compared to **1**( $PF_6$ )<sub>2</sub>, leads to higher lipophilicity and higher cell uptake for the former complexes. Such improved uptake is directly correlated to the cytotoxicity of these compounds in the dark: while **2**( $PF_6$ )<sub>2</sub> and **3**( $PF_6$ )<sub>2</sub> showed low  $EC_{50}$  values in human cancer cells, **1**( $PF_6$ )<sub>2</sub> is not cytotoxic due to poor cellular uptake. While stable in the dark, all complexes substituted the protecting thioether ligand upon light irradiation (520 nm), with the highest photosubstitution quantum yield found for **3**( $PF_6$ )<sub>2</sub> ( $\Phi_{[3]} = 0.070$ ). Compounds **2**( $PF_6$ )<sub>2</sub> and **3**( $PF_6$ )<sub>2</sub> were found both more cytotoxic after light activation than in the dark, with a photo index of 4. Considering the very low singlet oxygen quantum yields of these compounds, and the lack of cytotoxicity of the photoreleased  $Hmte$  thioether ligand, it can be concluded that the toxicity observed after light activation is due to the photoreleased aqua complexes  $[Ru(tpy)(NN)(OH_2)]^{2+}$ , and thus that **2**( $PF_6$ )<sub>2</sub> and **3**( $PF_6$ )<sub>2</sub> are promising PACT candidates.*

### 3.1 Introduction

In recent years, ruthenium polypyridyl complexes gained attention in the field of phototherapy for their favorable photophysical and photochemical properties.<sup>1</sup> Drug activation by light irradiation at the tumor site provides physical selectivity towards cancerous tissues and minimizes the effect of the drug on the healthy, non-irradiated tissues. Therefore, undesired side effects are expected to be reduced. Two different types of phototherapy are distinguished: photodynamic therapy (PDT) and photoactivated chemotherapy (PACT). In both cases, a molecule is promoted to a singlet metal-to-ligand charge transfer excited state (<sup>1</sup>MLCT) by photon absorption. From there, the molecule undergoes intersystem crossing (ISC) to a triplet metal-to-ligand charge transfer excited state (<sup>3</sup>MLCT). This <sup>3</sup>MLCT state can be deactivated *via* four different pathways: non-radiative deactivation, emission of a photon, energy transfer to molecular oxygen to generate singlet oxygen (<sup>1</sup>O<sub>2</sub>), or thermal population of a low-lying triplet metal-centered excited state (<sup>3</sup>MC), which leads to ligand photosubstitution. In PDT, the production of <sup>1</sup>O<sub>2</sub> leads to serious oxidative damage of the cells, culminating in cell death. In PACT, on the other hand, the prodrug, which is usually poorly toxic in the dark, is activated by ligand photosubstitution. The activated drug becomes capable of interacting with biomolecules, causing cell death in an oxygen-independent way.<sup>2-5</sup> Since thermal promotion from the photochemically generated <sup>3</sup>MLCT state into the photosubstitutionally active <sup>3</sup>MC state is a competitive pathway for the quenching of the <sup>3</sup>MLCT state, good PACT agents are usually not emissive and produce only small amounts of <sup>1</sup>O<sub>2</sub>.

In order to be a promising PACT agent, a metal complex has to fulfill three criteria: i) it should be thermally stable in solution in the dark, ii) it should be photoactivatable with acceptable photosubstitution quantum yields, typically in the order of  $\Phi \sim 0.01 - 0.05$ , and iii) it should show an increased cytotoxicity after light activation, compared to the dark. For example, [Ru(tpy)(bpy)(Hmte)](PF<sub>6</sub>)<sub>2</sub> (**[1]**(PF<sub>6</sub>)<sub>2</sub>, where tpy = 2,2':6',2''-terpyridine, bpy = 2,2'-bipyridine, and Hmte = 2-(methylthio)ethanol), is known to undergo photosubstitution under blue light irradiation.<sup>6</sup> Although its cytotoxic properties have not been reported yet, its activated aqua photoproduct [Ru(tpy)(bpy)(OH<sub>2</sub>)]<sup>2+</sup> is known to be non-cytotoxic.<sup>7</sup> To obtain high cytotoxicity, ruthenium complexes require efficient cellular uptake and interaction of the activated metal complex with biological molecules. Bicationic ruthenium complexes often show low cellular uptake.<sup>8</sup> This issue, however, can be solved either by

lowering the positive charge of the complex, *e.g. via* cyclometallation,<sup>9, 10</sup> or by increasing the hydrophobicity of the ligands, *e.g.* by expanding the aromatic surface of a polypyridyl ligand or by adding methyl groups.<sup>11, 12</sup> On the other hand, too lipophilic complexes often show too high dark cytotoxicity, which is a problem in phototherapy.<sup>13</sup> For PACT compounds, ligand expansion aimed at increasing steric hindrance and thus photosubstitution efficacy,<sup>14, 15</sup> may also lead to too distorted complex geometries, resulting in uncontrolled ligand release and thermal activation in the dark.<sup>6, 12, 16</sup> Overall, the design of a good PACT compound requires careful balancing of the lipophilicity of the complex and its photoreactivity altogether.

In this work, two new ruthenium-based PACT compounds with the formula  $[\text{Ru}(\text{tpy})(\text{NN})(\text{Hmte})](\text{PF}_6)_2$  (where NN = *i*-biq (3,3'-biisoquinoline), **[2]**(PF<sub>6</sub>)<sub>2</sub>; or *i*-Hdiqa (di(isoquinolin-3-yl)amine), **[3]**(PF<sub>6</sub>)<sub>2</sub>); Figure 3.1), are reported. The increased aromatic surface of the bidentate ligands, compared to bpy, is expected to improve the cellular uptake. In addition, the dipyridylamine (Hdpa) scaffold, on which *i*-Hdiqa is based, is known to play a role in cellular uptake, compared to bpy-based systems.<sup>17</sup> Considering the promising results obtained with the tetrapyridyl complex  $[\text{Ru}(\text{H}_2\text{biqbpy})(\text{dmsO})(\text{Cl})]^+$ , where  $\text{H}_2\text{biqbpy} = 6,6'$ -bis[*N*-(isoquinolyl)-1-amino]-2,2'-bipyridine,<sup>18</sup> an amine bridge is introduced to the *i*-biq ligand resulting in the *i*-Hdiqa analogue, thus extending the family of  $[\text{Ru}(\text{tpy})(\text{NN})(\text{SRR}') ]^{2+}$  complexes, which has been studied extensively.<sup>19</sup> Next to cellular uptake, the enlarged aromatic rings of the ligands *i*-biq and *i*-Hdiqa may also enhance intercalation of the complex with proteins, membranes, or DNA, which may lead to improved cytotoxicity.<sup>20</sup> The monodentate thioether ligand Hmte, on the other hand, provides excellent thermal stability in the dark, while offering good photochemical release.<sup>6</sup> The synthesis, photochemistry, cytotoxicity, and cellular uptake of these compounds are reported, and compared to that of the known complex **[1]**(PF<sub>6</sub>)<sub>2</sub>.

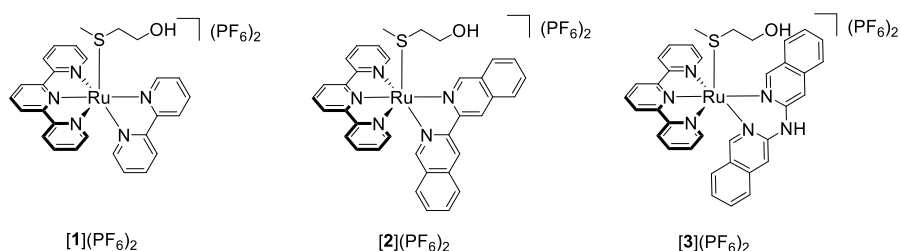


**Figure 3.1.** Chemical structures of the ruthenium-based PACT agents **[1]**(PF<sub>6</sub>)<sub>2</sub> – **[3]**(PF<sub>6</sub>)<sub>2</sub>.

## 3.2 Results and Discussion

### 3.2.1 Synthesis and Characterization

The bidentate ligand i-biq was obtained following a reported procedure.<sup>21</sup> The ligand i-Hdiqa was synthesized using a Buchwald-Hartwig coupling and purified by column chromatography. The two ruthenium-based PACT compounds **[2]**(PF<sub>6</sub>)<sub>2</sub> and **[3]**(PF<sub>6</sub>)<sub>2</sub> were synthesized following the same reaction route as for **[1]**(PF<sub>6</sub>)<sub>2</sub> (Scheme AIII.1). In short, the bidentate ligand was first coordinated to the ruthenium precursor [Ru(tpy)(Cl)<sub>3</sub>], before the monodentate chloride ligand was thermally substituted by the protecting thioether ligand Hmte. The desired complexes were obtained in good yield (50 and 60%, respectively), and their purity was confirmed with <sup>1</sup>H NMR, <sup>13</sup>C NMR, and elemental analysis.

Single crystals suitable for X-ray structure determination of complex **[2]**(PF<sub>6</sub>)<sub>2</sub> were obtained in the dark by slow vapor diffusion of diisopropyl ether in an acetonitrile solution of the complex (Figure 3.2). Selected bond lengths, angles, and torsion angles are summarized in Table 3.1 and are compared to those of **[1]**(PF<sub>6</sub>)<sub>2</sub>.<sup>6</sup> The coordination bond lengths of the i-biq complex are not significantly different from those with bpy *e.g.* Ru-N4 is 2.104(10) *vs.* 2.092(1) Å for **[2]**(PF<sub>6</sub>)<sub>2</sub> *vs.* **[1]**(PF<sub>6</sub>)<sub>2</sub>. The torsion angle of the coordinated i-biq is slightly smaller than that of bpy (N4-C24-C25-N5 = 1.9(14)° *vs.* N4-C20-C21-N5 = 5.3(2)°, Table 3.1). The Hmte ligand is bound *via* the sulfur atom to ruthenium, with similar bond lengths for both complexes (Ru-S = 2.368(3) and 2.3690(5) for **[2]**(PF<sub>6</sub>)<sub>2</sub> and **[1]**(PF<sub>6</sub>)<sub>2</sub>, respectively). As single crystals for complex **[3]**(PF<sub>6</sub>)<sub>2</sub> could not be obtained, density functional theory (DFT) was used to compare the structure of **[3]**<sup>2+</sup> (Figure 3.2) to that of **[2]**<sup>2+</sup> (Table AIII.2 and AIII.3). The bond distances and angles of the DFT models of **[2]**<sup>2+</sup> and **[3]**<sup>2+</sup> are also provided in Table 3.1. For **[2]**<sup>2+</sup>, the minimized geometry of the DFT model was very close to that of the X-ray structure. For **[3]**<sup>2+</sup>, no significant differences in bond lengths or angles are found compared to **[2]**<sup>2+</sup>, however, the position of the bidentate ligand towards the tpy ligand does differ. While i-biq is perpendicular to the tpy ligand, i-Hdiqa shows a characteristic bending at the amine bridge (Figure AIII.10).<sup>22, 23</sup> Calculations of the bond angle variance ( $\sigma^2 = 60.3$  and  $46.4$ , respectively),<sup>24</sup> and the mean quadratic elongation ( $\lambda = 3.65$  and  $3.46$ , respectively),<sup>25</sup> revealed that the octahedral geometry of both complexes is distorted, but that this distortion is mostly caused by the coordination of the tpy ligand (N1-Ru1-N3 =  $158.17$  and  $158.01^\circ$ , respectively). Overall, the extension of the bpy ligand into i-biq

or *i*-Hdiqa does not lead to significant changes of the coordination sphere or bond lengths to the ruthenium ion.

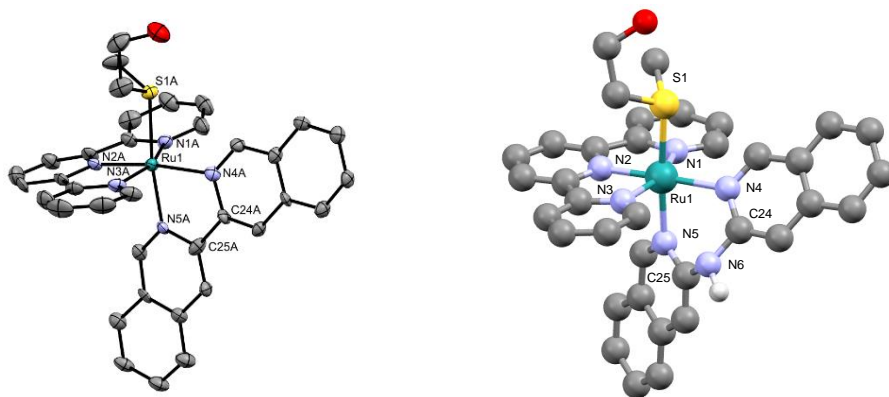


**Figure 3.2.** Displacement ellipsoid (50% probability level) of one crystallographically independent cationic part as observed in the crystal structure of [2]<sup>2+</sup> (left). The other cation, disorder, counter ions, and H atoms have been omitted for clarity. DFT-minimized structure of [3]<sup>2+</sup> (right).

**Table 3.1.** Selected bond lengths (Å), angles (°), and torsion angles (°) for [1](PF<sub>6</sub>)<sub>2</sub> – [3](PF<sub>6</sub>)<sub>2</sub>.

	[1](PF <sub>6</sub> ) <sub>2</sub> <sup>a)</sup>	[2](PF <sub>6</sub> ) <sub>2</sub> <sup>b)</sup>	[2] <sup>2+</sup> <sup>c)</sup>	[3] <sup>2+</sup> <sup>c)</sup>
Ru-N1	2.061(1)	2.071(9)	2.094	2.095
Ru-N2	1.961(1)	1.967(10)	1.979	1.978
Ru-N3	2.066(1)	2.073(10)	2.096	2.114
Ru-N4	2.092(1)	2.104(10)	2.117	2.138
Ru-N5	2.064(1)	2.074(9)	2.082	2.115
Ru-S1	2.3690(5)	2.368(3)	2.396	2.396
N1-Ru1-N2	80.08(6)	79.3(4)	79.14	79.17
N2-Ru1-N3	79.39(6)	80.1(4)	79.19	78.90
N1-Ru1-N3	159.31(6)	159.4(4)	158.17	158.01
N4-Ru1-N5	78.12(6)	79.4(4)	78.43	86.45
N4-C20-C21-N5	5.3(2)	—	—	—
N4-C24-C25-N5	—	1.9(14)	4.46	—
λ <sup>d)</sup>			3.65	3.46
σ <sup>2 e)</sup>			60.3	46.4

<sup>a)</sup> data from Bahreman *et al.*,<sup>6 b)</sup> data obtained by X-ray analysis (provided only for the crystallographically independent cation labelled A in the asymmetric unit of [2](PF<sub>6</sub>)<sub>2</sub>); <sup>c)</sup> data from DFT calculations at the PBE0/TZP/COSMO level in water. <sup>d)</sup>  $\lambda = \frac{1}{6} \sum_{n=1,6} \left[ \frac{d_n - \langle d \rangle}{\langle d \rangle} \right]^2$ , mean quadratic elongation, where d<sub>n</sub> is one of the six bond lengths and <d> is the mean of those bond lengths; <sup>e)</sup>  $\sigma^2 = \frac{1}{11} \sum_{n=1,12} (\theta_n - 90)^2$ , bond angle variance where θ<sub>n</sub> is one of the twelve angles.

### 3.2.2 Photochemistry

Compounds [2](PF<sub>6</sub>)<sub>2</sub> and [3](PF<sub>6</sub>)<sub>2</sub> are thermally stable in water in the dark at 37 °C for 24 h (Figure AIII.1a and b). The two complexes have an <sup>1</sup>MLCT absorption band at 429 and 470 nm for [2]<sup>2+</sup> and [3]<sup>2+</sup>, respectively, with similar molar absorption coefficients (Table 3.2, Figure AIII.2). Compared to [1](PF<sub>6</sub>)<sub>2</sub>, the <sup>1</sup>MLCT state of i-biq-based [2](PF<sub>6</sub>)<sub>2</sub> is shifted to lower wavelengths, while i-Hdiqa-based [3](PF<sub>6</sub>)<sub>2</sub> shows a bathochromic shift, caused by a lower π orbital overlap due to the bending of the i-Hdiqa ligand. Phosphorescence measurements upon irradiation of the complexes with blue light (450 nm) in deuterated methanol showed that phosphorescence quantum yields Φ<sub>P</sub> are lower than 5 · 10<sup>-4</sup> for all three complexes. In addition, the complexes show only very low singlet oxygen quantum yields Φ<sub>Δ</sub>, confirming that they are not suitable as PDT agents (Table 3.2 and Figure AIII.3).

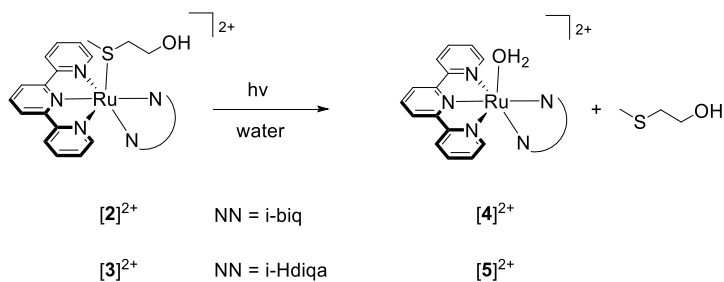


**Table 3.2.** Lowest-energy absorption maxima ( $\lambda_{\max}$  in nm), molar absorption coefficients at  $\lambda_{\max}$  ( $\epsilon_{\max}$  in  $M^{-1} \cdot \text{cm}^{-1}$ ) in water, singlet oxygen generation quantum yields ( $\Phi_{\Delta}$ ) in aerated methanol-d<sub>4</sub>, phosphorescence quantum yields ( $\Phi_P$ ) in aerated methanol-d<sub>4</sub>, and photosubstitution quantum yields upon irradiation at 517 nm ( $\Phi_{517}$ ) in water for complexes [1](PF<sub>6</sub>)<sub>2</sub> – [3](PF<sub>6</sub>)<sub>2</sub>.

complex	NN	$\lambda_{\max}$ ( $\epsilon_{\max}$ ) <sup>a)</sup>	$\Phi_P$ <sup>b)</sup>	$\Phi_{\Delta}$ <sup>b)</sup>	$\Phi_{517}$ <sup>a)</sup>
[1](PF <sub>6</sub> ) <sub>2</sub>	bpy	450 (6.60 · 10 <sup>3</sup> ) <sup>c)</sup>	< 1.0 · 10 <sup>-4</sup> <sup>d)</sup>	< 0.005 <sup>d)</sup>	0.022 <sup>c)</sup>
[2](PF <sub>6</sub> ) <sub>2</sub>	i-biq	429 (5.76 · 10 <sup>3</sup> )	1.5 · 10 <sup>-4</sup>	0.010	0.023
[3](PF <sub>6</sub> ) <sub>2</sub>	i-Hdiqa	470 (5.35 · 10 <sup>3</sup> )	4.5 · 10 <sup>-4</sup>	0.042	0.077

<sup>a)</sup> in water; <sup>b)</sup> in methanol-d<sub>4</sub>; <sup>c)</sup> data taken from Bahreman *et al.*; <sup>d)</sup> data from Chapter 2.

The photoreactivities of [2](PF<sub>6</sub>)<sub>2</sub> and [3](PF<sub>6</sub>)<sub>2</sub> upon green light irradiation (517 nm) in water at 37 °C were investigated using UV-vis spectroscopy (Figure 3.3). For each complex, upon irradiation a typical bathochromic shift of the absorption maximum was observed, due to the release of the thioether ligand and the formation of the corresponding aqua complex [Ru(tpy)(NN)(OH<sub>2</sub>)]<sup>2+</sup> ([4]<sup>2+</sup> and [5]<sup>2+</sup> for NN = i-biq and i-Hdiqa, respectively, see Scheme 3.1).<sup>19, 27, 28</sup> The formation of the aqua complexes was confirmed with mass spectrometry (Figure AIII.4). The UV-vis spectra recorded during irradiation showed isosbestic points (at 369; 375 and 404, respectively), indicating a one-step photosubstitution reaction. The Glotaran software package was used to fit the time evolution of the UV-vis absorption spectra to a single photoreaction, and to obtain the photosubstitution quantum yields  $\Phi_{517}$  (Table 3.2, Figure AIII.5).<sup>29</sup> The quantum yields of [1](PF<sub>6</sub>)<sub>2</sub> and [2](PF<sub>6</sub>)<sub>2</sub> were found similar ( $\Phi_{517} = 0.022$  and 0.023 for [1]<sup>2+</sup> and [2]<sup>2+</sup>, respectively). Thus, changing the bidentate ligand from bpy to i-biq does not alter the photosubstitution efficacy. However, the presence of i-Hdiqa in [3]<sup>2+</sup> increased the quantum yield by 3.5-fold ( $\Phi_{517} = 0.077$ ). The reason for the increased photosubstitution quantum yield of the Hmte ligand in [3]<sup>2+</sup> remains unclear. Overall, efficient quenching of the <sup>3</sup>MLCT state by population of the <sup>3</sup>MC state results for both complexes in non-emissive compounds with very low singlet oxygen production, and with significant to high photosubstitution quantum yields. Therefore, complexes [2](PF<sub>6</sub>)<sub>2</sub> and [3](PF<sub>6</sub>)<sub>2</sub> fulfill the photochemical criteria of potential PACT candidates.



**Scheme 3.1.** Photosubstitution of the protecting Hmte ligand in  $[\text{Ru}(\text{tpy})(\text{NN})(\text{Hmte})]^{2+}$  ( $[2]^{2+}$  and  $[3]^{2+}$ ) to form the corresponding aqua species  $[\text{Ru}(\text{tpy})(\text{NN})(\text{OH}_2)]^{2+}$  ( $[4]^{2+}$  and  $[5]^{2+}$ ).

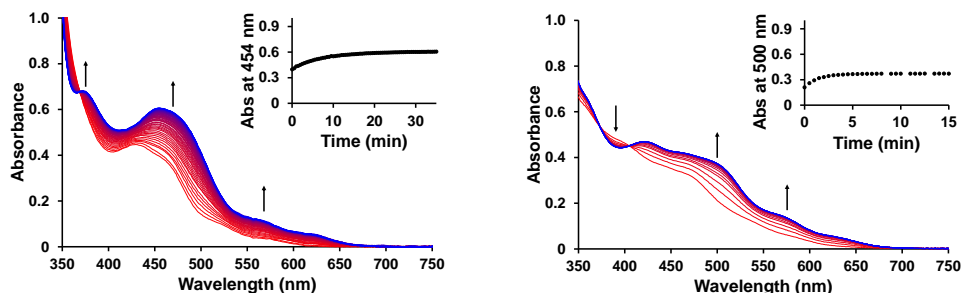


**Figure 3.3.** Evolution of the UV-vis absorption spectra of a solution of  $[2](\text{PF}_6)_2$  (left) and  $[3](\text{PF}_6)_2$  (right) upon green light irradiation in water. Conditions:  $[\text{Ru}] = 0.074$  and  $0.061$  mM for  $[2](\text{PF}_6)_2$  and  $[3](\text{PF}_6)_2$ , respectively,  $T = 37$  °C, light source:  $\lambda = 517$  nm,  $\Delta\lambda_{1/2} = 23$  nm,  $5.2$  mW, photon flux  $\Phi = 5.2 \cdot 10^{-8}$  mol  $\cdot$  s $^{-1}$  for  $[2](\text{PF}_6)_2$  and  $[3](\text{PF}_6)_2$ ,  $V = 3$  mL, under air atmosphere. Inset: Time evolution of absorbance at wavelength  $454$  nm for  $[2](\text{PF}_6)_2$  and  $500$  nm for  $[3](\text{PF}_6)_2$ .

### 3.2.3 Cytotoxicity and cellular uptake

For PACT agents, dark stability under cell growing conditions is essential, so the thermal stability of all complexes was also studied with UV-vis spectroscopy in cell medium (OptiMEM complete) at  $37$  °C (Figure AIII.1c and d). All complexes were found to be stable for at least  $24$  h under such conditions. Then, the cytotoxicity of complexes  $[1](\text{PF}_6)_2 - [3](\text{PF}_6)_2$  was tested under normoxic conditions ( $21\%$   $\text{O}_2$ ) in 2D monolayers of human lung carcinoma (A549) and human epidermoid carcinoma (A431) cell lines, following a protocol developed by Hopkins *et al.*<sup>30</sup> In short, cancer cells were seeded at  $t = 0$  h, treated with six different complex concentrations at  $t = 24$  h, and irradiated at  $t = 48$  h with the light of a green LED for  $30$  min ( $520$  nm,  $38$  J/cm $^2$ ). The irradiation time, necessary to fully activate the complexes, was determined using UV-vis spectroscopy (Appendix 1 and Figure AIII.6). At  $t = 96$  h a Sulforhodamine B (SRB) assay was performed to compare the cell viability in treated *vs.* untreated cells (Figure AIII.7 and AIII.8). The effective concentrations ( $\text{EC}_{50}$  values), *i.e.* the concentration at which the cell viability was reduced by  $50\%$

compared to untreated cells, are reported in Table 3.3. The photo index of each compound was calculated as the ratio of the EC<sub>50</sub> values obtained in the dark and upon light irradiation.

The bpy-based complex [1](PF<sub>6</sub>)<sub>2</sub> was found to be non-cytotoxic against A549 cancer cells, whether irradiated or not (EC<sub>50</sub> > 150 μM, Figure AIII.9). The complexes [2](PF<sub>6</sub>)<sub>2</sub> and [3](PF<sub>6</sub>)<sub>2</sub> showed low cytotoxicity in the dark (80 vs. 62 μM), but revealed a significant increase in cytotoxicity after light activation characterized by EC<sub>50</sub> values of 21 and 14 μM, respectively. These changes correspond to photo indices of ~ 4 for both complexes, indicating that a more cytotoxic species is released upon light activation. The released thioether ligand Hmte, tested independently, showed neither cytotoxicity in the dark nor upon light irradiation. Therefore, the cytotoxicity observed upon light irradiation of [2]<sup>2+</sup> or [3]<sup>2+</sup> must be based on the metal-containing photoproduct, *i.e.* the aqua complexes [5]<sup>2+</sup> and [6]<sup>2+</sup>, respectively.<sup>31</sup>  
<sup>32</sup> In A431 cancer cells, the same trends were observed (Table 3.3). Cytotoxicity experiments under hypoxic conditions (1% O<sub>2</sub>) need to be undertaken for complexes [2](PF<sub>6</sub>)<sub>2</sub> and [3](PF<sub>6</sub>)<sub>2</sub> to confirm whether they remain phototoxic also at low oxygen levels, as true PACT agents should.

**Table 3.3.** (Photo)cytotoxicity ( $EC_{50}$  with 95% confidence interval in  $\mu\text{M}$ ) of [1](PF<sub>6</sub>)<sub>2</sub>, [2](PF<sub>6</sub>)<sub>2</sub>, [3](PF<sub>6</sub>)<sub>2</sub>, and Hmte in lung cancer cells (A549) and skin cancer cells (A431) under normoxic conditions (21% O<sub>2</sub>).<sup>a)</sup> Cellular uptake (CU in nmol Ru/ mg cell protein) of [1](PF<sub>6</sub>)<sub>2</sub> – [3](PF<sub>6</sub>)<sub>2</sub> in lung cancer cells (A549) under normoxic conditions (21%).<sup>b)</sup>

		[1](PF <sub>6</sub> ) <sub>2</sub>	[2](PF <sub>6</sub> ) <sub>2</sub>	[3](PF <sub>6</sub> ) <sub>2</sub>	Hmte		
A549	dark	>150	79.7	+6.1 -5.7	62.1	+16.4 -13.8	>150
	light	>150	20.6	+3.0 -2.6	13.8	+4.3 -3.6	>150
	PI <sup>c)</sup>	—	3.9		4.5		—
	CU	0.16 ± 0.11	0.32 ± 0.14		0.69 ± 0.16		—
A431	dark	>150	55.2	+7.5 -6.5	42.9	+9.2 -7.5	>150
	light	>150	12.2	+1.5 -1.4	11.2	+2.7 -2.4	>150
	PI <sup>c)</sup>	—	4.5		3.8		—

<sup>a)</sup> Cytotoxicity experiments were performed in biological and technical triplicate; <sup>b)</sup> Results of cellular uptake experiments upon incubation for 24 h with 30  $\mu\text{M}$  drug in the dark. Experiments were performed in biological triplicate; <sup>c)</sup> photo index (PI) is defined as  $EC_{50, \text{dark}}/EC_{50, \text{light}}$ .

To quantify the effect of the increased hydrophilicity of the complexes, by extending the aromaticity of the ligands, on the cellular uptake, uptake experiments were performed. A549 cells were treated with 30  $\mu\text{M}$  of the complex, which is lower than the  $EC_{50}$  values, and the uptake was determined after 24 h incubation in the dark (Table 3.3). The ruthenium content in nmol per mg cell protein was determined by high-resolution continuum-source atomic absorption spectrometry (HRCS AAS, further details in Appendix 1) under normoxic (21% O<sub>2</sub>). Complex [1](PF<sub>6</sub>)<sub>2</sub> was very poorly taken up (0.16 nmol per mg cell protein), which explains its lack of cytotoxicity against cancer cells. For the other two complexes, the ruthenium uptake was higher, *i.e.* 0.32 and 0.69 nmol per mg cell protein, respectively, under normoxic conditions. According to these results, dipyriddyamine-based ligands such as i-Hdiqa enhance complex accumulation compared to their bpy analogues (here i-biq).<sup>17</sup>

### 3.3 Conclusions

The known photoactivatable ruthenium complex [1](PF<sub>6</sub>)<sub>2</sub> is very poorly taken up by cells and as a result shows no (photo)cytotoxicity. Therefore, it is not suitable as a

PACT agent. However, two analogue ruthenium complexes with more hydrophobic bidentate ligands were shown to be promising PACT compounds. Complex **[2]**(PF<sub>6</sub>)<sub>2</sub> shows comparable photochemical properties as **[1]**(PF<sub>6</sub>)<sub>2</sub>, but the higher lipophilicity significantly increases cellular uptake. This allows the photosubstitution reaction to occur inside the cell and to result into increased cytotoxicity upon green light irradiation. **[3]**(PF<sub>6</sub>)<sub>2</sub>, which has an additional non-coordinated amine bridge, shows an enhanced photosubstitution quantum yield compared to **[2]**<sup>2+</sup> and enhanced cellular uptake, but it has a similar photo index compared to **[2]**<sup>2+</sup>. Cytotoxicity studies under hypoxic conditions need to be undertaken with **[2]**(PF<sub>6</sub>)<sub>2</sub> and **[3]**(PF<sub>6</sub>)<sub>2</sub> to investigate whether the oxygen-independent activation mechanism translates into interesting biological photoactivation also in hypoxic cancer cells.

## 3.4 Experimental

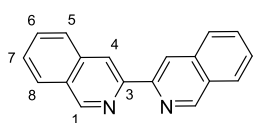
### 3.4.1 Methods and Materials

RuCl<sub>3</sub> was purchased from Alfa Aesar, 3-bromoisoquinoline from ABCR, isoquinolin-3-amine, tris(dibenzylideneacetone)dipalladium(0), 1,3-bis(diphenylphosphino)propane, and 2-(methylthio)ethanol from Sigma Aldrich, and potassium tert-butoxide from Acros Organics. **[1]**(PF<sub>6</sub>)<sub>2</sub> was synthesized according to literature.<sup>6</sup> All metal complexes were synthesized in dim light and stored in darkness. All reactants and solvents were used without further purification. <sup>1</sup>H NMR spectra were recorded on a Bruker AV-300 spectrometer. Chemical shifts are indicated in ppm. Mass spectra were recorded by using an MSQ Plus Spectrometer.

### 3.4.2 Synthesis

#### 3,3'-biisoquinoline (i-biq)

i-biq was synthesized according to literature.<sup>21</sup>



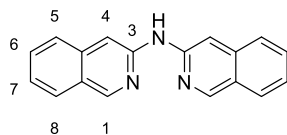
<sup>1</sup>H NMR (300 MHz, chloroform-*d*, 298 K) δ 9.38 (s, 2H, 1), 8.93 (s, 2H, 4), 8.08 – 7.96 (m, 4H, 8 + 5), 7.74 (ddd, *J* = 8.2, 6.9, 1.3 Hz, 2H, 6), 7.63 (ddd, *J* = 8.1, 6.9, 1.2 Hz, 2H, 7). <sup>13</sup>C NMR (75 MHz, chloroform-*d*, 298 K) δ 152.3 (1), 137.0 (3), 131.0 (6), 128.7 + 127.9 (4a + 8a), 127.9 + 127.8 (5 + 8), 127.8 (7), 118.1 (4). ES MS *m/z* (calc.): 257.3 (257.1 [M + H]<sup>+</sup>).

#### di(isoquinolin-3-yl)amine (i-Hdiqa)

i-Hdiqa was synthesized according to literature procedures described for the synthesis of other dipyriddyamine derivatives.<sup>33</sup>

Tris(dibenzylideneacetone)dipalladium(0) (18 mg, 0.020 mmol) and 1,3-bis(diphenylphosphino)propane (16 mg, 0.039 mmol) were dissolved in dry toluene (25 mL). 3-Bromoisoquinoline (200 mg, 0.97 mmol), isoquinolin-3-amine (170 mg, 1.2 mmol), and potassium tert-butoxide (150 mg, 1.4 mmol) were added in this order under dinitrogen atmosphere. The resultant mixture was stirred and heated to reflux under dinitrogen atmosphere overnight at 110 °C. The solution was cooled down to room temperature and

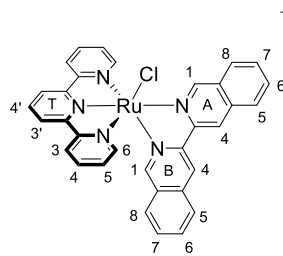
filtered over *Celite*. The cake was washed four times with ethyl acetate (30 mL). The solvent was evaporated with a rotary evaporator using a water bath set at 40 °C. The crude product was purified by column chromatography on silica with pentane/ethyl acetate 1:1 + 0.5% triethylamine as eluent ( $R_f = 0.75$ ), to yield i-Hdiqa as a yellow powder. Yield: 48% (130 mg, 0.48 mmol).



$^1\text{H NMR}$  (300 MHz, *chloroform-d*, 298 K)  $\delta$  (ppm) 9.05 (s, 2H, 1), 7.88 (dd,  $J = 8.2, 1.1$  Hz, 2H, 8), 7.80 (s, 2H, 4), 7.73 (dd,  $J = 8.3, 1.1$  Hz, 2H, 5), 7.64 (s, 1H, NH), 7.58 (ddd,  $J = 8.2, 6.8, 1.2$  Hz, 2H, 7), 7.37 (ddd,  $J = 8.1, 6.8, 1.1$  Hz, 2H, 6).  $^{13}\text{C NMR}$  (75 MHz, *chloroform-d*, 298 K)  $\delta$  (ppm) 151.6 (1), 150.0 (3), 138.6 (4a), 130.7 (6), 127.9 (8), 125.8 (5), 125.2 (8a), 124.4 (7), 103.0 (4). *ES MS*  $m/z$  (*calc.*): 272.4 (272.1,  $[\text{M} + \text{H}]^+$ ).

### [Ru(tpy)(i-biq)(Cl)]Cl

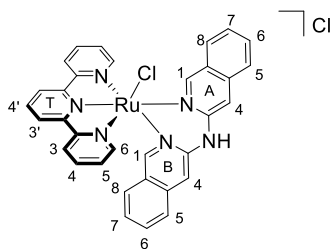
[Ru(tpy)(Cl) $_3$ ] (174 mg, 0.394 mmol), i-biq (101 mg, 0.394 mmol), and lithium chloride (18.4 mg, 0.433 mmol) were dissolved in a degassed ethanol/water mixture (3:1, 32 mL). Triethylamine (0.756 mL, 0.630 mmol) was added and the reaction mixture was refluxed under dinitrogen atmosphere overnight. The reaction mixture was filtered hot over *Celite* and the cake was washed with ethanol until the filtrate was colorless. After evaporation of the solvents, the crude product was purified by column chromatography on silica with dichloromethane/methanol (9:1) as eluent ( $R_f = 0.64$ ). The product was obtained as a dark brown solid. Yield: 94% (245 mg, 0.370 mmol).



$^1\text{H NMR}$  (300 MHz, *methanol-d<sub>4</sub>*, 298 K)  $\delta$  10.79 (s, 1H, A1), 9.32 (s, 1H, A4), 9.03 (s, 1H, B4), 8.69 (d,  $J = 8.1$  Hz, 2H, T3'), 8.55 (dt,  $J = 8.1, 1.2$  Hz, 2H, T3), 8.44 – 8.33 (m, 2H, A5 + A8), 8.20 (t,  $J = 8.1$  Hz, 1H, T4'), 8.10 – 7.82 (m, 8H, B5 + A6 + A7 + B1 + T6 + T4), 7.72 (ddd,  $J = 8.2, 6.5, 1.6$  Hz, 1H, B6), 7.66 – 7.50 (m, 2H, B7 + B8), 7.28 (ddd,  $J = 7.3, 5.6, 1.4$  Hz, 2H, T5).  $^{13}\text{C NMR}$  (75 MHz, *methanol-d<sub>4</sub>*, 298 K)  $\delta$  160.5 + 160.0 (C<sub>q</sub> T2 + T2'), 156.9 (A1), 156.0 (B1), 153.1 (T6), 152.6 + 151.1 (C<sub>q</sub> A3 + B3), 138.3 (T4), 136.8 + 135.7 (C<sub>q</sub> A4a + B4a), 135.3 (T4'), 133.7 (A6), 133.4 (B6), 131.3 (A7), 131.0 + 130.3 (C<sub>q</sub> A8a + B8a), 130.8 (B7), 129.0 + 128.7 + 128.5 (A5 + B5 + A8), 128.4 (T5), 127.2 (B8), 124.9 (T3), 123.7 T3'), 121.4 (A4), 120.8 (B4). *ES MS*  $m/z$  (*calc.*): 626.6 (626.1  $[\text{M} - \text{Cl}]^+$ ).

### [Ru(tpy)(i-Hdiqa)(Cl)]Cl

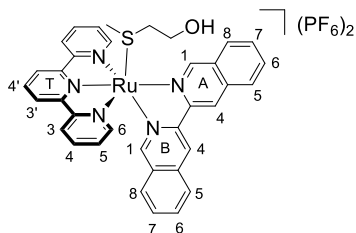
[Ru(tpy)(Cl) $_3$ ] (135 mg, 0.307 mmol), i-Hdiqa (100 mg, 0.369 mmol), and lithium chloride (65 mg, 1.5 mmol) were dissolved in a degassed ethanol/water mixture (3:1, 20 mL). Triethylamine (400  $\mu\text{L}$ , 2.6 mmol) was added and the reaction mixture was refluxed under dinitrogen atmosphere for 4 h. The reaction mixture was filtered hot over *Celite* and the cake was washed with ethanol until the filtrate was colorless. After evaporation of the solvents, the crude product was purified by column chromatography on silica with dichloromethane/methanol (9:1) as eluent ( $R_f = 0.42$ ), to yield a dark reddish brown solid. Yield: 83% (173 mg, 0.256 mmol).



$^1\text{H NMR}$  (300 MHz, *methanol-d*<sub>4</sub>, 298 K)  $\delta$  10.35 (s, 1H, A1), 8.61 (d,  $J = 8.1$  Hz, 2H, T3'), 8.61 – 8.56 (m, 2H, T6), 8.55 (dd,  $J = 8.0, 1.2$  Hz, 2H, T3), 8.14 (dd,  $J = 8.4, 1.1$  Hz, 1H, A8), 8.10 (t,  $J = 8.1$  Hz, 1H, T4'), 8.03 (dd,  $J = 8.3, 1.0$  Hz, 1H, A5), 8.01 (ddd,  $J = 8.0, 7.8, 1.5$  Hz, 2H, T4), 7.85 (ddd,  $J = 8.3, 6.9, 1.1$  Hz, 1H, A6), 7.84 (s, 1H, A4), 7.64 (ddd,  $J = 8.4, 6.9, 1.0$  Hz, 1H, A7), 7.59 (dd,  $J = 8.1, 1.1$  Hz, 1H, B5), 7.56 – 7.51 (m, 2H, T5), 7.50 (s, 1H, B1), 7.51 – 7.47 (m, 1H, B6), 7.31 (dd,  $J = 8.3, 1.0$  Hz, 1H, B8), 7.23 (s, 1H, B4), 7.23 (ddd,  $J = 8.3, 6.6, 1.1$  Hz, 1H, B7).  $^{13}\text{C NMR}$  (75 MHz, *methanol-d*<sub>4</sub>, 298 K)  $\delta$  160.8 + 160.8 (C<sub>q</sub> T2 + T2'), 160.1 (A1), 154.6 (T6), 154.4 (B1), 151.3 (C<sub>q</sub> A3 or B3), 139.6 (C<sub>q</sub> A4a or B4a), 138.4 (T4), 135.2 (T4'), 133.6 (A6), 133.4 (B6), 128.8 (A8), 128.3 (T5), 127.9 + 126.9 (C<sub>q</sub> A8a + B8a), 127.7 (A7), 127.4 (B7), 127.1 (B8), 126.8 (A5), 126.2 (B5), 124.9 (T3), 123.7 (T3'), 108.0 (A4), 107.3 (B4), two quaternary carbons are missing: C<sub>q</sub> A3 or B3, C<sub>q</sub> A4a or B4a. *ES MS m/z* (*calc.*): 641.6 (641.1 [M – Cl]<sup>+</sup>).

### [Ru(tpy)(i-biq)(Hmte)](PF<sub>6</sub>)<sub>2</sub>, [2](PF<sub>6</sub>)<sub>2</sub>

[Ru(tpy)(i-biq)(Cl)]Cl (21 mg, 0.032 mmol) and AgPF<sub>6</sub> (17 mg, 0.067 mmol) were dissolved in a degassed acetone/water mixture (3:5, 16 mL). 2-(Methylthio)ethanol (138  $\mu\text{L}$ , 1.53 mmol) was added in excess to the reaction mixture. The reaction was stirred and heated to reflux under dinitrogen atmosphere for 4 h, filtered hot over *Celite*, and the cake was washed with acetone until the filtrate was colorless. The solvents were removed by rotary evaporation. The product was dissolved in a minimum amount of acetone and reprecipitated by addition to an excess of diethyl ether. Filtration yielded the final product, which was dried in air and then under vacuum as a bright orange powder. Yield: 48% (15 mg, 0.015 mmol).

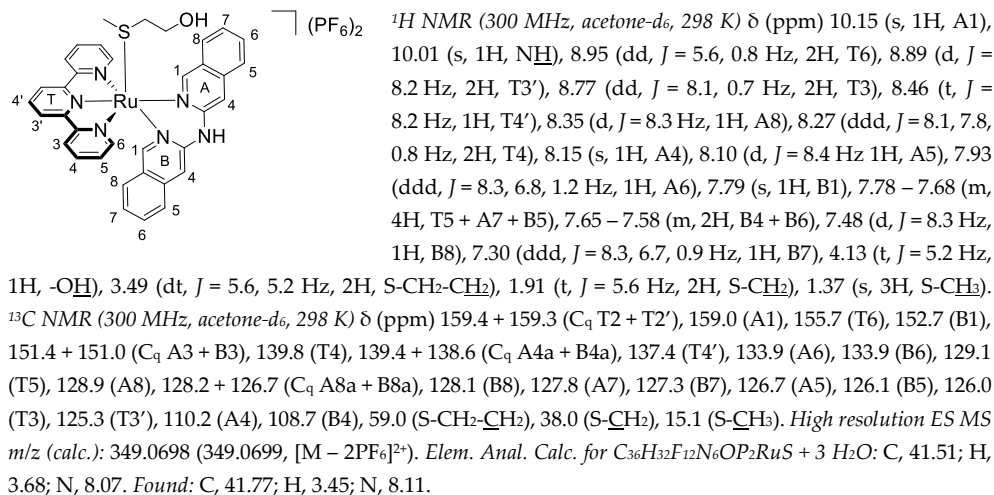


$^1\text{H NMR}$  (300 MHz, *acetone-d*<sub>6</sub>, 298 K)  $\delta$  (ppm) 10.64 (s, 1H, A1), 9.54 (s, 1H, A4), 9.32 (s, 1H, B4), 8.99 (d,  $J = 8.1$  Hz, 2H, T3'), 8.79 (dd,  $J = 8.0, 1.3$  Hz, 2H, T3), 8.57 (t,  $J = 8.1$  Hz, 1H, T4'), 8.54 (d,  $J = 8.3$  Hz, 2H, A8), 8.42 (d,  $J = 8.2$  Hz, 1H, A5), 8.27 – 8.22 (m, 3H, B1 + T6), 8.17 – 8.09 (m, 4H, T4 + B5 + A6), 8.04 (ddd,  $J = 8.2, 7.0, 1.2$  Hz, 1H, A7), 7.84 (ddd,  $J = 8.2, 6.7, 1.4$  Hz, 1H, B6), 7.71 (d,  $J = 8.0$  Hz, 1H, B8), 7.63 (ddd,  $J = 8.2, 6.7, 1.0$  Hz, 1H, B7), 7.47 (ddd,  $J = 7.7, 5.5, 1.3$  Hz, 2H, T5), 4.77 (t,  $J = 4.7$  Hz, 1H, OH), 3.59 (dt,  $J = 5.0, 4.7$  Hz, 2H, S-CH<sub>2</sub>-CH<sub>2</sub>), 2.10 (t,  $J = 5.0$  Hz, 2H, S-CH<sub>2</sub>), 1.54 (s, 3H, S-CH<sub>3</sub>).  $^{13}\text{C NMR}$  (300 MHz, *acetone-d*<sub>6</sub>, 298 K)  $\delta$  (ppm) 159.2 + 158.8 (C<sub>q</sub> T2 + T2'), 156.8 (A1), 154.7 (B1), 154.4 (T6), 150.8 + 150.4 (C<sub>q</sub> A3 + B3), 139.7 (T4), 137.7 (T4'), 136.7 + 136.1 (C<sub>q</sub> A4a + B4a), 134.0 (B6 + A6), 131.1 (A7), 130.8 + 129.8 (C<sub>q</sub> A8a + B8a), 130.6 (B7), 129.3 (T5), 129.1 (A8), 128.7 (A5), 128.3 (B5 + B8), 126.0 (T3), 125.3 (T3'), 122.1 (A4), 121.4 (B4), 58.8 (S-CH<sub>2</sub>-CH<sub>2</sub>), 38.4 (S-CH<sub>2</sub>), 14.8 (S-CH<sub>3</sub>). *High resolution ES MS m/z* (*calc.*): 341.5644 (341.5645 [M – 2PF<sub>6</sub>]<sup>2+</sup>). *Elem. Anal. Calc. for C<sub>36</sub>H<sub>31</sub>F<sub>12</sub>N<sub>5</sub>OP<sub>2</sub>RuS*: C, 44.45; H, 3.21; N, 7.20. *Found*: C, 43.75; H, 3.30; N, 7.12.

### [Ru(tpy)(i-Hdiqa)(Hmte)](PF<sub>6</sub>)<sub>2</sub>, [3](PF<sub>6</sub>)<sub>2</sub>

[Ru(tpy)(i-Hdiqa)(Cl)]Cl (150 mg, 0.222 mmol) and AgPF<sub>6</sub> (123 mg, 0.488 mmol) were dissolved in a degassed acetone/water mixture (3:5, 30 mL). 2-(Methylthio)ethanol (1 mL, 0.01 mol) was added in excess to the reaction mixture. The reaction was stirred and heated to reflux under dinitrogen atmosphere for 3 h, filtered hot over *Celite*, and the cake was washed with acetone until the filtrate was colorless. The solvents were removed by rotary evaporation. The product was dissolved in a minimum amount of

acetone and precipitated by addition to an excess of diethyl ether. Filtration yielded the final product as an orange powder, which was dried in air and then under vacuum. Yield: 60% (132 mg, 0.134 mmol).



### 3.4.3 Single Crystal X-Ray crystallography

Single crystals of [2](PF<sub>6</sub>)<sub>2</sub> were obtained by recrystallization through liquid-vapor diffusion using acetonitrile as solvent and diisopropyl ether as counter-solvent. In short, 1 mg of [2](PF<sub>6</sub>)<sub>2</sub> was dissolved in acetonitrile (1 mL) and placed in a small vial. This vial was placed in a larger vial containing diisopropyl ether (2.8 mL). The large vial was closed and vapor diffusion within a few days afforded X-ray quality crystals.

All reflection intensities were measured at 110(2) K using a SuperNova diffractometer (equipped with Atlas detector) with Cu  $K\alpha$  radiation ( $\lambda = 1.54178$  Å) under the program CrysAlisPro (Version CrysAlisPro 1.171.39.29c, Rigaku OD, 2017). The same program was used to refine the cell dimensions and for data reduction. The structure was solved with the program SHELXS-2014/7 (Sheldrick, 2015) and was refined on  $F^2$  with SHELXL-2014/7 (Sheldrick, 2015). Analytical numeric absorption correction using a multifaceted crystal model was applied using CrysAlisPro. The temperature of the data collection was controlled using the system Cryojet (manufactured by Oxford Instruments). The H atoms were placed at calculated positions using the instructions AFIX 23, AFIX 43 or AFIX 137 with isotropic displacement parameters having values 1.2 or 1.5 U<sub>eq</sub> of the attached C atoms. The H atoms attached to the disordered hydroxyl groups O1A/O1A' and O1B/O1B' could not be retrieved reliably from difference Fourier maps, and no AFIX 147 was used because of the disorder. The crystal refines in the space group  $Pca2_1$  and is racemically twinned. The Flack parameter refines to 0.539(16).

The structure of [2](PF<sub>6</sub>)<sub>2</sub> is significantly disordered. Two of the four crystallographically independent counter ions were found to be disordered over (at least) 3 different orientations. The terpyridine ligand on one of the two ruthenium complexes is disordered over two orientations. The hydroxyl groups of the Hmtc ligands for both Ru1 and Ru2 complexes are disordered over two orientations. [2](PF<sub>6</sub>)<sub>2</sub>: 0.51 × 0.10 × 0.05 mm<sup>3</sup>, Orthorhombic,  $Pca2_1$ ,  $a = 22.0959$  (11),  $b = 8.8289$  (2),  $c = 37.3521$  (9) Å,  $V = 7286.7$  (4) Å<sup>3</sup>,  $Z = 8$ ,  $\mu = 5.78$  mm<sup>-1</sup>, transmission factor range: 0.280–0.812. 23674 Reflections were measured up to a resolution of  $(\sin \theta/\lambda)_{\text{max}} = 0.616$  Å<sup>-1</sup>. 11592 Reflections were unique ( $R_{\text{int}} = 0.037$ ), of which 10905



were observed [ $I > 2\sigma(I)$ ]. 1423 Parameters were refined. R1/wR2 [ $I > 2\sigma(I)$ ]: 0.0525/ 0.1383. R1/wR2 [all refl.]: 0.0558/ 0.1407. S= 1.11. Residual electron density found between  $-0.87$  and  $1.63 \text{ e } \text{\AA}^{-3}$ .

#### 3.4.4 DFT calculations

DFT was used to perform electronic structure calculations. The structure of  $[2]^{2+}$  and  $[3]^{2+}$  was optimized using ADF from SCM,<sup>34</sup> using the PBE0 hybrid functional, a triple zeta basis set (TZP) for all atoms, and COSMO to simulate solvent effects in water.

#### 3.4.5 Irradiation experiments monitored with UV-vis and MS

Photoreactions monitored with UV-vis spectroscopy were performed on a Cary Varian spectrometer equipped with temperature control set to 310 K and a magnetic stirrer. The measurements were performed in a quartz cuvette, containing 3 mL of solution. The stirred sample was irradiated perpendicularly to the axis of the spectrometer with the beam of an LED fitted to the top of the cuvette.

For photoactivation with green light, an LED light source ( $\lambda = 517 \text{ nm}$ ,  $\Delta\lambda_{1/2} = 23 \text{ nm}$ ,  $5.2 \text{ mW}$ ) was used, an absorption spectrum was measured every 30 sec for 70 min for  $[2](\text{PF}_6)_2$  and 47 min for  $[3](\text{PF}_6)_2$ .  $[\text{Ru}] = 0.074$  and  $0.061 \text{ mM}$  and  $\Phi = 5.2 \cdot 10^{-8} \text{ mol} \cdot \text{s}^{-1}$  for  $[2](\text{PF}_6)_2$  and  $[3](\text{PF}_6)_2$ . Data were analyzed using Microsoft Excel. Mass spectrometry was performed at the beginning and at the end of the irradiation to confirm the nature of the reagent and products. Photosubstitution quantum yield calculations were performed using the Glotaran Software package as described in Appendix I. The conditions are summarized in Table AIII.1.

#### 3.4.6 Cytotoxicity and cellular uptake

Cytotoxicity assays and cellular uptake experiments were performed using the protocols described in Appendix I.

#### 3.4.7 Supporting information

DFT models, dark stability measurements, determination of molar extinction coefficients, singlet oxygen production and phosphorescence spectra, photosubstitution conditions, and light dose determinations for  $[2](\text{PF}_6)_2$  and  $[3](\text{PF}_6)_2$  are provided in Appendix III.

### 3.5 Contribution

Ingrid Flashpohler helped performing cytotoxicity tests, Dr. Claudia Schmidt and Prof. Ingo Ott performed HRCS-AAS measurements for cell uptake, Xuequan Zhou performed singlet oxygen measurements, Dr. Vincent van Rixel grew single crystals, and Dr. Maxime Siegler performed X-ray diffraction experiments and crystal structure determination. Dr. Sylvestre Bonnet performed DFT studies and, together with Prof. Lies Bouwman, he provided experimental guidance and significant editorial feedback.

### 3.6 References

- 1 L. Zayat, O. Filevich, L. M. Baraldo, and R. Etchenique, *Philos. Trans. Royal Soc. A* **2013**, 371 (1995), 20120330.
- 2 A. Li, C. Turro, and J. J. Kodanko, *Chem. Commun.* **2018**, 54 (11), 1280-1290.
- 3 J. Wei and A. K. Renfrew, *J. Inorg. Biochem.* **2018**, 179 (-), 146-153.

- 4 H. Chan, J. B. Ghrayche, J. Wei, and A. K. Renfrew, *Eur. J. Inorg. Chem.* **2017**, 2017 (12), 1679-1686.
- 5 U. Basu, J. Karges, F. Chotard, C. Balan, P. Le Gendre, G. Gasser, E. Bodio, and R. Malacea Kabbara, *Polyhedron* **2019**, doi.org/10.1016/j.poly.2019.02.041.
- 6 A. Bahreman, B. Limburg, M. A. Siegler, E. Bouwman, and S. Bonnet, *Inorg. Chem.* **2013**, 52 (16), 9456-69.
- 7 O. Novakova, J. Kasparkova, O. Vrana, P. M. van Vliet, J. Reedijk, and V. Brabec, *Biochemistry* **1995**, 34 (38), 12369-12378.
- 8 E. Alessio, *Eur. J. Inorg. Chem.* **2017**, 2017 (12), 1549-1560.
- 9 L. N. Lameijer, C. van de Griend, S. L. Hopkins, A.-G. Volbeda, S. H. C. Askes, M. A. Siegler, and S. Bonnet, *J. Am. Chem. Soc.* **2019**, 141 (1), 352-362.
- 10 H. Huang, P. Zhang, H. Chen, L. Ji, and H. Chao, *Chem. Eur. J.* **2015**, 21 (2), 715-725.
- 11 U. Schatzschneider, J. Niesel, I. Ott, R. Gust, H. Alborzina, and S. Wölfl, *ChemMedChem* **2008**, 3 (7), 1104-1109.
- 12 J.-A. Cuello-Garibo, C. C. James, M. A. Siegler, and S. Bonnet, *Chem. Sq* **2017**, 1 (2), 1-19.
- 13 B. Siewert, V. H. van Rixel, E. J. van Rooden, S. L. Hopkins, M. J. Moester, F. Ariese, M. A. Siegler, and S. Bonnet, *Chem. Eur. J.* **2016**, 22 (31), 10960-10968.
- 14 B. S. Howerton, D. K. Heidary, and E. C. Glazer, *J. Am. Chem. Soc.* **2012**, 134 (20), 8324-8327.
- 15 L. Kohler, L. Nease, P. Vo, J. Garofolo, D. K. Heidary, R. P. Thummel, and E. C. Glazer, *Inorg. Chem.* **2017**, 56 (20), 12214-12223.
- 16 L. N. Lameijer, D. Ernst, S. L. Hopkins, M. S. Meijer, S. H. Askes, S. E. Le Dévédec, and S. Bonnet, *Angew. Chem., Int. Ed.* **2017**, 56 (38), 11549-11553.
- 17 A. C. Komor, C. J. Schneider, A. G. Weidmann, and J. K. Barton, *J. Am. Chem. Soc.* **2012**, 134 (46), 19223-19233.
- 18 V. H. S. van Rixel, B. Siewert, S. L. Hopkins, S. H. C. Askes, A. Busemann, M. A. Siegler, and S. Bonnet, *Chem. Sci.* **2016**, 7 (8), 4922-4929.
- 19 L. N. Lameijer, T. G. Brevé, V. H. S. van Rixel, S. H. C. Askes, M. A. Siegler, and S. Bonnet, *Chem. Eur. J.* **2018**, 24 (11), 2709-2717.
- 20 W. Han Ang and P. J. Dyson, *Eur. J. Inorg. Chem.* **2006**, 2006 (20), 4003-4018.
- 21 T. Funayama, M. Kato, H. Kosugi, M. Yagi, J. Higuchi, and S. Yamauchi, *Bull. Chem. Soc. Jpn.* **2000**, 73 (7), 1541-1550.
- 22 M. Toyama, R. Suganoya, D. Tsuduura, and N. Nagao, *Bull. Chem. Soc. Jpn.* **2007**, 80 (5), 922-936.
- 23 N. Chanda, S. M. Mobin, V. G. Puranik, A. Datta, M. Niemeyer, and G. K. Lahiri, *Inorg. Chem.* **2004**, 43 (3), 1056-1064.
- 24 K. Robinson, G. V. Gibbs, and P. H. Ribbe, *Science* **1971**, 172 (3983), 567-570.
- 25 M. E. Fleet, *Mineral. Mag.* **1976**, 40 (313), 531-533.
- 26 D. Garcia-Fresnadillo, Y. Georgiadou, G. Orellana, A. M. Braun, and E. Oliveros, *Helv. Chim. Acta* **1996**, 79 (4), 1222-1238.
- 27 R. E. Goldbach, I. Rodriguez-Garcia, J. H. van Lenthe, M. A. Siegler, and S. Bonnet, *Chem. Eur. J.* **2011**, 17 (36), 9924-9929.
- 28 B. Siewert, M. Langerman, Y. Hontani, J. T. M. Kennis, V. H. S. van Rixel, B. Limburg, M. A. Siegler, V. Talens Saez, R. E. Kieltyka, and S. Bonnet, *Chem. Commun.* **2017**, 53 (81), 11126-11129.
- 29 J. Snellenburg, J., S. Laptanok, R. Seger, K. Mullen, M., and I. Van Stokkum, H.M., *J. Stat. Softw.* **2012**, 49 (3), 1-22.
- 30 S. Hopkins, B. Siewert, S. Askes, P. Veldhuizen, R. Zwier, M. Heger, and S. Bonnet, *Photochem. Photobiol. Sci.* **2016**, 15 (5), 644-653.

- 31 J.-A. Cuello-Garibo, M. S. Meijer, and S. Bonnet, *Chem. Commun.* **2017**, 53 (50), 6768-6771.
- 32 D. F. Azar, H. Audi, S. Farhat, M. El-Sibai, R. J. Abi-Habib, and R. S. Khnayzer, *Dalton Trans.* **2017**, 46 (35), 11529-11532.
- 33 R. Marion, F. Sguerra, F. Di Meo, E. Sauvageot, J.-F. Lohier, R. Daniellou, J.-L. Renaud, M. Linares, M. Hamel, and S. Gaillard, *Inorg. Chem.* **2014**, 53 (17), 9181-9191.
- 34 G. te Velde, F. M. Bickelhaupt, E. J. Baerends, C. Fonseca Guerra, S. J. A. van Gisbergen, J. G. Snijders, and T. Ziegler, *J. Comput. Chem.* **2001**, 22 (9), 931-967.



# 4

## VISUALIZING THE INVISIBLE: IMAGING OF RUTHENIUM-BASED PACT AGENTS IN FIXED CANCER CELLS

*Two alkyne-functionalized complexes with the formula  $[Ru(HCC-tpy)(NN)(Hmte)](PF_6)_2$  were synthesized, where HCC-tpy = 4'-ethynyl-2,2':6',2''-terpyridine, NN = 3,3'-biisoquinoline (i-biq, [2](PF<sub>6</sub>)<sub>2</sub>), or di(isoquinolin-3-yl)amine (i-Hdiqa, [4](PF<sub>6</sub>)<sub>2</sub>), and Hmte = 2-(methylthio)ethanol. The geometry of the complexes is preserved after functionalization, and the alkyne moiety has no effect on the photosubstitution quantum yield ( $\Phi_{[2]} = 0.022$  and  $\Phi_{[4]} = 0.080$ ). Cellular uptake, on the other hand, was doubled after alkyne functionalization, resulting in increased cytotoxicity against A549 cancer cells for both complexes in the dark and after light activation ( $EC_{50, \text{light}} = 5$  and  $7 \mu\text{M}$ ). Post-treatment fluorophore labelling via copper-catalyzed azide-alkyne cycloaddition in fixed cells showed that the complexes accumulate in the cytoplasm, and are located in the perinuclear region.*

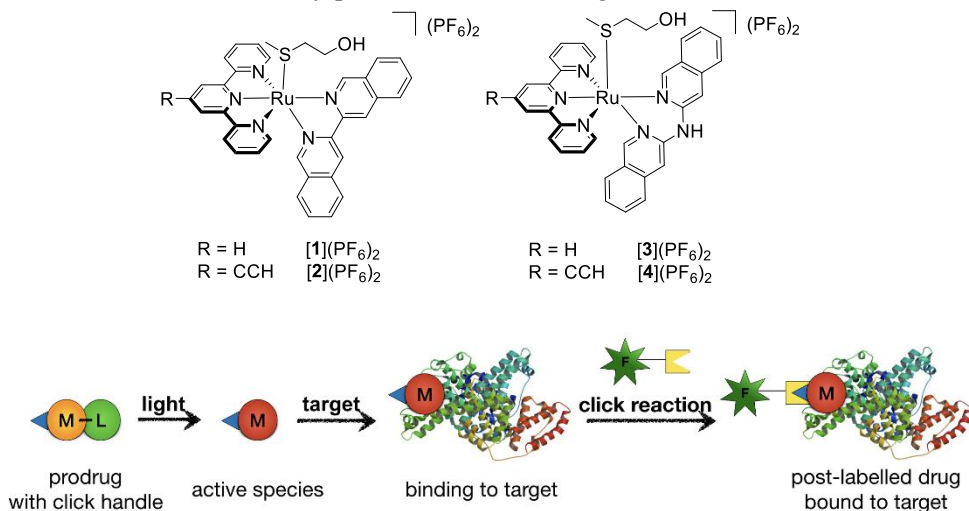
## 4.1 Introduction

While the photosubstitution properties of ruthenium-based photoactivated chemotherapy (PACT) agents are studied extensively, the behavior of these newly designed complexes in the cell environment stays rather unexplored. To obtain information about the fate of a drug in a biological context, the drug distribution and its interaction with cellular targets must be studied *in cellulo*. When such studies are possible, notably when the compound is emissive, its mode of action can be more easily correlated to its efficiency and cytotoxicity profile, enabling improvement of the drug design and increasing its chances to get into the clinics.<sup>1</sup> However, most ruthenium-based PACT agents are non-emissive because their photoactivation mechanism is based on low-lying <sup>3</sup>MC states that quench the <sup>3</sup>MLCT-based emission and lead to photosubstitution. If the PACT drug candidate does not contain ligands with inherent fluorescence properties, such as anthraquinone and anthracene,<sup>2,3</sup> the study of the cellular fate of those photoactivatable complexes is very challenging.

A common method to visualize non-emissive drugs in cells is the synthesis of drug conjugates that are covalently linked to an organic fluorophore moiety to enable microscopy imaging of the compounds. The first example for a metal-based drug, a cisplatin derivative covalently bound to an emissive carboxyfluorescein diacetate (CFDA) moiety, was reported by Molenaar *et al.*<sup>4</sup> They confirmed the accumulation of the platinum compound in the nucleus, as expected for cisplatin. Hereafter, many other groups investigated fluorophore-labeled drug derivatives.<sup>5-9</sup> However, the fluorophore moiety can drastically change the chemical properties of the original drug, which affects its cell uptake and intracellular distribution.<sup>10</sup> In addition, due to its size and/or charge, the fluorophore moiety might strongly modify the interaction of the drug with its target, leading to a mode of action that does not necessarily resemble that of the original drug.<sup>11</sup> Therefore, a new method for the visualization of non-emissive compounds was developed by Bierbach and coworkers.<sup>11</sup> This method is based on labelling after cell treatment and cell fixation, which allows for the preservation of the chemical and biological properties of the drug. Cellular uptake, intracellular distribution, and target interaction are not affected by the fluorophore moiety. The fluorophore can be attached in the fixed cells using different methods, *e.g.* click chemistry. So far, the groups of DeRose<sup>12</sup> and Che<sup>13, 14</sup> have picked up this method and studied the cellular distribution of their metal complexes. To be able to perform the labeling, the drug needs to be functionalized with a handle (*e.g.* an alkyne), which is a chemical group that

specifically reacts with a complementary reactive group (*e.g.* an azide) attached to the fluorophore. While the biological activity of the complex thus is not affected by the fluorophore, the effect of the handle on the drug's properties has not been discussed extensively.

In this work, the PACT agents described in Chapter 3,  $[\text{Ru}(\text{tpy})(\text{i-biq})(\text{Hmte})](\text{PF}_6)_2$  **[1]** $(\text{PF}_6)_2$  and  $[\text{Ru}(\text{tpy})(\text{i-Hdiqa})(\text{Hmte})](\text{PF}_6)_2$  **[3]** $(\text{PF}_6)_2$  (where tpy = 2,2':6',2''-terpyridine, i-biq = 3,3'-biisoquinoline, i-Hdiqa = di(isoquinolin-3-yl)amine, and Hmte = 2-(methylthio)ethanol), were functionalized with the smallest handle possible, *i.e.* a simple alkyne group, to obtain the drug analogues **[2]** $(\text{PF}_6)_2$  and **[4]** $(\text{PF}_6)_2$  ( $[\text{Ru}(\text{HCC-tpy})(\text{NN})(\text{Hmte})](\text{PF}_6)_2$ , where NN = i-biq or i-Hdiqa, Scheme 4.1). With these complexes in hand, we considered answering the following questions: i) does even such minimal functionalization of the PACT agent have an effect on its photochemical and biological properties? ii) Does the small handle allow for fluorophore labeling *via* click chemistry in fixed cells? And iii) if so, what is the cellular localization of the PACT agent? By doing so, non-emissive PACT agents and their light-dependent interactions are visualized for the first time in fixed cells by post-treatment labeling.



**Scheme 4.1.** Alkyne-functionalized PACT agents (top) for post-treatment labeling to preserve their biological activity (bottom).

## 4.2 Results and Discussion

### 4.2.1 Synthesis and Characterization

The alkyne-functionalized PACT agents **[2]**(PF<sub>6</sub>)<sub>2</sub> and **[4]**(PF<sub>6</sub>)<sub>2</sub> were synthesized following the synthetic route described in Chapter 2 for [Ru(HCC-tpy)(bpy)(Hmte)](PF<sub>6</sub>)<sub>2</sub> (where bpy = 2,2'-bipyridine, Scheme AIV.1). Like for the synthesis of [Ru(HCC-tpy)(bpy)(Hmte)](PF<sub>6</sub>)<sub>2</sub>, the terminal alkyne was protected with a TBDMS group (TBDMS = *tert*-butyldimethylsilyl) during all synthetic steps. Such protection prevents the reaction between the terminal alkyne and the metal center, as it would result in the formation of undesired side products that are difficult to remove. After TBDMS removal with five equivalents of potassium fluoride and precipitation of the complex as its PF<sub>6</sub> salt, the products were isolated as NMR-pure solids in 62 and 83% yield, respectively. <sup>1</sup>H NMR spectra in acetone-d<sub>6</sub> showed the singlet for the free alkyne at 4.59 and 4.52 ppm for **[2]**(PF<sub>6</sub>)<sub>2</sub> and **[4]**(PF<sub>6</sub>)<sub>2</sub>, respectively, demonstrating successful deprotection (Figure AIV.1 and AIV.2).

Single crystals suitable for X-ray structure determination for complex **[2]**(PF<sub>6</sub>)<sub>2</sub> were obtained by slow vapor diffusion of diethyl ether into a solution of the complex in cyclopentane (see Figure 4.1). Selected bond lengths and angles are summarized in Table 4.1, together with those reported for the alkyne-free complex **[1]**(PF<sub>6</sub>)<sub>2</sub> (Chapter 3). The terminal alkyne has a bond length (C≡C) of 1.188(7) which is similar to published data,<sup>15</sup> and it lies in the plane of the tpy ligand (N2-C8-C37 = 177.46°). The Ru-N bond lengths of the polypyridyl ligands tpy and i-biq are not significantly different in complexes **[2]**(PF<sub>6</sub>)<sub>2</sub> and **[1]**(PF<sub>6</sub>)<sub>2</sub>. The bond length of the S-bound thioether ligand is also not affected by alkyne functionalization (Ru-S = 2.3623(10) and 2.368(3) Å for **[2]**(PF<sub>6</sub>)<sub>2</sub> and **[1]**(PF<sub>6</sub>)<sub>2</sub>, respectively). Density functional theory (DFT) calculations for **[2]**(PF<sub>6</sub>)<sub>2</sub> are in agreement with the X-ray results. Since crystal growth for complexes **[4]**(PF<sub>6</sub>)<sub>2</sub> was unsuccessful, the complex structure obtained by DFT modeling was compared to that of **[3]**(PF<sub>6</sub>)<sub>2</sub> (Table 4.1). The comparison of the results obtained by DFT calculations showed that the structures of **[4]**<sup>2+</sup> and **[3]**<sup>2+</sup> are very similar. Overall, the addition of the alkyne moiety to the tpy ligand has no significant effect on the bond lengths or the geometry of the complexes.



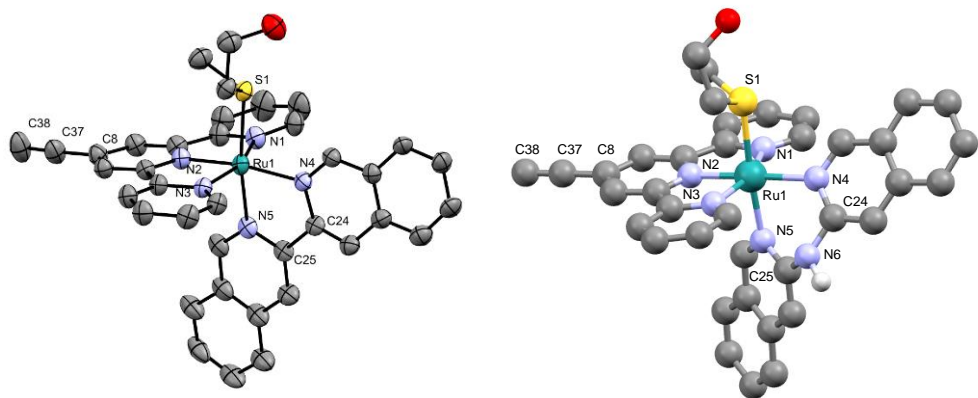


**Figure 4.1.** Displacement ellipsoid (50% probability level) of the cationic part as observed in the crystal structure of  $[2](PF_6)_2$  (left). Disorder, counter ions, and H atoms have been omitted for clarity. DFT model of  $[4]^{2+}$  (right).

**Table 4.1.** Selected bond lengths (Å) and angles (°) of  $[1](PF_6)_2$ ,  $[2](PF_6)_2$ ,  $[3]^{2+}$ , and  $[4]^{2+}$ .

	$[1](PF_6)_2$ <sup>a)</sup>	$[2](PF_6)_2$	$[3]^{2+}$ <sup>a),b)</sup>	$[4]^{2+}$ <sup>b)</sup>
Ru-N1	2.071(9)	2.086(3)	2.095	2.098
Ru-N2	1.967(10)	1.963(3)	1.978	1.974
Ru-N3	2.073(10)	2.073(3)	2.114	2.111
Ru-N4	2.104(10)	2.093(3)	2.138	2.141
Ru-N5	2.074(9)	2.069(6)	2.115	2.112
Ru-S1	2.368(3)	2.3623(10)	2.396	2.402
C8-C37	-	1.435(6)	-	1.423
C37-C38	-	1.188(7)	-	1.202
N1-Ru1-N2	79.3(4)	79.61(13)	79.17	79.13
N2-Ru1-N3	80.1(4)	79.59(13)	78.90	79.01
N1-Ru1-N3	159.4(4)	159.17(13)	158.01	158.10
N4-Ru1-N5	79.4(4)	79.7(4)	86.45	86.47
$\lambda$ <sup>c)</sup>	3.65	2.73	2.46	3.63
$\sigma^2$ <sup>d)</sup>	60.3	59.8	46.4	46.1

<sup>a)</sup> data from Chapter 3; <sup>b)</sup> data from DFT calculations; <sup>c)</sup>  $\lambda = \frac{1}{6} \sum_{n=1,6} \left[ \frac{d_n - \langle d \rangle}{\langle d \rangle} \right]^2$ , mean quadratic elongation where  $d_n$  is one of the six bond lengths calculated by DFT and  $\langle d \rangle$  is the mean of those bond lengths;

<sup>d)</sup>  $\sigma^2 = \frac{1}{11} \sum_{n=1,12} (\theta_n - 90)^2$ , bond angle variance where  $\theta_n$  is one of the twelve angles calculated by DFT.

### 4.2.2 Photochemistry

Because of the low water solubility of [2](PF<sub>6</sub>)<sub>2</sub> the PF<sub>6</sub><sup>-</sup> counter ions were exchanged to Cl<sup>-</sup> (see experimental section for details), to be able to study the photochemistry in aqueous solution. In aqueous solution, the two complexes [2]Cl<sub>2</sub> and [4](PF<sub>6</sub>)<sub>2</sub> show a <sup>1</sup>MLCT absorption band at 470 and 485 nm, thus, the alkyne functionalization causes a shift of the <sup>1</sup>MLCT absorption band to the red region, compared to the non-functionalized analogues [1](PF<sub>6</sub>)<sub>2</sub> and [3](PF<sub>6</sub>)<sub>2</sub> (Table 4.2 and Figure AIV.3). DFT studies pointed out that the lowest unoccupied molecular orbitals (LUMOs) of these complexes is the π\* orbital of the tpy ligand, as it is for [Ru(tpy)(bpy)(Hmte)](PF<sub>6</sub>)<sub>2</sub> ([5](PF<sub>6</sub>)<sub>2</sub>).<sup>16</sup> The red shift of the MLCT state is caused by the stabilization of this orbital by the electron-withdrawing alkyne substituent (σ<sub>P</sub> = 0.23),<sup>17</sup> resulting in a lower energy of the LUMO and therefore, a smaller HOMO – LUMO gap (HOMO = highest occupied molecular orbital). The complexes show very little singlet oxygen generation (Φ<sub>Δ</sub> < 0.03), and their phosphorescence quantum yields are very low (Φ<sub>P</sub> < 5 · 10<sup>-4</sup>, see Table 4.2 and Figure AIV.4).

The photoreactivity of [2]Cl<sub>2</sub> and [4](PF<sub>6</sub>)<sub>2</sub> was investigated by irradiation of solutions of the complexes in water with a green LED (517 nm) at 37 °C and recorded by UV-vis spectroscopy (Figure AIV.5). For each complex, a bathochromic shift of the absorption maxima was observed, typical for the release of the thioether ligand and the formation of the corresponding aqua complex (mass spectrometry data in Figure AIV.6).<sup>18-20</sup> The photosubstitution quantum yields (Φ<sub>517</sub>) were determined using the Glotaran software package.<sup>21</sup> Φ<sub>517</sub> Values of 0.022 and 0.080 were obtained for [2]Cl<sub>2</sub> and [4](PF<sub>6</sub>)<sub>2</sub>, respectively (Table 4.2 and Figure AIII.7), which are comparable with the values reported for complexes [1](PF<sub>6</sub>)<sub>2</sub> and [3](PF<sub>6</sub>)<sub>2</sub> (Chapter 3). Overall, functionalization of tpy with a single alkyne group directly attached at the 4'-position had no significant effect on the photosubstitution properties of the ruthenium complex. Due to potential competition between photosubstitution, phosphorescence, and singlet oxygen production in ruthenium polypyridyl complexes, the observation of excellent photosubstitution quantum yields mean that these PACT complexes are essentially non-emissive, and thus cannot be visualized in cells by optical microscopy.

**Table 4.2.** Lowest-energy absorption maxima ( $\lambda_{\text{max}}$  in nm) in MilliQ water, molar absorption coefficients at  $\lambda_{\text{max}}$  ( $\epsilon_{\text{max}}$  in  $\text{M}^{-1} \cdot \text{cm}^{-1}$ ) in MilliQ water, phosphorescence quantum yields ( $\Phi_{\text{P}}$ ) in methanol- $d_4$ , singlet oxygen quantum yields ( $\Phi_{\Delta}$ ) in methanol- $d_4$ , and photosubstitution quantum yields ( $\Phi_{517}$ ) in MilliQ water for complexes [1]X<sub>2</sub> – [4]X<sub>2</sub>.

complex	NN	R	$\lambda_{\text{max}}$ ( $\epsilon_{\text{max}}$ ) <sup>a)</sup>	$\Phi_{\text{P}}$ <sup>b)</sup>	$\Phi_{\Delta}$ <sup>b)</sup>	$\Phi_{517}$ <sup>a)</sup>
[1](PF <sub>6</sub> ) <sub>2</sub> <sup>c)</sup>	i-biq	H	429 (5.76 · 10 <sup>3</sup> )	1.5 · 10 <sup>-4</sup>	0.010	0.023
[2]Cl <sub>2</sub>	i-biq	CCH	470 (7.65 · 10 <sup>3</sup> )	2.4 · 10 <sup>-4</sup>	0.017	0.022
[3](PF <sub>6</sub> ) <sub>2</sub> <sup>c)</sup>	i-Hdiqa	H	470 (5.35 · 10 <sup>3</sup> )	4.5 · 10 <sup>-4</sup>	0.042	0.077
[4](PF <sub>6</sub> ) <sub>2</sub>	i-Hdiqa	CCH	485 (6.86 · 10 <sup>3</sup> )	< 1.0 · 10 <sup>-4</sup>	0.010	0.080

<sup>a)</sup> in MilliQ water; <sup>b)</sup> in methanol- $d_4$ ; <sup>c)</sup> data from Chapter 3.

### 4.2.3 Cytotoxicity and cellular uptake

All ruthenium complexes were found to be thermally stable in cell growing medium (OptiMEM complete) when kept in the dark at 37 °C for 24 h (Figure AIV.8). The cytotoxicity of complexes [2]Cl<sub>2</sub> and [4](PF<sub>6</sub>)<sub>2</sub> was then tested under normoxic conditions (21% O<sub>2</sub>) in human lung carcinoma (A549) and human epidermoid carcinoma (A431) cell lines. Prodrug incubation for 24 h in the dark was followed by light activation (green LED, 520 nm, 38 J/cm<sup>2</sup>, for 30 min) (Figure AIV.9), and incubation of the cells with the activated drug for an additional 48 h.<sup>22</sup> A sulforhodamine B (SRB) assay was performed at  $t = 96$  h to compare cell proliferation in treated *vs.* untreated cells. The dose response curves are shown in Figure AIV.10, the effective concentrations to inhibit cell growth (EC<sub>50</sub> values) as well as the ratio of the EC<sub>50</sub> values obtained in the dark and that under light irradiation, also called the photo index (PI), are reported in Table 4.3.

In the dark, the cytotoxicity of [2]Cl<sub>2</sub> was comparable to its non-functionalized analogue [1](PF<sub>6</sub>)<sub>2</sub> (66 *vs.* 79  $\mu\text{M}$ ), while [4](PF<sub>6</sub>)<sub>2</sub> was twice as toxic as [3](PF<sub>6</sub>)<sub>2</sub> (29 *vs.* 62  $\mu\text{M}$ ). After light activation, both complexes showed increased cytotoxicity with similar EC<sub>50</sub> values (5 and 7  $\mu\text{M}$  for [2]Cl<sub>2</sub> and [4](PF<sub>6</sub>)<sub>2</sub>, respectively). These values are lower than that of their corresponding non-functionalized analogues. Interestingly, while the PI for both i-Hdiqa-based complexes is 4, alkyne functionalization of the i-biq complex led to an increase of the PI from 4 to 12. Thus, the effect of the alkyne group on the EC<sub>50</sub> values is different for the two complexes. Overall, alkyne functionalization in [2]Cl<sub>2</sub> and [4](PF<sub>6</sub>)<sub>2</sub> led to an increased cytotoxicity compared to their non-functionalized analogues [1](PF<sub>6</sub>)<sub>2</sub> and [3](PF<sub>6</sub>)<sub>2</sub> in the dark and after light activation.

**Table 4.3.** (Photo)cytotoxicity ( $EC_{50}$  with 95% confidence interval in  $\mu\text{M}$ )<sup>a)</sup> and cellular uptake (CU with mean deviation in nmol Ru/mg cell protein)<sup>b)</sup> of [1]X<sub>2</sub> – [4]X<sub>2</sub> in lung cancer cells (A549) under normoxic conditions (21% O<sub>2</sub>).

R	[1](PF <sub>6</sub> ) <sub>2</sub>		[2]Cl <sub>2</sub>		[3](PF <sub>6</sub> ) <sub>2</sub>		[4](PF <sub>6</sub> ) <sub>2</sub>	
	H		CCH		H		CCH	
dark	79.7	+6.1	66.0	+12.4	62.1	+16.4	29.4	+2.7
		-5.7				-9.9		
light	20.6	+3.0	5.3	+1.4	13.8	+4.3	7.0	+1.5
		-2.6				-1.1		
PI <sup>c)</sup>	3.9		12.5		4.5		4.2	
CU	0.32 ± 0.14		0.73 ± 0.12		0.69 ± 0.16		1.19 ± 0.20	

<sup>a)</sup> The (photo)cytotoxicity experiments were performed in biological and technical triplicates; <sup>b)</sup> Cell uptake upon incubation for 24 h with 30  $\mu\text{M}$  drug. Results are averaged over three independent experiments; <sup>c)</sup> the photo index (PI) is defined as  $EC_{50, \text{dark}}/EC_{50, \text{light}}$ .

Cell uptake experiments in A549 cancer cells were undertaken to explain the different cytotoxicity behavior of the complexes. The concentration of ruthenium in nmol per mg cell protein was determined by high-resolution continuum-source atomic absorption spectrometry (HRCS AAS) after incubation of the cells for 24 h with 30  $\mu\text{M}$  drug in the dark. The results revealed that the alkyne-functionalized complexes [2]Cl<sub>2</sub> and [4](PF<sub>6</sub>)<sub>2</sub> were taken up twice as much in A549 cells than their non-functionalized analogues [1](PF<sub>6</sub>)<sub>2</sub> and [3](PF<sub>6</sub>)<sub>2</sub> (Table 4.4). For [4](PF<sub>6</sub>)<sub>2</sub>, the doubled concentration in the cells correlates well to a halved  $EC_{50}$  value, found both in the dark and after light activation (PI stays at 4). Therefore, the cytotoxicity can directly be correlated to the cellular uptake and the amount of ruthenium present in the cells. For [2]Cl<sub>2</sub>, doubling the amount of ruthenium taken up in the cells had only little effect on its dark cytotoxicity. After light activation, however, the  $EC_{50}$  value of [2]Cl<sub>2</sub> was reduced to a quarter of the corresponding  $EC_{50}$  value of [1](PF<sub>6</sub>)<sub>2</sub>. Therefore, it can be concluded that i) the alkyne functionalization has a significant effect on the cell uptake of both complexes and thus on their cytotoxicity, and that ii) [2]Cl<sub>2</sub> is a better prodrug than [4](PF<sub>6</sub>)<sub>2</sub>. In the dark, it showed only little cytotoxic interactions with biological targets compared to [4](PF<sub>6</sub>)<sub>2</sub>. In addition, while [2]Cl<sub>2</sub> is taken up in cells in lower amounts than [4](PF<sub>6</sub>)<sub>2</sub>, both complexes show similar  $EC_{50}$  values after light activation. The differences in dark and light cytotoxicity of complexes [2]Cl<sub>2</sub> and [4](PF<sub>6</sub>)<sub>2</sub> point out that depending on the bidentate ligand, the complexes interact differently in the cells and thus, probably possess different biological targets or mode of actions.

#### 4.2.4 Subcellular localization of the ruthenium complexes

To shed light on the different cytotoxic behaviors of these PACT agents, more insight into their cellular distribution and resulting target interactions is required. Since the PACT agents are non-emissive, these complexes need to be labeled with a fluorophore moiety to be visualized in cells. The alkyne handle of [2]Cl<sub>2</sub> and [4](PF<sub>6</sub>)<sub>2</sub> offers the opportunity to label the compounds *via* click chemistry after cell treatment. Azide-alkyne copper-catalyzed cycloaddition (CuAAC) with azide AlexaFluor™ 488 in fixed and permeabilized A549 lung cancer cells 24 h after green light activation were performed on [2]Cl<sub>2</sub> and [4](PF<sub>6</sub>)<sub>2</sub>, according to a protocol established by DeRose and coworkers (Figure AIV.11).<sup>12</sup> Confocal microscopy was applied for the imaging of the complexes.

At concentrations equal to their EC<sub>50</sub> values (5 and 7 μM), no fluorescence signal was observed for [2]Cl<sub>2</sub> and [4](PF<sub>6</sub>)<sub>2</sub>, respectively (data not shown). Therefore, the prodrug concentrations were increased to 25 μM. As this concentration is highly toxic to the cells, the incubation time after light activation was reduced from 48 to 24 h. By doing so, the cells were stressed but survived and could be imaged. The fluorescence signal was located outside the nucleus, in the cytoplasm (Figure 4.2), and appeared as little dots, mainly on one side of the nucleus. This observation can be taken as an indication for a different mode of action of [2]Cl<sub>2</sub> and [4](PF<sub>6</sub>)<sub>2</sub> compared to DNA-interacting ruthenium complexes (Figure AIV.12 and AIV.13).<sup>23</sup> <sup>24</sup> The localization of the signals for [2]Cl<sub>2</sub> and [4](PF<sub>6</sub>)<sub>2</sub> were found to be identical (results for [2]Cl<sub>2</sub> shown in Figure AIV.14), but the fluorescence signal intensity of [2]Cl<sub>2</sub> was weaker, which correlates to the lower uptake of [2]Cl<sub>2</sub> compared to [4](PF<sub>6</sub>)<sub>2</sub> (see Table 4.3). In the absence of catalytic copper (Cu-, Figure 4.2) and any ruthenium complex, no fluorescent signal was observed, indicating that the click reaction is selective for the complex and background fluorescence was minimal. Without light, the complexes are not activated and should not covalently interact with their targets. This was confirmed by the lower signal, due to washing out of the fluorophore-labeled complexes of the permeabilized cells, a procedure needed for labelling before microscopy. Overall, the alkyne handle on the complexes allowed for labeling of [2]Cl<sub>2</sub> and [4](PF<sub>6</sub>)<sub>2</sub> with Alexa Fluor™ 488 inside fixed cells.

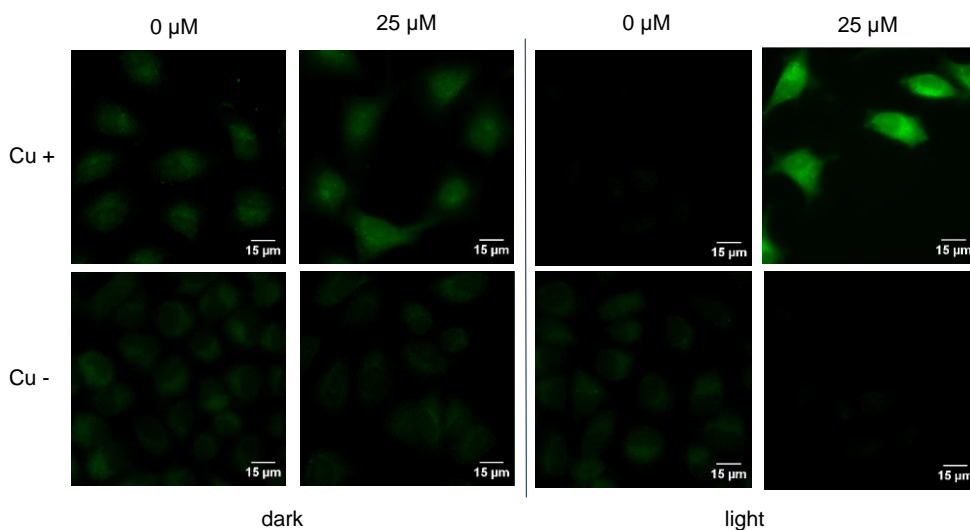


**Figure 4.2.** Confocal images of fluorescent labeling of A549 cancer cell lines treated for 24 h with 0 or 25  $\mu\text{M}$  of  $[\mathbf{4}](\text{PF}_6)_2$  after fixation, permeabilization, and CuAAC-based labeling with Alexa Fluor™ 488 azide, either with or without light activation. Cu-free controls show no fluorescence. Bar represents 15  $\mu\text{m}$ .

This encouraging result was used to further investigate the intracellular localization of  $[\mathbf{4}](\text{PF}_6)_2$ . Co-staining of cell compartments in the cytoplasm were hence undertaken after treatment with the ruthenium compound. Possible targets within the cytoplasm are hydrophobic organelles such as mitochondria, endoplasmic reticulum (ER), lysosomes, and Golgi apparatus. Mitochondria are well-known targets for lipophilic, charged ruthenium polypyridyl complexes. Recently, the weakly emissive tpy-based ruthenium complex  $[\text{Ru}(\text{tpy})(\text{dppn})(\text{X})](\text{PF}_6)_2$  (where  $\text{dppn}$  = benzo[i]dipyrido-[3,2-a:2',3'-c]phenazine and  $\text{X}$  = a thioether-glucose conjugate) was localized in this subcellular organelle.<sup>25</sup> Comparison of the localization and structure of the fluorescent signal of this complex with the results obtained for  $[\mathbf{4}](\text{PF}_6)_2$  showed that the distribution of our compound is different. Thus, mitochondria were excluded as possible target for  $[\mathbf{4}](\text{PF}_6)_2$ . In addition, examples of ruthenium complexes that cause ER stress have been reviewed recently.<sup>26</sup> Here as well, the ER was excluded as target for  $[\mathbf{4}](\text{PF}_6)_2$ , based on the structure of the observed compartment (Figure AIV.15). Lysosomes, however, seemed to be likely subcellular targets from the observed emission patterns, and therefore, co-staining of these cell compartments was undertaken using immunostaining of lysosomal-associated membrane protein 1 (LAMP1). As shown in Figure 4.3, the fluorescent signal corresponding to the lysosome stain (in red) was

localized close to the nucleus in the cytoplasm, but the fluorescence of the complex (in green) did not significantly overlap with these signals, indicating that [4](PF<sub>6</sub>)<sub>2</sub> did not co-localize in the lysosomes. Co-localization quantification for the immunostaining (Pearson coefficient) was attempted but the resolution of the images was too low to obtain reliable results. Thus, after ruling out all these organelles, and considering the shape of the emission signal, it is hypothesized that [4](PF<sub>6</sub>)<sub>2</sub> localizes in the Golgi apparatus. To confirm this hypothesis, co-staining of this cell compartment must be undertaken.

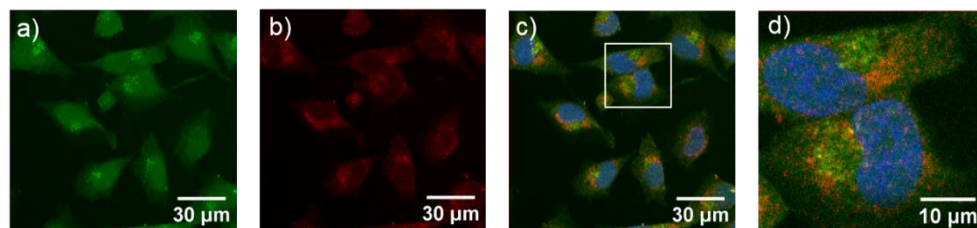


**Figure 4.3.** Confocal images of fluorescent labeling of A549 cancer cell lines treated with 25 μM of [4](PF<sub>6</sub>)<sub>2</sub> after fixation and permeabilization. a) labeling of [4](PF<sub>6</sub>)<sub>2</sub> with Alexa Fluor™ 488 azide (green), b) antibody staining of LAMP1 for lysosomes with 647 dye (red), c) overlay of LAMP1, [4](PF<sub>6</sub>)<sub>2</sub>, and nucleus staining (with Hoechst in blue), and d) zoom of c).

The Golgi apparatus is a membrane-coated cell organelle close to the endoplasmic reticulum near the nucleus. It plays an important role in the intracellular traffic of lysosomal and secretory materials, and it is responsible for the processing and packaging of proteins.<sup>27</sup> The Golgi apparatus has repeatedly been suggested as target of luminescent ruthenium compounds when the fluorescence is located in perinuclear regions,<sup>28</sup> but strong evidence of subcellular organelle localization is often missing.<sup>29</sup> Luminescent probes based on rhenium and iridium, however, proved to accumulate in the Golgi apparatus.<sup>30, 31</sup> To the best of our knowledge, the Golgi apparatus was not yet pointed out as target for ruthenium-based anticancer compounds. Nevertheless, the subcellular organelle does play a central role in the trafficking and processing of the anticancer compound cisplatin. Molenaar *et al.* reported on a fluorophore-functionalized cisplatin derivative still present in the Golgi apparatus of human bone osteosarcoma epithelial cells (U2-OS) after 24 h, while not localized in the nucleus anymore.<sup>4</sup> In human ovarian carcinoma cells, fluorescein-labeled cisplatin was also found to pass through the Golgi apparatus.<sup>6</sup> The metal complex was transported *via* lysosomal vesicles to the Golgi and then further from Golgi associated vesicles into the secretory pathway, leading to the efflux of the complex. On the other hand, Liang *et al.* demonstrated that in human

epidermoid carcinoma cells (KB-3-1) Alexa-labeled cisplatin accumulates first in the Golgi apparatus, before it is transferred to the nucleus.<sup>32</sup> In addition, transport from the Golgi compartment to the nucleus is decelerated in KB cisplatin-resistant cells, which suggests a failure of proper trafficking within these cells. To conclude, the Golgi apparatus strongly participates in vesicle transportation, and thus can be an effective target for anticancer compounds. As above mentioned examples with cisplatin pointed out, an involvement in metal transportation is highly possible, in the early stages of drug uptake as well as drug efflux. Therefore, time dependent fluorescent imaging experiment will need to be undertaken for [2]Cl<sub>2</sub> and [4](PF<sub>6</sub>)<sub>2</sub> to follow the drug *in cellulo* to understand their intracellular trafficking and processing.

### 4.3 Conclusions

Two new alkyne-functionalized ruthenium-based PACT agents were synthesized. This small modification, made of only two atoms directly connected to the prodrug, had no significant effect on the X-ray structure and photosubstitution properties of the complexes. However, it results in doubling of the cellular uptake of both complexes, which influenced their cytotoxicity. Still, such alkyne group appears as a promising method to monitor the fate of non-emissive PACT compounds in cells, while minimally influencing their biological properties. The alkyne handles indeed allowed for the labeling of the complexes with a fluorophore moiety in fixed cells, *i.e.*, after the drug has distributed inside the cell and interacted with its cellular target. With this method, it was possible to i) visualize the light-dependent activation of the complexes inside cells, as the non-activated prodrug was washed away during the procedure to not appear on the microscopy images, ii) localize the complexes intracellularly, and in particular demonstrating that it stays outside the nucleus, and probably resides, after 24 h, in the Golgi apparatus. The latter suggests that the mode of action of these ruthenium-based PACT agents is DNA independent and thus, different from that of cisplatin. To obtain more information about the mode of action of the complexes, it will be necessary to investigate the time-dependent cellular distribution and to identify the cellular targets of the complexes. We foresee that the alkyne handles used here to visualize the compound in cells, will also allow for attaching reporter tags to perform pull-down experiments.<sup>13, 14, 33-35</sup>



## 4.4 Experimental

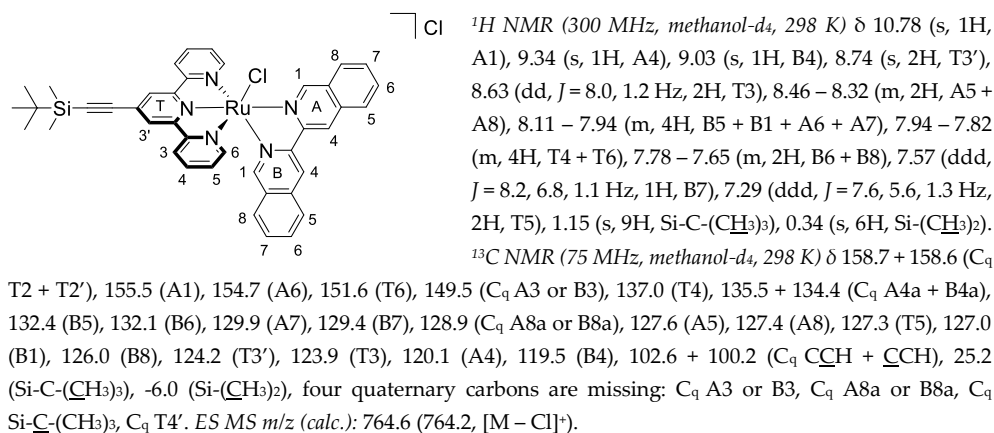
### 4.4.1 Methods and Materials

4'-Bromo-2,2':6',2''-terpyridine was purchased from TCI Europe; RuCl<sub>3</sub> and potassium fluoride from Alfa Aesar; 3-bromoisoquinoline from ABCR; isoquinolin-3-amine, tris(dibenzylideneacetone)dipalladium(0), 1,3-bis(diphenylphosphino)propane, 2-(methylthio)ethanol, and *tert*-butyldimethylsilylethyne from Sigma Aldrich; and potassium *tert*-butoxide from Acros Organics. The ligand i-biq was synthesized according to literature;<sup>36</sup> i-Hdiqa, [1](PF<sub>6</sub>)<sub>2</sub>, and [3](PF<sub>6</sub>)<sub>2</sub> as described in Chapter 3; and [Ru(HCC-tpy)(bpy)(Hmte)](PF<sub>6</sub>)<sub>2</sub> as described in Chapter 2. All metal complexes were synthesized in dim light and stored in darkness. All reactants and solvents were used without further purification. <sup>1</sup>H NMR spectra were recorded using a Bruker AV-300 spectrometer. Chemical shifts are indicated in ppm. Mass spectra were recorded using an MSQ Plus Spectrometer.

### 4.4.2 Synthesis

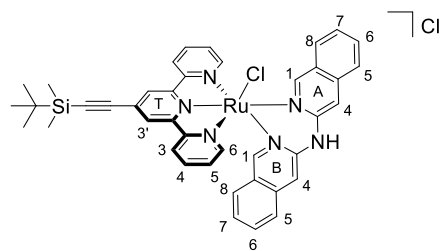
#### [Ru(RCC-tpy)(i-biq)(Cl)]Cl (R = TBDMS)

[Ru(RCC-tpy)(Cl)<sub>3</sub>] (251 mg, 0.445 mmol), i-biq (114 mg, 0.445 mmol), and lithium chloride (105 mg, 2.50 mmol) were dissolved in degassed ethanol/water mixture (3:1, 40 mL). Triethylamine (160 μL, 1.15 mmol) was added and the reaction mixture was refluxed (60 °C) under dinitrogen atmosphere overnight. The reaction mixture was filtered hot over Celite and the cake was washed with ethanol. After evaporation of the solvents, the crude was purified by column chromatography on silica with dichloromethane/methanol (9:1) as eluent (R<sub>f</sub> = 0.70). Yield: 73% (260 mg, 0.325 mmol).



#### [Ru(RCC-tpy)(i-Hdiqa)(Cl)]Cl (R = TBDMS)

[Ru(RCC-tpy)(Cl)<sub>3</sub>] (400 mg, 0.709 mmol), i-Hdiqa (192 mg, 0.709 mmol), and lithium chloride (165 mg, 3.94 mmol), were dissolved in degassed ethanol/water mixture (3:1, 64 mL). Triethylamine (252 μL, 1.81 mmol) was added and the reaction mixture was refluxed (60 °C) under dinitrogen atmosphere for 5 h. The reaction mixture was filtered hot over Celite and the cake was washed with ethanol. After evaporation of the solvents, the crude was purified by column chromatography on silica with dichloromethane/methanol (9:1) as eluent (R<sub>f</sub> = 0.74). Yield: 71% (413 mg, 0.507 mmol).

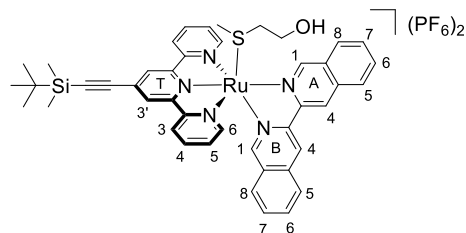


$^1\text{H NMR}$  (300 MHz, methanol- $d_4$ , 298 K)  $\delta$  10.34 (s, 1H, A1), 8.64 (s, 2H, T3'), 8.60 (dd,  $J$  = 8.0, 1.2 Hz, 2H, T3), 8.58 (ddd,  $J$  = 5.6, 1.6, 0.7 Hz, 2H, T6), 8.13 (d,  $J$  = 8.6 Hz, 1H, A8), 8.04 (dd,  $J$  = 8.5, 1.0 Hz, 1H, A5), 7.99 (td,  $J$  = 7.8, 1.6 Hz, 2H, T4), 7.88 (s, 1H, A4), 7.85 (ddd,  $J$  = 8.3, 6.9, 1.2 Hz, 1H, A6), 7.66 – 7.59 (m, 1H, A7), 7.58 – 7.47 (m, 4H, B5 + T5 + B6), 7.45 (s, 1H, B1), 7.39 (d,  $J$  = 8.3 Hz, 1H, B8), 7.27 (s, 1H, B4), 7.26 – 7.18 (m, 1H, B7), 1.11 (s, 9H,

Si-C-( $\text{CH}_3$ ) $_3$ ), 0.30 (s, 6H, Si-( $\text{CH}_3$ ) $_2$ ).  $^{13}\text{C NMR}$  (75 MHz, methanol- $d_4$ , 298 K)  $\delta$  160.9 + 160.4 (C $_q$  T2 + T2'), 160.0 (A1) 154.5 (T6), 154.3 (B1), 152.3 + 151.3 (C $_q$  A3+ B3), 139.7 + 138.5 (C $_q$  A4a + B4a), 138.5 (T4), 133.7 (A6), 133.5 (B6), 129.1 (C $_q$  T4'), 128.9 (A8), 128.5 (T5), 127.9 + 126.9 (C $_q$  A8a + B8a), 127.7 (A7), 127.5 (B7), 127.4 (B8), 126.8 (A5), 126.1 (B5), 125.6 (T3'), 125.3 (T3), 108.2 (A4), 107.6 (B4), 103.8 + 101.7 (C $_q$  C $\underline{\text{C}}\text{H}$  + C $\underline{\text{C}}\text{H}$ ), 26.6 (Si-C-( $\text{CH}_3$ ) $_3$ ), 17.6 (C $_q$  Si-C-( $\text{CH}_3$ ) $_3$ ), -4.6 (Si-( $\text{CH}_3$ ) $_2$ ). *ES MS*  $m/z$  (calc.): 779.5 (779.2, [M - Cl] $^+$ ).

### [Ru(RCC-tpy)(i-biq)(Hmte)](PF $_6$ ) $_2$ (R = TBDMS)

[Ru(RCC-tpy)(i-biq)(Cl)]Cl (151 mg, 0.189 mmol) and 2-(methylthio)ethanol (1 mL, 11 mmol) were dissolved in a degassed water/acetone mixture (4:1, 25 mL). The resultant mixture was stirred and heated to 60 °C under dinitrogen atmosphere overnight. The reaction mixture was filtered hot over Celite and the cake was washed with ethanol. The amount of solvents was reduced by rotary evaporation. The product was precipitated by addition of saturated hexafluoridophosphate, filtered, and washed with cold water. Yield: 93% (195 mg, 0.176 mmol).



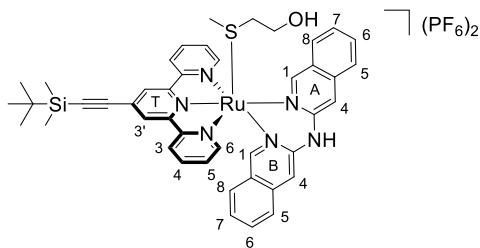
$^1\text{H NMR}$  (300 MHz, acetone- $d_6$ , 298 K)  $\delta$  10.64 (s, 1H, A1), 9.52 (s, 1H, A4), 9.28 (s, 1H, B4), 9.01 (s, 2H, T3'), 8.88 (dt,  $J$  = 8.0, 1.1 Hz, 2H, T3), 8.49 (dd,  $J$  = 8.2, 1.2 Hz, 1H, A8), 8.43 (d,  $J$  = 8.2 Hz, 1H, A5), 8.38 (s, 1H, B1), 8.26 (dd,  $J$  = 8.0, 1.1 Hz, 2H, T6), 8.20 – 8.09 (m, 4H, T4 + A6 + B5), 8.05 (ddd,  $J$  = 8.1, 6.9, 1.2 Hz, 1H, A7), 7.84 (ddd,  $J$  = 8.2, 6.8, 1.3 Hz, 1H, B6), 7.74 (d,  $J$  = 8.1 Hz, 1H, B8), 7.64 (ddd,  $J$  = 8.2, 6.8, 1.1 Hz, 1H, B7),

7.50 (ddd,  $J$  = 7.7, 5.5, 1.3 Hz, 2H, T5), 4.22 (t,  $J$  = 5.1 Hz, 1H, OH), 3.64 (dt,  $J$  = 5.6, 5.1 Hz, 2H, S-CH $_2$ -CH $_2$ ), 2.11 (t,  $J$  = 5.6 Hz, 2H, S-CH $_2$ ), 1.58 (s, 3H, S-CH $_3$ ), 1.13 (s, 9H, Si-C-( $\text{CH}_3$ ) $_3$ ), 0.36 (s, 6H, Si-( $\text{CH}_3$ ) $_2$ ).  $^{13}\text{C NMR}$  (75 MHz, acetone- $d_6$ , 298 K)  $\delta$  159.0 + 158.7 (C $_q$  T2 + T2'), 156.6 (A1), 154.8 (B1), 154.3 (T6), 150.7 + 150.2 (C $_q$  A3 + B3), 139.8 (T4), 136.8 + 136.2 (C $_q$  A4a + B4a), 134.2 (A6), 134.1 (B6), 131.4 + 130.7 (C $_q$  A8a + B8a), 131.2 (A7), 130.7 (B7), 129.8 (C $_q$  T4'), 129.7 (T5), 129.0 (A8), 128.7 (B8), 128.4 (A5), 128.3 (B5), 127.1 (T3'), 126.3 (T3), 122.2 (A4), 121.5 (B4), 103.2 + 103.0 (C $_q$  C $\underline{\text{C}}\text{H}$  + C $\underline{\text{C}}\text{H}$ ), 59.0 (S-CH $_2$ -CH $_2$ ), 38.1 (S-CH $_2$ ), 26.5 (Si-C-( $\text{CH}_3$ ) $_3$ ), 17.3 (C $_q$  Si-C-( $\text{CH}_3$ ) $_3$ ), 14.7 (S-CH $_3$ ), -4.6 (Si-( $\text{CH}_3$ ) $_2$ ). *ES MS*  $m/z$  (calc.): 410.5 (410.6, [M - 2PF $_6$ ] $^{2+}$ ).

### [Ru(RCC-tpy)(i-Hdiqa)(Hmte)](PF $_6$ ) $_2$ (R = TBDMS)

[Ru(RCC-tpy)(i-Hdiqa)(Cl)]Cl (300 mg, 0.368 mmol) and 2-(methylthio)ethanol (2 mL, 22 mmol) were dissolved in a degassed water/acetone mixture (4:1, 50 mL). The resultant mixture was stirred and heated to 60 °C under dinitrogen atmosphere overnight. The reaction mixture was filtered hot over Celite and the cake was washed with ethanol. The amount of solvents was reduced by rotary evaporation. The

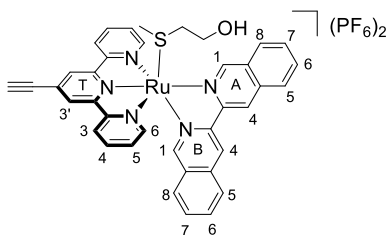
product was precipitated by addition of saturated hexafluoridophosphate, filtered, and washed with cold water. Yield: 95% (395 mg, 0.351 mmol).



$^1\text{H NMR}$  (300 MHz, acetone- $d_6$ , 298 K)  $\delta$  10.16 (s, 1H, A1), 9.64 (s, 1H, NH), 8.95 (dd,  $J = 5.6, 1.6$  Hz, 2H, T6), 8.91 (s, 2H, T3'), 8.87 (dd,  $J = 8.1, 1.4$  Hz, 2H, T3), 8.35 (dd,  $J = 8.4, 1.1$  Hz, 1H, A8), 8.28 (td,  $J = 7.9, 1.5$  Hz, 2H, T4), 8.15 (dd,  $J = 8.5, 1.0$  Hz, 1H, A5), 8.10 (s, 1H, A4), 7.95 (ddd,  $J = 8.3, 6.8, 1.2$  Hz, 1H, A6), 7.82 (s, 1H, B1), 7.81 – 7.70 (m, 4H, T5 + B5 + A7), 7.63 (ddd,  $J = 8.4, 6.7, 1.2$  Hz, 1H, B6), 7.58 (s, 1H, B4), 7.54 (dd,  $J = 8.4, 1.1$  Hz, 1H, B8), 7.32 (ddd,  $J = 8.3, 6.7, 1.2$  Hz, 1H, B7), 4.06 (t,  $J = 5.1$  Hz, 1H, OH), 3.50 (dt,  $J = 5.6, 5.1$  Hz, 2H, S-CH<sub>2</sub>-CH<sub>2</sub>), 1.92 (t,  $J = 5.6$  Hz, 2H, S-CH<sub>2</sub>), 1.39 (s, 3H, S-CH<sub>3</sub>), 1.09 (s, 9H, Si-C-(CH<sub>3</sub>)<sub>3</sub>), 0.31 (s, 6H, Si-(CH<sub>3</sub>)<sub>2</sub>).  $^{13}\text{C NMR}$  (75 MHz, acetone- $d_6$ , 298 K)  $\delta$  159.5 + 159.0 (C<sub>q</sub> T2 + T2'), 159.1 (A1), 155.7 (T6), 153.0 (B1), 151.4 + 150.9 (C<sub>q</sub> A3 + B3), 139.9 (T4), 139.5 + 138.6 (C<sub>q</sub> A4a + B4a), 134.1 (A6), 134.0 (B6), 131.0 (C<sub>q</sub> T4'), 129.4 (T5), 129.0 (A8), 128.3 (B8), 128.3 + 126.8 (C<sub>q</sub> A8a + B8a) 127.9 (A7), 127.4 (B7), 127.1 (T3'), 126.7 (A4), 126.4 (T3), 126.1 (B5), 110.3 (A4), 109.0 (B4), 103.0 (C<sub>q</sub> CCH or CCH), 58.9 (S-CH<sub>2</sub>-CH<sub>2</sub>), 37.8 (S-CH<sub>2</sub>), 26.5 (Si-C-(CH<sub>3</sub>)<sub>3</sub>), 17.3 (C<sub>q</sub> Si-C-(CH<sub>3</sub>)<sub>3</sub>), 15.0 (S-CH<sub>3</sub>), -4.7 (Si-(CH<sub>3</sub>)<sub>2</sub>), one quaternary carbon is missing: C<sub>q</sub> CCH or CCH. *ES MS m/z* (calc.): 417.8 (418.1, [M – 2PF<sub>6</sub>]<sup>2+</sup>).

#### [Ru(HCC-tpy)(i-biq)(Hmte)](PF<sub>6</sub>)<sub>2</sub>, [2](PF<sub>6</sub>)<sub>2</sub>

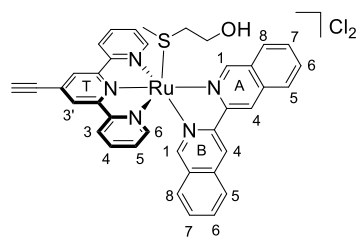
A solution of [Ru(RCC-tpy)(i-biq)(Hmte)](PF<sub>6</sub>)<sub>2</sub> (120 mg, 0.108 mmol) in methanol (5 mL) was combined with a solution of potassium fluoride (63 mg, 1.1 mmol) in methanol (5 mL). The resulting reaction mixture was stirred at 30 °C overnight. The amount of solvent was reduced by rotary evaporation and aqueous potassium hexafluoridophosphate was added dropwise to the solution till a precipitate was formed. The precipitate was filtered and washed with cold water. Yield: 82% (88 mg, 0.089 mmol).



$^1\text{H NMR}$  (300 MHz, acetone- $d_6$ , 298 K)  $\delta$  10.65 (s, 1H, A1), 9.53 (s, 1H, A4), 9.29 (s, 1H, B4), 9.03 (s, 2H, T3'), 8.88 (d,  $J = 8.1$  Hz, 2H, T3), 8.50 (d,  $J = 8.1$  Hz, 1H, A8), 8.43 (d,  $J = 8.2$  Hz, 1H, A5), 8.34 (s, 1H, B1), 8.27 (d,  $J = 5.0$  Hz, 2H, T6), 8.23 – 8.01 (m, 5H, T4 + A6 + B5 + A7), 7.85 (ddd,  $J = 8.2, 6.7, 1.4$  Hz, 1H, B6), 7.72 (d,  $J = 8.2$  Hz, 1H, B8), 7.64 (ddd,  $J = 8.2, 6.8, 1.1$  Hz, 1H, B7), 7.51 (ddd,  $J = 7.7, 5.5, 1.3$  Hz, 2H, T5), 4.59 (s, 1H, CCH), 4.26 (t,  $J = 4.7$  Hz, 1H, OH), 3.63 (dt,  $J = 5.6, 4.7$  Hz, 2H, S-CH<sub>2</sub>-CH<sub>2</sub>), 2.12 (t,  $J = 5.6$  Hz, 2H, S-CH<sub>2</sub>), 1.59 (s, 3H, S-CH<sub>3</sub>).  $^{13}\text{C NMR}$  (75 MHz, acetone- $d_6$ , 298 K)  $\delta$  159.0 + 158.7 (C<sub>q</sub> T2 + T2'), 156.6 (A1), 154.8 (B1), 154.4 (T6), 150.8 + 150.2 (C<sub>q</sub> A3 + B3), 139.8 (T4), 136.8 + 136.2 (C<sub>q</sub> A4a + B4a), 134.2 (A6), 134.2 (B6), 131.2 (A7), 131.0 + 130.7 + 129.8 (C<sub>q</sub> A8a + B8a + T4'), 130.7 (B7), 129.7 (T5), 129.1 (A8), 128.7 (A5), 128.4 + 128.3 (B5 + B8), 127.4 (T3'), 126.3 (T3), 122.2 (A4), 121.4 (B4), 87.9 (CCH), 81.3 (C<sub>q</sub> CCH), 58.9 (S-CH<sub>2</sub>-CH<sub>2</sub>), 38.1 (S-CH<sub>2</sub>), 14.8 (S-CH<sub>3</sub>). *ES MS m/z* (calc.): 354.0 (353.6, [M – 2PF<sub>6</sub>]<sup>2+</sup>).

#### [Ru(HCC-tpy)(i-biq)(Hmte)]Cl<sub>2</sub>, [2]Cl<sub>2</sub>

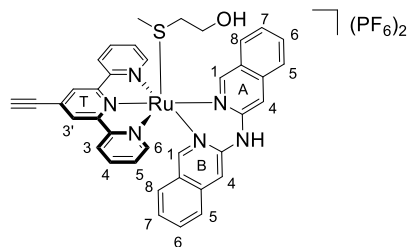
[2](PF<sub>6</sub>)<sub>2</sub> (65 mg, 0.065 mmol) was dissolved in a minimum amount of acetone (1 mL) and saturated Bu<sub>4</sub>NCl solution (4 mL) was added dropwise. The formed precipitate was filtered and washed several times with acetone. The product was obtained as brownish red solid. Yield: 99% (50 mg, 0.064 mmol).



$^1\text{H NMR}$  (300 MHz, methanol- $d_4$ , 298 K)  $\delta$  10.53 (s, 1H, A1), 9.43 (s, 1H, A4), 9.19 (s, 1H, B4), 8.97 (s, 2H, T3'), 8.71 (dt,  $J = 7.9, 1.1$  Hz, 2H, T3), 8.49 (d,  $J = 8.1$  Hz, 1H, A8), 8.42 (d,  $J = 7.9$  Hz, 1H, A5), 8.16–7.98 (m, 6H, A6 + B5 + T4 + B1 + A7), 7.94 (dd,  $J = 5.5, 1.5$  Hz, 2H, T6), 7.89–7.78 (m, 2H, B8 + B6), 7.65 (ddd,  $J = 7.8, 6.5, 1.1$  Hz, 1H, B7), 7.42 (ddd,  $J = 7.7, 5.5, 1.3$  Hz, 2H, T5), 4.53 (s, 1H, CCH), 3.61–3.46 (m, 2H, S-CH<sub>2</sub>-CH<sub>2</sub>), 1.98–1.80 (m, 2H, S-CH<sub>2</sub>), 1.42 (s, 3H, S-CH<sub>3</sub>).  $^{13}\text{C NMR}$  (214 MHz, methanol- $d_4$ , 298 K)  $\delta$  159.3 + 159.1 (C<sub>q</sub> T2 + T2'), 156.8 (A1), 154.5 (B1), 154.2 (T6), 151.0 + 150.5 (C<sub>q</sub> A3 + B3), 140.2 (T4), 137.3 + 136.7 (C<sub>q</sub> A4a + B4a), 134.6 + 134.5 (A6 + B6), 132.1 (C<sub>q</sub> A8a), 131.6 (A7), 131.2 (B7), 130.3 (C<sub>q</sub> A8b), 130.0 (T5), 129.2 (A8), 129.0 (A5), 128.6 + 128.6 (B8 + B5), 127.8 (T3'), 126.6 (T3), 122.6 (A4), 121.9 (B4), 88.0 (CCH), 81.0 (C<sub>q</sub> CCH), 58.6 (S-CH<sub>2</sub>-CH<sub>2</sub>), 38.4 (S-CH<sub>2</sub>), 14.3 (S-CH<sub>3</sub>). High resolution ES MS  $m/z$  (calc.): 353.56450 (353.56457,  $[\text{M} - 2\text{Cl}]^{2+}$ ). Elem. Anal. Calc. for C<sub>38</sub>H<sub>31</sub>Cl<sub>2</sub>N<sub>5</sub>ORuS + 3 H<sub>2</sub>O: C, 54.87; H, 4.48; N, 8.42. Found: C, 54.08; H, 4.08; N, 8.39.

#### [Ru(HCC-tpy)(i-Hdiqa)(Hmte)](PF<sub>6</sub>)<sub>2</sub>, [4](PF<sub>6</sub>)<sub>2</sub>

A solution of [Ru(RCC-tpy)(i-Hdiqa)(Hmte)](PF<sub>6</sub>)<sub>2</sub> (200 mg, 0.178 mmol) in methanol (10 mL) was combined with a solution of potassium fluoride (103 mg, 1.78 mmol) in methanol (5 mL). The resulting reaction mixture was stirred at 30 °C overnight. The amount of solvent was reduced by rotary evaporation and aqueous potassium hexafluoridophosphate was added dropwise to the solution till a precipitate was formed. The precipitate was filtered and washed with cold water. The product was obtained as brownish red solid. Yield: 83% (150 mg, 0.148 mmol).



$^1\text{H NMR}$  (300 MHz, acetone- $d_6$ , 298 K)  $\delta$  10.17 (s, 1H, A1), 9.66 (s, 1H, NH), 8.96 (dd,  $J = 5.6, 1.6$  Hz, 2H, T6), 8.93 (s, 2H, T3'), 8.87 (dd,  $J = 8.2, 1.4$  Hz, 2H, T3), 8.36 (dd,  $J = 8.3, 1.1$  Hz, 1H, A8), 8.30 (td,  $J = 7.9, 1.5$  Hz, 2H, T4), 8.15 (dd,  $J = 8.6, 1.1$  Hz, 1H, A5), 8.11 (s, 1H, A4), 7.95 (ddd,  $J = 8.3, 6.8, 1.2$  Hz, 1H, A6), 7.80 (s, 1H, B1), 7.79–7.70 (m, 4H, T5 + B5 + A7), 7.63 (ddd,  $J = 8.4, 6.7, 1.2$  Hz, 1H, B6), 7.58 (s, 1H, B4), 7.53 (dd,  $J = 8.5, 1.0$  Hz, 1H, B8), 7.32 (ddd,  $J = 8.2, 6.7, 1.2$  Hz, 1H, B7), 4.52 (s, 1H, CCH), 4.07 (t,  $J = 5.1$  Hz, 1H, -OH), 3.50 (dt,  $J = 5.6, 5.1$  Hz, 2H, S-CH<sub>2</sub>-CH<sub>2</sub>), 1.93 (t,  $J = 5.6$  Hz, 2H, S-CH<sub>2</sub>), 1.39 (s, 3H, S-CH<sub>3</sub>).  $^{13}\text{C NMR}$  (75 MHz, acetone- $d_6$ , 298 K)  $\delta$  159.6 + 159.0 (C<sub>q</sub> T2 + T2'), 159.1 (A1), 155.7 (T6), 152.9 (B1), 151.4 + 150.9 (C<sub>q</sub> A3 + B3), 140.0 (T4), 139.5 + 138.6 (C<sub>q</sub> A4a + B4a), 134.1 (A6), 134.0 (B6), 130.7 (C<sub>q</sub> T4'), 129.4 (T5), 129.0 (A8), 128.3 + 126.8 (C<sub>q</sub> A8a + B8a), 128.3 (B8), 127.9 (A7), 127.4 (B7), 127.4 (T3'), 126.7 (A5), 126.4 (T3), 126.1 (B5), 110.3 (A4), 108.9 (B4), 87.9 (CCH), 81.1 (C<sub>q</sub> CCH), 59.0 (S-CH<sub>2</sub>-CH<sub>2</sub>), 37.9 (S-CH<sub>2</sub>), 15.0 (S-CH<sub>3</sub>). ES MS  $m/z$  (calc.): 361.0 (361.1,  $[\text{M} - 2\text{PF}_6]^{2+}$ ). High resolution ES MS  $m/z$  (calc.): 361.06995 (361.07001,  $[\text{M} - 2\text{PF}_6]^{2+}$ ). Elem. Anal. Calc. for C<sub>38</sub>H<sub>32</sub>F<sub>12</sub>N<sub>6</sub>OP<sub>2</sub>RuS: C, 45.11; H, 3.19; N, 8.31. Found: C, 44.54; H, 3.24; N, 8.20.

#### 4.4.3 Single Crystal X-Ray crystallography

Single crystals of [2](PF<sub>6</sub>)<sub>2</sub> were obtained by recrystallization through liquid-vapor diffusion using cyclopentane as solvent and diethyl ether as counter-solvent. In short, 1 mg of [2](PF<sub>6</sub>)<sub>2</sub> was dissolved in cyclopentane (1 mL) and placed in a small vial. This vial was placed in a larger vial containing diethyl ether (2.8 mL). The large vial was closed and vapor diffusion within a few days afforded X-ray quality crystals.

All reflection intensities were measured at 110(2) K using a SuperNova diffractometer (equipped with Atlas detector) with Cu  $K\alpha$  radiation ( $\lambda = 1.54178 \text{ \AA}$ ) under the program CrysAlisPro (Version CrysAlisPro 1.171.39.29c, Rigaku OD, 2017). The same program was used to refine the cell dimensions and for data reduction. The structure was solved with the program SHELXS-2014/7 (Sheldrick, 2015) and was refined on  $F^2$  with SHELXL-2014/7 (Sheldrick, 2015). Analytical numeric absorption correction using a multifaceted crystal model was applied using CrysAlisPro. The temperature of the data collection was controlled using the system Cryojet (manufactured by Oxford Instruments). The H atoms were placed at calculated positions using the instructions AFIX 23, AFIX 43, AFIX 137, AFIX 147 or AFIX 163 with isotropic displacement parameters having values 1.2 or 1.5  $U_{eq}$  of the attached C or O atoms.

The structure of  $[2](PF_6)_2$  is partly disordered.

The 3,3'-biquinoline ligand and one of the two  $PF_6^-$  counter ions are found to be disordered over two orientations, and the occupancy factors of the major components of the disorder refine to 0.54(3) and 0.699(17).  $[2](PF_6)_2$ :  $0.07 \times 0.04 \times 0.02 \text{ mm}^3$ , triclinic,  $P-1$ ,  $a = 9.6220 (3)$ ,  $b = 11.2316 (4)$ ,  $c = 19.3633 (7) \text{ \AA}$ ,  $\alpha = 97.533 (3)$ ,  $\beta = 92.211 (3)$ ,  $\gamma = 109.604 (3)^\circ$ ,  $V = 1946.63 (12) \text{ \AA}^3$ ,  $Z = 2$ ,  $\mu = 5.43 \text{ mm}^{-1}$ , transmission factor range: 0.779–0.924. 25285 Reflections were measured up to a resolution of  $(\sin \theta/\lambda)_{\text{max}} = 0.616 \text{ \AA}^{-1}$ . 7581 Reflections were unique ( $R_{\text{int}} = 0.058$ ), of which 6081 were observed [ $I > 2\sigma(I)$ ]. 761 Parameters were refined using 1434 restraints.  $R1/wR2 [I > 2\sigma(I)]$ : 0.0428/0.1013.  $R1/wR2 [\text{all refl.}]$ : 0.0609/0.1119.  $S = 1.02$ . Residual electron density found between  $-0.57$  and  $0.80 \text{ e \AA}^{-3}$ .

#### 4.4.4 DFT Calculations

DFT was used to perform electronic structure calculations. The structure of  $[2]^{2+}$  and  $[4]^{2+}$  was optimized using ADF from SCM,<sup>37</sup> the PBE0 hybrid functional, a triple zeta basis set (TZP) for all atoms, and COSMO to simulate solvent effects in water. The nuclear coordinates ( $\text{\AA}$ ) of  $[2]^{2+}$  and  $[4]^{2+}$  are given in Table AIV.2 and AIV.3, respectively.

#### 4.4.5 Irradiation experiments monitored with MS and UV-vis

Photoreactions monitored with UV-vis spectroscopy were performed using a Cary Varian spectrometer equipped with temperature control set to 310 K and a magnetic stirrer. The measurements were performed in a quartz cuvette, containing 3 mL of solution. The stirred sample was irradiated perpendicularly to the axis of the spectrometer with the beam of an LED fitted to the top of the cuvette.

For photoactivation with green light, an LED light source ( $\lambda = 517 \text{ nm}$ ,  $\Delta\lambda_{1/2} = 23 \text{ nm}$ ,  $5.2 \text{ mW}$ ,  $5.43 \cdot 10^{-8} \text{ mol} \cdot \text{s}^{-1}$ ) was used, an absorption spectrum was measured every 30 sec until the end of the experiment.  $[Ru]_0 = 0.074, 0.077, 0.061, \text{ and } 0.127 \text{ mM}$  for  $[1](PF_6)_2$ ,  $[2]Cl_2$ ,  $[3](PF_6)_2$ , and  $[4](PF_6)_2$ , respectively. The data were analyzed using Microsoft Excel. Mass spectrometry was performed at the beginning and at the end of the irradiation to confirm the nature of the reagent and products. Photosubstitution quantum yield calculations were performed using the Glotaran Software package as described in Appendix I. The conditions are summarized in Table AIV.1.

#### 4.4.6 Cytotoxicity and cellular uptake

Cytotoxicity assays and cellular uptake experiments were performed using the protocols described in Appendix I.

### 4.4.7 Click reaction

#### Materials

Black 96-well Screenstar plates (Product number #655866, Greiner Bio-One, Frickenhausen, Germany) were used for immunostaining; copper sulfate, sodium ascorbate, Triton X-100, tris(3-hydroxypropyl-triazolylmethyl)amine (THPTA), phosphate buffered saline (PBS), and bovine serum albumin (BSA) were purchased from Sigma Aldrich; paraformaldehyde (PFA 16%) from Alfa Aesar; and Alexa Fluor™ 488 Azide (A10266) and Alkyne (A10267) from Invitrogen (Thermo Fisher Scientific). Azidoplatin was kindly provided by the DeRose lab.

#### Cell culture, treatment, and click reaction

Cells were cultured as described in Appendix I. A549 cells were seeded at  $t = 0$  h in 96-well plates at a density of 5000 cells/well (100  $\mu$ L) in OptiMEM complete and incubated for 24 h at 37 °C and 7.0% CO<sub>2</sub>. At  $t = 24$  h, the cells were treated with aliquots (100  $\mu$ L) of either [2]Cl<sub>2</sub> (50  $\mu$ M), [4](PF<sub>6</sub>)<sub>2</sub> (50  $\mu$ M), or Azidoplatin (10  $\mu$ M) and incubated for another 24 h. At  $t = 48$  h, the plate was irradiated under air atmosphere using the cell-irradiation system (520 nm, 1 h, 76 J/cm<sup>2</sup>) and further incubated. At  $t = 72$  h, 24 h after irradiation, the wells were washed twice with 1X PBS (200  $\mu$ L) and fixed with 4% PFA in PBS (100  $\mu$ L) for 20 min under gentle shaking. Then, PFA was aspirated and 0.5% Triton X-100 in PBS (100  $\mu$ L) was added and shacked for 20 min. After aspiration, the wells were washed twice with 3% BSA in PBS (100  $\mu$ L) for 10 min while shaking. Hereafter, the 3% BSA solution was removed and the click cocktail in PBS was added (33  $\mu$ L of 3 mM CuSO<sub>4</sub> in 15 mM THPTA or 33  $\mu$ L of only 15 mM THPTA for Cu-free controls, 33  $\mu$ L of 15  $\mu$ M Alexa Fluor™ 488 (azide or alkyne, depending on tested compound), and 33  $\mu$ L of 83 mM sodium ascorbate). The click mixture was shacked at room temperature for 1 h. Hereafter, the mixture was aspirated, and the wells were washed with 3% BSA in PBS, PBS, 0.5% Triton X-100, and finally PBS.

### 4.4.8 Imaging

#### Materials

Tween was purchased from Sigma Aldrich. PBST is 0.1% Tween in PBS. LAMP1 was purchased from Abcam (ab25245), Cy5 Goat Anti-Rat from Molecular Probes (Life Technologies Europe BV, Bleiswijk, The Netherlands). Anti-Giantin from Abcam (ab37266), Alexa Fluor™ 647 AffiniPure Goat Anti-Mouse IgG (H+L) from Jackson ImmunoResearch (115-605-146), NucBlue™ from Invitrogen (R37605).

#### Co-staining

The co-staining was performed in dim light. Wells were washed twice with 1% BSA in PBST for 10 min while gently shaking. For lysosome co-staining, the primary antibody (LAMP1 1:100 in PBST, 100  $\mu$ L) was added and incubated for 1 h at r.t. After washing the wells three times with PBST (100  $\mu$ L) for 5 min at r.t while shaking, the secondary antibody (Cy5 Goat Anti-Rat, 1:1000, 100  $\mu$ L) was incubated for 1 h at r.t. For Golgi co-staining, the primary antibody (Anti-Giantin 1:500 in PBST, 100  $\mu$ L) was added and incubated overnight at 4 °C. The wells were washed three times with PBST (100  $\mu$ L) for 5 min at r.t while shaking. After aspiration, the secondary antibody (Alexa Fluor® 647 AffiniPure Goat Anti-Mouse IgG (H+L), 1:1500, 100  $\mu$ L) was incubated for 1 h at r.t while shaking. After every co-staining, the wells were washed three times with PBST (100  $\mu$ L) for 5 min at r.t while shaking. After aspiration, nuclear co-staining (NucBlue™, 1 drop/2 mL, 100  $\mu$ L) was added and incubated for 1 h at r.t while shaking. Finally, the co-staining was aspirated, and the wells were filled with PBS (100  $\mu$ L) for imaging.

## Microscopy imaging

Inverted epifluorescence microscopy imaging was performed on a Leica fluorescent microscope (model DMi8) with Leica LAS X acquisition software using the 63x oil immersion objective. Modular excitation/emission filter cubes were used: DAPI (405 nm) for Hoechst 33342 (ex./em. 360/460 nm), GFP (470/40 nm) for Alexa Fluor™ 488 (ex./em. 495/519 nm), and Y5 (620/60 nm) for Alexa Fluor™ 647 (ex./em. 651/667 nm). Confocal imaging was performed on an Eclipse Ti2-C2+ Nikon confocal microscope using the 20x air objective (0.75 NA and 1.00 WD). Lasers used: 405 nm for Hoechst 33342 (ex./em. 360/460 nm), 488 nm for [2]<sup>2+</sup> and [4]<sup>2+</sup> labeled with Alexa Fluor™ 488 (ex./em. 495/519 nm), and 640 nm for Alexa Fluor™ 647 (ex./em. 651/667 nm). The settings for image acquisition (laser power and PMT gain) were identical for all conditions.

Fiji ImageJ software was used to process the images. The settings during image processing were identical for each condition. Hoechst, AlexaFluor488, and Anti-Giantin 647 were shown in blue, green, and red, respectively.

### 4.4.9 Supporting Information

The synthetic route for the synthesis of [2](PF<sub>6</sub>)<sub>2</sub> and [4](PF<sub>6</sub>)<sub>2</sub>, <sup>1</sup>H NMR spectra of [2](PF<sub>6</sub>)<sub>2</sub> and [4](PF<sub>6</sub>)<sub>2</sub>, geometry data of the DFT models, the molar extinction coefficients, singlet oxygen production and phosphorescence spectra, UV-vis and MS spectra of the green light activation, photosubstitution conditions for the calculations of the photosubstitution quantum yield by Glotaran, UV-vis spectra of the dark stability in water and cell medium, the light dose determination for [2]Cl<sub>2</sub> and [4](PF<sub>6</sub>)<sub>2</sub>, as well as microscopy images of A549 cells treated with [2]Cl<sub>2</sub> and [4](PF<sub>6</sub>)<sub>2</sub> are provided in Appendix IV.

## 4.5 Contribution

Dr. Sylvia Le Dévédec performed confocal microscopy, Ingrid Flashpohler helped performing cytotoxicity tests, Dr. Claudia Schmidt and Prof. Ingo Ott performed HRCS-AAS measurements for cell uptake, Xuequan Zhou performed singlet oxygen measurements, Dr. Vincent van Rixel grew single crystals, and Dr. Maxime Siegler performed X-ray diffraction experiments and crystal structure determination. Dr. Sylvestre Bonnet performed DFT calculations and together with Prof. Lies Bouwman, he provided experimental guidance and significant editorial feedback.

## 4.6 References

- 1 H. U. Holtkamp and C. G. Hartinger, *Trends Anal. Chem.* **2018**, 104 (-), 110-117.
- 2 L. Zeng, Y. Chen, H. Huang, J. Wang, D. Zhao, L. Ji, and H. Chao, *Chem. Eur. J.* **2015**, 21 (43), 15308-15319.
- 3 R. A. Alderden, H. R. Mellor, S. Modok, T. W. Hambley, and R. Callaghan, *Biochem. Pharmacol.* **2006**, 71 (8), 1136-1145.
- 4 C. Molenaar, J.-M. Teuben, R. J. Heetebrij, H. J. Tanke, and J. Reedijk, *J. Biol. Inorg. Chem.* **2000**, 5 (5), 655-665.
- 5 K. Katano, R. Safaei, G. Samimi, A. Holzer, M. Tomioka, M. Goodman, and S. B. Howell, *Clinical Cancer Research* **2004**, 10 (13), 4578-4588.
- 6 R. Safaei, K. Katano, B. J. Larson, G. Samimi, A. K. Holzer, W. Naerdemann, M. Tomioka, M. Goodman, and S. B. Howell, *Clinical Cancer Research* **2005**, 11 (2), 756-767.

- 7 R. Safaei, B. J. Larson, T. C. Cheng, M. A. Gibson, S. Otani, W. Naerdemann, and S. B. Howell, *Mol. Cancer Ther.* **2005**, 4 (10), 1595-1604.
- 8 A. A. Nazarov, J. Risse, W. H. Ang, F. Schmitt, O. Zava, A. Ruggi, M. Groessler, R. Scopelitti, L. Juillerat-Jeanneret, C. G. Hartinger, and P. J. Dyson, *Inorg. Chem.* **2012**, 51 (6), 3633-3639.
- 9 A. Bahreman, J.-A. Cuello-Garibo, and S. Bonnet, *Dalton Trans.* **2014**, 43 (11), 4494-4505.
- 10 M. D. Hall, M. Okabe, D.-W. Shen, X.-J. Liang, and M. M. Gottesman, *Annu. Rev. Pharmacol. Toxicol.* **2008**, 48 (1), 495-535.
- 11 S. Ding, X. Qiao, J. Suryadi, G. S. Marrs, G. L. Kucera, and U. Bierbach, *Angew. Chem.* **2013**, 125 (12), 3434-3438.
- 12 R. Wirth, J. D. White, A. D. Moghaddam, A. L. Ginzburg, L. N. Zakharov, M. M. Haley, and V. J. DeRose, *J. Am. Chem. Soc.* **2015**, 137 (48), 15169-15175.
- 13 D. Hu, Y. Liu, Y.-T. Lai, K.-C. Tong, Y.-M. Fung, C.-N. Lok, and C.-M. Che, *Angew. Chem., Int. Ed.* **2016**, 55 (4), 1387-1391.
- 14 S. K. Fung, T. Zou, B. Cao, P.-Y. Lee, Y. M. E. Fung, D. Hu, C.-N. Lok, and C.-M. Che, *Angew. Chem.* **2017**, 129 (14), 3950-3954.
- 15 J. B. Gerken, M. L. Rigsby, R. E. Ruther, R. J. Pérez-Rodríguez, I. A. Guzei, R. J. Hamers, and S. S. Stahl, *Inorg. Chem.* **2013**, 52 (6), 2796-2798.
- 16 A. J. Göttle, F. Alary, M. Boggio-Pasqua, I. M. Dixon, J.-L. Heully, A. Bahreman, S. H. C. Askes, and S. Bonnet, *Inorg. Chem.* **2016**, 55 (9), 4448-4456.
- 17 C. Hansch, A. Leo, and R. Taft, *Chem. Rev.* **1991**, 91 (2), 165-195.
- 18 R. E. Goldbach, I. Rodriguez-Garcia, J. H. van Lenthe, M. A. Siegler, and S. Bonnet, *Chem. Eur. J.* **2011**, 17 (36), 9924-9929.
- 19 B. Siewert, M. Langerman, Y. Hontani, J. T. M. Kennis, V. H. S. van Rixel, B. Limburg, M. A. Siegler, V. Talens Saez, R. E. Kiełtyka, and S. Bonnet, *Chem. Commun.* **2017**, 53 (81), 11126-11129.
- 20 L. N. Lameijer, T. G. Brevé, V. H. S. van Rixel, S. H. C. Askes, M. A. Siegler, and S. Bonnet, *Chem. Eur. J.* **2018**, 24 (11), 2709-2717.
- 21 J. Snellenburg, J., S. Laptinok, R. Seger, K. Mullen, M., and I. Van Stokkum, H.M., *J. Stat. Softw.* **2012**, 49 (3), 1-22.
- 22 S. Hopkins, B. Siewert, S. Askes, P. Veldhuizen, R. Zwier, M. Heger, and S. Bonnet, *Photochem. Photobiol. Sci.* **2016**, 15 (5), 644-653.
- 23 F. Wang, J. Bella, J. A. Parkinson, and P. J. Sadler, *J. Biol. Inorg. Chem.* **2005**, 10 (2), 147-155.
- 24 C. Mari, V. Pierroz, R. Rubbiani, M. Patra, J. Hess, B. Spingler, L. Oehninger, J. Schur, I. Ott, L. Salassa, S. Ferrari, and G. Gasser, *Chem. Eur. J.* **2014**, 20 (44), 14421-14436.
- 25 L. N. Lameijer, S. L. Hopkins, T. G. Brevé, S. H. C. Askes, and S. Bonnet, *Chem. Eur. J.* **2016**, 22 (51), 18484-18491.
- 26 F. E. Poynton, S. A. Bright, S. Blasco, D. C. Williams, J. M. Kelly, and T. Gunnlaugsson, *Chem. Soc. Rev.* **2017**, 46 (24), 7706-7756.
- 27 A. Ellinger and M. Pavelka, *Cell Tissue Res.* **1984**, 235 (1), 187-194.
- 28 V. Fernández-Moreira, F. L. Thorp-Greenwood, and M. P. Coogan, *Chem. Commun.* **2010**, 46 (2), 186-202.
- 29 K. K.-W. Lo, T. K.-M. Lee, J. S.-Y. Lau, W.-L. Poon, and S.-H. Cheng, *Inorg. Chem.* **2008**, 47 (1), 200-208.
- 30 K. K.-W. Lo, M.-W. Louie, K.-S. Sze, and J. S.-Y. Lau, *Inorg. Chem.* **2008**, 47 (2), 602-611.
- 31 C. L. Ho, K. L. Wong, H. K. Kong, Y. M. Ho, C. T. L. Chan, W. M. Kwok, K. S. Y. Leung, H. L. Tam, M. H. W. Lam, X. F. Ren, A. M. Ren, J. K. Feng, and W. Y. Wong, *Chem. Commun.* **2012**, 48 (19), 2525-2527.



- 32 X.-J. Liang, D.-W. Shen, K. G. Chen, S. M. Wincovitch, S. H. Garfield, and M. M. Gottesman, *J. Cell. Physiol.* **2005**, 202 (3), 635-641.
- 33 M. V. Babak, S. M. Meier, K. V. M. Huber, J. Reynisson, A. A. Legin, M. A. Jakupec, A. Roller, A. Stukalov, M. Gridling, K. L. Bennett, J. Colinge, W. Berger, P. J. Dyson, G. Superti-Furga, B. K. Keppler, and C. G. Hartinger, *Chem. Sci.* **2015**, 6 (4), 2449-2456.
- 34 S. M. Meier, D. Kreutz, L. Winter, M. H. M. Klose, K. Cseh, T. Weiss, A. Bileck, B. Alte, J. C. Mader, S. Jana, A. Chatterjee, A. Bhattacharyya, M. Hejl, M. A. Jakupec, P. Heffeter, W. Berger, C. G. Hartinger, B. K. Keppler, G. Wiche, and C. Gerner, *Angew. Chem., Int. Ed.* **2017**, 56 (28), 8267-8271.
- 35 R. M. Cunningham and V. J. DeRose, *ACS Chem. Biol.* **2017**, 12 (11), 2737-2745.
- 36 T. Funayama, M. Kato, H. Kosugi, M. Yagi, J. Higuchi, and S. Yamauchi, *Bull. Chem. Soc. Jpn.* **2000**, 73 (7), 1541-1550.
- 37 G. te Velde, F. M. Bickelhaupt, E. J. Baerends, C. Fonseca Guerra, S. J. A. van Gisbergen, J. G. Snijders, and T. Ziegler, *J. Comput. Chem.* **2001**, 22 (9), 931-967.



# 5

## SYNTHESIS OF OTHER ALKYNE-FUNCTIONALIZED RUTHENIUM POLYPYRIDYL COMPLEXES

*The synthesis of three alkyne-functionalized polypyridyl complexes is reported. The complex  $[\text{Ru}(\text{RCC-tpy})(\text{bpy})(\text{MTI-SRR}')](\text{PF}_6)_2$ , where  $\text{MTI-SRR}'$  = a thioether-rigidin conjugate,  $\text{RCC-tpy}$  = 4'-(tert-butyltrimethylsilyl)-2,2':6',2''-terpyridyne, and  $\text{bpy}$  = 2,2'-bipyridine, was synthesized starting from an acetonitrile precursor. The reaction resulted in the formation of a reaction mixture. The complex  $[\text{Ru}(\text{Ph}_2\text{phen})(\text{mtmp})(\text{RCC-bpy})](\text{PF}_6)_2$ , where  $\text{Ph}_2\text{phen}$  = 4,7-diphenyl-1,10-phenanthroline,  $\text{mtmp}$  = 2-(methylthio)methylpyridine, and  $\text{RCC-bpy}$  = 4'-(tert-butyltrimethylsilyl)-2,2'-bipyridine, was synthesized starting from the known acetonitrile precursor  $[\text{Ru}(\text{Ph}_2\text{phen})(\text{mtmp})(\text{MeCN})_2](\text{PF}_6)_2$ . Despite the potentially increased reactivity due to the presence of two cis coordination positions on the metal center during coordination of the alkyne-functionalized bipyridine ligand, the desired complex was isolated in good yield as a mixture of two diastereoisomers. Reaction of  $[\text{Ru}(\text{DMSO})_4(\text{Cl})_2]$  with alkyne-functionalized  $\text{H}_2\text{bapbpy}$  ( $\text{RCC-bapbpy}$ ,  $\text{R}$  = trimethylsilyl) in ethanol led to the formation of various side products, e.g.  $^1\text{H}$  NMR analysis showed the formation of enol esters.*

## 5.1 Introduction

NAMI-A and KP1019 represent two milestones in the development of ruthenium-based anticancer compounds. Both complexes entered clinical trials and showed promising results.<sup>1, 2</sup> They were studied extensively to understand their chemical and biological properties, as well as their anticancer mode of action.<sup>3, 4</sup> However, for both complexes clinical trials ended without success and therefore the search for other ruthenium-based anticancer drugs continues. A promising new family of anticancer drug candidates is based on ruthenium complexes that can be activated by visible light. Those phototherapeutic agents are based on either bidentate, tridentate, or tetradentate ligands. The largest family of polypyridyl complexes is based on bidentate ligands, mostly of the 2,2'-bipyridine (bpy) family. Glazer, Salassa, Gasser, and McFarland for example have reported many new complexes of this kind,<sup>5-8</sup> while Turro and Bonnet, among others, developed complexes based on derivatives of the tridentate ligand 2,2':6',2''-terpyridine (tpy).<sup>9-13</sup> Finally, tetradentate pyridyl ligands have also been used to synthesize ruthenium compounds.<sup>14-17</sup> One promising example of such a tetrapyrindyl ligand is N6,N6'-di(pyridine-2-yl)-2,2'-bipyridine-6,6'-diamine (H<sub>2</sub>bapbpy) and its derivatives. Many ruthenium(II) complexes comprising these ligands are light-activatable, but non-emissive and thus cannot be monitored in cells by microscopy to study their intracellular distribution. For such complexes, referred to as photoactivated chemotherapy agents, alkyne functionalization, followed by post-treatment click chemistry with an azido-functionalized fluorophore, is one of the few methods available to monitor their distribution in cells.

Here, we report the synthesis of alkyne-functionalized ruthenium complexes using the synthesis method developed in Chapter 2. The alkyne handle allows fluorophore labeling *via* a CuAAC reaction to investigate the cellular distribution and mode of action of the complexes. Three ruthenium compounds were investigated (Figure 5.1): [Ru(tpy)(bpy)(MTI-SRR')](PF<sub>6</sub>)<sub>2</sub> (**[1]**(PF<sub>6</sub>)<sub>2</sub>) where MTI-SRR' is a thioether-rigidin conjugate. The rigidin derivative is known to cause cell death through impeding microtubule function,<sup>18</sup> while the thioether moiety allows the coordination of the rigidin to ruthenium. The ruthenium complex is non-toxic and "cages" the rigidin toxin in the dark.<sup>19</sup> The toxicity after light activation is hence due to the photoreleased ligand. In contrast, the tris-heteroleptic ruthenium complex [Ru(Ph<sub>2</sub>phen)(mtmp)(bpy)](PF<sub>6</sub>)<sub>2</sub> (**[2]**(PF<sub>6</sub>)<sub>2</sub>), where Ph<sub>2</sub>phen = 4,7-diphenyl-1,10-phenanthroline, and mtmp = 2-(methylthio)methylpyridine, is a

photoactivated chemotherapy compound where phototoxicity comes from the metal center. The combination of spectator ligands provides an excellent balance between lipophilicity and photosubstitution.<sup>20</sup> In this complex, light irradiation releases the non-toxic N,S ligand mtmp and the cytotoxic aqua ruthenium complex. Alkyne functionalization of the ancillary 2,2'-bipyridine ligand would allow for tracing of the toxic aqua complex within a cell. Finally, [Ru(H<sub>2</sub>bapbpy)(DMSO)(Cl)]Cl ([3]Cl), is a tetrapyridyl ruthenium complex that is cytotoxic due to the photogenerated *trans*-[Ru(H<sub>2</sub>bapbpy)(OH<sub>2</sub>)]<sup>2+</sup> species.<sup>15</sup> Alkyne functionalization of the H<sub>2</sub>bapbpy ligand is performed on its non-coordinated amine bridges,<sup>14</sup> which are in principle easier to functionalize than the pyridyl rings.

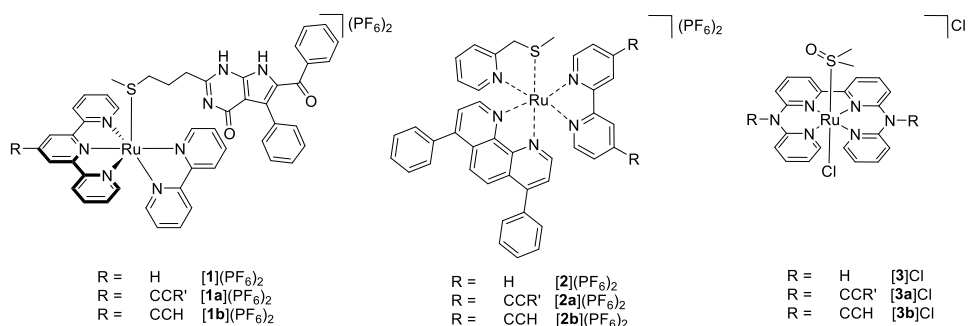


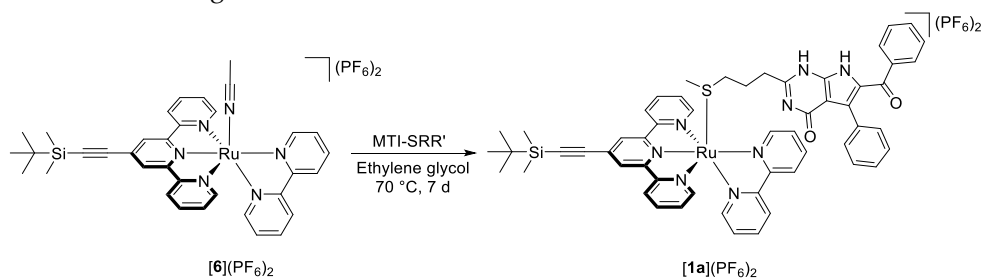
**Figure 5.1.** Schematic structures of the complexes [1](PF<sub>6</sub>)<sub>2</sub>, [2](PF<sub>6</sub>)<sub>2</sub>, and [3]Cl, described in this Chapter. For [1a](PF<sub>6</sub>)<sub>2</sub> and [2a](PF<sub>6</sub>)<sub>2</sub>, R' = *tert*-butyldimethylsilyl, for complex [3a]Cl, R' = trimethylsilyl. For complex [2](PF<sub>6</sub>)<sub>2</sub>, two isomers are formed, which are not specified here.

## 5.2 Results and Discussion

### 5.2.1 Alkyne functionalization of a tpy-based PACT complex

For the alkyne functionalization of the complex [1](PF<sub>6</sub>)<sub>2</sub>, the tpy ligand was modified as described in Chapter 2. Coordination of RCC-tpy (where R = *tert*-butyldimethylsilyl) to ruthenium(III) precursor RuCl<sub>3</sub>, followed by reaction with bpy resulted in the chloride complex [Ru(RCC-tpy)(bpy)(Cl)]Cl ([4]Cl). Attempts to synthesize [Ru(RCC-tpy)(bpy)(MTI-SRR')](PF<sub>6</sub>)<sub>2</sub> ([1a](PF<sub>6</sub>)<sub>2</sub>) according to the known reaction procedure *via* the aqua complex [Ru(RCC-tpy)(bpy)(OH<sub>2</sub>)]<sup>2+</sup> ([5]<sup>2+</sup>) failed due to the hydrophobicity of the MTI-SRR' ligand: the addition of water is necessary to drive the hydrolysis of the chloride ligand and to produce some aqua complex [5]<sup>2+</sup> in solution, but it also results in precipitation of the MTI-SRR' ligand. In addition, the ligand is non-commercial and cannot be added in large excess to the reaction mixture to drive the reaction to completion, as was done with

2-(methylthio)ethanol in Chapter 2. A new synthetic route was hence developed, *via* the acetonitrile intermediate  $[\text{Ru}(\text{RCC-tpy})(\text{bpy})(\text{MeCN})](\text{PF}_6)_2$  ( $[\mathbf{6}](\text{PF}_6)_2$ ).  $[\mathbf{6}](\text{PF}_6)_2$  was obtained by white light irradiation of  $[\mathbf{4}]\text{Cl}$  in acetonitrile for 22 h. It was expected that the acetonitrile ligand, in contrast to a labile water ligand, protects the coordination sphere of the metal ion from alkyne reactivity. For  $[\mathbf{1}](\text{PF}_6)_2$ , coordination of the MTI-SRR' ligand took place in ethylene glycol at 100 °C. Knowing from previous reactions that the reaction temperature in presence of the alkyne group should be lower than 80 °C,  $[\mathbf{1a}](\text{PF}_6)_2$  was synthesized by coordination of MTI-SRR' to  $[\mathbf{6}](\text{PF}_6)_2$  at 70 °C and the reaction time was extended to 7 d (Scheme 5.1). Precipitation yielded an off-white solid with peaks in the MS spectrum at  $m/z = 334.7, 516.3,$  and  $330.6$ , indicating that the reaction product is a mixture of starting material  $[\mathbf{6}](\text{PF}_6)_2$  (calc.  $m/z = 335.1, [\text{Ru}(\text{RCC-tpy})(\text{bpy})(\text{MeCN})]^{2+}$ ) and the desired complex  $[\mathbf{1a}](\text{PF}_6)_2$  (calc.  $m/z = 516.2, [\text{Ru}(\text{RCC-tpy})(\text{bpy})(\text{MTI-SRR}')^{2+}$ ) and a third species.  $^1\text{H}$  NMR analysis confirmed the presence of  $[\mathbf{6}](\text{PF}_6)_2$  and  $[\mathbf{1a}](\text{PF}_6)_2$  with their characteristic A6 peaks at 9.75 and 9.71 ppm in methanol- $d_4$  and showed the signal of the third species at 9.57 ppm. This signal might belong to either the aqua species  $[\mathbf{5}]^{2+}$  or the methanol complex  $[\text{Ru}(\text{RCC-tpy})(\text{bpy})(\text{MeOH})]^{2+}$  (calc.  $m/z = 330.6$ ). Separation of the complexes by size exclusion column chromatography was not successful, as the complex mixture was unstable under these conditions. Thus, so far, the complex was isolated as 2:1:2 ratio mixture of  $[\mathbf{1a}](\text{PF}_6)_2 : [\mathbf{6}](\text{PF}_6)_2 : \text{unknown side product}$  (Figure 5.2). The deprotection of the alkyne group with potassium fluoride to obtain  $[\mathbf{1b}](\text{PF}_6)_2$  was not attempted on the complex mixture. Overall, the acetonitrile complex offers an alternative starting point for coordination reaction with hydrophobic ligands that cannot be added in excess, but driving the coordination reaction to completion without increasing the temperature above 80 °C remains a challenge.



**Scheme 5.1.** Reaction scheme of the synthesis of the alkyne-functionalized complex  $[\mathbf{1a}](\text{PF}_6)_2$ .

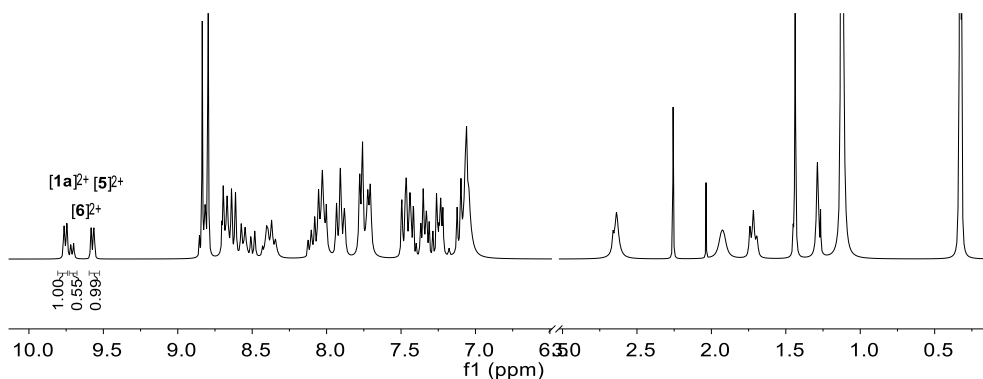
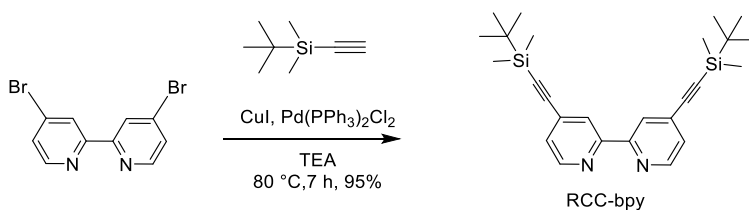


**Figure 5.2**  $^1\text{H}$  NMR spectrum of a solution of the product mixture in methanol- $d_4$  of the reaction between  $[\mathbf{6}](\text{PF}_6)_2$  and MTI-SRR'.

### 5.2.2 Alkyne functionalization of a bpy-based PACT complex

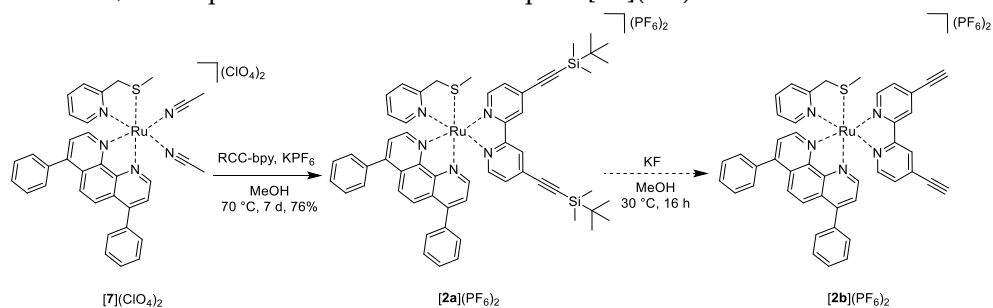
Alkyne functionalization of the bpy ligand is well-reported in literature with trimethylsilyl (TMS) as protecting group.<sup>21, 22</sup> Here, *tert*-butyldimethylsilyl (TBDMS, R) was used. 4,4'-Bis(*tert*-butyldimethylsilylethynyl)-2,2'-bipyridine (RCC-bpy) was synthesized from 4,4'-dibromo-2,2'-bipyridine and *tert*-butyldimethylsilylethyne in a 1:18 ratio in triethylamine (TEA) (Scheme 5.2), followed by purification on a silica column. The MS spectrum of the product showed signals at  $m/z = 433.6$  corresponding to  $(\text{RCC-bpy} + \text{H})^+$  (calc.  $m/z = 433.3$ ), and the  $^1\text{H}$  NMR spectrum in chloroform- $d$  shows the characteristic relative ratio (9:6) of the *tert*-butyl protons to the protons of the two dimethyl groups of the protecting R group at 1.00 and 0.20 ppm, respectively.



**Scheme 5.2.** Reaction scheme of the synthesis of the alkyne-functionalized RCC-bpy ligand.

The known acetonitrile precursor  $[\text{Ru}(\text{Ph}_2\text{phen})(\text{mtmp})(\text{MeCN})_2](\text{ClO}_4)_2$  ( $[\mathbf{7}](\text{ClO}_4)_2$ ) was reacted with the RCC-bpy ligand to obtain the heteroleptic light-activatable ruthenium complex  $[\text{Ru}(\text{Ph}_2\text{phen})(\text{mtmp})(\text{RCC-bpy})](\text{PF}_6)_2$  ( $[\mathbf{2a}](\text{PF}_6)_2$ , Scheme 5.3).<sup>20, 23</sup> Here again, the acetonitrile groups of the precursor complex  $[\mathbf{7}]^{2+}$  prevented the reaction of the alkynes with the ruthenium center. For the synthesis of  $[\mathbf{2a}](\text{PF}_6)_2$ , the presence of these acetonitrile groups is even more important

because of the increased number of free coordination sites compared to precursors such as  $[6]^{2+}$ . The formation of additional side products is known for ruthenium complexes with two available coordination sites in *cis*-position.<sup>21</sup> The reaction conditions used for the synthesis of the non-functionalized complex  $[2](PF_6)_2$  had to be adapted for the presence of the alkynes: instead of ethylene glycol, the reaction was performed in methanol at reflux temperature (70 °C) for 7 d (experimentally determined by NMR experiments, Figure AV.1). After precipitation with aqueous potassium hexafluoridophosphate solution, MS analysis ( $m/z = 502.6$ ; calc.  $m/z = 502.7$  for  $[Ru(Ph_2phen)(mtmp)(RCC-bpy)]^{2+}$ ) and  $^1H$  NMR spectroscopy in chloroform-*d* (Figure 5.3) confirmed the formation of the desired complex  $[2a](PF_6)_2$ . The complex was isolated as a mixture of configuration isomers, like for  $[2](PF_6)_2$ .<sup>20</sup> Removal of the TBDMS protecting group was attempted with five equivalents of potassium fluoride in methanol overnight at 30 °C. A decrease of the  $^1H$  NMR peaks in methanol-*d*<sub>6</sub> belonging to the protecting group (1.04 and 0.24 ppm) and the appearance of new singlet peaks at 4.61 and 4.47 ppm for the free alkynes of both isomers indicated that partial deprotection of the terminal alkynes had occurred. However, full deprotection and isolation of pure  $[2b](PF_6)_2$  was not achieved.



**Scheme 5.3.** Reaction scheme of the synthesis of the alkyne-functionalized complex  $[2a](PF_6)_2$ .

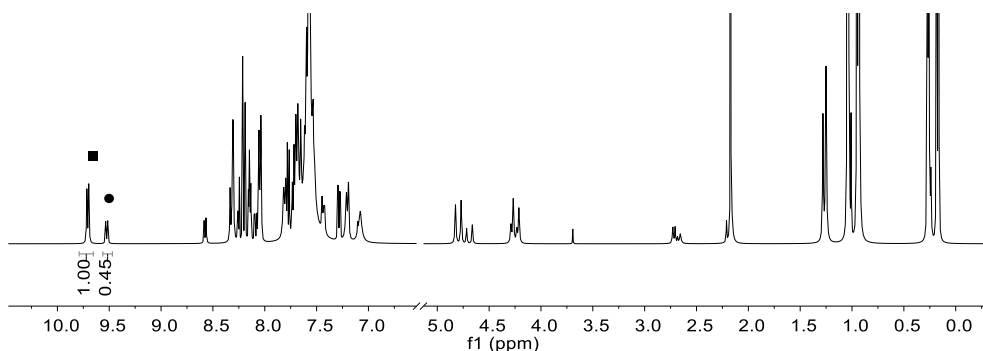
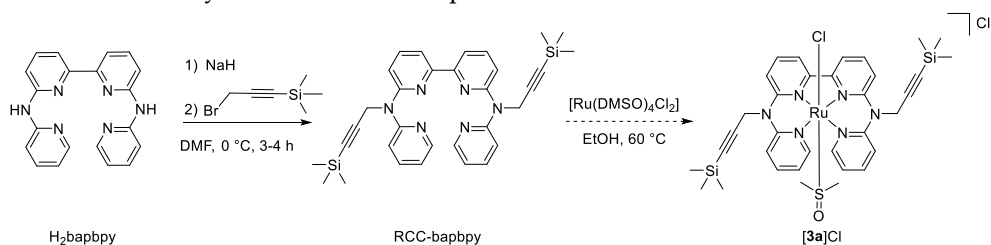


**Figure 5.3**  $^1H$  NMR spectrum of a solution of  $[2a](PF_6)_2$  in chloroform-*d*. Signals indicated with black square (■) and circle (●) correspond to the two isomers of complex  $[2a](PF_6)_2$ .



### 5.2.3 Alkyne-functionalized bapbpy-based ruthenium complex

The tetradentate ligand H<sub>2</sub>bapbpy was functionalized on both non-coordinating amine bridges. The alkyne-functionalized RCC-bapbpy ligand (R = trimethylsilyl, Scheme 5.4) was synthesized by the reaction of H<sub>2</sub>bapbpy and commercially available 3-(trimethylsilyl)propargyl bromide in the presence of sodium hydride in DMF for 3 h at 0 °C, as TBDMS-protected propargyl bromide is not commercially available. After extraction with ethyl acetate, evaporation, and washing with methanol, RCC-bapbpy was isolated in a yield of 17%. The nature of the ligand was confirmed by mass spectrometry ( $m/z = 561.5$ ; calc.  $m/z = 561.3$  for (RCC-bapbpy + H)<sup>+</sup>) and <sup>1</sup>H NMR spectroscopy (Figure 5.4). Coordination of RCC-bapbpy to the ruthenium precursor [Ru(DMSO)<sub>4</sub>(Cl)<sub>2</sub>] was then studied in NMR experiments in deuterated ethanol-d<sub>6</sub> over several hours at 60 °C (Figure and Scheme 5.4). The signals of the free ligand decreased, and new signals appeared in the aromatic as well as in the aliphatic region. The number of new signals indicated that the reaction yielded a mixture of products.



**Scheme 5.4.** Reaction scheme of the synthesis of the functionalized ligand RCC-bapbpy and its coordination to ruthenium to obtain [3a]Cl.

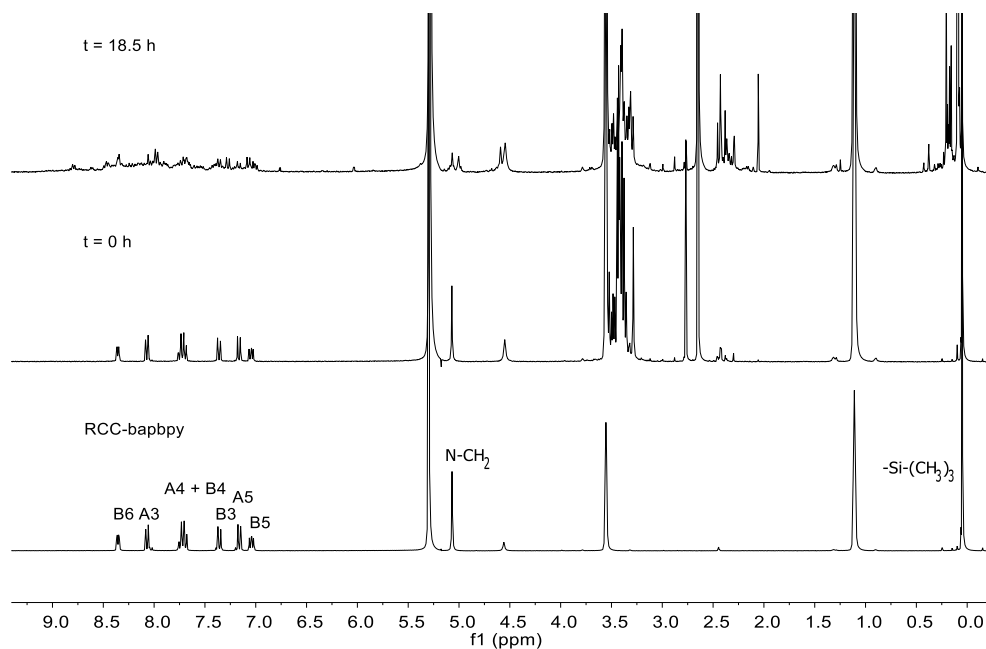
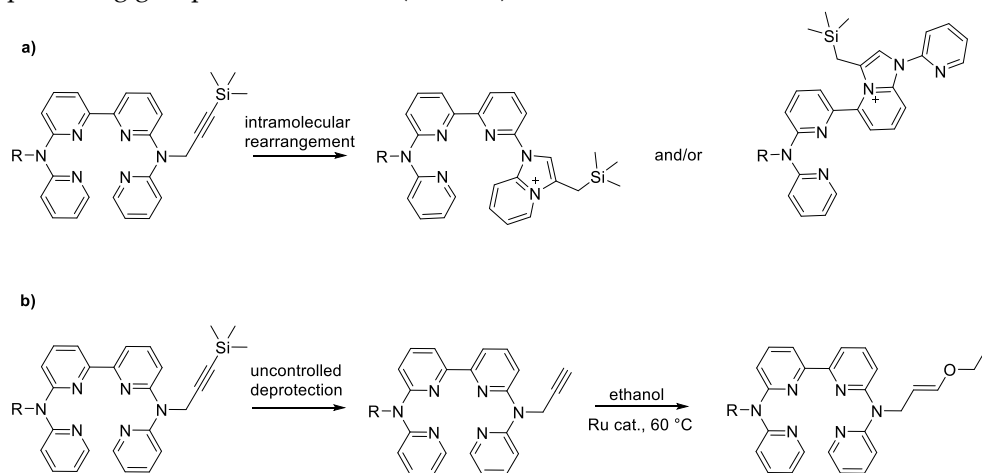


**Figure 5.4.**  $^1\text{H}$  NMR evolution of the reaction of  $[\text{Ru}(\text{DMSO})_4(\text{Cl})_2]$  and RCC-babppy in ethanol- $\text{d}_6$  at  $60\text{ }^\circ\text{C}$ .

To identify the nature of these products, several control experiments were conducted. The thermal stability of the RCC-babppy ligand under the reaction conditions was monitored by  $^1\text{H}$  NMR spectroscopy in deuterated ethanol- $\text{d}_6$  in absence of a metal precursor for several days at  $60\text{ }^\circ\text{C}$  (Figure AV.3). The  $^1\text{H}$  NMR spectra did show the appearance of new signals while the peaks belonging to the starting ligand disappeared, indicating that the ligand is not stable in solution. When stored at room temperature in solution, the NMR spectrum showed signals belonging to the RCC-ligand, the product seen after heating the ligand at  $60\text{ }^\circ\text{C}$ , and additional peaks (Figure AV.3). Noteworthy, upon functionalization of the bidentate ligand *N,N*-dipyridylamine (Hdpa), which represents one half of  $\text{H}_2\text{babppy}$ , with the same alkyne handle, an unexpected intramolecular rearrangement took place at room temperature (Scheme AV.2 and Figure AV.4). It cannot be excluded that such an intramolecular rearrangement will take place for RCC-babppy (Scheme 5.5a). The NMR reaction of  $[\text{Ru}(\text{DMSO})_4(\text{Cl})_2]$  in deuterated ethanol- $\text{d}_6$  was also performed with the non-protected HCC-babppy ligand. After 1 h at  $60\text{ }^\circ\text{C}$ , the signals of the starting materials disappeared and very broad, ill-defined signals appeared (Figure AV.5). A dark insoluble precipitate was formed that could not be analyzed by NMR spectroscopy or mass spectrometry. Polymerization might have taken place here.<sup>24</sup> When working with the protected RCC-babppy ligand, the solution stayed clear

without precipitate formation for the entire time of the experiment (18.5 h). Therefore, polymerization can be excluded as possible side reaction when working with TMS-protected alkynes. In Chapter 2, the formation of an enol ester was reported as side reaction when functionalizing tpy with an alkyne group (Scheme AII.1). Thus, the reaction of  $[\text{Ru}(\text{DMSO})_4(\text{Cl})_2]$  and RCC-bapbpy was repeated in non-deuterated ethanol to investigate possible side reactions involving ethanol. The aromatic regions of the  $^1\text{H}$  NMR spectra of the reaction mixtures obtained in deuterated ethanol- $\text{d}_6$  and non-deuterated ethanol showed similar signals, but in the aliphatic region additional signals at 4.05, 3.59, and 1.16 ppm were found (Figure 5.5) when working in non-deuterated solvent. The fact that these signals were not visible when the reaction was performed in deuterated ethanol- $\text{d}_6$  confirmed that these peaks are the result of a side reaction with ethanol (Scheme 5.5b). The signals are indeed characteristic for an enol ester (Figure AV.6). Repeating the reaction in a non-alcoholic solvent should prevent enol ester formation. Whether this side reaction occurs on both sides of the bapbpy ligand and whether coordination of this new ligand to the ruthenium precursor is possible remained unclear since the MS spectrum of the reaction mixture did not give conclusive results (Figure AV.7). Overall, the functionalization of the amine bridges of  $\text{H}_2\text{bapbpy}$  is not a viable strategy since several side reactions may occur in parallel, and alternative positions of the alkyne groups on the tetradentate ligand should be considered. In addition, the TMS protecting group is not fully protecting the alkyne groups, and a better protecting group should be used (TBDMS).



**Scheme 5.5.** Overview of possible side products in the reaction of RCC-bapbpy with  $[\text{Ru}(\text{DMSO})_4(\text{Cl})_2]$  in ethanol: a) intramolecular rearrangement of the RCC-bapbpy ligand, and b) enol ester formation after

deprotection of the alkyne groups. The ruthenium(II) species can act as catalyst, and/or coordinate to the new ligands.

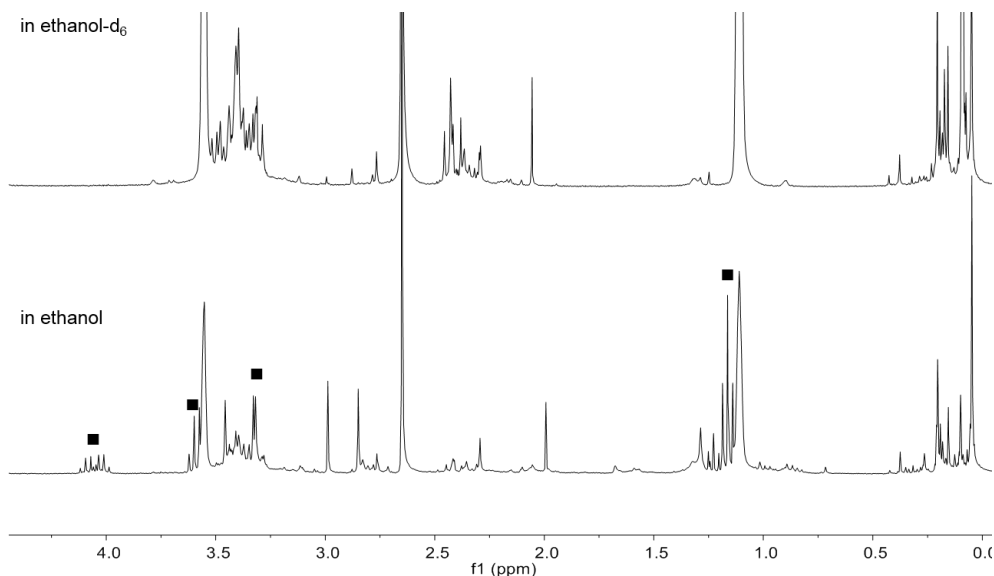


**Figure 5.5.**  $^1\text{H}$  NMR spectrum (aliphatic region) of a solution of the reaction product of the reaction between RCC-bapbpy and  $[\text{Ru}(\text{DMSO})_4(\text{Cl})_2]$  in ethanol- $\text{d}_6$  or ethanol. The  $^1\text{H}$  NMR is taken in ethanol- $\text{d}_6$ . Signals indicated with black squares (■) correspond to enol esters.

## 5.3 Conclusion

In conclusion, two polypyridyl ligands were functionalized with short alkyne handles showing that the series of functionalized ligands can easily be extended. The alkyne handle always needs protection during metal coordination to prevent the formation of side products in the following complexation steps. It is necessary to adapt the conditions of the coordination reaction of the functionalized ligand to the instability of the alkyne protecting group. There is not one universal method for all complexation reactions, but specific strategies for each target ruthenium complex have to be found. Those adjustments require effort and time and the optimal conditions are not always easy to predict.

## 5.4 Experimental

### 5.4.1 Materials and Methods

(S)-2,2'-Bis(diphenylphosphino)-1,1'-binaphthalene ((S)-BINAP), potassium *tert*-butoxide (KOtBu), bis(dibenzylideneacetone)palladium(0) ( $\text{Pd}(\text{dba})_2$ ), 2-amino-4-chloropyridine, *p*-toluenesulfonic anhydride ( $\text{Ts}_2\text{O}$ ), trifluorotoluene ( $\text{PhCF}_3$ ), 6-bromo-2,2'-bipyridine, racemic BINAP, 3-bromo-1-(trimethylsilyl)-1-propyne, sodium hydride (NaH) (60% in mineral oil), triethylamine ( $\text{Et}_3\text{N}$ ),

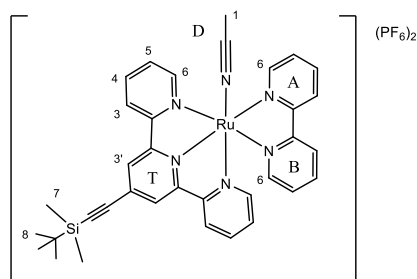
sodium oxalate (Na<sub>2</sub>C<sub>2</sub>O<sub>4</sub>), and potassium hexafluoridophosphate (KPF<sub>6</sub>) were purchased from Sigma Aldrich; 6,6'-dibromo-2,2'-bipyridine from Tokyo Chemical Industry; trifluoroacetic acid and 2,2'-bipyridine from Alpha Aesar; bis(triphenylphosphine)palladium(II) dichloride (PdCl<sub>2</sub>(PPh<sub>3</sub>)<sub>2</sub>), tert-butylamine and copper iodide (CuI) from Acros Organics; tert-butyltrimethylsilyl ethyne, dipyridylamine (Hdpa), and 4,7-diphenyl-1,10-phenanthroline from ABCR; 4,4'-dibromo-2,2'-bipyridine, and Pd(PPh<sub>3</sub>)<sub>2</sub>Cl<sub>2</sub> from Fischer Scientific. 2-[(Methylthio)methyl]pyridine, cis-RuCl<sub>2</sub>(dimethylsulfoxide)<sub>4</sub>, [Ru(RCC-tpy)(bpy)(Cl)]Cl, H<sub>2</sub>bapbpy, and microtubule polymerization inhibitor (MTI-SRR') were synthesized according to literature.<sup>18, 25-28</sup> All syntheses were completed under dinitrogen atmosphere unless otherwise noted and, apart from 4,4'-bis(tert-butyltrimethylsilyl ethynyl)-2,2'-bipyridine and [Ru(RCC-tpy)(bpy)(MeCN)](PF<sub>6</sub>)<sub>2</sub>, under dim light. Et<sub>3</sub>N and DMF were dried over molecular sieves (4 Å). All reagents were used without further purification.

NMR spectra were recorded on an AV-300 Bruker spectrometer with chemical shifts indicated in ppm. Mass spectra were recorded on a Thermo Scientific Dionex UltiMate 3000 system. A LOT 1000 W Xenon Arc lamp with an IR short pass filter and a 400 nm long pass filter from Andover Corporation was used for the preparative scale photoreaction.

## 5.4.2 Synthesis

### Synthesis of [Ru(RCC-tpy)(bpy)(MeCN)](PF<sub>6</sub>)<sub>2</sub> (R = TBDMS), [6](PF<sub>6</sub>)<sub>2</sub>

[Ru(RCC-tpy)(bpy)(Cl)]Cl (21 mg, 0.029 mmol) was dissolved in a mixture of acetonitrile/water (100 mL, 3:1 ratio) under air atmosphere in a 100 mL photoreactor (diameter = 5.0 cm, depth = 5.5 cm) placed 7 cm from the focusing lens. This mixture was stirred with a magnetic stirrer and kept at 25 °C with a water-cooling system and irradiated at 800 W with a LOT 1000 W Xenon Arc lamp fitted with IR short pass and 400 nm long pass filters from Andover Corporation. Irradiation was done for periods of 4 to 7 h over 4 d for a total of 22 h. During this time the solution changed from pink-purple to red-orange. The reaction was followed by TLC on silica using a mobile phase of acetone/water/KPF<sub>6</sub> (16:4:1). R<sub>f</sub> values for [Ru(RCC-tpy)(bpy)(Cl)]Cl and [5](PF<sub>6</sub>)<sub>2</sub> are 0.75 and 0.55, respectively. The mixture was added to a stirred saturated aqueous potassium hexafluoridophosphate solution, chilled overnight in the fridge, filtered, and washed with water. [6](PF<sub>6</sub>)<sub>2</sub> was obtained as dark orange powder in a yield of 50% (6.0 mg, 7.7 μmol).



<sup>1</sup>H NMR (300 MHz, methanol-*d*<sub>4</sub>, 298 K) δ 9.71 (d, *J* = 5.6 Hz, 1H, A6), 8.81 (d, *J* = 8.0 Hz, 1H, A3), 8.81 (s, 2H, T3'), 8.68 (d, *J* = 8.2 Hz, 2H, T3), 8.55 (d, *J* = 8.1 Hz, 1H, B3), 8.40 (t, *J* = 7.4 Hz, 1H, A4), 8.06 (td, *J* = 7.9, 2.2 Hz, 3H, T4 + A5), 7.94–7.82 (m, 1H, B4), 7.77 (d, *J* = 5.3 Hz, 2H, T6), 7.50–7.37 (m, 3H, T5 + B6), 7.23–7.13 (m, 1H, B5), 2.26 (s, 3H, D1), 1.12 (s, 9H, T8), 0.33 (s, 6H, T7). <sup>13</sup>C NMR (75 MHz, acetonitrile-*d*<sub>3</sub>, 298 K) δ 153.0, 152.3, 150.9, 138.8, 137.7, 137.4, 128.3, 127.7, 126.6, 125.3, 124.5, 124.2, 123.7, 25.5. ES MS *m/z* (calc.): 334.7 (335.1 [M – 2PF<sub>6</sub>]<sup>2+</sup>).

### Synthesis of [Ru(RCC-tpy)(bpy)(MTI-SRR')](PF<sub>6</sub>)<sub>2</sub> (R = TBDMS), [1a](PF<sub>6</sub>)<sub>2</sub>

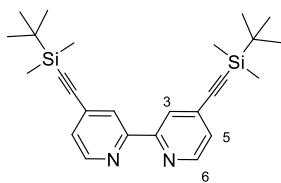
[Ru(RCC-tpy)(bpy)(MeCN)](PF<sub>6</sub>)<sub>2</sub> (9.0 mg, 9.4 μmol) and MTI-SRR' (3.8 mg, 9.4 μmol) were dissolved in ethylene glycol (3 mL) and heated for 7 d at 70 °C. The reaction was followed by silica gel TLC on Al foil

plates (16:4:1 acetone/water/KPF<sub>6</sub>, R<sub>f</sub> = 0.69). After cooling to room temperature, the solution was added to a saturated aqueous solution of potassium hexafluoridophosphate (40 g/L) and chilled in the fridge overnight. Then, the orange precipitate was collected on a Millipore filter and washed with water and diethyl ether (3 x 10 mL each). The complex was then re-dissolved in acetone (20 mL) and added to saturated aqueous potassium hexafluoridophosphate solution (40 g/L, 20 mL). A rotary evaporator was used to remove acetone until the complex precipitated, at which point it was filtered and washed again with water and diethyl ether (3 x 10 mL each). A dark red solid was obtained (8.0 mg).

The <sup>1</sup>H NMR spectrum showed a mixture of [1a](PF<sub>6</sub>)<sub>2</sub> : [6](PF<sub>6</sub>)<sub>2</sub> : unknown byproduct in a ratio 2:1:2. ESI-MS *m/z* (*calc.*): 330.6, (330.6, [Ru(RCC-tpy)(bpy)(MeOH)]<sup>2+</sup>), 334.7, (335.1, [Ru(RCC-tpy)(bpy)(MeCN)]<sup>2+</sup>), 516.3 (516.2, [Ru(RCC-tpy)(bpy)(MTI-SRR)]<sup>2+</sup>).

#### Synthesis of 4,4'-bis(*tert*-butyldimethylsilylethynyl)-2,2'-bipyridine, RCC-bpy (R = TBDMS)

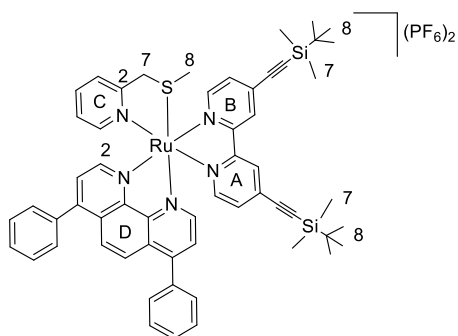
4,4'-Bis(*tert*-butyldimethylsilylethynyl)-2,2'-bipyridine was synthesized according to a modified literature procedure.<sup>1</sup> Under dry conditions, 4,4'-dibromo-2,2'-bipyridine (250 mg, 0.80 mmol), CuI (19 mg, 0.10 mmol), Pd(PPh<sub>3</sub>)<sub>2</sub>Cl<sub>2</sub> (35 mg, 0.050 mmol), and *tert*-butyldimethylsilylethyne (0.90 mL, 4.8 mmol) were added to triethylamine (4 mL) and refluxed for 7 h at 80 °C. During the reflux, the same amounts of triethylamine and *tert*-butyldimethylsilylethyne were added twice (after 2 h 20 min and 4 h 40 min). After 7 h, the solvents were evaporated, the solid was dissolved in *n*-hexane, and filtered. The filtrate was purified by silica column with hexane/ethyl acetate (8:2) as eluent (R<sub>f</sub> = 0.83). Yield: 95% (327 mg, 0.757 mmol).



<sup>1</sup>H NMR (300 MHz, chloroform-*d*, 298 K) δ 8.62 (dd, *J* = 5.0, 0.9 Hz, 2H, 6), 8.42 (dd, *J* = 1.6, 0.9 Hz, 2H, 3), 7.33 (dd, *J* = 5.0, 1.6 Hz, 2H, 5), 1.00 (s, 18H, -Si-C(CH<sub>3</sub>)<sub>3</sub>), 0.20 (s, 12H, -Si-(CH<sub>3</sub>)<sub>2</sub>). <sup>13</sup>C NMR (75 MHz, chloroform-*d*, 298 K) δ 155.7 (2), 149.2 (6), 132.5 (4), 126.1 (5), 123.6 (3), 103.0 (-CC-Si), 98.6 (-CC-Si), 26.2 (-Si-C(CH<sub>3</sub>)<sub>3</sub>), 16.8 (-Si-C(CH<sub>3</sub>)<sub>3</sub>), -4.6 (-Si-(CH<sub>3</sub>)<sub>2</sub>). ES MS *m/z* (*calc.*): 433.6 (433.3, [M + H]<sup>+</sup>).

#### Synthesis of [Ru(Ph<sub>2</sub>phen)(mtmp)(RCC-bpy)](PF<sub>6</sub>)<sub>2</sub>, [2a](PF<sub>6</sub>)<sub>2</sub> (R = TBDMS)

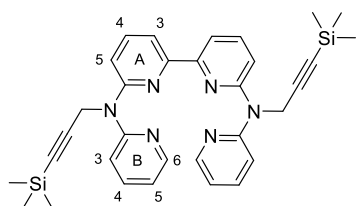
[Ru(Ph<sub>2</sub>phen)(mtmp)(MeCN)<sub>2</sub>](ClO<sub>4</sub>)<sub>2</sub> (10.0 mg, 0.0117 mmol) and 4,4'-bis(*tert*-butyldimethylsilylethynyl)-2,2'-bipyridine (5.0 mg, 0.012 mmol) were dissolved in methanol (3 mL). The mixture was heated for 7 d at 70 °C. After cooling to room temperature, the bright red-orange mixture was added to a stirred, saturated aqueous solution of potassium hexafluoridophosphate (40 g/L) and chilled in the fridge overnight. The precipitate was filtered and washed with water and diethyl ether. [2a](PF<sub>6</sub>)<sub>2</sub> was obtained in a yield of 76% (9 mg, 9 μmol) as a mixture of two coordination isomers in a 0.45:1 ratio.



$^1\text{H NMR}$  (300 MHz, *chloroform-d*, 298 K)  $\delta$  9.71 (d,  $J = 5.5$  Hz), 9.52 (d,  $J = 5.9$  Hz), 8.36 – 7.99 (m), 7.84 – 7.41 (m), 7.28 (dd,  $J = 5.9, 1.7$  Hz), 7.20 (d,  $J = 5.8$  Hz), 7.09 (d,  $J = 7.6$  Hz), 5.30 (s), 4.80 (d,  $J = 16.3$  Hz), 4.69 (d,  $J = 16.5$  Hz), 4.25 (dd,  $J = 16.5, 6.5$  Hz), 3.49 (s), 2.17 (s), 1.27 (d,  $J = 8.7$  Hz), 1.04 (s), 1.03 (s), 0.95 (s), 0.94 (s), 0.27 (s), 0.26 (s), 0.18 (s), 0.17 (s).  $^{13}\text{C NMR}$  (75 MHz, *chloroform-d*, 298 K)  $\delta$  156.6, 150.3, 150.3, 135.2, 135.1, 133.9, 133.1, 129.3, 129.0, 77.4, 77.0, 76.6. *ESI-MS*  $m/z$  (*calc.*): 502.6 (502.7,  $[\text{M} - 2\text{PF}_6]^{2+}$ ).

### Synthesis of RCC-babppy, (R = TMS)

The reaction was performed under anhydrous conditions. Sodium hydride (52 mg, 1.3 mmol) was added portion wise to a solution of H<sub>2</sub>babppy (100 mg, 0.29 mmol) in DMF (1.7 mL) at 0 °C. The reaction mixture was stirred at 0 °C for 30 min and 3-(trimethylsilyl)propargyl bromide (1.1 mL, 6.5 mmol) was added dropwise. The mixture was stirred at 0 °C for 3 h. Then, water (60 ml) was added and the mixture was extracted with ethyl acetate (4 × 25 mL). The combined organic layers were dried over sodium sulfate, filtered and concentrated. The residue was purified by chromatography over silica gel (gradient from 100% dichloromethane to 95:5 dichloromethane/methanol). The product fractions were collected, and the solvent was evaporated. The RCC-babppy was obtained in a yield of 17% (28 mg, 0.05 mmol).



$^1\text{H NMR}$  (300 MHz, *DMSO-d*<sub>6</sub>, 298 K)  $\delta$  8.38 (ddd,  $J = 5.0, 2.0, 0.8$  Hz, 2H, B6), 7.98 (d,  $J = 7.5$  Hz, 2H, A3), 7.88 – 7.76 (m, 2H, A4), 7.79 – 7.71 (m, 2H, B4), 7.36 (dt,  $J = 8.4, 1.0$  Hz, 2H, B3), 7.27 (d,  $J = 8.2$  Hz, 2H, A5), 7.06 (ddd,  $J = 7.3, 4.8, 0.9$  Hz, 2H, B5), 5.06 (s, 4H, N-CH<sub>2</sub>-), 0.05 (s, 18H, -Si(CH<sub>3</sub>)<sub>3</sub>).  $^{13}\text{C NMR}$  (75 MHz, *DMSO-d*<sub>6</sub>, 298 K)  $\delta$  155.6 + 154.9 + 153.5 (A2 + A6 + B2), 148.0 (B6), 138.5 (A4), 137.9 (B4), 118.1 (B5), 114.9 (B3), 114.2 (A5), 114.0 (A3), 104.0 (CH<sub>2</sub>-CC-), 86.5 (-CC-Si), 38.1 (N-CH<sub>2</sub>-), -0.1 (-Si(CH<sub>3</sub>)<sub>3</sub>). *ES MS*  $m/z$  (*calc.*): 561.5 (561.3,  $[\text{M} + \text{H}]^+$ ).

### Attempted synthesis of [Ru(RCC-babppy)(DMSO)(Cl)]Cl

[Ru(DMSO)<sub>4</sub>(Cl)<sub>2</sub>] (2.5 mg, 5.1 μmol) and RCC-babppy (2.3 mg, 4.1 μmol) were dissolved in deuterated ethanol-*d*<sub>6</sub> (0.5 mL) under dinitrogen atmosphere in an NMR tube with PTFE stopper. The reaction mixture was heated at 60 °C in the NMR tube.  $^1\text{H NMR}$  spectra of the reaction were recorded at different reaction times.

[Ru(DMSO)<sub>4</sub>(Cl)<sub>2</sub>] (10.4 mg, 0.021 mmol) and RCC-babppy (10.0 mg, 0.018 mmol) were dissolved in ethanol (5 mL) under dinitrogen atmosphere. The reaction mixture was heated at 60 °C while stirring for 18.5 h. The solvent was evaporated, and the reaction mixture was analyzed by MS and  $^1\text{H NMR}$  analysis.

## 5.4.3 Supporting Information

The synthetic routes for the synthesis of HCC-dpa and HCC-babppy are reported.  $^1\text{H NMR}$  spectra of the synthesis of [2a](PF<sub>6</sub>)<sub>2</sub> and of stability measurements of RCC-babppy, as well as the characterization of the HCC-babppy intramolecular rearrangement product are provided in Appendix IV.

## 5.5 Contribution

Emma Cleary and Dr. Sipeng Zheng helped to synthesize some of the ligands and ruthenium complexes. Dr. Sylvestre Bonnet and Prof. Lies Bouwman provided experimental guidance and significant editorial feedback.

## 5.6 References

- 1 C. G. Hartinger, S. Zorbas-Seifried, M. A. Jakupec, B. Kynast, H. Zorbas, and B. K. Keppler, *J. Inorg. Biochem.* **2006**, 100 (5), 891-904.
- 2 E. Alessio, *Eur. J. Inorg. Chem.* **2017**, 2017 (12), 1549-1560.
- 3 J. Malina, O. Novakova, B. K. Keppler, E. Alessio, and V. Brabec, *J. Biol. Inorg. Chem.* **2001**, 6 (4), 435-445.
- 4 C. G. Hartinger, M. A. Jakupec, S. Zorbas-Seifried, M. Groessler, A. Egger, W. Berger, H. Zorbas, P. J. Dyson, and B. K. Keppler, *Chem. Biodiversity* **2008**, 5 (10), 2140-2155.
- 5 Y. Arenas, S. Monro, G. Shi, A. Mandel, S. McFarland, and L. Lilje, *Photodiagnosis Photodyn. Ther.* **2013**, 10 (4), 615-625.
- 6 B. S. Howerton, D. K. Heidary, and E. C. Glazer, *J. Am. Chem. Soc.* **2012**, 134 (20), 8324-8327.
- 7 E. Wachter, D. K. Heidary, B. S. Howerton, S. Parkin, and E. C. Glazer, *Chem. Commun.* **2012**, 48 (77), 9649-9651.
- 8 C. Mari, V. Pierroz, R. Rubbiani, M. Patra, J. Hess, B. Spingler, L. Oehninger, J. Schur, I. Ott, L. Salassa, S. Ferrari, and G. Gasser, *Chem. Eur. J.* **2014**, 20 (44), 14421-14436.
- 9 R. E. Goldbach, I. Rodriguez-Garcia, J. H. van Lenthe, M. A. Siegler, and S. Bonnet, *Chem. Eur. J.* **2011**, 17 (36), 9924-9929.
- 10 B. Siewert, V. H. van Rixel, E. J. van Rooden, S. L. Hopkins, M. J. Moester, F. Ariese, M. A. Siegler, and S. Bonnet, *Chem. Eur. J.* **2016**, 22 (31), 10960-10968.
- 11 L. N. Lameijer, S. L. Hopkins, T. G. Brevé, S. H. C. Askes, and S. Bonnet, *Chem. Eur. J.* **2016**, 22 (51), 18484-18491.
- 12 L. M. Loftus, J. K. White, B. A. Albani, L. Kohler, J. J. Kodanko, R. P. Thummel, K. R. Dunbar, and C. Turro, *Chem. Eur. J.* **2016**, 22 (11), 3704-3708.
- 13 O. Novakova, J. Kasparkova, O. Vrana, P. M. van Vliet, J. Reedijk, and V. Brabec, *Biochemistry* **1995**, 34 (38), 12369-12378.
- 14 V. H. S. van Rixel, B. Siewert, S. L. Hopkins, S. H. C. Askes, A. Busemann, M. A. Siegler, and S. Bonnet, *Chem. Sci.* **2016**, 7 (8), 4922-4929.
- 15 V. H. S. van Rixel, G. F. Moolenaar, M. A. Siegler, L. Messori, and S. Bonnet, *Dalton Trans.* **2018**, 47 (2), 507-516.
- 16 D. Havrylyuk, M. Deshpande, S. Parkin, and E. C. Glazer, *Chem. Commun.* **2018**, 54 (88), 12487-12490.
- 17 R. Sharma, J. D. Knoll, P. D. Martin, I. Podgorski, C. Turro, and J. J. Kodanko, *Inorg. Chem.* **2014**, 53 (7), 3272-3274.
- 18 D. C. Medellin, Q. Zhou, R. Scott, R. M. Hill, S. K. Frail, R. Dasari, S. J. Ontiveros, S. C. Pelly, W. A. L. van Otterlo, T. Betancourt, C. B. Shuster, E. Hamel, R. Bai, D. V. LaBarbera, S. Rogelj, L. V. Frolova, and A. Kornienko, *J. Med. Chem.* **2016**, 59 (1), 480-485.
- 19 V. H. S. Van Rixel, Toward selective anticancer metallodrugs **2017**, Leiden University, Leiden.
- 20 J.-A. Cuello-Garibo, Caging ruthenium complexes with non-toxic ligands for photoactivated chemotherapy **2017**, Leiden University, Leiden.



- 21 N. Zabarska, D. Sorsche, F. W. Heinemann, S. Glump, and S. Rau, *Eur. J. Inorg. Chem.* **2015**, 2015 (29), 4869-4877.
- 22 R. Ziesel, J. Suffert, and M.-T. Youinou, *J. Org. Chem.* **1996**, 61 (19), 6535-6546.
- 23 C. S. Burke and T. E. Keyes, *RSC Advances* **2016**, 6 (47), 40869-40877.
- 24 C. Slugovc, D. Doberer, C. Gemel, R. Schmid, K. Kirchner, B. Winkler, and F. Stelzer, *Monatsh. Chem.* **1998**, 129 (3), 221-233.
- 25 E. Reisner, T. C. Abikoff, and S. J. Lippard, *Inorg. Chem.* **2007**, 46 (24), 10229-10240.
- 26 J. R. Alston, S. Kobayashi, T. J. Younts, and J. C. Poler, *Polyhedron* **2010**, 29 (13), 2696-2702.
- 27 J. B. Gerken, M. L. Rigsby, R. E. Ruther, R. J. Pérez-Rodríguez, I. A. Guzei, R. J. Hamers, and S. S. Stahl, *Inorg. Chem.* **2013**, 52 (6), 2796-2798.
- 28 S. Bonnet, M. A. Siegler, J. S. Costa, G. Molnar, A. Bousseksou, A. L. Spek, P. Gamez, and J. Reedijk, *Chem. Commun.* **2008**, (43), 5619-5621.



# 6

## SUMMARY, DISCUSSION, AND CONCLUSION

## 6.1 Summary

### 6.1.1 PACT as selective treatment against cancer cells

Currently used chemotherapy agents go along with undesirable side effects due to poor selectivity of the drug: healthy cells are as much affected as cancerous cells. To direct the cytotoxicity towards tumor tissue only, cancer cells can be targeted in different ways: either by targeting a protein that is abundant in cancer cells (biological selectivity), or by the selective release of the cytotoxic species only at the tumor site (physical selectivity). The latter can for example be achieved by light. A non-toxic prodrug is injected in the patient and distributes through the whole body. However, only light-activation can trigger the release of the cytotoxic species that causes cell death. Depending on the cytotoxic species, two types of phototherapy are distinguished: photodynamic therapy (PDT), in which the chemotherapy agent and light lead to the production of toxic reactive oxygen species, or oxygen-independent photoactivated chemotherapy (PACT) in which the cleavage of a protecting moiety of the complex leads to the release of the cytotoxic species. The direct interaction of the released cytotoxic moiety with intracellular targets such as proteins or DNA, leads to cell death. Depending on the nature of the released cytotoxic species, different targets and modes of action of the chemotherapy agent are possible. In this thesis, different ruthenium-based photoactivatable complexes are reported and their properties were investigated for their suitability as PACT agents.

### 6.1.2 Investigation of intracellular behavior of metal complexes

A better understanding of the biological activity of the metal-based anticancer compound allows for improving drug design and tuning drug interaction with its cellular targets. To gather knowledge about the interaction of the complex with biomolecules, many different techniques can be utilized. The interaction of the complex with isolated biomolecules can be studied by *e.g.* mass spectrometry, UV-vis spectroscopy, or X-ray diffraction, and proteomic studies help to understand the effect of a drug on the protein expression within cells. To obtain a complete picture of the effect of the drug on a cell, results of different techniques need to be combined and new methods need to be developed to study the compound under physiologically relevant conditions. In this thesis, the intracellular distribution of a ruthenium-based PACT agent was investigated by fluorophore labeling of the complex in cells *via* copper-catalyzed azide-alkyne cycloaddition (CuAAC).

### 6.1.3 Alkyne functionalization of photoactivatable ruthenium complex

To attach a reporter tag such as a fluorophore *via* CuAAC to the ruthenium-based PACT agent, it is necessary to functionalize the complex with a click handle. Here, we decided to choose for a minimal handle, *i.e.* a simple alkyne group (Figure 6.1). To date, reaction procedures for the synthesis of alkyne-functionalized ruthenium complexes proceed with low yield due to side reactions in presence of the ruthenium center, or they require silver ions. However, even small traces of the heavy metal are toxic to living cells. Thus, the use of silver ions should be avoided when synthesizing complexes that are intended for therapeutic applications. We developed a new synthetic route to synthesize such alkyne-functionalized complexes as described in **Chapter 2**. Thereby, we optimized the alkyne-protecting group, found that *tert*-butyldimethylsilyl (TBDMS) is strong enough to cope with the metalation and ligand exchange conditions, and on the other hand is easy to remove using fluoride, *i.e.* without involving silver ions.

### 6.1.4 Improved ruthenium-based PACT agents

PACT is an oxygen-independent way of releasing a toxic species in a light-triggered manner, in order to fight cancer. Ruthenium-based anticancer compounds suitable as PACT agents have to be stable in the dark, activated by light, and show cytotoxic behavior after light activation.  $[\text{Ru}(\text{tpy})(\text{bpy})(\text{Hmte})](\text{PF}_6)_2$  is known to be photoactivatable, but this complex is weakly taken up by cells, so that the photoproduct is non-toxic. In **Chapter 3**, we report the development of new ruthenium complexes with improved cellular uptake by increasing the lipophilicity of the complex, which was obtained by increasing the aromatic surface of the bidentate ligand. Higher cellular uptake resulted in increased cytotoxicity after light activation, while complexes are still stable in the dark. Furthermore, addition of a non-coordinating amine bridge to the bidentate ligand led to a ruthenium complex with improved photosubstitution quantum yield, therefore demonstrating that ligand alteration can be used for fine-tuning the properties of ruthenium complexes and develop compounds with better PACT properties.

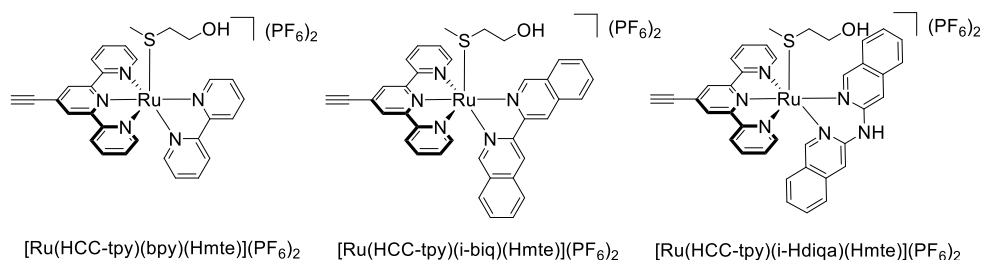


**Figure 6.1.** Chemical structures of the complexes described in this thesis.

### 6.1.5 Effect of click handle on complex properties

The purpose of an alkyne handle is the labeling of the complex with a reporter tag for visualization or isolation of the complexes in intracellular environment. To use such alkyne-functionalized complexes to study the original, non-functionalized complex, the photophysical and biological properties of the functionalized and non-functionalized complexes need to be compared with each other (**Chapter 2 and 4**). Comparison of crystal structures, photosubstitution quantum yields, singlet oxygen generation, cell uptake, and cytotoxicity revealed that the alkyne click handle has no significant effect on the complex geometry or its light activation, and all complexes remain very poor PDT agents due to their low singlet oxygen production. On the other hand, the alkyne does increase the cellular uptake of the complex: the concentrations of ruthenium in the cells was doubled after alkyne functionalization. Nevertheless, alkyne functionalization offers a great opportunity to label the complex *via* CuAAC with minimal effect on the photochemical and biological activity of the complexes.

### 6.1.6 Visualization of non-emissive PACT agents

Usually PACT agents are non-emissive due to the quenching by the thermally generated  $^3\text{MC}$  state. Therefore, monitoring the complex in the cell by microscopy is not possible, and a fluorophore moiety is necessary to visualize the complex. The alkyne functionalization allows for the attachment of a fluorophore moiety by CuAAC reaction on the ruthenium complex. By doing so, we were able to visualize the complex after binding to model protein BSA (**Chapter 2**). Only after light activation, the complex releases its protecting ligand, resulting in a free coordination site with which it can interact with the protein. If kept inactivated in the dark, no fluorescent signal was visible. Noteworthy, the interaction could not be detected by traditional techniques such as mass spectrometry or UV-vis spectroscopy, which are suitable for the detection of covalent interactions. This indicates that the interaction is rather weak and disrupted in the latter mentioned techniques, while fluorophore

labeling in combination with gel electrophoresis is soft enough to preserve the weak metallodrug-protein interaction.

From studying the interaction of the ruthenium complexes with isolated proteins as described in Chapter 2, we moved to the use of mammalian cancer cells (**Chapter 4**). The labeling of the complex was again achieved *via* CuAAC chemistry, performed inside fixed cells. This method allowed for the preservation of the biological activity of the alkyne-functionalized complex: their uptake, distribution, and interaction within the cells resembles as much as possible that of the non-functionalized drug. A fluorescent signal was observed after attachment of the fluorophore moiety, but only for the light-activated species that can interact with a target and are therefore not washed away. Here again, this experiment is a proof for the light-controlled interaction of the complex with proteins. The results show that the complexes did not enter the nucleus. In contrast, the complexes stayed outside the nucleus in the perinuclear region. Co-staining of the cellular compartments outside the nucleus revealed that the complexes are not located in the lysosomes or in the endoplasmic reticulum. The fluorescent distribution and pattern suggest that the complexes localize in the Golgi apparatus after 24 h after activation.

#### **6.1.7 Universal application of click handle method**

In **Chapter 5**, alkyne functionalization was described for three other polypyridyl ruthenium complexes. The synthesis is challenging since the alkyne handle can react with a ruthenium center that has free coordination sites, even in presence of a TBDMS protecting group. Working with two free coordination sites and alkyne handles increases the amount of possible byproducts. In general, side reactions occur if the reaction conditions are not adapted. Fine-tuning the reaction conditions is time consuming and not straightforward, but it is usually possible. Therefore, the method of post-treatment labeling can also be applied to other complexes.

## **6.2 Discussion**

### **6.2.1 Azide *vs.* alkyne: functionalization of ligands and complexes**

The initial idea was to functionalize ruthenium complexes with the smallest handle possible, to keep the structure and properties of the drug derivative as similar as possible to that of the original ruthenium complex. Suitable candidates for such handles are azide ( $N_3$ ) and alkyne (CCH) click handles. The functionalization of polypyridyl ligands and the binding of these ligands to ruthenium, are well reported in literature.<sup>1,2</sup> An overview is given below.

Azide functionalization of polypyridyl ligands such as 2,2'-bipyridine (bpy) and 2,2':6',2''-terpyridine (tpy) are reported to be challenging (Table 6.1). Starting from dibromo,<sup>3</sup> diamino,<sup>3</sup> or diazido dioxide precursor<sup>4</sup> (Figure 6.2), functionalization of the bpy ligand resulted in the formation of the desired diazido compound, however, in low yields and sometimes as a mixture of mono-functionalized products. The best result was obtained using 4,4'-dinitro-bpy and sodium azide (95% yield).<sup>5</sup> For the tpy ligand, the desired azide-functionalized tpy ligand was obtained with a yield of 75% when using the 4'-nitroterpyridine precursor.<sup>6</sup> Noteworthy, thermal lability of the azide-functionalized ligands is frequently reported. Extension of reaction time or increase of reaction temperature led to the decomposition of the azide.<sup>3</sup> This instability is also put forward to explain the unsuccessful CuAAC reaction on the azide-functionalized bpy ligand.<sup>3</sup> So far, only the group of Elliott succeeded in this reaction.<sup>5</sup>

Alkyne functionalization of polypyridyl ligands has been reported more frequently, usually starting from a bromide precursor (Table 6.1). The synthesis typically proceeds using a protected alkyne intermediate to prevent the formation of side products by reaction of the alkyne with metal centers present in the catalytic reaction mixture. For the bpy ligand, the terminal alkyne is protected by a trimethylsilyl (TMS) group that can be easily removed with a base. The reactions always proceed in good yields.<sup>3,7,8</sup> For terpyridine, yields of 87% were reported for the reaction with a TMS protecting group,<sup>9</sup> while using the stronger triisopropylsilyl (TIPS) protecting group the ligand was obtained in 93% yield.<sup>10</sup> While the CuAAC reaction was difficult on the azide, the reaction on the alkyne proceeded without any problems.<sup>3</sup>

4

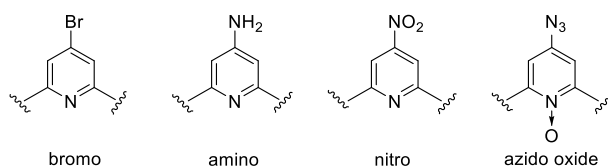


**Figure 6.2.** Possible starting materials for the functionalization of polypyridyl ligands.

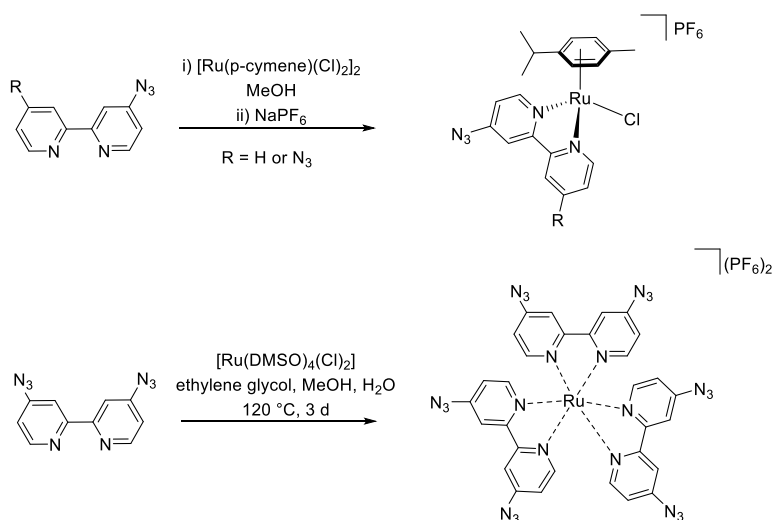


**Table 6.1.** Ligand functionalization reported in literature.

handle	ligand	Starting material	conditions	yield	Ref.
azide	bpy	bromo	NaN <sub>3</sub> , DMF, 100 °C, 18 h	27%	3
		amino	NaNO <sub>2</sub> , HCl, NaN <sub>3</sub>	20%	3
		azido oxide	PCl <sub>3</sub> , ACN, reflux, 4 h	n.s. <sup>a)</sup>	4
		nitro	NaN <sub>3</sub> , DMF, 100 °C, 3h	95%	5
	tpy	nitro	NaN <sub>3</sub> , DMF, 100 °C, 3 h	75%	6
alkyne	bpy	bromo	Me <sub>3</sub> SiCCH, CuI, Pd(PPh <sub>3</sub> ) <sub>2</sub> Cl <sub>2</sub> , K <sub>2</sub> CO <sub>3</sub>	86%	3
			Me <sub>3</sub> SiCCH, CuI, Pd(PPh <sub>3</sub> ) <sub>2</sub> Cl <sub>2</sub> , THF, MeOH, NaOH, r.t., 2 h	78%	
		bromo	Me <sub>3</sub> SiCCH, CuI, Pd(PPh <sub>3</sub> ) <sub>2</sub> Cl <sub>2</sub> , THF, MeOH, NaOH, r.t., 2 h	63%	7
			Me <sub>3</sub> SiCCH, CuI, Pd(PPh <sub>3</sub> ) <sub>2</sub> Cl <sub>2</sub> , MeOH, K <sub>2</sub> CO <sub>3</sub>	91%	
	tpy	bromo	Me <sub>3</sub> SiCCH, CuI, Pd(PPh <sub>3</sub> ) <sub>2</sub> Cl <sub>2</sub> , THF, MeOH, K <sub>2</sub> CO <sub>3</sub>	98%	8
			Me <sub>3</sub> SiCCH, CuI, Pd(PPh <sub>3</sub> ) <sub>2</sub> Cl <sub>2</sub> , THF, MeOH, KF	68%	
	bromo	TIPS-SiCCH, CuI, Pd(PPh <sub>3</sub> ) <sub>2</sub> Cl <sub>2</sub> ,	87%	9	
	bromo	TIPS-SiCCH, CuI, Pd(PPh <sub>3</sub> ) <sub>2</sub> Cl <sub>2</sub> ,	87%		
	bromo	TIPS-SiCCH, CuI, Pd(PPh <sub>3</sub> ) <sub>2</sub> Cl <sub>2</sub> ,	93%	10	

<sup>a)</sup> n.s. = not specified

With the functionalized ligands at hands, coordination to ruthenium can be undertaken. In literature, only a few examples have been reported in which coordination of the azide-functionalized ligand to a ruthenium precursor complex was successful (Table 6.2). Elliott and co-workers reported the successful complexation of a mono-azido bpy ligand at room temperature.<sup>5</sup> Chitre *et al.* reported a ruthenium(II) complex with three diazido-bpy ligands, but no experimental details are reported for the synthesis of the complex (Scheme 6.1).<sup>4</sup> Noteworthy, in general the synthesis of ruthenium complexes with azide-functionalized ligands is described as challenging and often unsuccessful.<sup>4, 8</sup> The higher the number of azide-substituents is, the more difficult the coordination to a ruthenium center seems to be, due to the instability of the ligand. In addition, the desired azide-functionalized complex is often reported to be unstable. A report of Aukauloo and co-workers, for example, stated: “*However, Ru-N<sub>3</sub> ([Ru(bpy)<sub>2</sub>(4-azido-bpy)]<sup>2+</sup>) proved to be very unstable towards light, as well as under reductive and oxidative conditions, and could neither be fully characterized nor successfully engaged into click chemistry reactions*”.<sup>8</sup> Coordination of the azide-functionalized tpy ligand was reported to be possible when working with a ruthenium(II) precursor, however, the exact reaction conditions or the yield of the reaction were not reported.<sup>11</sup>



**Scheme 6.1.** Coordination of azide-functionalized bipyridyl ligands to ruthenium precursors.<sup>4, 5</sup>

The coordination of alkyne-functionalized polypyridyl ligands to ruthenium centers afforded higher yields than with the azide equivalents. Some research groups succeeded in the coordination of the ligand without any protection of the alkyne group,<sup>4, 8</sup> while Rau and co-workers showed that the absence of protecting groups leads to the formation of side products due to the coordination of the alkyne triple bond and the ruthenium center.<sup>12</sup> Click reaction on the functionalized complexes was successfully demonstrated many times.<sup>8, 10</sup> Overall, from a synthetic point of view, the functionalization of polypyridyl ligands and ruthenium complexes is more efficient with alkyne than with azide substituents. The alkyne-functionalized ligands and complexes are obtained in higher yields and the products are more stable and therefore, easier to handle in subsequent steps such as CuAAC reactions. The use of alkynes, however, requires working with an alkyne-protecting group.

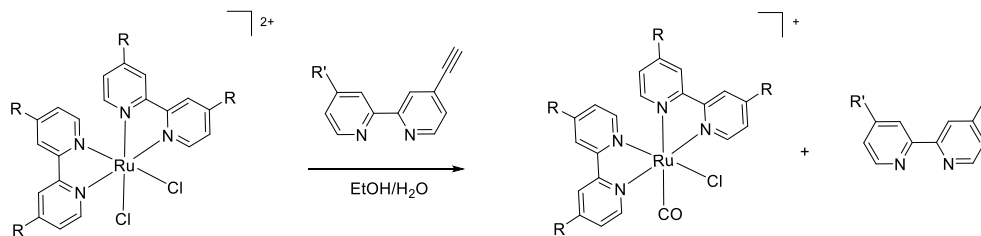
**Table 6.2.** Complex synthesis with azide- or alkyne-functionalized ligands reported in literature.

handle	ligand	Starting material	conditions	yield	Ref.
azide	bpy	[Ru(DMSO) <sub>4</sub> (Cl) <sub>2</sub> ]	Ethylene glycol, MeOH, 120 °C, 3 d	n.s. <sup>a)</sup>	4
		[Ru( <i>p</i> -cymene)(Cl) <sub>2</sub> ] <sub>2</sub>	MeOH, r.t., 12 h	66%	5
		[Ru(bpy) <sub>2</sub> (Cl) <sub>2</sub> ]	AgNO <sub>3</sub> , MeOH	-	8
	tpy	[Ru(tpy-Cl)(Cl) <sub>3</sub> ]	MeOH, 64 °C, 2 h	-	6
		[Ru(Cl-tpy)(MeCN)(Cl) <sub>2</sub> ] <sup>2+</sup>	MeOH	n.s. <sup>a)</sup>	11
alkyne	bpy	[Ru(DMSO) <sub>4</sub> (Cl) <sub>2</sub> ]	Ethylene glycol, MeOH, 120 °C, 3 d	n.s. <sup>a)</sup>	4
		[Ru(bpy) <sub>2</sub> (Cl) <sub>2</sub> ]	AgNO <sub>3</sub> , MeOH	91%	8
		[Ru(R-bpy) <sub>2</sub> (Cl) <sub>2</sub> ]	EtOH/H <sub>2</sub> O, reflux, 3 h	20%	12
	[Ru(bpy) <sub>2</sub> (Cl) <sub>2</sub> ]	Bis-substituted	EtOH/H <sub>2</sub> O, reflux, 3 h	50%	12
		mono-substituted			
tpy	[Ru(DMSO) <sub>4</sub> (Cl) <sub>2</sub> ]	DCE, 10 h	88%	10	

<sup>a)</sup> n.s. = not specified

As mentioned above and described in Chapters 2 and 5, use of a non-protected terminal alkyne may result in a lower yield due to the formation of side products. The metal center, here ruthenium, can act as a catalyst for the reaction of the click handle with alcohols, such as ethanol.<sup>13</sup> Moreover, the formed enol ester is also difficult to remove from the reaction mixture and isolation of the pure desired complex is challenging. In addition, Rau and co-workers reported that alkyne and ruthenium can react directly with each other, resulting in the formation of the methyl-substituted polypyridyl ligand and a complex containing carbon monoxide, if two coordination sites are free on the metal center (Scheme 6.2).<sup>12</sup> Protecting groups at the alkyne functionality preventing these reactions are usually silyl-based. An overview of different protecting groups and their deprotection strategies have been summarized by Greene.<sup>14</sup> The most common groups are trimethylsilyl (TMS), *tert*-butyldimethylsilyl (TBDMS), and triisopropylsilyl (TIPS) (Figure 6.3). The bulkier the group, the better the protection of the acidic acetylenic hydrogen. The TMS group is frequently used for the protection of the alkyne on polypyridyl ligands (Table 6.1), but in our hands, the protection was too weak and uncontrolled deprotection took place during metal coordination. The TIPS group is one of the strongest alkyne protecting groups, and deprotection was reported to be rather difficult by the group of Stahl.<sup>10</sup> Thus, we investigated the use of the TBDMS protecting group. It is more stable than the TMS group, but sensitive to many reaction conditions. Adaption of the reaction conditions appeared to be necessary in order to retain the group on the alkyne functionality. Other possible groups are

benzyltrimethylsilyl or biphenyldimethylsilyl (Figure 6.3), but these are not commercially available as their propargyl bromides.



**Scheme 6.3.** Reaction between ruthenium(II) precursor and alkyne-functionalized bpy ligand in ethanol/water mixture leads to the decomposition of the alkyne, resulting in the methyl-substituted polypyridyl ligand and a complex containing carbon monoxide.<sup>12</sup>

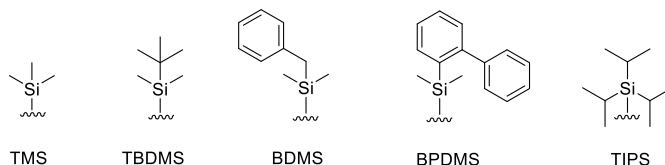


**Figure 6.3.** Chemical structures of common protecting groups for alkynes.<sup>14</sup>

### 6.2.2 Azide vs. alkyne: biological application

When choosing a click handle for ruthenium complexes, several aspects of biological applications need to be considered. Alkynes and azides are regarded to be inert under physiological conditions. However, Ovaa and co-workers reported the reaction of an alkyne with an active site cysteine in proteases.<sup>15</sup> Noteworthy, the reaction only took place with alkynes attached to the substrate protein of the target protease. Thiols and cysteine residues of other proteins were not affected. In addition, working with alkyne-functionalized ruthenium complexes restricts the application in living systems since the reaction with the corresponding azides requires a catalytic amount of Cu(I) which is cytotoxic due to generation of reactive oxygen species (ROS).<sup>16</sup> Nevertheless, there are reports of CuAAC reactions on the surface of living cells after optimization of the reaction conditions.<sup>17-19</sup> For example, use of chelating ligands allows for lower Cu(I) concentrations, which decreases the cytotoxicity. Cai and co-workers also tested different chelating ligands to perform CuAAC in mammalian cancer cells.<sup>19</sup> They demonstrated that CuAAC is possible in the cytosol of cells, unfortunately with a yield of only 0.8%. They explain the low yield with the deactivation of the catalytic amount of copper due to the presence of copper-binding ligands. Furthermore, the yield of the CuAAC reaction also depends

on the reagent concentrations present in the cell, which are limited by their cellular uptake. On the other hand, azide-functionalized complexes allow for the labeling of living systems using Cu-free reactions such as the strain promoted azide-alkyne cycloaddition (SPAAC) or Staudinger ligation.<sup>20</sup> These reactions do not require copper and are therefore suitable for *in vivo* experiments.<sup>21</sup> A comparison of the non-catalyzed reactions was published by Bertozzi.<sup>22</sup> They showed that SPAAC and Staudinger ligation are not as efficient as CuAAC, but that labeling on cell surfaces and inside cells is successful. An important drawback of SPAAC is the non-selective reaction of the strained alkyne such as cyclooctyne with cysteine residues. This causes a decrease in complex labeling efficiency and increase in background fluorescence.<sup>23</sup> In addition, attention has to be paid when working with alkyne functional groups (in particular when working with alkyne-fluorophores) since alkyne/copper complexation might affect the localization of the species and cause false fluorescent labeling.<sup>24</sup>

In recent years, interest grew on performing CuAAC also on ruthenium complexes for easy modulation of the complexes.<sup>2</sup> To the best of our knowledge, examples of CuAAC involving ruthenium complexes in cells are not reported yet. DeRose and co-workers compared the labelling efficiency of CuAAC reaction in fixed cells for their platinum-based complexes, either functionalized with an azide or alkyne.<sup>25</sup> The functionalization was reported to have no effect on the localization of the complexes, however, the resulting fluorescent signal from the azide-functionalized complex was more intense than with the alkyne-functionalized complex. Overall, azide as well as alkyne functionalization is suited for the use in fixed cells, while azides are easier to apply in living cells. In both cases, the limitations and drawbacks are known and should be considered when choosing one handle over the other.

### **6.2.3 Fluorescent labeling in comparison with other techniques**

Compared to traditional fluorescent microscopy, in which fluorophore-derivatives of the drug were studied that might have different properties compared to the unlabeled drug, post-labeling allows in principle for preservation of the biological activity of the drug. In addition, in post-treatment labeling there is no drug-fluorophore processing which might lead to false fluorescent signals. Drawbacks of fluorescent microscopy are the high concentrations that are needed to obtain a signal. Here, drug concentrations were needed that are a 5-fold higher than the EC<sub>50</sub> values and thus rather toxic to the cells. The complex distribution and processing in stressed cells might be different, and therefore the concentrations used

during imaging may not represent the situation in treated cells. Sample preparation requires time (here more than 24 h) and photo bleaching can cause loss of the signal. The signal-to-noise ratio depends on the background fluorescence and the accessibility of the complex for labeling and therefore efficiency of the CuAAC reaction. Overall, post-treatment fluorescent labeling is a method that can easily be applied in every lab, with moderate to good sensitivity and resolution.

Laser ablation inductively coupled plasma mass spectrometry (LA ICP MS) is a microanalytical methodology characterized by a very high sensitivity ( $0.01 \mu\text{g} / \text{g}$ ).<sup>26</sup> A laser beam generates fine particles on the surface of the sample. These small particles are directed into the ICP MS machine by a carrier gas. After ionization, the molecules are analyzed by the mass spectrometer detector. No sample preparation is required and the results are obtained quickly (within seconds). However, the resolution is moderate ( $12 - 20 \mu\text{m}$ ).<sup>26, 28</sup> Therefore, LA ICP MS is not suited for subcellular imaging but an excellent choice for sample analysis of 2D gels.

Energy dispersive X-ray analysis (EDX) is an elemental analysis technique in which an electron beam is used to create an electron vacancy in the sample. This vacancy is quickly filled with an electron of a higher energy shell. This process is accompanied by X-ray radiation that is specific for each element. In this way, the elemental composition of the sample can be identified.<sup>29</sup> The sensitivity of the method is moderate due to electron scattering but the resolution is high, enabling the imaging of subcellular compartments at nanometer (nm) range resolution.<sup>29</sup> EDX measurements were attempted for our samples in collaboration with Jeroen Kuipers and Dr. Ben Giepmans of the department of Cell Biology at the University Medical Center in Groningen for the ruthenium complexes reported in Chapter 4 to compare the results with those obtained by confocal microscopy imaging. Unfortunately, signals corresponding to ruthenium were not found. This might be due either to the strong overlapping of the EDX signals of ruthenium and that of the chloride ion, which is abundant in cells, or to the fact that the ruthenium complexes might be washed out of the cells during EDX sample preparation steps, which are time consuming (several days).

Stimulated Raman scattering (SRS) microscopy is another intracellular imaging technique based on molecular vibrations.<sup>30, 31</sup> Alkynes produce Raman signals within the cell-silent region ( $1800 - 2800 \text{ cm}^{-1}$ ),<sup>32</sup> and large Raman scattering cross sections allow for strong signals even at low concentrations. It is a non-invasive method and

therefore the only technique described here that allows for imaging in live cells.<sup>33</sup> Whether SRS can be used depends on the intracellular ruthenium concentration.

Overall, post-treatment fluorescence microscopy (PT-FL) is neither very sensitive nor yielding high resolution, but LA ICP MS also does not provide better resolution for cell mapping and EDX on ruthenium complexes is not well established and did not allow us to obtain clear results (Table 6.3). Noteworthy, the alkyne-functionalized complexes can be used for all four imaging techniques.

**Table 6.3.** Overview of techniques and their properties

Technique	Sensitivity	Resolution	Sample preparation	Destructive
PT-FL	$\mu\text{M}$	$\mu\text{m}$	moderate	yes
LA ICP MS	nM	$\mu\text{m}$	easy	yes
EDX	$\mu\text{M}$	nm	challenging	yes
SRS	$\mu\text{M}$	$\mu\text{m}$	easy	no

## 6.3 General conclusion

In this thesis successful development is described of a new synthetic route for the alkyne functionalization of ruthenium-based complexes that allows for fluorophore labeling. The alkyne functionalization only marginally influences the properties of the ruthenium complex, therefore the alkyne-functionalized compound is a suitable model for the non-functionalized compound, with comparable biological activity. Alkyne functionalization is a powerful method to study weak interactions between ruthenium complex and isolated biomolecules. In addition, post-treatment labeling in fixed mammalian cancer cells was successful. It provided clear evidence that the complexes do not enter the nucleus and that DNA is not the main target of these compounds. Therefore, their mode of action is different from that of cisplatin, and proteins have to be considered as potential binding partners.

In order to obtain a better understanding of the complex behavior and its mode of action *in cellulo*, a combination of analytical methods has to be applied, as one technique only does not offer enough information to draw a complete picture of the localization of a compound and its mode of action. The use of different techniques that reveal different properties (oxidation state, thermal or photochemical stability, interaction with biomolecules under different conditions) may provide information on different levels (molecular, proteomic, etc.). Despite the difficulties during the

synthesis of the alkyne-functionalized ruthenium complexes, they offer a new, inexpensive way to obtain insight in the complex distribution in cells.

## 6.4 Outlook

The complexes synthesized in Chapter 3 are intended to be PACT agents, which work independently of cellular dioxygen levels. So far, the cytotoxicity of the complexes was tested under normoxic conditions (21% O<sub>2</sub>). To confirm the PACT character of the ruthenium compounds, cytotoxicity assays under hypoxic conditions (1% O<sub>2</sub>) in tumor spheroids have to be undertaken. Imaging of the PACT agent derivatives 24 h after light activation revealed the localization of the complexes outside the nucleus in the cytosol. To confirm the hypothesized accumulation in the Golgi apparatus, additional co-staining experiments are required. In addition, time-lapse experiments would give insights in the intracellular distribution of the complexes over time. This would allow for differentiation between localization of the molecular target of the drug, and simple visualization of how its trafficking is organized within the cell. In order to be able to perform drug labeling in living cells, it would be necessary to change the alkyne handle into an azide handle. However, since azide functional groups in the 4'-position of the tpy ligand are not stable, a non-conjugated spacer between the tpy and azide moieties is required. Consequently, the design and synthesis of the functionalized complex needs to be substantially revised. The shortest spacer possible, a simple CH<sub>2</sub> group may allow to mimic the original complex as much as possible. Examples of such complexes are reported by Guillo *et al.*<sup>34</sup> and Kroll *et al.*<sup>35</sup> (Figure 6.3). On the other hand, if the spacer needs to be expanded anyway, a flexible longer spacer can be chosen as well, which may ensure accessibility of the click handle for the CuAAC or SPAAC reaction after interaction of the drug with its target. For example, Wirth *et al.* showed that fluorescent labeling is more efficient for complexes with a linker than without.<sup>25</sup> Chemical and biological properties of the new derivatives would need to be investigated to guarantee the preservation of the properties of the original drug. Thus, the balance between preserving the drug biological properties and its efficient labeling requires more research.



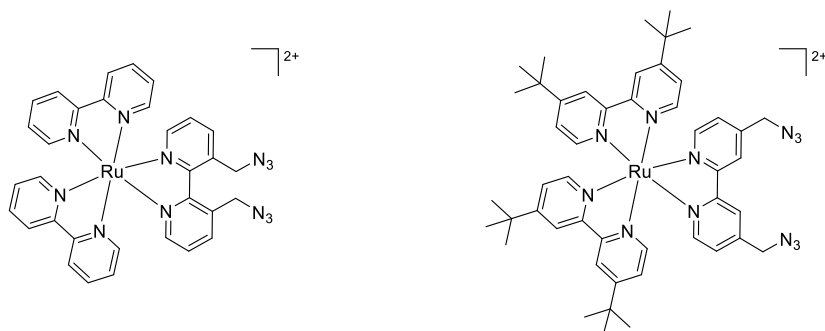
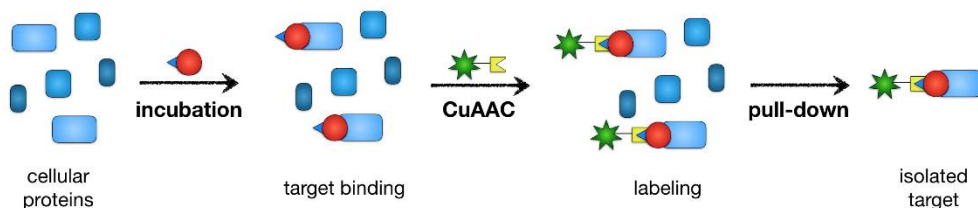


**Figure 6.3.** CH<sub>2</sub> spacer enables synthesis of stable azide-functionalized ruthenium complexes.<sup>34, 35</sup>

Meanwhile, the alkyne-functionalized ruthenium complexes at hand can be implemented in pull-down experiments to isolate and identify possible targets (Scheme 6.3). This would be the first example of pull-down experiments of ruthenium complexes after drug incubation in mammalian cancer cells. Different types of enrichment methods (separation by 2D gel, beads, or affinity column) can be considered and compared.<sup>36-38</sup> The obtained information can increase our understanding of the mode of action of these photoactivatable ruthenium complexes.



**Scheme 6.3.** Schematic representation of pull-down experiment using an alkyne-functionalized ruthenium complex.

## 6.5 References

- 1 R. Ziessel, J. Suffert, and M.-T. Youinou, *J. Org. Chem.* **1996**, 61 (19), 6535-6546.
- 2 N. Zabarska, A. Stumper, and S. Rau, *Dalton Trans.* **2016**, 45 (6), 2338-2351.
- 3 P. Fabbrizzi, B. Cecconi, and S. Cicchi, *Synlett* **2011**, 2011 (02), 223-226.
- 4 K. P. Chitre, E. Guillén, A. S. Yoon, and E. Galoppini, *Eur. J. Inorg. Chem.* **2012**, 2012 (33), 5461-5464.
- 5 B. S. Uppal, A. Zahid, and P. I. P. Elliott, *Eur. J. Inorg. Chem.* **2013**, 2013 (14), 2571-2579.
- 6 R.-A. Fallahpour, M. Neuburger, and M. Zehnder, *Synthesis* **1999**, (6), 1051-1055.
- 7 P. V. James, K. Yoosaf, J. Kumar, K. G. Thomas, A. Listorti, G. Accorsi, and N. Armaroli, *Photochem. Photobiol. Sci.* **2009**, 8 (10), 1432-1440.

- 8 A. Baron, C. Herrero, A. Quaranta, M.-F. Charlot, W. Leibl, B. Vauzeilles, and A. Aukauloo, *Inorg. Chem.* **2012**, 51 (11), 5985-5987.
- 9 V. Grosshenny and R. Ziesel, *J. Organomet. Chem.* **1993**, 453 (2), C19-C22.
- 10 J. B. Gerken, M. L. Rigsby, R. E. Ruther, R. J. Pérez-Rodríguez, I. A. Guzei, R. J. Hamers, and S. S. Stahl, *Inorg. Chem.* **2013**, 52 (6), 2796-2798.
- 11 R.-A. Fallahpour, *Synthesis* **2003**, 2003 (02), 0155-0184.
- 12 N. Zabarska, D. Sorsche, F. W. Heinemann, S. Glump, and S. Rau, *Eur. J. Inorg. Chem.* **2015**, 2015 (29), 4869-4877.
- 13 C. Ruppin and P. H. Dixneuf, *Tetrahedron Lett.* **1986**, 27 (52), 6323-6324.
- 14 P. G. M. Wuts and T. W. Greene, Protection for the Alkyne-CH in *Greene's Protective Groups in Organic Synthesis* **2007**, 927-933.
- 15 R. Ekkebus, S. I. van Kasteren, Y. Kulathu, A. Scholten, I. Berlin, P. P. Geurink, A. de Jong, S. Goerdalay, J. Neeffjes, A. J. R. Heck, D. Komander, and H. Ovaa, *J. Am. Chem. Soc.* **2013**, 135 (8), 2867-2870.
- 16 E. M. Sletten and C. R. Bertozzi, *Angew. Chem., Int. Ed.* **2009**, 48 (38), 6974-6998.
- 17 V. Hong, N. F. Steinmetz, M. Manchester, and M. G. Finn, *Bioconjugate Chem.* **2010**, 21 (10), 1912-1916.
- 18 D. Soriano del Amo, W. Wang, H. Jiang, C. Besanceney, A. C. Yan, M. Levy, Y. Liu, F. L. Marlow, and P. Wu, *J. Am. Chem. Soc.* **2010**, 132 (47), 16893-16899.
- 19 S. Li, L. Wang, F. Yu, Z. Zhu, D. Shobaki, H. Chen, M. Wang, J. Wang, G. Qin, U. J. Erasquin, L. Ren, Y. Wang, and C. Cai, *Chem. Sci.* **2017**, 8 (3), 2107-2114.
- 20 N. J. Agard, J. A. Prescher, and C. R. Bertozzi, *J. Am. Chem. Soc.* **2004**, 126 (46), 15046-15047.
- 21 K. E. Beatty, J. D. Fisk, B. P. Smart, Y. Y. Lu, J. Szychowski, M. J. Hangauer, J. M. Baskin, C. R. Bertozzi, and D. A. Tirrell, *ChemBioChem* **2010**, 11 (15), 2092-2095.
- 22 N. J. Agard, J. M. Baskin, J. A. Prescher, A. Lo, and C. R. Bertozzi, *ACS Chem. Biol.* **2006**, 1 (10), 644-648.
- 23 R. van Geel, G. J. M. Pruijn, F. L. van Delft, and W. C. Boelens, *Bioconjugate Chem.* **2012**, 23 (3), 392-398.
- 24 J. Lefebvre, C. Guetta, F. Poyer, F. Mahuteau-Betzer, and M.-P. Teulade-Fichou, *Angew. Chem., Int. Ed.* **2017**, 56 (38), 11365-11369.
- 25 R. Wirth, J. D. White, A. D. Moghaddam, A. L. Ginzburg, L. N. Zakharov, M. M. Haley, and V. J. DeRose, *J. Am. Chem. Soc.* **2015**, 137 (48), 15169-15175.
- 26 M. Ralle and S. Lutsenko, *BioMetals* **2009**, 22 (1), 197-205.
- 27 A. Sussulini, J. S. Becker, and J. S. Becker, *Mass Spectrom. Rev.* **2017**, 36 (1), 47-57.
- 28 B. Busser, S. Moncayo, J.-L. Coll, L. Sancey, and V. Motto-Ros, *Coord. Chem. Rev.* **2018**, 358 70-79.
- 29 N. M. Pirozzi, J. P. Hoogenboom, and B. N. G. Giepmans, *Histochem. Cell Biol.* **2018**, 150 (5), 509-520.
- 30 C. W. Freudiger, W. Min, B. G. Saar, S. Lu, G. R. Holtom, C. He, J. C. Tsai, J. X. Kang, and X. S. Xie, *Science* **2008**, 322 (5909), 1857-1861.
- 31 L. Wei, F. Hu, Y. Shen, Z. Chen, Y. Yu, C.-C. Lin, M. C. Wang, and W. Min, *Nat. Methods* **2014**, 11 410.
- 32 W. J. Tipping, M. Lee, A. Serrels, V. G. Brunton, and A. N. Hulme, *Chem. Sci.* **2017**, 8 (8), 5606-5615.
- 33 H. Yamakoshi, K. Dodo, A. Palonpon, J. Ando, K. Fujita, S. Kawata, and M. Sodeoka, *J. Am. Chem. Soc.* **2012**, 134 (51), 20681-20689.

- 34 P. Guillo, O. Hamelin, J. Pécaut, and S. Ménage, *Tetrahedron Lett.* **2013**, 54 (8), 840-842.
- 35 A. Kroll, K. Monczak, D. Sorsche, and S. Rau, *Eur. J. Inorg. Chem.* **2014**, 2014 (22), 3462-3466.
- 36 S. M. Meier, D. Kreutz, L. Winter, M. H. M. Klose, K. Cseh, T. Weiss, A. Bileck, B. Alte, J. C. Mader, S. Jana, A. Chatterjee, A. Bhattacharyya, M. Hejl, M. A. Jakupec, P. Heffeter, W. Berger, C. G. Hartinger, B. K. Keppler, G. Wiche, and C. Gerner, *Angew. Chem., Int. Ed.* **2017**, 56 (28), 8267-8271.
- 37 R. M. Cunningham and V. J. DeRose, *ACS Chem. Biol.* **2017**, 12 (11), 2737-2745.
- 38 L. M. Schiapparelli, D. B. McClatchy, H.-H. Liu, P. Sharma, J. R. Yates, and H. T. Cline, *J. Proteome Res.* **2014**, 13 (9), 3966-3978.



# APPENDIX I: GENERAL EXPERIMENTAL PROCEDURES

## AI.1 Photosubstitution quantum yield measurements

The photosubstitution quantum yield can be calculated in different ways, either *via* irradiation close to an isobestic point,<sup>1</sup> or *via* irradiation at a wavelength that is not an isobestic point provided the molar extinction coefficient of the photoreaction product is known.<sup>2</sup> In this work, both cases were not valid and therefore, the time-dependent evolution of the UV-vis spectra were fitted using the Glotaran software package.<sup>3</sup> The global fitted absorption spectra of the starting material and the photoproduct allow for the calculation of their molar absorption coefficients. The time evolution of the relative concentrations of the two species was also modelled. From the time evolution of the relative concentrations and the molar absorption coefficient of all species, the time evolution of  $n_R$  and  $n_P$ , as well as  $Q_{i,R}$ , the total number of mol of photons absorbed between  $t_0$  and  $t_i$  by the starting material, could be derived. The slope of the plot of  $n_R$  vs.  $Q_{i,R}$  gives the quantum yield of the reaction.

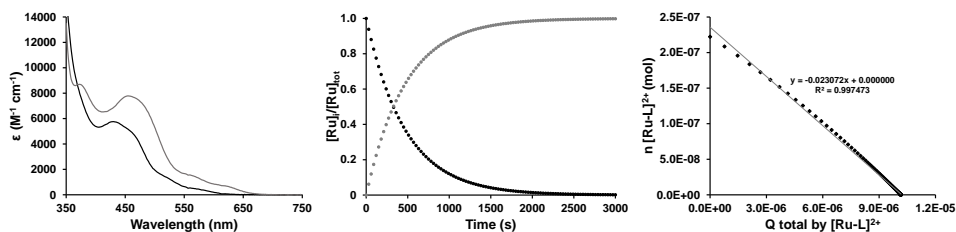


**Figure AI.1.** Example of the Glotaran global fitting of a one-step photosubstitution, here for the time evolution of the absorbance's of  $[Ru(HCC-tpy)(i-biq)(Hmte)](PF_6)_2$  in  $H_2O$  under air atmosphere. a) Globally fitted absorption spectra of the starting material  $[Ru(HCC-tpy)(i-biq)(Hmte)](PF_6)_2$  (black) and its aqua product  $[Ru(HCC-tpy)(i-biq)(OH_2)]^{2+}$  (grey). b) Modelled evolution of the relative concentration of  $[Ru(HCC-tpy)(i-biq)(Hmte)]^{2+}$  vs. irradiation time according to global fitting using Glotaran. c) Plot of the amount of  $[Ru(HCC-tpy)(i-biq)(Hmte)]^{2+}$  (mol) vs. total amount of photons absorbed by  $[Ru(HCC-tpy)(i-biq)(Hmte)]^{2+}$  (mol). The slope of the obtained line is the opposite of the quantum yield of the formation of the aqua complex. Conditions: 0.074 mM solution of  $[Ru(HCC-tpy)(i-biq)(Hmte)](PF_6)_2$  in  $H_2O$  irradiated at 298 K under air atmosphere using a 517 nm LED at  $5.43 \cdot 10^{-8} \text{ mol} \cdot \text{s}^{-1}$ .

## AI.2 Singlet Oxygen quantum yield measurement

The quantum yield of singlet oxygen generation was determined in a custom-built setup (shown in Figure I.2), in which both UV-vis absorption and infrared emission spectroscopy could be performed. All optical parts were connected with optical fibers from Avantes (Apeldoorn, The Netherlands), with a diameter of 200-600  $\mu\text{m}$ . For each measurement, 500  $\mu\text{L}$  of sample, consisting of the compound in deuterated methanol ( $A_{450} \leq 0.1$  for 4.0 mm pathlength), was placed in a stirred 104F-OS semi-micro fluorescence cuvette (Hellma Analytics, Müllheim, Germany) in a CUV-UV/VIS-TC temperature-controlled cuvette holder from Avantes. The sample was allowed to equilibrate at 293 K for 5 min. Emission spectroscopy

was performed with a 450 nm fiber-coupled laser (Laser system LRD-0450; Laserglow, Toronto, Canada), at 50 mW optical power (4 mm beam diameter;  $0.4 \text{ W} \cdot \text{cm}^{-2}$ ) at a  $90^\circ$  angle with respect to the spectrometer. The excitation power was measured using a S310C thermal sensor connected to a PM100USB power meter (Thorlabs, Dachau, Germany). Infrared emission spectra were measured from 1000 nm to 1400 nm using an Avantes NIR256-1.7TEC spectrometer. The infrared emission spectrum was acquired within 9 s, after which the laser was turned off directly. UV-vis absorption spectra before and after emission spectroscopy were measured using an Avalight-DHc halogen-deuterium lamp (Avantes) as light source (turned off during emission spectroscopy) and an Avantes 2048L StarLine UV-vis spectrometer as detector, both connected to the cuvette holder at a  $180^\circ$  angle. No difference in UV-vis absorption spectrum was found due to exposure to the blue laser, showing that the singlet oxygen emission is that of the starting compound. All spectra were recorded with Avasoft 8.5 software from Avantes and further processed with Microsoft Office Excel 2010 and Origin Pro 9.1 software.

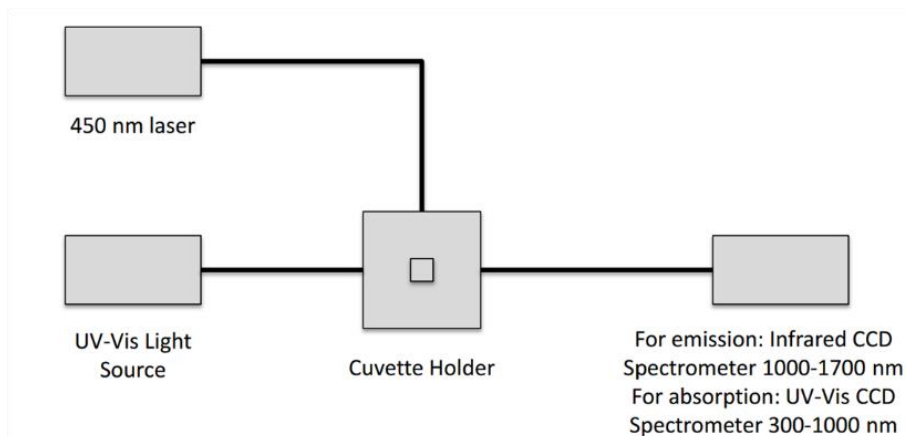


**Figure AI.2.** Setup for  $^1\text{O}_2$  quantum yield measurement.

The quantum yield of singlet oxygen production was calculated using the relative method with  $[\text{Ru}(\text{bpy})_3]\text{Cl}_2$  as the standard ( $\Phi_\Delta = 0.73$  in methanol- $\text{d}_4$ ),<sup>4</sup> according to:

$$\Phi_{\Delta,sam} = \Phi_{\Delta,std} \times \frac{A_{450,std}}{A_{450,sam}} \times \frac{E_{sam}}{E_{std}} \quad \text{Equation AI.1.}$$

where  $\Phi_\Delta$  is the quantum yield of singlet oxygen generation,  $A_{450}$  is the absorbance at 450 nm,  $E$  is the integrated emission peak of singlet oxygen at 1274 nm, and *sam* and *std* denote the sample and standard, respectively.

## AI.3 Cell culture and EC50 (photo)cytotoxicity studies

### Materials

Human cancer cell line A549 (human lung carcinoma) and A431 (human epidermoid carcinoma) were distributed by the European Collection of Cell Cultures (ECACC) and purchased from Sigma Aldrich. Dulbecco's Modified Eagle Medium (DMEM, without phenol red, without glutamine), Glutamine-S (GM; 200 mM), trichloroacetic acid (TCA), glacial acetic acid, sulforhodamine B (SRB), and tris(hydroxymethyl)aminomethane (Trisbase) were purchased from Sigma Aldrich. Fetal calf serum (FCS) was purchased from Hyclone. Penicillin and streptomycin were purchased from Duchefa and were diluted to a 100 mg/mL penicillin/streptomycin solution (P/S). Trypsin and OptiMEM (without phenol red) were purchased from Gibco Life Technologies. Trypan blue (0.4% in 0.81% sodium chloride and 0.06% potassium phosphate dibasic solution) was purchased from BioRad. Plastic disposable flasks and 96-well plates for cytotoxicity assays were purchased from Sarstedt. Cells were counted by using a BioRad TC10 automated cell counter with Biorad cell-counting slides. Cells were inspected with an Olympus IX81 microscope. UV-vis measurements for analysis of 96-well plates were performed with a M1000 Tecan Reader.

### Cell Culturing

Cells were cultured in Dulbecco's Modified Eagle Medium containing phenol red, supplemented with 9.0% v/v FCS, 0.2% v/v P/S and 0.9% v/v GM (called DMEM complete) and incubated at 37 °C at 7.0% CO<sub>2</sub> in 75 cm<sup>2</sup> T-flasks. Fresh cells were passaged at least twice after being thawed and splitted once a week at 80-90% confluency. Cells were cultured for a maximum of 8 weeks for all biological experiment.

### (Photo)cytotoxicity assays

For each photocytotoxicity experiment, a parallel control plate was prepared and treated identically, but without irradiation. A549 and A431 cells were seeded at  $t = 0$  in 96-well plates at a density of 5000 and 8000 cells/well (100  $\mu$ L), respectively in OptiMEM supplemented with 2.4% v/v FCS, 0.2% v/v P/S, and 1.0% v/v GM (called OptiMEM complete) and incubated for 24 h at 37 °C and 7.0% CO<sub>2</sub>. Only the inner 60 wells were used for seeding, the outer wells were kept cell free to prevent border effects during irradiation. At  $t = 24$  h, aliquots (100  $\mu$ L) of six different concentrations of freshly prepared stock solutions of the compounds in OptiMEM complete were added to the wells in triplicate (see plate design in Figure I.3) and incubated for 24 h. Sterilized dimethylsulfoxide (DMSO) was used to dissolve the compounds in such amounts that the maximum v/v% of DMSO per well did not exceed 0.5%. At  $t = 48$  h, the plates were irradiated with the cell-irradiation setup (520 nm, 30 min, 38 J/cm<sup>2</sup>) and the control plate was kept in the dark. After irradiation, all the plates were incubated in the dark until a total time of  $t = 96$  h after seeding. The cells were fixated by adding cold TCA (10% w/v; 100  $\mu$ L) in each well and the plates were stored at 4 °C for at least 4 h as part of the SRB assay that was adapted from Vichai *et al.*<sup>5</sup> In short, after fixation, the TCA medium mixture was removed from the wells, rinsed with demineralized water three times. Then, each well was stained with 100  $\mu$ L SRB (0.6% w/v in 1% v/v acetic acid) for 30 min, the SRB was removed by washing with acetic acid (1% v/v), and air dried. The SRB dye was solubilized with Tris base (10 mM; 200  $\mu$ L) overnight, and the absorbance in each well was read at  $\lambda = 510$  nm.

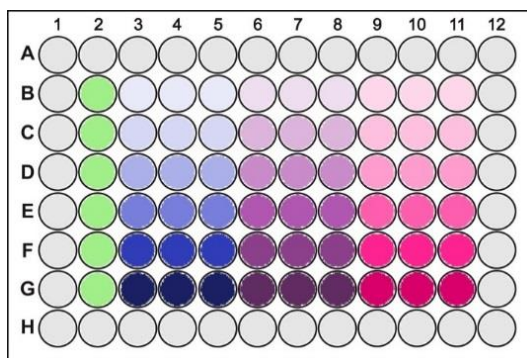


**Figure AI.3.** Design of a 96-well plate used in the (photo)cytotoxicity assays. Grey: Outer wells are not used for seeding to prevent border effects; green: non-treated cells ( $n_t = 6$ ); blue: cells treated with compound A; purple: cells treated with compound B; pink: cells treated with compound C. Each compound was added in six different concentrations (one per row) per triplicate ( $n_t = 3$ ).

The SRB absorbance data per compound per concentration was averaged over three identical wells (technical replicates,  $n_t = 3$ ) in Excel and was exported to GraphPad Prism. Relative cell populations were calculated by dividing the average absorbance of the treated wells by the average absorbance of the untreated wells. It was checked that the cell viability of the untreated cells of the samples irradiated were similar (maximum difference of 10%) to the non-irradiated samples to make sure no harm was done by light alone. The resulting dose-response curve for each compound under dark and irradiated conditions was fitted to a non-linear regression function with fixed  $y$  maximum (100%) and minimum (0%) (relative cell viability) and a variable Hill slope. The data of three independent biological replications was used to obtain the effective concentrations ( $EC_{50}$  in  $\mu\text{M}$ ). Photo indices (PI) were calculated, for each compound, by dividing the  $EC_{50}$  value obtained in the dark by the  $EC_{50}$  value determined under light irradiation.

## AI.4 Green light irradiation in the cell irradiation setup

### Cell-irradiation setup

The cell-irradiation system consisted of a Ditabis thermostat (980923001) fitted with two flat-bottomed micro-plate thermoblocks (800010600) and a 96-LED array fitted to a standard 96-well plate. The 520 nm LED (OVL-3324), fans (40 mm, 24 VDC, 9714839), and power supply (EA-PS 2042-06B) were obtained from Farnell. See Hopkins *et al.* for a full description.<sup>6</sup>

### Determination of irradiation times

To determine which light dose is necessary to fully activate the complexes during the cytotoxicity assay, the photochemical reactivity of the ruthenium-based complexes was tested. Therefore, the inner 60 wells of a 96-well plate were filled with OptiMEM complete (100  $\mu\text{L}$ , seeding without cells), and aliquots of the complexes (at their highest concentration used in the cytotoxicity assay, 250  $\mu\text{M}$ ) were added to the first column. The plate was irradiated for a certain amount of time, hereafter a new column was filled, and the plate was irradiated again. This process was repeated several times (irradiation times: 15, 15, 5, 5, and 5 min), and was finished with the last column filled but not irradiated. In this way, the columns were irradiated cumulative for a total time of 0, 5, 10, 15, 30, and 45 min, respectively. The absorbance of each well was measured (between 350 and 700 nm) by a M1000Tecan Reader, and corrected for the absorbance



of OptiMEM complete. The data was analyzed using Excel and the absorbance as function of time was plotted to check the time necessary for full activation (shown in Figure AIII.6).

## AI.5 Cellular uptake

Cell uptake studies for the ruthenium-based complexes were conducted on A549 cancer cells at 37 °C and 21% O<sub>2</sub>. Per compound,  $1.6 \cdot 10^6$  cells were seeded in 10 mL OptiMEM complete in a 75 cm<sup>2</sup> flask at t = 0 h. At t = 24 h, the media was aspirated and the cells were treated with solutions of the complexes in 12 mL OptiMEM complete at a concentration of 30 μM. Treatment at the same concentration for all complexes allows for comparison of the amount of ruthenium taken up by the cells. 30 μM correlates to the lowest EC<sub>50</sub> value of all complexes in the dark (EC<sub>50</sub> value of [Ru(HCC-tpy)(i-Hdiqa)(Hmte)](PF<sub>6</sub>)<sub>2</sub>). At t = 48 h, the medium was aspirated and the cells were washed twice with PBS (5 mL). The cells were trypsinized (2 mL, 5 min), suspended in OptiMEM complete (8 mL), and centrifuged (4 min, 1200 rpm). The supernatant was removed, the cells were resuspended in PBS (1 mL), and the cell count determined. The cells were centrifuged for a second time (4 min, 1200 rpm), the supernatant was aspirated, and the cell pellet stored at -80 °C.

For metal and protein quantification, the pellets were resuspended in demineralized water (200 μL) and lysed for 30 min by ultrasonication. The protein content of cell lysates was determined by the Bradford method. For the ruthenium measurements a contraAA 700 high-resolution continuum-source atomic absorption spectrometer (Analytik Jena AG) was used. All reagents were purchased from Sigma Aldrich. Stock solutions of the respective complexes in graded concentrations (solvent: DMSO) were used as standards and calibration was done in a matrix-matched manner. Meaning all samples and standards were adjusted to the same cellular protein concentration (1.0 mg cell protein per mL) by dilution (final DMSO concentration: 0.5 %). Triton X-100 (1%, 10 μL) as well as nitric acid (13%, 10 μL), were added to each standard sample (120 μL). Samples were injected (50 μL) into coated standard graphite tubes (Analytik Jena AG) and thermally processed as previously described by Schatzschneider *et al.*<sup>7</sup> Drying steps were adjusted and the atomization temperature set to 2400 °C. Ruthenium was quantified at a wavelength of 349.90 nm. The mean integrated absorbance of double injections was used throughout the measurements. The data of three independent biological replications was used to obtain the uptake values, calculated as nmol metal (ruthenium) per mg cell protein.

## AI.6 References

- 1 A. Bahreman, B. Limburg, M. A. Siegler, E. Bouwman, and S. Bonnet, *Inorg. Chem.* **2013**, 52 (16), 9456-69.
- 2 A. Bahreman, J.-A. Cuello-Garibo, and S. Bonnet, *Dalton Trans.* **2014**, 43 (11), 4494-4505.
- 3 J. Snellenburg, J., S. Laptienok, R. Seger, K. Mullen, M., and I. Van Stokkum, H.M., *J. Stat. Softw.* **2012**, 49 (3), 1-22.
- 4 D. Garcia-Fresnadillo, Y. Georgiadou, G. Orellana, A. M. Braun, and E. Oliveros, *Helv. Chim. Acta* **1996**, 79 (4), 1222-1238.
- 5 V. Vichai and K. Kirtikara, *Nat. Protoc.* **2006**, 1 (3), 1112-1116.
- 6 S. Hopkins, B. Siewert, S. Askes, P. Veldhuizen, R. Zwier, M. Heger, and S. Bonnet, *Photochem. Photobiol. Sci.* **2016**, 15 (5), 644-653.
- 7 U. Schatzschneider, J. Niesel, I. Ott, R. Gust, H. Alborzina, and S. Wölfl, *ChemMedChem* **2008**, 3 (7), 1104-1109.



# APPENDIX II: SUPPORTING INFORMATION FOR CHAPTER 2

## AII.1 $^1\text{H}$ NMR spectra

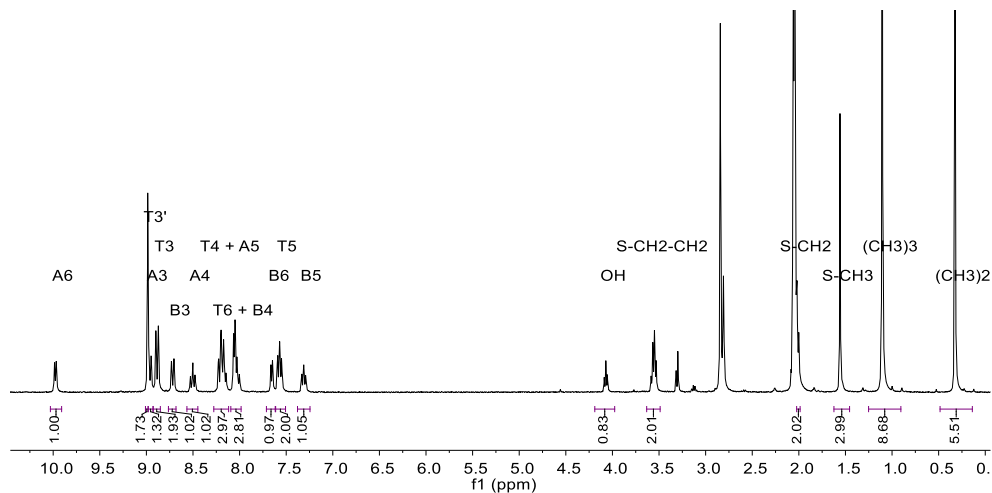


**Figure AII.1.**  $^1\text{H}$  NMR spectrum (region 10.5 – 0.0 ppm) of a solution of  $[5](\text{PF}_6)_2$  in acetone- $d_6$ .

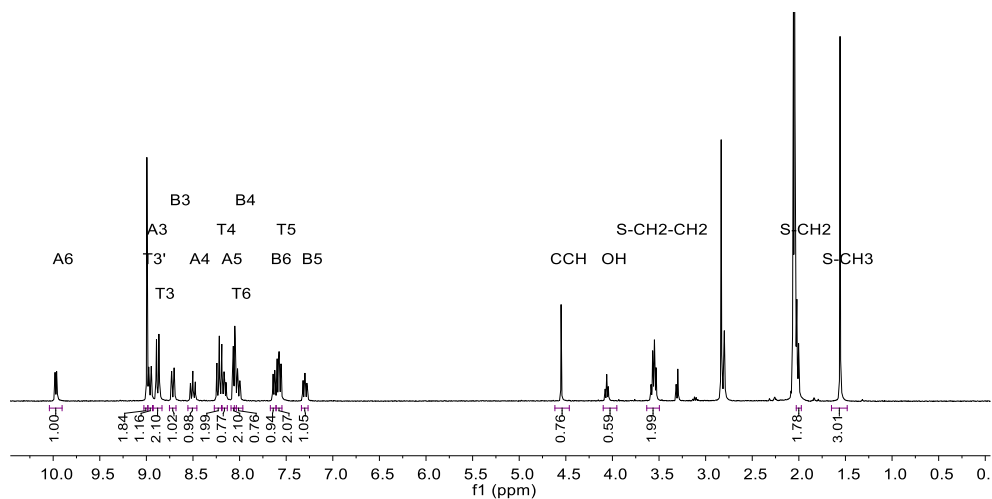
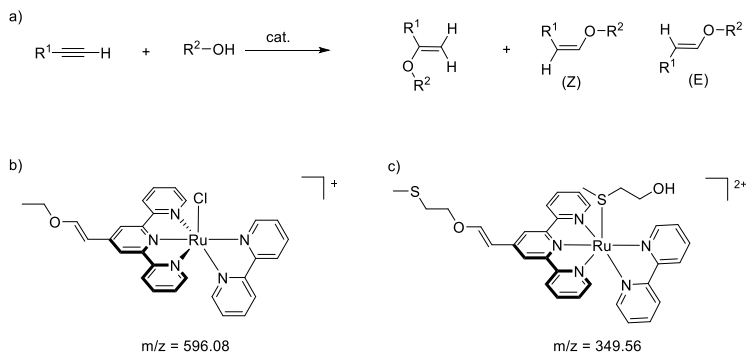


**Figure AII.2.**  $^1\text{H}$  NMR spectrum (region 10.5 – 0.0 ppm) of a solution of  $[2](\text{PF}_6)_2$  in acetone- $d_6$ .

## AII.2 Enol ester formation catalyzed by ruthenium



**Scheme AII.1.** a) General overview of reaction between terminal alkyne and alcohol, catalyzed by ruthenium, and possible products as described by Ruppin *et al.*<sup>1</sup> b) Byproduct observed by mass spectrometry during the coordination of bpy to  $[Ru(RCC-tpy)(Cl)_3]$  in ethanol/water (3:1) at reflux. TMS is not strong enough as protecting group for the terminal alkyne, allowing ethanol to react with the free alkyne generated in situ. The labile chloride ligand can easily be exchanged, creating a free coordination site on the ruthenium center. c) Byproduct during the exchange reaction of chloride for Hmte in water at 80 °C with an excess of Hmte present that can react with the free alkyne.

### AII.3 Dark stability

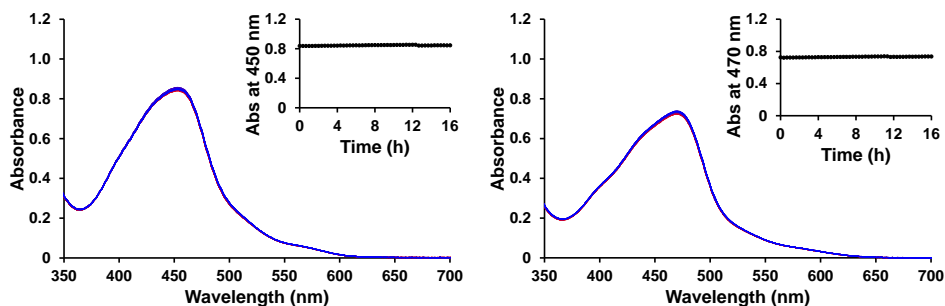


**Figure AII.3.** Evolution of the UV-vis spectra (region 350 – 700 nm) of a solution of [1](PF<sub>6</sub>)<sub>2</sub> (left) or [2](PF<sub>6</sub>)<sub>2</sub> (right) in water in the dark. Conditions: [Ru]<sub>0</sub> = 0.14 and 0.084 mM for [1](PF<sub>6</sub>)<sub>2</sub> and [2](PF<sub>6</sub>)<sub>2</sub>, respectively, t = 16 h, T = 37 °C, V = 3 mL, under air atmosphere. Inset: Time evolution of absorbance at wavelength 450 nm for [1](PF<sub>6</sub>)<sub>2</sub> and 470 nm for [2](PF<sub>6</sub>)<sub>2</sub>.

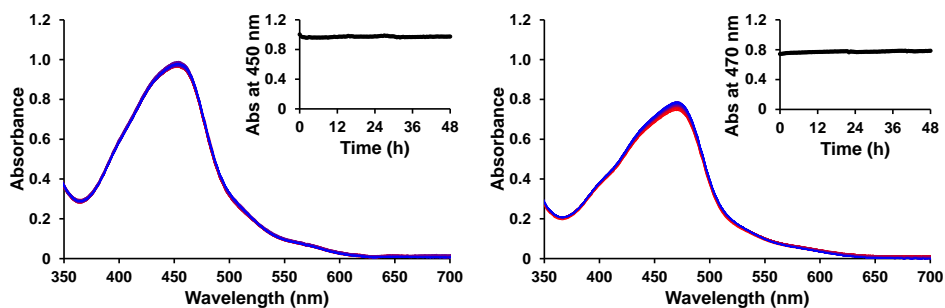


**Figure AII.4.** Evolution of the UV-vis spectra (region 350 – 700 nm) of a solution of [1](PF<sub>6</sub>)<sub>2</sub> (left) and [2](PF<sub>6</sub>)<sub>2</sub> (right) in PBS buffer in the dark. Conditions: [Ru]<sub>0</sub> = 0.15 and 0.089 mM for [1](PF<sub>6</sub>)<sub>2</sub> and [2](PF<sub>6</sub>)<sub>2</sub>, respectively, t = 48 h, T = 37 °C, V = 3 mL, under air atmosphere. Inset: Time evolution of absorbance at wavelength 450 nm for [1](PF<sub>6</sub>)<sub>2</sub> and 470 nm for [2](PF<sub>6</sub>)<sub>2</sub>.

## AII.4 MS after green light activation

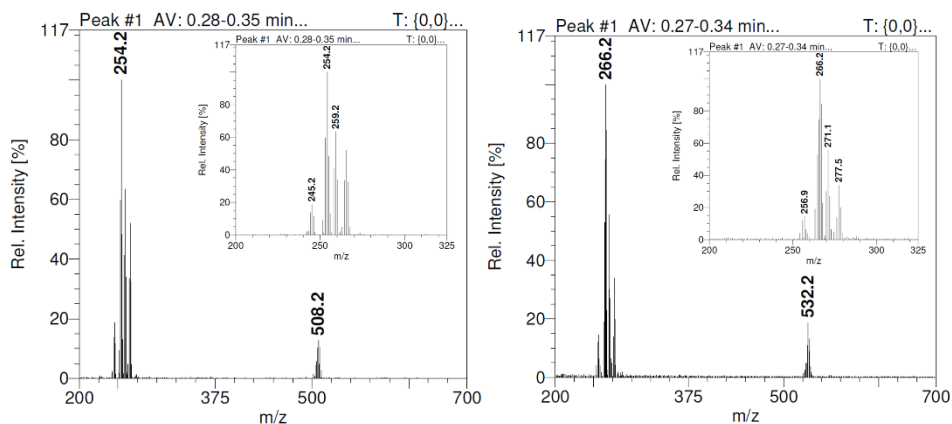


**Figure AII.5.** Mass spectrum of a solution of **[1](PF<sub>6</sub>)<sub>2</sub>** or **[2](PF<sub>6</sub>)<sub>2</sub>** in water after 70 min of light irradiation at 310 K with a 517 nm LED (5.42 mW, photon flux  $\Phi_{517} = 5.4 \cdot 10^{-8} \text{ mol} \cdot \text{s}^{-1}$ ) under air atmosphere with peaks corresponding to a) **[Ru(tpy)(bpy)(OH<sub>2</sub>)<sub>2</sub>]<sup>2+</sup>** (calc. m/z = 254.5) and **[Ru(tpy)(bpy)(OH)]<sup>+</sup>** (calc. m/z = 508.1); and b) **[Ru(HCC-tpy)(bpy)(OH<sub>2</sub>)<sub>2</sub>]<sup>2+</sup>** (calc. m/z = 266.5) and **[Ru(HCC-tpy)(bpy)(OH)]<sup>+</sup>** (calc. m/z = 532.0).

## AII.5 Singlet oxygen production and phosphorescence

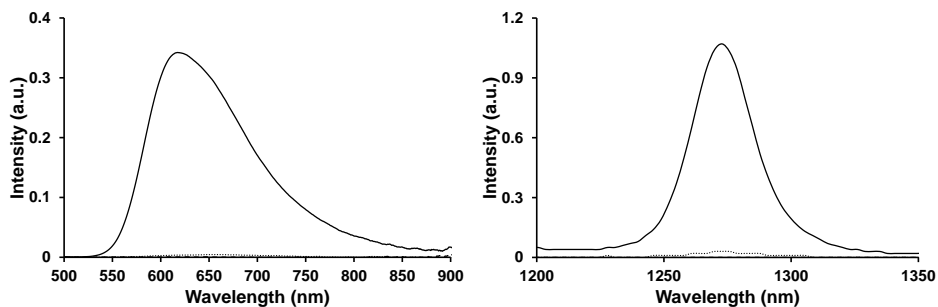


**Figure AII.6.** Visible emission spectra of **[1](PF<sub>6</sub>)<sub>2</sub>** (···), **[2](PF<sub>6</sub>)<sub>2</sub>** (- -), and **[Ru(bpy)<sub>3</sub>]Cl<sub>2</sub>** (—) (left) and near-infrared spectra of <sup>1</sup>O<sub>2</sub> phosphorescence ( $\lambda_{em} = 1275 \text{ nm}$ ) sensitized by **[1](PF<sub>6</sub>)<sub>2</sub>** (···), **[2](PF<sub>6</sub>)<sub>2</sub>** (- -), and **[Ru(bpy)<sub>3</sub>]Cl<sub>2</sub>** (—) (right) in aerated methanol-d<sub>4</sub> at 20 °C under blue-light irradiation (450 nm, 0.4 W · cm<sup>-2</sup>).

## AII.6 CuAAC click reaction with [2](PF<sub>6</sub>)<sub>2</sub>

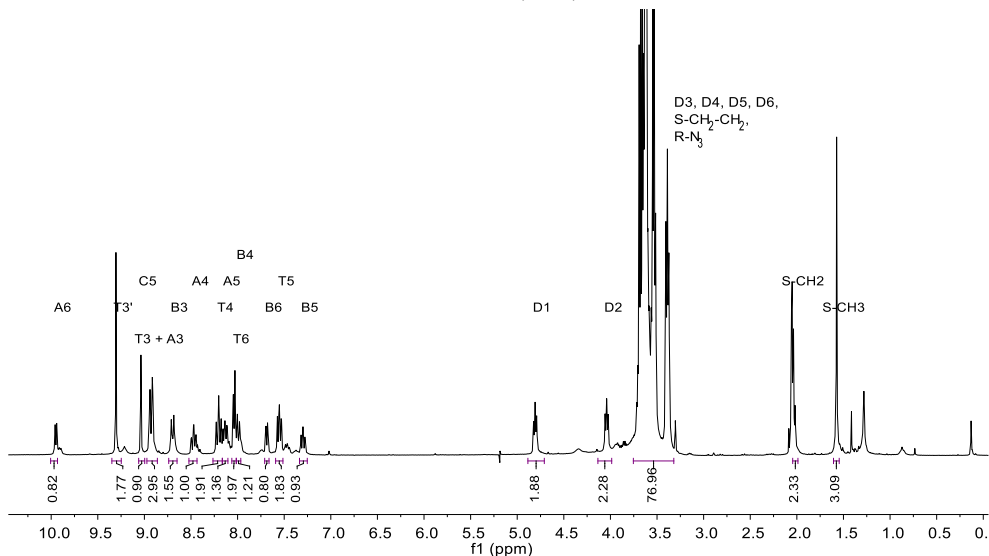


**Figure AII.7.** <sup>1</sup>H NMR spectrum (region 10.5 – 0.0 ppm) of a solution of the click product [8](PF<sub>6</sub>)<sub>2</sub> in acetone-d<sub>6</sub>.

## AII.7 Ratio and concentration optimization

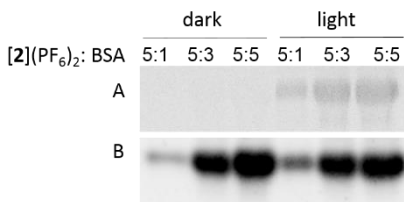


**Figure AII.8.** SDS PAGE analysis for optimization of ratio between [2](PF<sub>6</sub>)<sub>2</sub> (50 μM) and BSA (10, 30 or 50 μM) before and after light activation (520 nm, 1 h, 76 J/cm<sup>2</sup>). Click reactions were performed as described under section 2.4.6. Fluorescence labeling (A) and Coomassie blue staining (B).

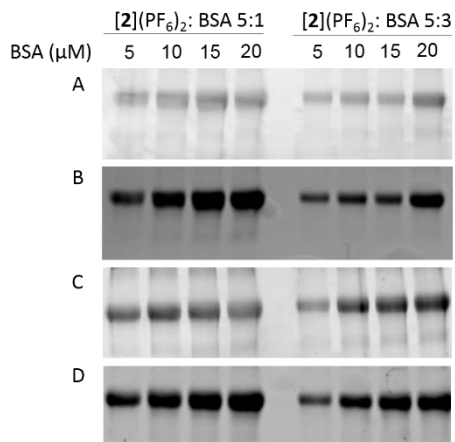


**Figure AII.9.** SDS PAGE for optimization of concentration of  $[\mathbf{2}](\text{PF}_6)_2$  and BSA at ratio 5:1 or 5:3 after light activation (520 nm, 1 h, 76 J/cm<sup>2</sup>). Click reactions were performed as described under 2.4.5. Fluorescence labeling (A) and (C) and Coomassie blue staining (B) and (D) after 6 h and 24 h incubation after light activation, respectively.

## AII.8 UV-vis spectra Ru:BSA interaction

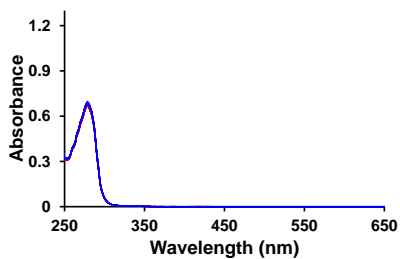


**Figure AII.10.** Evolution of the UV-vis spectra (region 250 – 650 nm) of a solution of BSA (0.015 mM) in PBS under air atmosphere for 24 h at 37 °C.



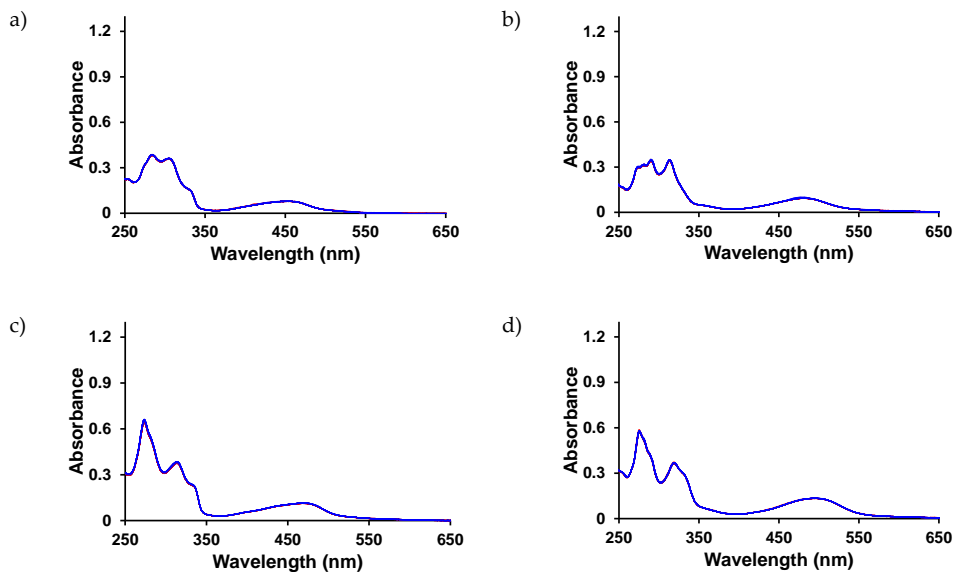


**Figure AII.11.** Evolution of the UV-vis spectra (region 250 – 650 nm) of a solution of ruthenium complex (0.015 mM) in PBS under air atmosphere for 24 h at 37 °C. a) [1](PF<sub>6</sub>)<sub>2</sub>, b) [6]<sup>2+</sup>, c) [2](PF<sub>6</sub>)<sub>2</sub>, d) [7]<sup>2+</sup>.

## AII.9 ESI MS spectra Ru:BSA interaction

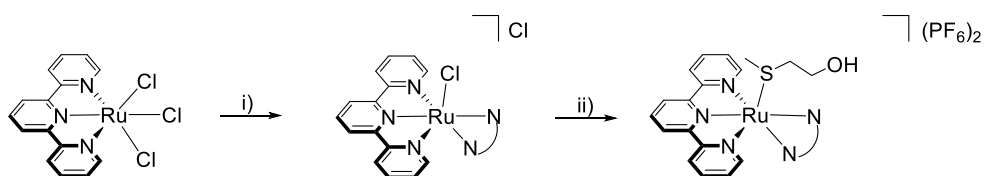
**Table AII.1.** ICP-AES quantification of ruthenium bound to BSA.

Compound	Ru (g)	Ru (mol)	BSA (mol)	BSA/Ru ratio (mol/mol)
[7] <sup>2+</sup>	$1.13 \cdot 10^{-6}$	$1.12 \cdot 10^{-8}$		1:0.12
[2] <sup>2+</sup>	$3.77 \cdot 10^{-6}$	$3.73 \cdot 10^{-8}$	$9.0 \cdot 10^{-8}$	1: 0.41
[6] <sup>2+</sup>	$3.01 \cdot 10^{-7}$	$2.97 \cdot 10^{-9}$		1: 0.03
[1] <sup>2+</sup>	$3.31 \cdot 10^{-7}$	$3.27 \cdot 10^{-9}$		1: 0.04



# APPENDIX III: SUPPORTING INFORMATION FOR CHAPTER 3

## III.1 Synthetic route



**Scheme AIII.1.** Route for the synthesis of [2](PF<sub>6</sub>)<sub>2</sub> and [3](PF<sub>6</sub>)<sub>2</sub>. Conditions: (i) LiCl, Et<sub>3</sub>N, ethanol/water (3:1), N<sub>2</sub>, reflux, i-biq (overnight, 94%) or i-Hdiqa (4 h, 83%); (ii) Hmte, AgPF<sub>6</sub>, water, N<sub>2</sub>, reflux, 4 h for [2](PF<sub>6</sub>)<sub>2</sub> (48%) and 3 h for [3](PF<sub>6</sub>)<sub>2</sub> (60%).

## III.2 Dark stability in water and OptiMEM

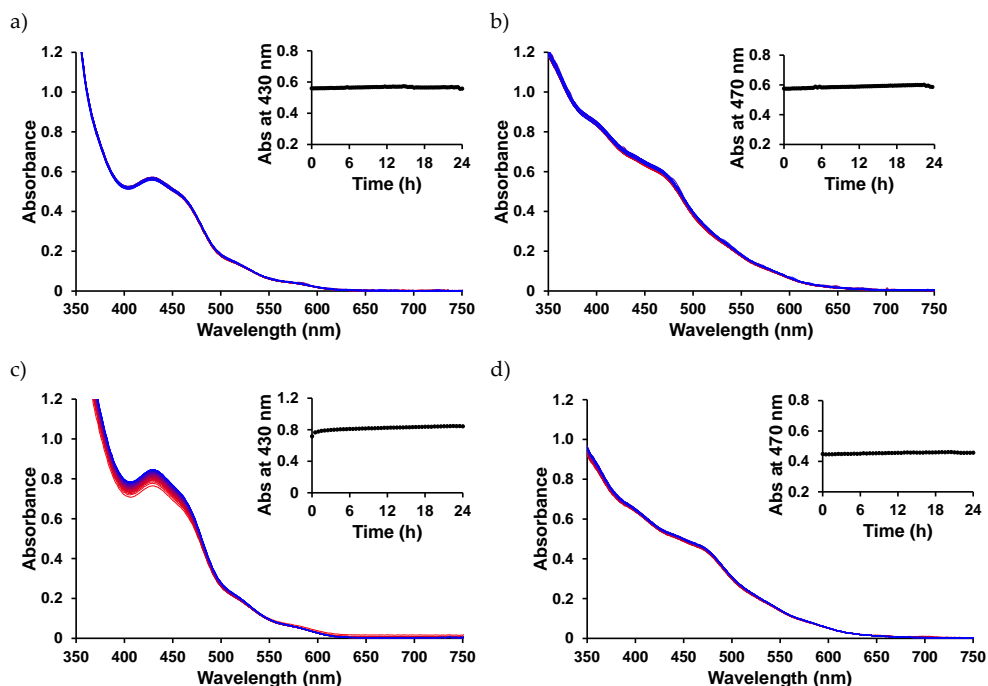


**Figure AIII.1.** Evolution of the UV-vis spectra (region 350 – 750 nm) of a solution of a) [2](PF<sub>6</sub>)<sub>2</sub> and b) [3](PF<sub>6</sub>)<sub>2</sub> in water, and c) [2](PF<sub>6</sub>)<sub>2</sub> and d) [3](PF<sub>6</sub>)<sub>2</sub> in OptiMEM complete. Conditions: [Ru] = 0.097, 0.104, 133, and 0.081 mM, respectively, T = 37 °C, t = 24 h, V = 3 mL, under air atmosphere and in the dark. Inset: Time evolution of absorbance at wavelength 430nm for [2](PF<sub>6</sub>)<sub>2</sub> and 470 nm for [3](PF<sub>6</sub>)<sub>2</sub>.

## III.3 Molar extinction coefficient in water

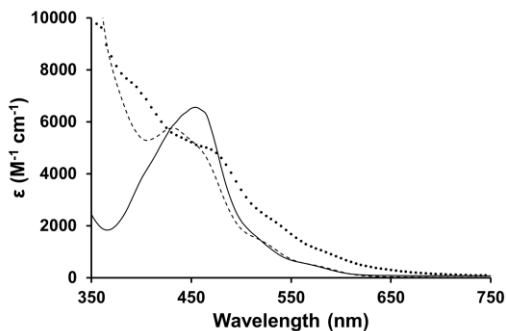


Figure AIII.2. Molar absorbance of solutions of [1](PF<sub>6</sub>)<sub>2</sub> (—), [2](PF<sub>6</sub>)<sub>2</sub> (---), and [3](PF<sub>6</sub>)<sub>2</sub> (- · -) in water.

## III.4 Singlet oxygen production and phosphorescence

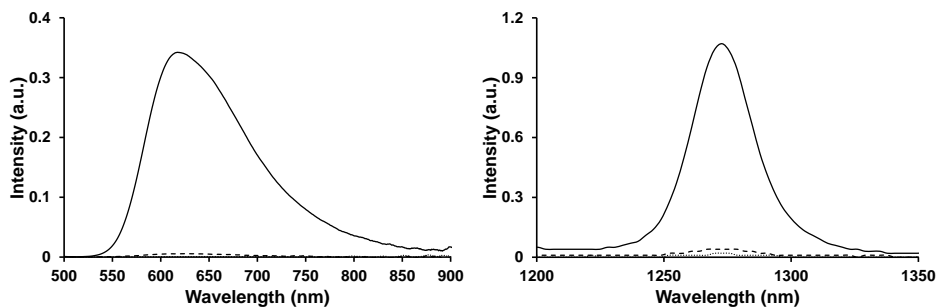
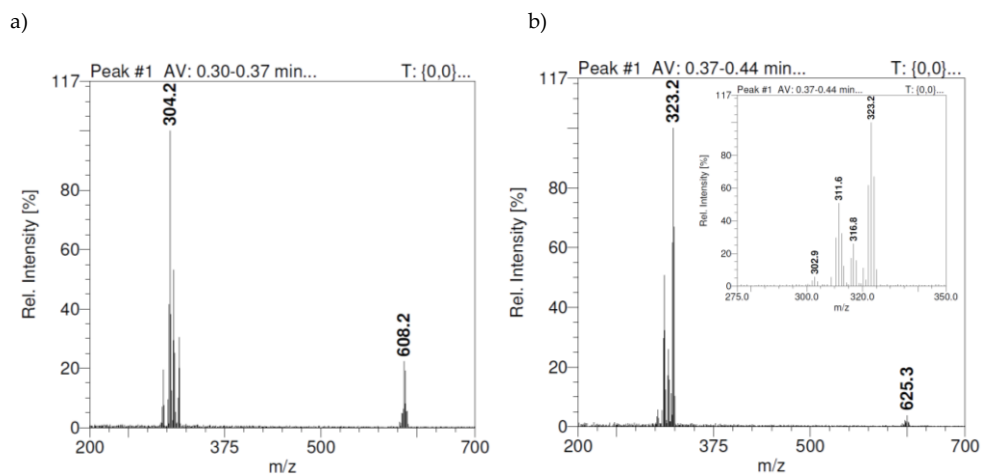


Figure AIII.3. Visible emission spectra (left) of and near-infrared spectra of <sup>1</sup>O<sub>2</sub> phosphorescence ( $\lambda_{\text{em}} = 1275$  nm) (right) sensitized by [2](PF<sub>6</sub>)<sub>2</sub> (- · -), [3](PF<sub>6</sub>)<sub>2</sub> (---), and [Ru(bpy)<sub>3</sub>]Cl<sub>2</sub> (—) in aerated methanol-d<sub>4</sub> at 293 K under blue-light irradiation (450 nm, 0.4 W · cm<sup>-2</sup>).

### III.5 MS of the ruthenium species after green light irradiation



**Figure AIII.4.** Mass spectrum of a solution of **[2]**(PF<sub>6</sub>)<sub>2</sub> and **[3]**(PF<sub>6</sub>)<sub>2</sub> in water after 50 min of light irradiation at 310 K with a 517 nm LED with a photon flux of  $\Phi_{517} = 5.2 \cdot 10^{-8} \text{ mol} \cdot \text{s}^{-1}$  under air atmosphere. Peaks corresponding to a) **[Ru(tpy)(i-biq)(OH<sub>2</sub>)]<sup>2+</sup>** (calc. m/z = 304.5) and **[Ru(tpy)(i-biq)(OH)]<sup>+</sup>** (calc. m/z = 608.1); and b) **[Ru(tpy)(i-Hdiqa)(OH<sub>2</sub>)]<sup>2+</sup>** (calc. m/z = 312.1) and **[Ru(tpy)(i-Hdiqa)(OH)]<sup>+</sup>** (calc. m/z = 623.1). **[Ru(tpy)(i-Hdiqa)(MeCN)]<sup>2+</sup>** (calc. m/z = 323.6).

### III.6 Photosubstitution quantum yield simulated by Glotaran

**Table AIII.1.** Conditions of the photoreactions used for Glotaran calculations.

	<b>[2]</b> (PF <sub>6</sub> ) <sub>2</sub>	<b>[3]</b> (PF <sub>6</sub> ) <sub>2</sub>
irradiation wavelength ( $\lambda$ in nm)	517	517
volume (V in L)	0.003	0.003
path length (l in m)	0.01	0.01
concentration (c in M)	$7.41 \cdot 10^{-5}$	$6.11 \cdot 10^{-5}$
photon flux ( $\Phi$ in mol $\cdot$ s <sup>-1</sup> )	$5.2 \cdot 10^{-8}$	$5.2 \cdot 10^{-8}$
epsilon Ru-L ( $\epsilon$ in M <sup>-1</sup> $\cdot$ cm <sup>-1</sup> ) at 517 nm	1435	2651
epsilon Ru-OH <sub>2</sub> ( $\epsilon$ in M <sup>-1</sup> $\cdot$ cm <sup>-1</sup> ) at 517 nm	3305	5025

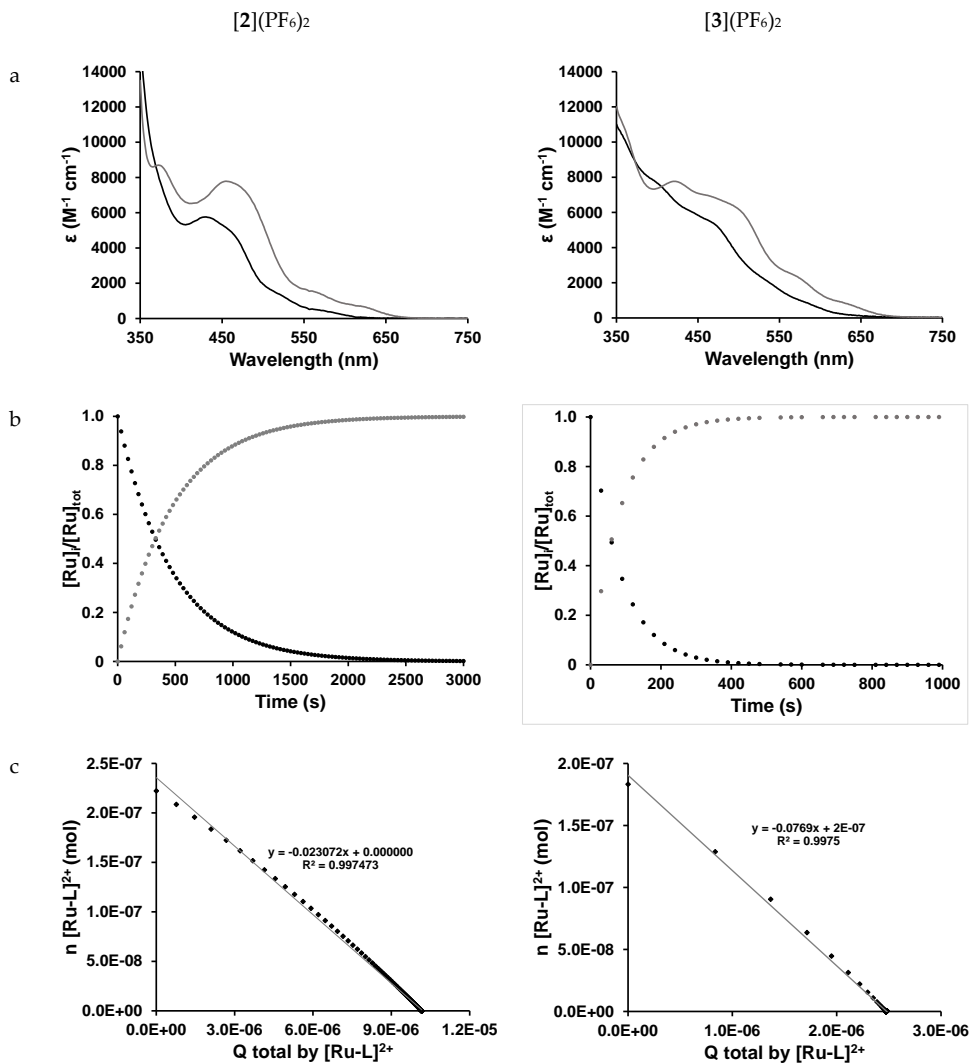


**Figure AIII.5.** Kinetic data for the photosubstitution of Hmte according to the time evolution of the absorbance spectra of solutions of  $[2](PF_6)_2$  and  $[3](PF_6)_2$  in  $H_2O$  irradiated with green light under air atmosphere. a) Globally fitted absorption spectra of the starting material  $[2](PF_6)_2$  and  $[3](PF_6)_2$  (black) and their aqua products  $[Ru(tpy)(NN)(H_2O)]^{2+}$  ( $[5]^{2+}$  and  $[6]^{2+}$ , grey). b) Modelled evolution of the relative concentration of  $[2]^{2+}$  and  $[3]^{2+}$  vs. irradiation time according to global fitting using Glotaran. c) Plot of the amount of  $[2]^{2+}$  and  $[3]^{2+}$  (mol) vs. total amount of photons absorbed by  $[2]^{2+}$  and  $[3]^{2+}$  since  $t = 0$  (mol). The slope of the obtained line is the opposite of the quantum yield of the formation for the aqua complex. Conditions: 0.074 and 0.061 mM solution of  $[2](PF_6)_2$  and  $[3](PF_6)_2$  in MilliQ  $H_2O$  irradiated at 298 K under air atmosphere using a 517 nm LED.

### III.7 Determination of light dose

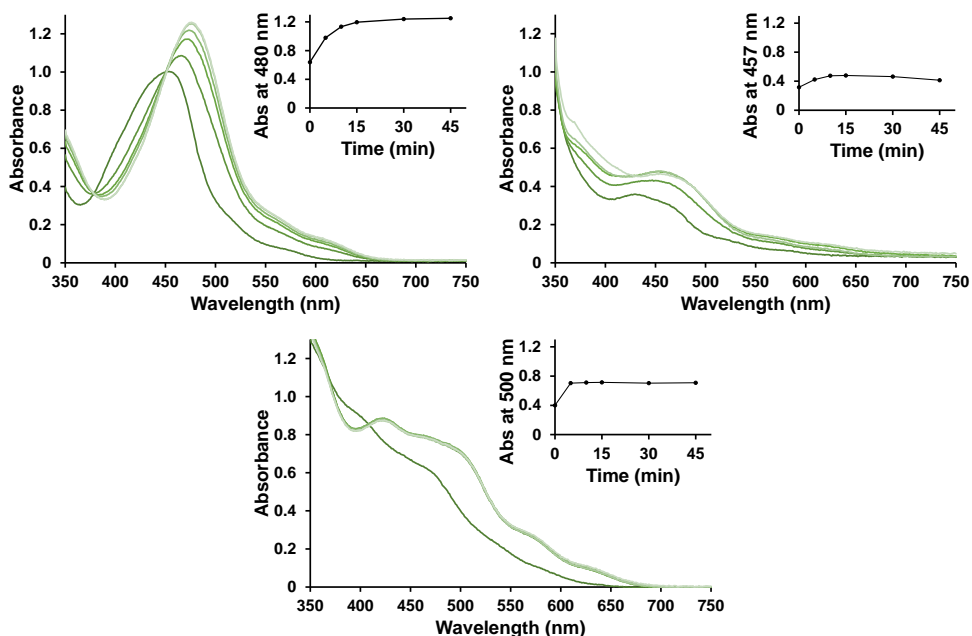


**Figure AIII.6.** Evolution of the UV-vis spectra (region 350 – 750 nm) of solutions of [1](PF<sub>6</sub>)<sub>2</sub>, [2](PF<sub>6</sub>)<sub>2</sub>, and [3](PF<sub>6</sub>)<sub>2</sub> in demineralized water upon green light irradiation in a 96 well plate, *i.e.* under the conditions of the cytotoxicity experiment. Conditions: [Ru] = 250 μM, T = 37 °C, t = 0, 5, 10, 15, 30, and 45 min, light source: λ = 520 ± 20 nm, 20.9 ± 1.6 mW · cm<sup>-2</sup>, V = 200 μL, under air atmosphere. Inset: Time dependent absorbance at wavelength 480 nm for [1](PF<sub>6</sub>)<sub>2</sub>, 457 nm for [2](PF<sub>6</sub>)<sub>2</sub>, and 500 nm for [3](PF<sub>6</sub>)<sub>2</sub>.

### III.8 Dose response curves

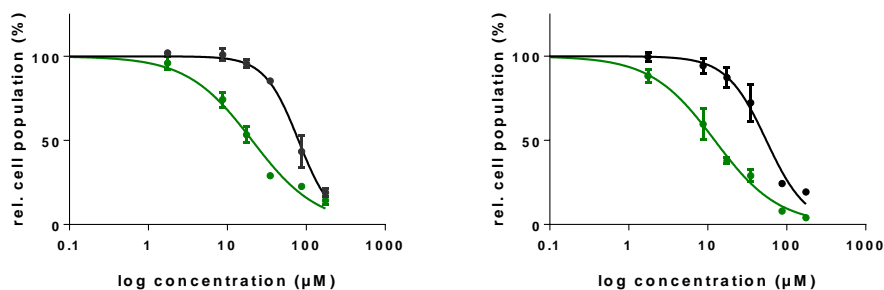


**Figure AIII.7.** Dose response curves for A549 (left) and A431 (right) cells under normoxia treated with [2](PF<sub>6</sub>)<sub>2</sub> and irradiated with green light (520 nm, 38 J · cm<sup>-2</sup>) 24 h after treatment (green line) or left in the dark (black line).

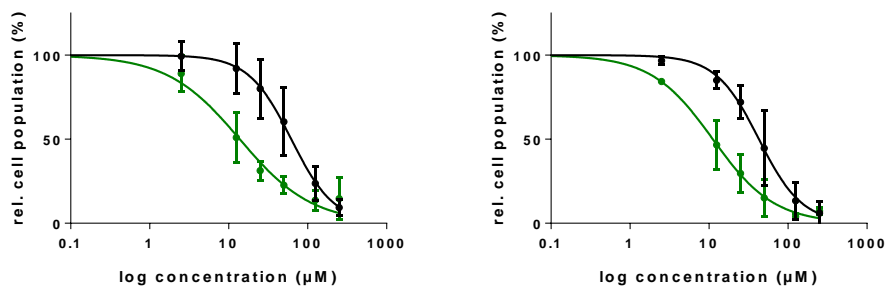


**Figure AIII.8.** Dose response curves for A549 (left) and A431 (right) cells under normoxia treated with  $[3](PF_6)_2$  and irradiated with green light (520 nm,  $38 J \cdot cm^{-2}$ ) 24 h after treatment (green line) or left in the dark (black line).

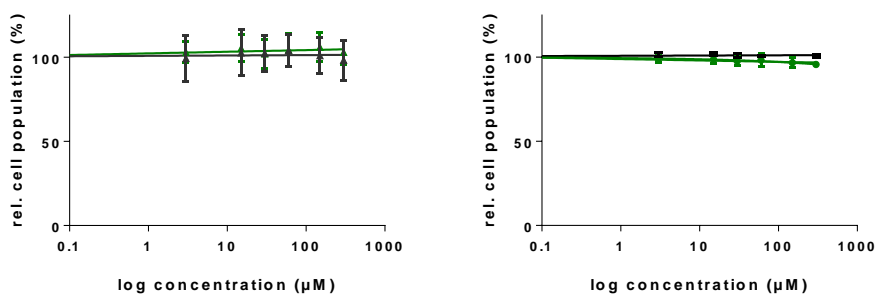


**Figure AIII.9.** Dose response curves for A549 (left) and A431 (right) cells under normoxia treated with Hmte and irradiated with green light (520 nm,  $38 J \cdot cm^{-2}$ ) 24 h after treatment (green line) or left in the dark (black line).

### III.9 DFT models

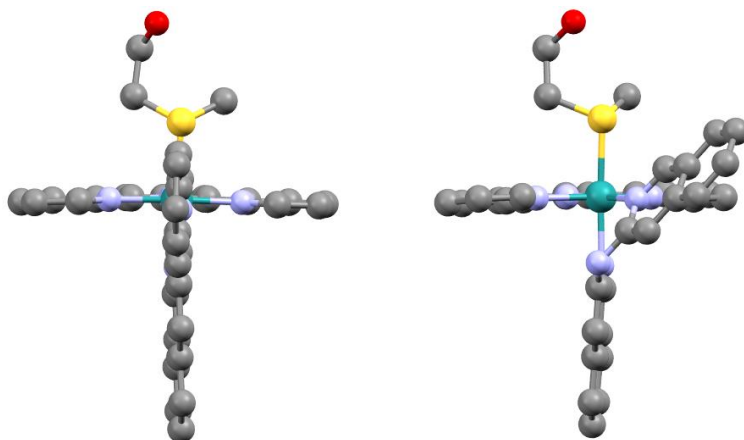


**Figure AIII.10.** Structure of  $[2]^{2+}$  (left) and  $[3]^{2+}$  (right) optimized by DFT in water (PBE0/TZP/COSMO).



**Table AIII.2.** Nuclear coordinates (Å) of [2]<sup>2+</sup> minimized at the DFT/PBE0/TZP/COSMO level in water.

Ru	0.2083679912835394	0.1173257488624371	-0.4497260606369664
C	2.617688291197344	1.551691430961221	0.8778959156333664
H	1.857834723905196	2.194107365239715	1.303929122195062
C	3.960724497568178	1.757383403522149	1.140285727173813
H	4.259364033605204	2.574252274544991	1.783782159741243
C	4.891346110905469	0.9093727917714107	0.5645562903325541
H	5.950558632083908	1.044179909507778	0.7443494360975174
C	4.449423115777398	-0.1204577020940638	-0.2487779181973365
H	5.155694252807213	-0.7977375012028864	-0.7088039053973125
C	3.090989925868592	-0.2730406395506106	-0.4753439169672215
C	2.533237691960434	-1.335857551720791	-1.328301706298766
C	3.24285674836314	-2.335225550213443	-1.978912100918067
H	4.32070659561827	-2.385278263505907	-1.911214340227477
C	2.541408426845852	-3.2790411417088	-2.71469642305054
H	3.077944774229405	-4.064769733795076	-3.231211161867237
C	1.156996670256847	-3.232433503697451	-2.780687894325799
H	0.6099674258378032	-3.979493832041498	-3.33905212121223
C	0.4914302203796511	-2.215204872614736	-2.110663654230446
C	-0.9663137900903168	-2.026747110554691	-2.028111322046999
C	-1.874312333061412	-2.881566233875994	-2.63310977491304
H	-1.523919404415143	-3.729021445980387	-3.205898770903363
C	-3.23104238745723	-2.642827798302436	-2.493237908275751
H	-3.951118650153515	-3.303471327805739	-2.959801392166215
C	-3.646801608685728	-1.552403023972211	-1.748574323300601
H	-4.695930715786754	-1.327391176975751	-1.608973696487936
C	-2.691418078707873	-0.735645884162886	-1.170154147794213
H	-2.976950582867617	0.1268942144785017	-0.5821875845477985
N	2.181101327220925	0.5696892440728344	0.08564824812676824
N	1.193127783541921	-1.292947215174845	-1.428454131776693
N	-1.380273947620814	-0.9533329238833577	-1.300656196754388
C	-1.393471196027837	2.620438170814063	0.4042623143945007
H	-1.123517509182634	2.982728791416989	-0.5810566183846197
C	-2.224418866223735	3.405665344486646	1.222109528721864
C	-2.731133568375314	4.652450412072225	0.7970144697214701
H	-2.468443933913542	5.02654395471265	-0.1860829517911313
C	-3.549338171103099	5.368288412613389	1.628822890872407
H	-3.945387392170889	6.32499123524617	1.309115936429985
C	-3.88659000780193	4.869922864403923	2.906130137038371
H	-4.536344582108921	5.453683178073768	3.548019418805768
C	-3.405350469976215	3.663905255783805	3.340981060735985
H	-3.66480327149348	3.281463589915676	4.321561084089738
C	-2.56174053922833	2.902782978070626	2.502551807086794
C	-2.036867370346503	1.651496909829876	2.867256944336066
H	-2.286884652361376	1.243146706633071	3.83718914403587

C	-1.234445289862512	0.9509121106635542	2.004871535615553
C	-0.6746534617535808	-0.3656145324083772	2.327139504982696
C	-0.8120766943186178	-0.9670797830453756	3.551022905313966
H	-1.345504549671184	-0.4692047206310123	4.349612189657306
C	-0.2576293826036777	-2.23558456112777	3.793765811601495
C	-0.3627007341662732	-2.902001914470313	5.034634070331201
H	-0.8953416259472317	-2.42567385196123	5.849745089448689
C	0.2068437316836899	-4.137077308358533	5.193449610592506
H	0.1269353185372501	-4.648526270948042	6.14575587128791
C	0.9009830081163462	-4.759006110143837	4.133027000650242
H	1.342220211706593	-5.73671420002553	4.286629201206821
C	1.018922983066359	-4.136117889852509	2.920213002683382
H	1.551252541269151	-4.605643235267709	2.100633046145049
C	0.440979876583827	-2.86258273534604	2.733079986925966
C	0.5381980767687432	-2.170445857365483	1.514638400497948
H	1.072812194832305	-2.626424479700958	0.6905127176816017
N	-0.9158350918367943	1.443457645808958	0.7573950146199396
N	0.01568183074122983	-0.9802156170868606	1.309043635434526
C	2.039591911060169	1.894933036207212	-2.793011015717027
H	2.479452552716376	0.9574003560668584	-3.129175837202628
H	2.585227519727869	2.284298858196861	-1.937192715796087
H	2.058902075030991	2.634795642469756	-3.589979927944774
S	0.3282090149283553	1.670940353476732	-2.269301183090305
C	-0.398815967668077	0.9542844710175553	-3.777184870498797
H	-0.1197380759669304	-0.09748519177659898	-3.853889739659892
H	-1.4766145139828	1.014202997494053	-3.616679799483083
C	0.004354563648658137	1.653403455773825	-5.063472499084149
H	1.051528319682407	1.454367110703531	-5.289316150214599
H	-0.5900092427384502	1.215525147282966	-5.871739545699212
O	-0.132554221558341	3.063845517400228	-5.03379825696929
H	-1.072162150087336	3.275246969664708	-4.971018119851347

**Table AIII.3.** Nuclear coordinates (Å) of [3]<sup>2+</sup> minimized at the DFT/PBE0/TZP/COSMO level in water.

Ru	0.161709	0.107889	-0.624947
C	2.534685	1.634117	0.6795
H	1.759708	2.227168	1.147331
C	3.87283	1.908686	0.900925
H	4.14734	2.731564	1.547451
C	4.828243	1.119831	0.284229
H	5.884184	1.30953	0.430199
C	4.414284	0.07201299999999999	-0.520744
H	5.139515	-0.567732	-1.004342
C	3.059003	-0.151129	-0.704146
C	2.531576	-1.261463	-1.513959
C	3.276551	-2.245425	-2.148115

H	4.357141	-2.23066	-2.117325000000001
C	2.607317	-3.260847	-2.815113
H	3.171099	-4.038527	-3.314433
C	1.221694	-3.291515	-2.836848
H	0.70038	-4.089249	-3.3476
C	0.520649	-2.280657	-2.193243
C	-0.942152	-2.135796	-2.13235
C	-1.809778	-3.03867	-2.727602
H	-1.421817	-3.91215	-3.233121
C	-3.17354	-2.8087	-2.673833
H	-3.862786	-3.506292	-3.133235
C	-3.634027	-1.670487	-2.035314
H	-4.689488	-1.438774	-1.978518
C	-2.717003	-0.814173	-1.451956
H	-3.042935	0.08209	-0.943654
N	2.122056	0.642547	-0.113939
N	1.187603	-1.296183	-1.567129
N	-1.399724	-1.033302	-1.478919
C	-0.784934	2.883257	0.251161
H	0.018774	3.174929	-0.413982
C	-1.593178	3.879968	0.809882
C	-1.387706	5.2529	0.538616
H	-0.571385	5.548936	-0.110979
C	-2.220565	6.183609000000001	1.092671
H	-2.073204	7.237455	0.888224
C	-3.282525	5.779798	1.935187
H	-3.93175	6.534141	2.365079
C	-3.501556	4.458668	2.214762
H	-4.316191	4.154731	2.86234
C	-2.657993	3.472143	1.653635
C	-2.790482	2.099351	1.905009
H	-3.55748	1.740296	2.581217
C	-1.937868	1.201067	1.310411
C	-1.095307	-1.044427	1.895014
C	-1.271482	-1.887152	2.965573
H	-2.181608	-1.823141	3.550141
C	-0.273561	-2.808106	3.314467
C	-0.3796	-3.706505	4.401566
H	-1.28331	-3.711596	5.000156
C	0.655828	-4.554234	4.687181
H	0.572726	-5.241765	5.521352
C	1.839476	-4.551702	3.912671
H	2.642006	-5.235738	4.162189
C	1.971663	-3.692583	2.858424
H	2.87436	-3.680517	2.25769
C	0.916255	-2.804887	2.54265

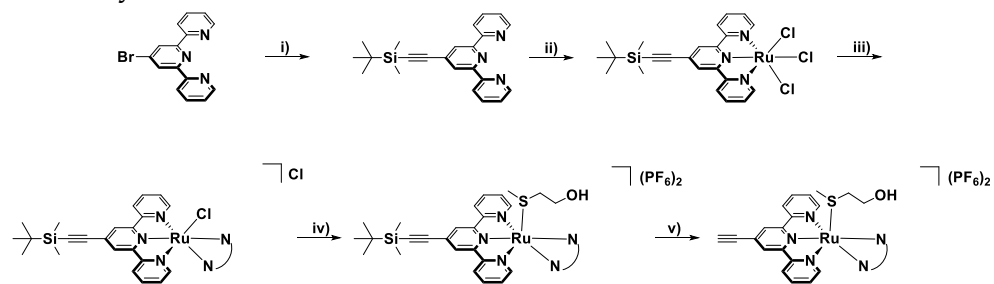
C	0.9946120000000001	-1.910447	1.469447
H	1.891249	-1.903154	0.86431
N	-0.954047	1.583713	0.446298
N	0.029752	-1.072408	1.125377
C	1.886228	1.935304	-3.00795
H	2.417364	1.030255	-3.298116
H	2.375263	2.401652	-2.155578
H	1.862595	2.645112	-3.831636
S	0.187945	1.578699	-2.516694
C	-0.418341	0.724009	-4.006151
H	-0.027849	-0.294179	-4.028884
H	-1.500273	0.67875	-3.874731
C	-0.053696	1.409174	-5.3109980000000001
H	1.014585	1.315088	-5.502802
H	-0.5744469999999999	0.876715	-6.113368
O	-0.342038	2.7963	-5.345442
H	-1.300419	2.906381	-5.312955
N	-2.113618	-0.161765	1.543382
H	-2.942264	-0.329492	2.096443

## AIII.10 References

- 1 C. Ruppin and P. H. Dixneuf, *Tetrahedron Lett.* **1986**, 27 (52), 6323-6324.
- 2 R. Wirth, J. D. White, A. D. Moghaddam, A. L. Ginzburg, L. N. Zakharov, M. M. Haley and V. J. DeRose, *J. Am. Chem. Soc.* **2015**, 137 (48), 15169-15175.

# APPENDIX IV:SUPPORTING INFORMATION FOR CHAPTER 4

## AIV.1 Synthesis



**Scheme AIV.1.** Reaction scheme of the stepwise synthesis of [2](PF<sub>6</sub>)<sub>2</sub> and [4](PF<sub>6</sub>)<sub>2</sub>. Conditions: i) CuI, Pd(PPh<sub>3</sub>)<sub>2</sub>Cl<sub>2</sub>, TBDMS-ethyne, Et<sub>3</sub>N, 80 °C, N<sub>2</sub>, 7 h, 95%; ii) RuCl<sub>3</sub>, ethanol, 80 °C, 16 h, 75%; iii) LiCl, Et<sub>3</sub>N, ethanol/water (3:1), 60 °C, i-biq (overnight, 73%) or i-Hdiqa (5 h, 71%); (iv) Hmte, water, 60 °C, N<sub>2</sub>, 16 h, aq. KPF<sub>6</sub>; 93 and 95%, respectively; v) KF, methanol, 30 °C, 16 h, aq. KPF<sub>6</sub>; 82 and 83%, respectively.

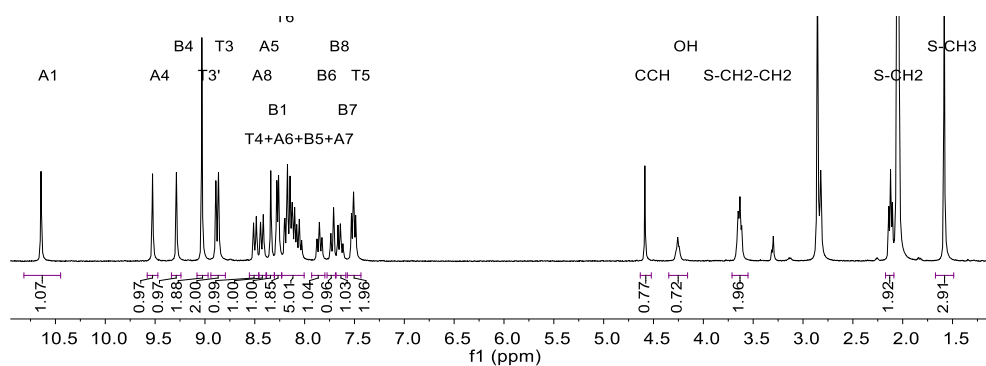


**Figure AIV.1.** <sup>1</sup>H NMR spectrum (region 11.0 – 1.0 ppm) of a solution of [2](PF<sub>6</sub>)<sub>2</sub> in acetone-d<sub>6</sub> at 25 °C. Atom numbering as donated in the experimental section 4.4.2.

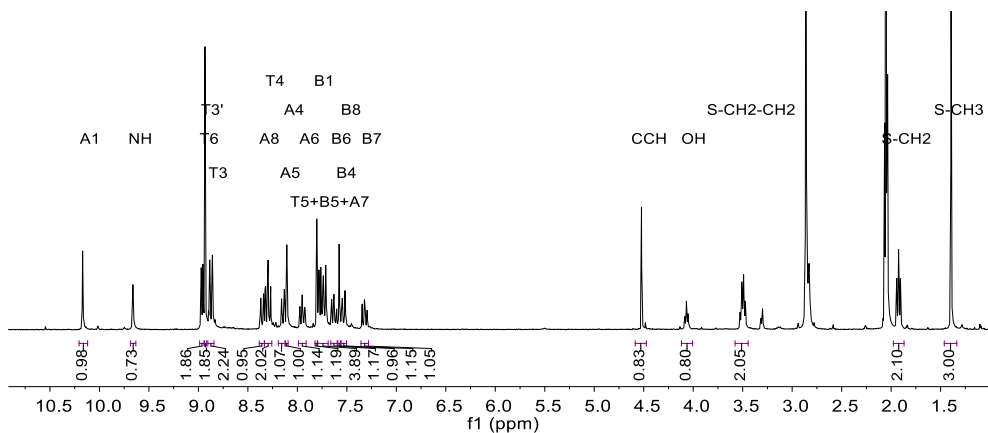


**Figure AIV.2.**  $^1\text{H}$  NMR spectrum (region 11.0 – 1.0 ppm) of a solution of  $[\mathbf{4}](\text{PF}_6)_2$  in acetone- $\text{d}_6$  at 25  $^\circ\text{C}$ . Atom numbering according to the experimental section 4.4.2.

## AIV.2 Molar extinction coefficient in water

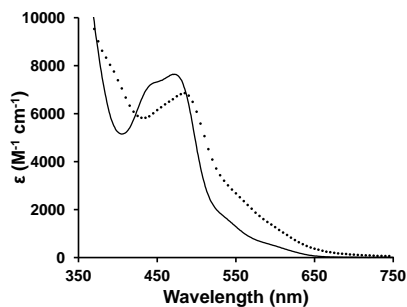


**Figure AIV.3.** Molar extinction coefficient of aqueous solutions of  $[\mathbf{2}]\text{Cl}_2$  (—) and  $[\mathbf{4}](\text{PF}_6)_2$  (···) in water.

## AIV.3 Singlet oxygen production and phosphorescence

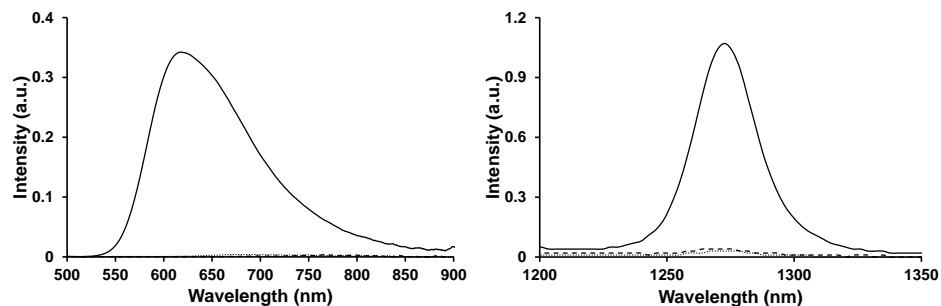


**Figure AIV.4.** Visible emission spectra of  $[\mathbf{2}]\text{Cl}_2$  (···),  $[\mathbf{4}](\text{PF}_6)_2$  (- -), and  $[\text{Ru}(\text{bpy})_3]\text{Cl}_2$  (—) (left) and near-infrared spectra of  $^1\text{O}_2$  phosphorescence ( $\lambda_{\text{em}} = 1275$  nm) sensitized by  $[\mathbf{2}]\text{Cl}_2$  (···),  $[\mathbf{4}](\text{PF}_6)_2$  (- -), and  $[\text{Ru}(\text{bpy})_3]\text{Cl}_2$  (—) (right) in aerated methanol- $\text{d}_4$  at 293 K under blue-light irradiation (450 nm,  $0.4 \text{ W} \cdot \text{cm}^{-2}$ ).

## AIV.4 Green light activation

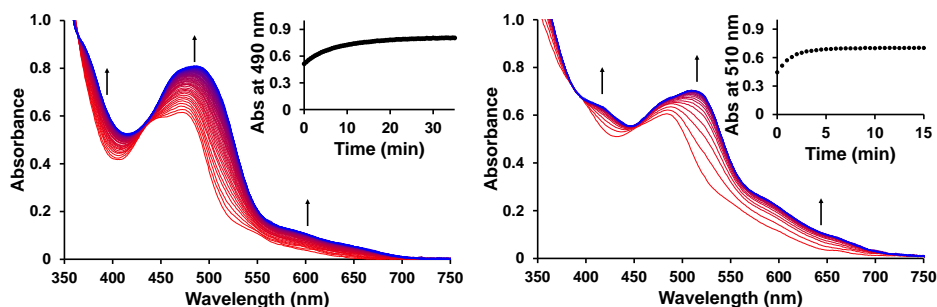


**Figure AIV.5.** Evolution of the UV-vis absorption spectra of a solution of [2]Cl<sub>2</sub> and [4](PF<sub>6</sub>)<sub>2</sub> in water upon green light irradiation. Conditions: [Ru] = 0.077 and 0.127 mM for [2]Cl<sub>2</sub> and [4](PF<sub>6</sub>)<sub>2</sub>, respectively, T = 37 °C, light source: λ = 517 nm, Δλ<sub>1/2</sub> = 23 nm, 5.2 mW, photon flux Φ<sub>517</sub> = 5.3 · 10<sup>-8</sup> and 5.2 · 10<sup>-8</sup> mol · s<sup>-1</sup>, V = 3 mL, under air atmosphere. Inset: Time evolution of absorbance at wavelength 490 nm for [2]Cl<sub>2</sub> and 510 nm for [4](PF<sub>6</sub>)<sub>2</sub>.

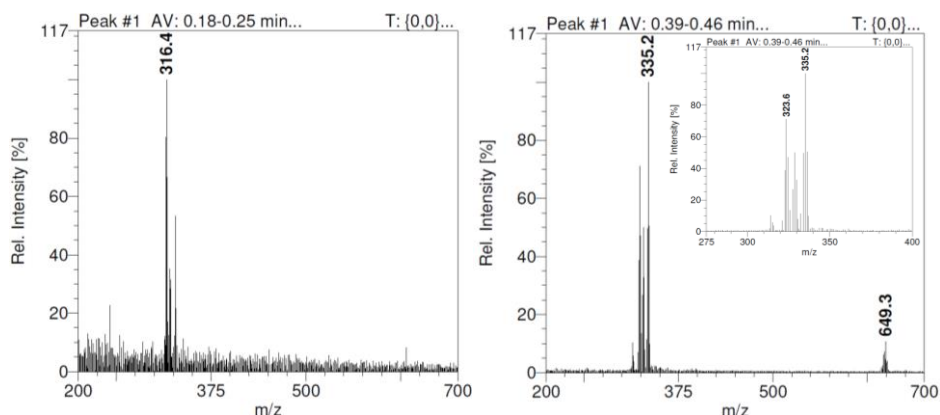


**Figure AIV.6.** Mass spectrum of a solution of [2]Cl<sub>2</sub> and [4](PF<sub>6</sub>)<sub>2</sub> in water after 80 and 50 min, respectively, of light irradiation at 310 K with a 517 nm LED with a photon flux Φ<sub>517</sub> = 5.3 · 10<sup>-8</sup> and 5.2 · 10<sup>-8</sup> mol · s<sup>-1</sup>, respectively, under air atmosphere with peaks corresponding to a) [Ru(HCC-tpy)(i-biq)(OH<sub>2</sub>)<sub>2</sub>]<sup>2+</sup> (calc. m/z = 316.5); and b) [Ru(HCC-tpy)(i-Hdiqa)(OH<sub>2</sub>)<sub>2</sub>]<sup>2+</sup> (calc. m/z = 324.1) and [Ru(HCC-tpy)(i-Hdiqa)(OH)]<sup>+</sup> (calc. m/z = 647.1). [Ru(HCC-tpy)(i-Hdiqa)(MeCN)]<sup>2+</sup> (calc. m/z = 335.6).

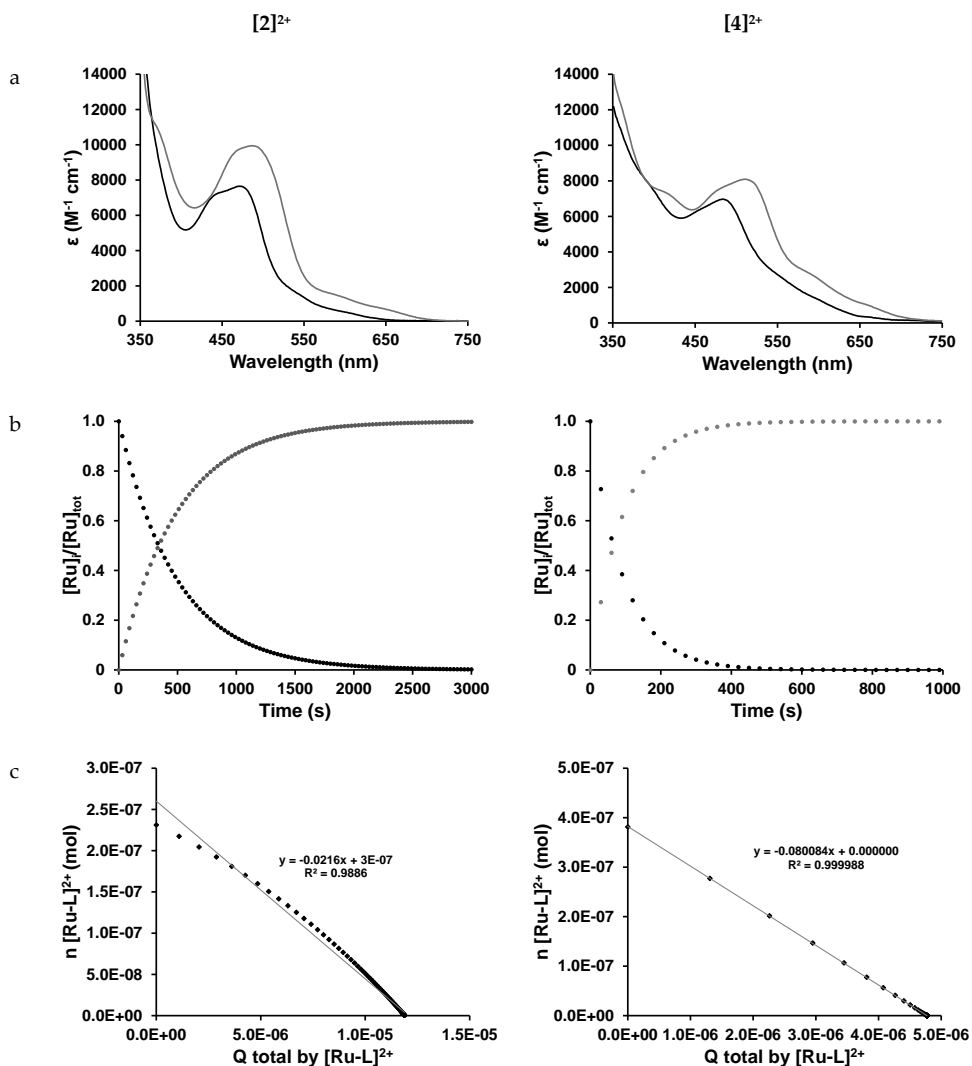


**Figure AIV.7.** Kinetic data for the photosubstitution of Hmte according to the time evolution of the absorbance spectra of solutions of  $[2]\text{Cl}_2$  and  $[4](\text{PF}_6)_2$  in  $\text{H}_2\text{O}$  under air atmosphere. a) Globally fitted absorption spectra of the starting material  $[2]\text{Cl}_2$  and  $[4](\text{PF}_6)_2$  (black) and their aqua products  $[\text{Ru}(\text{HCC-tpy})(\text{i-biq})(\text{H}_2\text{O})]^{2+}$  and  $[\text{Ru}(\text{HCC-tpy})(\text{i-Hdiqa})(\text{H}_2\text{O})]^{2+}$  (grey). b) Modelled evolution of the relative concentration of  $[2]^{2+}$  and  $[4]^{2+}$  vs. irradiation time according to global fitting using Glotaran. c) Plot of the amount of  $[2]^{2+}$  and  $[4]^{2+}$  (mol) vs. total amount of photons absorbed by  $[1]^{2+}$  and  $[3]^{2+}$  since  $t = 0$  (mol). The slope of the obtained line is the opposite of the quantum yield of the formation of the aqua complex. Conditions: 0.077 and 0.127 mM solution of  $[2]\text{Cl}_2$  and  $[4](\text{PF}_6)_2$  in MilliQ  $\text{H}_2\text{O}$  irradiated at 298 K under air atmosphere using a 517 nm LED.



**Table AIV.1.** Conditions of the photoreactions used for Glotaran calculations.

	[2]Cl <sub>2</sub>	[4](PF <sub>6</sub> ) <sub>2</sub>
irradiation wavelength ( $\lambda$ in nm)	517	517
volume (V in L)	0.003	0.003
path length (l in m)	0.01	0.01
concentration (c in M)	$7.71 \cdot 10^{-5}$	$1.27 \cdot 10^{-4}$
photon flux ( $\Phi$ in mol $\cdot$ s <sup>-1</sup> )	$5.3 \cdot 10^{-8}$	$5.2 \cdot 10^{-8}$
epsilon Ru-L ( $\epsilon$ in M <sup>-1</sup> $\cdot$ cm <sup>-1</sup> ) at 517 nm	2531	4458
epsilon Ru-OH <sub>2</sub> ( $\epsilon$ in M <sup>-1</sup> $\cdot$ cm <sup>-1</sup> ) at 517 nm	7536	8014

### AIV.5 Dark stability

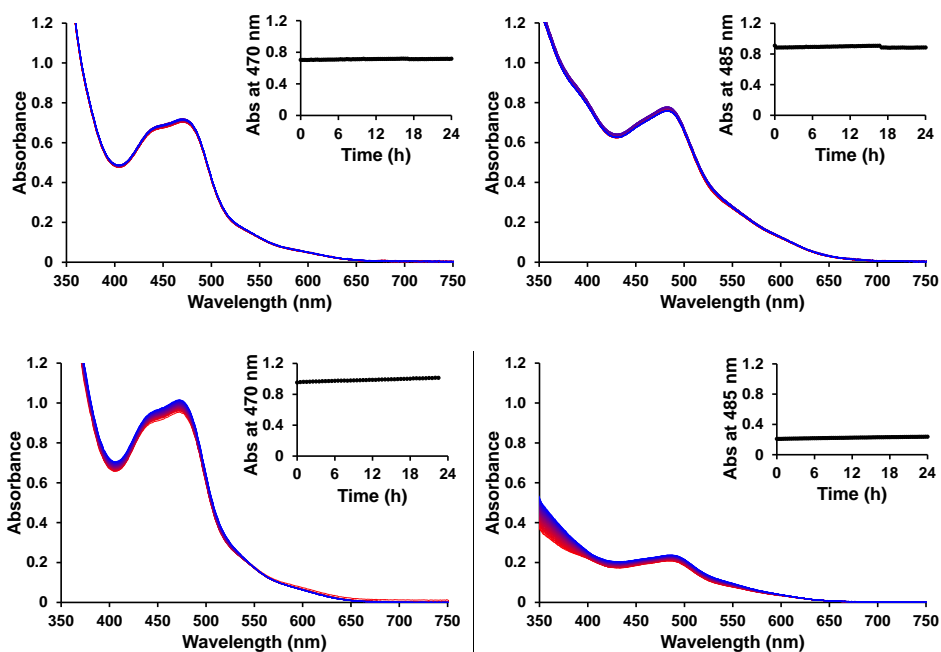


**Figure AIV.8.** Evolution of the UV-vis spectra (region 350 – 750 nm) of a solution of a) [2]Cl<sub>2</sub> and b) [4](PF<sub>6</sub>)<sub>2</sub> in water, and c) [2]Cl<sub>2</sub> and d) [4](PF<sub>6</sub>)<sub>2</sub> in OptiMEM complete. Conditions: [Ru] = 0.094, 0.111, 0.130, and 0.035 mM, respectively, T = 37 °C, t = 24 h, V = 3 mL, under air atmosphere and in the dark. Inset: Time evolution of absorbance at wavelength 470 nm for [2]Cl<sub>2</sub> and 485 nm for [4](PF<sub>6</sub>)<sub>2</sub>.

## AIV.6 Determination of light dose

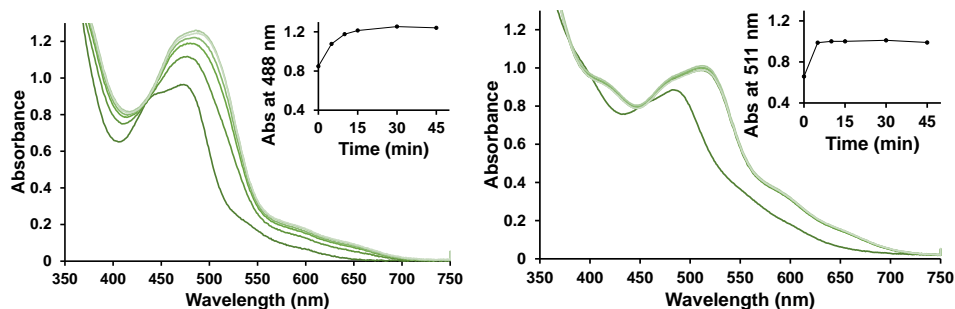


**Figure AIV.9.** Evolution of the UV-vis spectra (region 350 – 750 nm) of a solution of [2]Cl<sub>2</sub> and [4](PF<sub>6</sub>)<sub>2</sub> in demineralized water upon green light irradiation in a 96 well plate *i.e.* under the conditions of the cytotoxicity experiment. Conditions: [Ru] = 250 μM, T = 37 °C, t = 0, 5, 10, 15, 30, and 45 min, light source: λ = 520 ± 20 nm, 20.9 ± 1.6 mW · cm<sup>-2</sup>, V = 200 μL, under air atmosphere. Inset: Time dependent absorbance at wavelength 488 nm for [2]Cl<sub>2</sub> and 511 nm for [4](PF<sub>6</sub>)<sub>2</sub>.

## AIV.7 Dose response curves for A549 cells

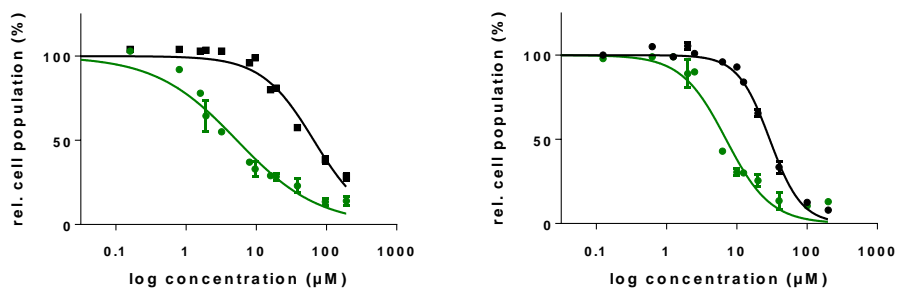


**Figure AIV.10.** Dose response curves for A549 cells under normoxic conditions treated with [2]Cl<sub>2</sub> (left) or [4](PF<sub>6</sub>)<sub>2</sub> (right) and irradiated with green light (520 nm, 38 J · cm<sup>-2</sup>) 24 h after treatment (green line) or left in the dark (black line).

## AIV.8 Microscopy imaging of A549 cells

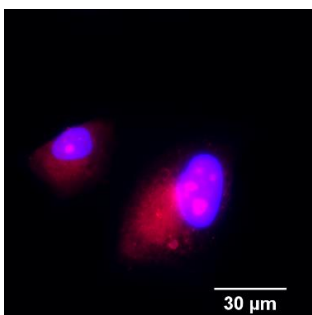


**Figure AIV.11.** Confocal microscopy imaging of A549 lung cancer cells treated with 25  $\mu\text{M}$  of Azidoplatin and labeled with Rhodamine-alkyne (red) and nuclear stain (Hoechst, blue). The fluorescence mainly accumulates in the nucleoli (merged magenta) of the nucleus, as reported by DeRose and co-workers for HeLA cells.<sup>1</sup>

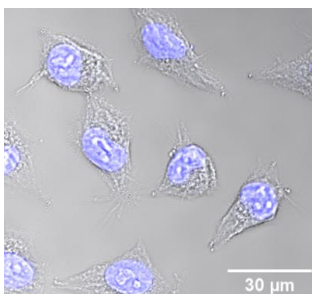


**Figure AIV.12.** Confocal microscopy imaging of A549 lung cancer cells treated with 25  $\mu\text{M}$  of [4](PF<sub>6</sub>)<sub>2</sub> and incubated for 24 h after light irradiation. While the cells look unhealthy, the shape of the nucleus (staining with Hoechst, in blue) is unchanged.

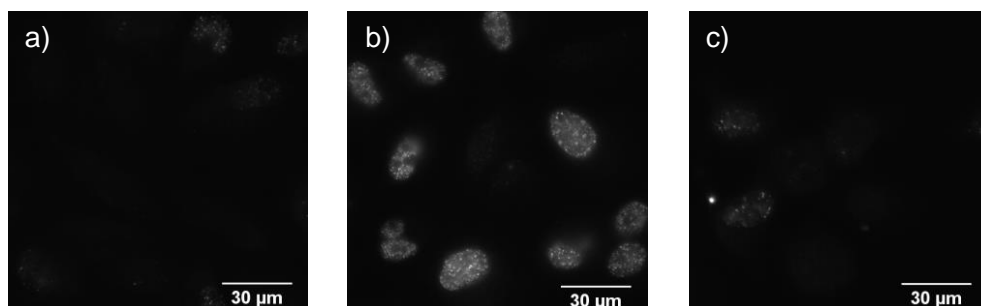


**Figure AIV.13.** Inverted microscopy imaging of DNA damage co-staining (Phospho-Histone H2A.X (Ser139) Monoclonal Antibody (CR55T33), eBioscience™) in the nucleus of A549 lung cancer cells. Cells are seeded at  $t = 0$  h, treated at  $t = 24$  h, irradiated (517 nm) at  $t = 48$  h, and fixed and co-stained at  $t = 72$  h. a) Untreated cell control, b) cells treated with 10  $\mu\text{M}$  cisplatin, and c) cells treated with 25  $\mu\text{M}$  [4](PF<sub>6</sub>)<sub>2</sub>. No visible signal in cells treated with [4](PF<sub>6</sub>)<sub>2</sub> indicates that the compound does not cause DNA damage.

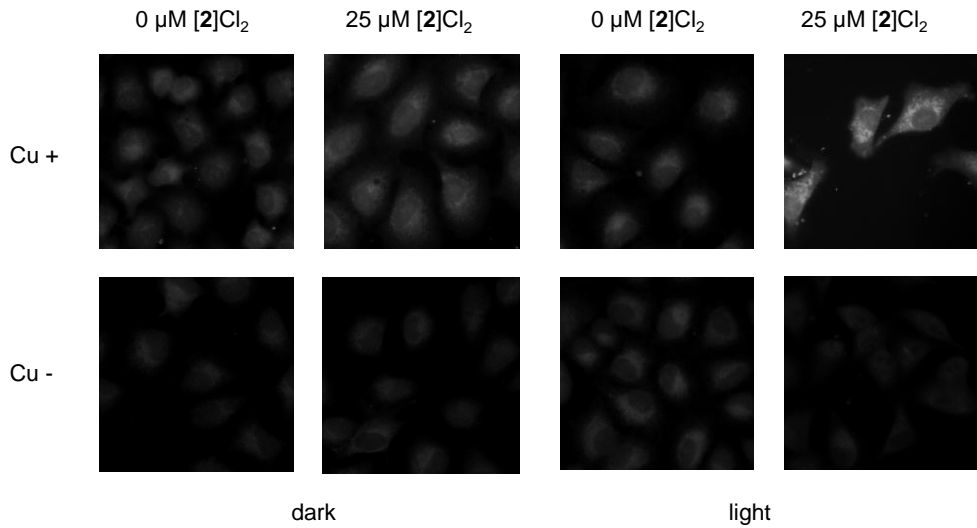


**Figure AIV.14.** Confocal image of fluorescent labeling of A549 cancer cell lines treated with 0 or 25  $\mu\text{M}$  of [2]Cl<sub>2</sub> after fixation, permeabilization, and labeling with Alexa Fluor™ 488 azide, either with or without light activation. Cu-free controls show no fluorescence.

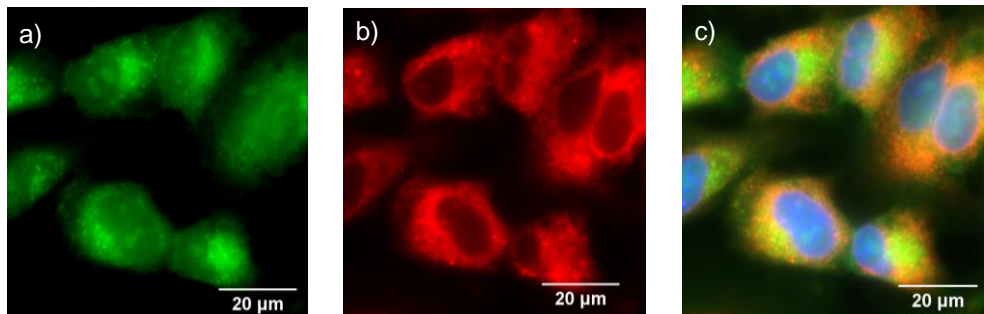


**Figure AIV.15.** Inverted microscopy imaging of A549 lung cancer cells treated with 25  $\mu\text{M}$  of [2]Cl<sub>2</sub> and incubated for 24 h after light irradiation. a) Labeling of [2]Cl<sub>2</sub> with AlexaFluor™ 488 azide (green), b) antibody staining (Anti-P4HB antibody [RL90] (ab2792)) for ER with 647 dye (red), and c) overlay of [2]Cl<sub>2</sub>, ER staining, and nuclear staining (with Hoechst in blue). No co-localization between [2]Cl<sub>2</sub> and ER.

## AIV.9 DFT studies

**Table AIV.2.** Nuclear coordinates (Å) of [2]<sup>2+</sup> minimized at the DFT/PBE0/TZP/COSMO level in water.

Ru	-0.2371536913409365	-0.04131143665661324	0.3460659281257489
C	-1.532890793872343	-2.602328684055745	-0.8306710061644537
H	-2.251842348881358	-1.911567141887859	-1.252225677621425
C	-1.642526304531791	-3.96624060809431	-1.038131573614926
H	-2.459204774094477	-4.350589289423185	-1.634600041543079
C	-0.7013743566126036	-4.806788840837971	-0.4691272946413964
H	-0.7606423864704916	-5.879266502288916	-0.6057782673450046
C	0.3244371977643025	-4.256496998357359	0.280980597153343
H	1.073834674795002	-4.891602003092336	0.7329816069243424
C	0.3796309229394406	-2.882849869395558	0.452020830275026
C	1.433658431222659	-2.209775445273846	1.229689737130766
C	2.508944179645303	-2.816744716864388	1.854185679326281
H	2.638186424226729	-3.889234316979597	1.828005450072141
C	3.442045979451416	-2.018614854871485	2.521557608428701
C	3.283798981528712	-0.6306698787685715	2.528909377656344
H	4.013082308074423	-0.008006548648022216	3.02708294803903
C	2.188715956496207	-0.07747895341463253	1.888875034334967
C	1.878763640275484	1.357303476414452	1.77341761348179
C	2.678870773488598	2.350340032078643	2.314778091310427
H	3.578432050871337	2.089844977980936	2.855303860191404
C	2.31659698085506	3.677117784872823	2.154734344427466
H	2.932303671824132	4.463886659186145	2.572391886780417
C	1.161037402799495	3.976758199036288	1.453955813852466
H	0.8391700867768646	4.99842639341749	1.301868740976054
C	0.4044605322992431	2.939773235551277	0.9370884192813959
H	-0.5053942363915487	3.133427350325226	0.3837876110025992
N	-0.5561908969102859	-2.061993051065329	-0.09824363547775791
N	1.290643964402534	-0.8729698396351607	1.27972252057514
N	0.7411276968266891	1.656692544693616	1.088450397646056
C	-2.904625694685204	1.30973345151026	-0.4209406170955253
H	-3.159074546272399	1.119331693394778	0.6153244934058034
C	-3.829177188865098	1.972253477042693	-1.246029962462154
C	-5.081237029510736	2.409650093749971	-0.7637294254597728
H	-5.34448276509836	2.229980511678045	0.2726116553637966
C	-5.942831019191246	3.053993630841919	-1.609664473666664
H	-6.905897726169232	3.394462803479109	-1.247638822633878
C	-5.587886540448488	3.281488799698712	-2.957145039524841
H	-6.285976707378517	3.793348696266316	-3.609247377279859
C	-4.378358036899172	2.866462360594738	-3.44723482297753
H	-4.10634271209199	3.042710941226021	-4.48166277226628
C	-3.468728735758551	2.200987135832057	-2.596392809941774
C	-2.203426748938691	1.754980424235831	-3.015489735763675

H	-1.899498739328031	1.931003313573584	-4.038612887354921
C	-1.359976511614206	1.121721902231646	-2.140462249179792
C	-0.01824501729549672	0.6605926787291667	-2.512434950916393
C	0.4817824490667824	0.7264095862799352	-3.787041401434702
H	-0.1230407470131745	1.118646591073996	-4.593612221254457
C	1.783479099821239	0.2780379653931098	-4.071161829436831
C	2.347824843120327	0.3072217645920173	-5.365585833815256
H	1.761832927559798	0.6925704049691234	-6.191994422088704
C	3.622713063068739	-0.1525423362894255	-5.562329286576039
H	4.054548323476805	-0.1323788859786376	-6.556309515466841
C	4.388417037766485	-0.6562377893677332	-4.488377113651005
H	5.394308928850761	-1.014394626269369	-4.672973123771951
C	3.867364508486003	-0.6958141573343313	-3.223514558866063
H	4.446312734937969	-1.082510559177432	-2.392379184937099
C	2.554916147170921	-0.230109285010957	-2.997186517892855
C	1.960413925012303	-0.26628564356595	-1.7255621992893
H	2.526526438672298	-0.6588921698128807	-0.8899822557854268
N	-1.721971209636388	0.8960550899409376	-0.8299180173908062
N	0.7347211632291468	0.1464650390181449	-1.483104476989038
C	-1.845296623246403	-1.922477263098712	2.772395908558176
H	-0.8846884645075135	-2.357346109867444	3.043471661669178
H	-2.280987263610525	-2.460060610957463	1.933930936543366
H	-2.533878589227942	-1.960646866782089	3.613296643274097
S	-1.673802141698928	-0.2010169341142989	2.261105957526909
C	-0.8691121165985981	0.5154409185747081	3.72972950747809
H	0.1926272029382035	0.2662976853549588	3.724018072673569
H	-0.9719533058539879	1.59397919133606	3.600518103505578
C	-1.459294903964237	0.06171005892970272	5.053209670958381
H	-1.217232791103629	-0.9847746283939892	5.235726672069032
H	-0.9774779337303118	0.6479115885820277	5.842142915206382
O	-2.870901701229117	0.1610228170340286	5.131215462211711
H	-3.109650250974828	1.095982201588678	5.115647872970135
C	4.555317496604483	-2.613200219557823	3.179299539713295
C	5.495611468742798	-3.110518769450443	3.738768862794749
H	6.330862662385483	-3.553482201032657	4.23575063131157

**Table AIV.3.** Nuclear coordinates (Å) of [4]<sup>2+</sup> minimized at the DFT/PBE0/TZP/COSMO level in water.

Ru	-0.1386272406317239	-0.1728871042070829	0.5035144302613997
C	-1.531207832588218	-2.757551541285255	-0.5218677891833204
H	-2.24524195140538	-2.072423656384397	-0.9594936734264196
C	-1.675997338141558	-4.126788522859417	-0.6665537013911703
H	-2.518821125742265	-4.516548561628556	-1.221494992827352
C	-0.7357222835419303	-4.963510374135509	-0.09270650390146704
H	-0.8206172645433322	-6.039053545348915	-0.1819074272165476

C	0.327600867434155	-4.40433911662796	0.5972036675306582
H	1.081112834402843	-5.035730075210719	1.047221963386152
C	0.417181389439417	-3.026298802234863	0.7064797035326705
C	1.523544100393143	-2.343645777494022	1.399681667297997
C	2.60281546127147	-2.953909223144666	2.013882645173779
H	2.693778989773381	-4.030211278213327	2.045507268159674
C	3.586680046685451	-2.153612667407497	2.600332753500335
C	3.467366308803155	-0.7634784683642144	2.545008518012292
H	4.228782042746849	-0.140463455060503	2.991546172989982
C	2.364411606499144	-0.208128963985455	1.920371284871431
C	2.073021538164229	1.227764094915739	1.792468720753408
C	2.913329210355384	2.210394634842851	2.291747916711746
H	3.841052838678216	1.938060530988706	2.775454190403192
C	2.551363903356648	3.540969230760397	2.171238195072737
H	3.197464461409832	4.319428153682459	2.557460879337389
C	1.349901365986842	3.852472938321198	1.559496479888117
H	1.016793496740082	4.876031773882573	1.450620045206895
C	0.5603224057869644	2.825035087576484	1.074174813912468
H	-0.3838218829951246	3.03477308698064	0.5916879604034408
N	-0.5216293835766055	-2.206354272701332	0.155047587701827
N	1.42392386809426	-1.001338278164124	1.379606451031281
N	0.902153017557386	1.537635809657449	1.171604041385557
C	-3.055834875307845	0.4626045292003551	-0.1810695788521076
H	-3.209630041363103	-0.2996710710699634	0.5728062088056303
C	-4.167432105358489	1.128597058235949	-0.7100348312821501
C	-5.487296559209559	0.8327259701647999	-0.295188126423042
H	-5.649178011916466	0.05867265660458093	0.4465769691020724
C	-6.535715999421286	1.52738318379346	-0.8292910015529869
H	-7.549881263621116	1.310463002625711	-0.5151715060764455
C	-6.306593740841212	2.535264578067364	-1.795257130406514
H	-7.15257921015576	3.073712147075788	-2.207278291116568
C	-5.040420298126659	2.839731075786094	-2.214178389097393
H	-4.87024200718328	3.61229575551311	-2.955176724920513
C	-3.935014326520808	2.141688821798193	-1.675169778541516
C	-2.606826972902733	2.373549805060031	-2.057235752150853
H	-2.380759725806299	3.106536976228194	-2.822597109822626
C	-1.583380804479718	1.665282006510563	-1.475154195189084
C	0.6905300303639436	1.006677217215075	-2.179636241328131
C	1.44494098073945	1.188420920758492	-3.313804367195852
H	1.251664988497113	2.043527364600589	-3.950555883023393
C	2.443378017206619	0.2660112487094222	-3.657204325507613
C	3.263160180950746	0.3825685116658833	-4.804067621013719
H	3.141168472402774	1.237076690469951	-5.45994451635968
C	4.196855512988538	-0.5806372607944117	-5.07424441519364
H	4.824449937422036	-0.4888223908618392	-5.953518405341535
C	4.362405104514678	-1.6998334163743	-4.225019509237881

H	5.111492072668192	-2.445424680994455	-4.46387209501423
C	3.582462178063681	-1.841231656677604	-3.112471637118505
H	3.69794148806238	-2.69522755607542	-2.453977974064316
C	2.608949485465777	-0.8600149567651078	-2.811330471509063
C	1.792650759123127	-0.9500685301219021	-1.679588086642163
H	1.914030288175524	-1.799387189712885	-1.020944257503333
N	-1.797857072116594	0.7287145290616694	-0.5059219985511247
N	0.8825410455729213	-0.05063428862247677	-1.341413318084977
C	-0.9111555926772327	-1.705518949397671	3.524696615773443
H	0.1164597094902461	-1.580235719766127	3.861243941079369
H	-1.006703992411256	-2.604271538494385	2.920455738034669
H	-1.585396778980701	-1.785680575273563	4.374319552610008
S	-1.451298510998732	-0.3169425161030515	2.509487491827477
C	-1.105690736513914	1.072592885094073	3.63265678449639
H	-0.03282458910066699	1.265640227898179	3.659755221938439
H	-1.599986077124376	1.928814860253459	3.17030927504548
C	-1.595596377644129	0.8542962781429553	5.05325523832981
H	-0.982706794336715	0.1042891559679136	5.552218599118054
H	-1.457715785829314	1.796290445726972	5.593716128308011
O	-2.93425964451962	0.3989196147537361	5.149703473115839
H	-3.516598099268223	1.102244418313223	4.837021328797476
C	4.704407288681812	-2.748790957023131	3.249952879084972
C	5.64754672222498	-3.246019440854954	3.804782716088554
H	6.486489020537687	-3.687566003023037	4.296774628787286
N	-0.2688007680057821	1.954491933437816	-1.836436878591254
H	-0.2315834179832435	2.747514473869215	-2.461243340831531

## AIV.10 References

- 1 C. Ruppin and P. H. Dixneuf, *Tetrahedron Lett.* **1986**, 27 (52), 6323-6324.
- 2 R. Wirth, J. D. White, A. D. Moghaddam, A. L. Ginzburg, L. N. Zakharov, M. M. Haley and V. J. DeRose, *J. Am. Chem. Soc.* **2015**, 137 (48), 15169-15175.



# APPENDIX V: SUPPORTING INFORMATION FOR CHAPTER 5

## AV.1 Synthesis of $[\text{Ru}(\text{Ph}_2\text{phen})(\text{mtmp})(\text{RCC-bpy})](\text{PF}_6)_2$ , **[2a]** $(\text{PF}_6)_2$

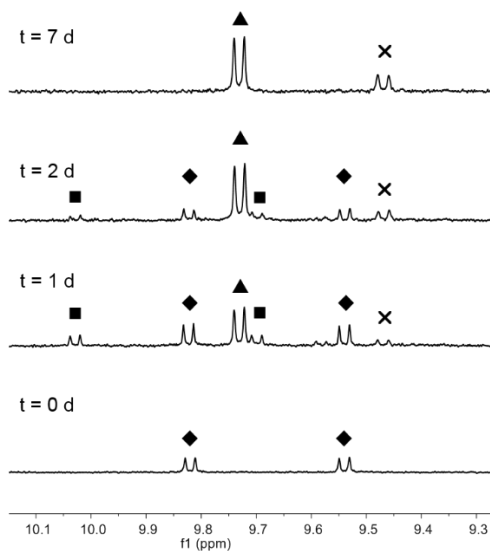


**Figure AV.1.**  $^1\text{H}$  NMR evolution during the reaction of  $[\text{7}](\text{ClO}_4)_2$  and RCC-bpy in methanol- $d_4$  over 7 d at 70 °C. **Key:** ◆ indicates the starting compound  $[\text{7}](\text{ClO}_4)_2$ , ■ indicates an intermediate, ▲ and × indicate the two isomers of **2a**.

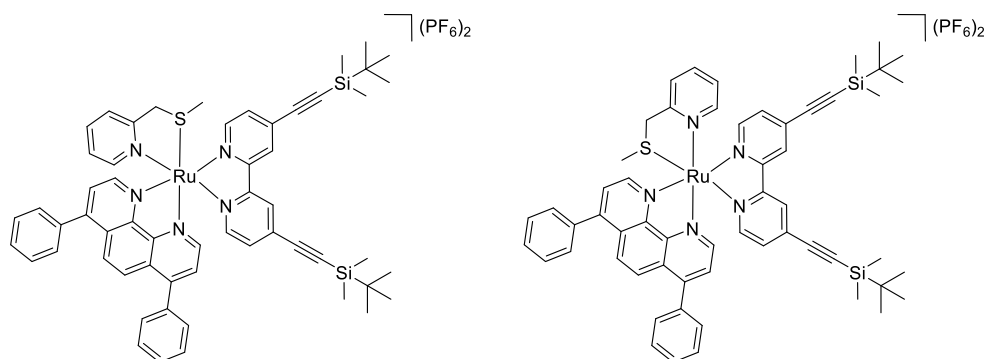


**Figure AV.2.** The two isomers of **[2a]** $(\text{PF}_6)_2$ . Assignment of the two isomers was attempted by 2D NMR NOESY, but was unsuccessful.

## AV.2 Stability of RCC-bapbpy over time in solution

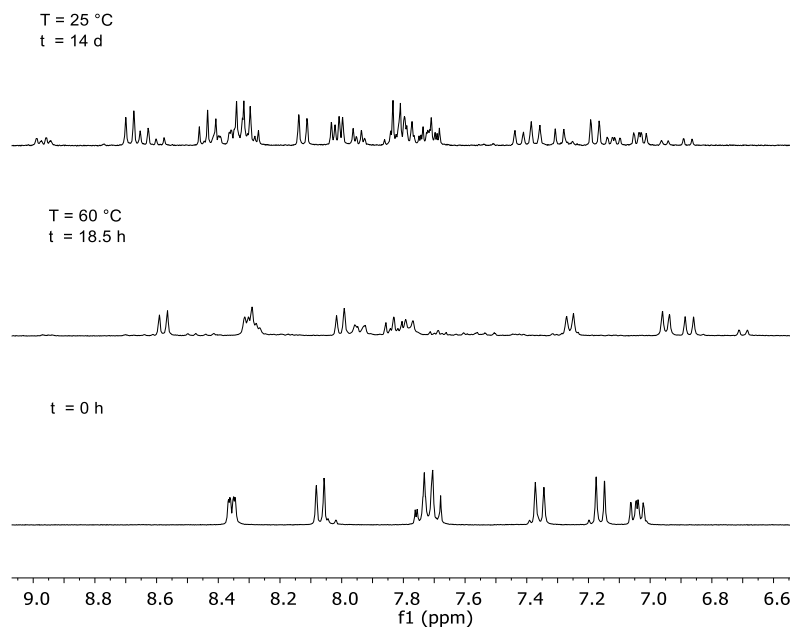
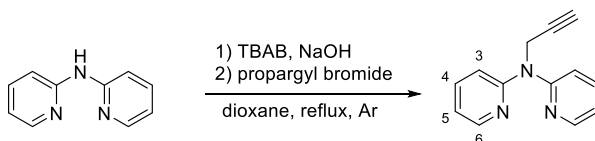


**Figure AV.3.**  $^1\text{H}$  NMR spectra of a solution of RCC-bapbpy in ethanol- $\text{d}_6$  over time at room temperature and at 60 °C.

### AV.3 Synthesis and rearrangement of HCC-dpa

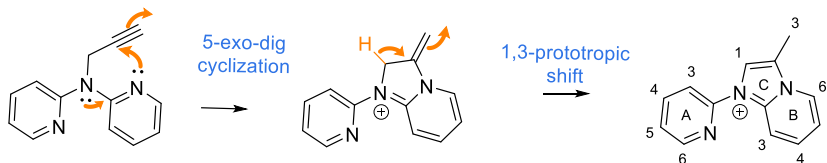
The reaction procedure was adapted from literature.<sup>1</sup> The reaction was prepared under dry and degassed conditions. Dipyriddyamine (0.150 g, 0.880 mmol), tetrabutyl ammonium bromide (TBAB, 0.284 g, 0.880 mmol), and sodium hydroxide (0.176 g, 4.40 mmol) were dissolved in dry dioxane (30 mL), and the reaction mixture was heated to reflux for 1 h while stirring. Thereafter, propargyl bromide (0.1 mL, 0.88 mmol) was added dropwise and the reaction mixture was reacted further for 4 h at reflux. The reaction mixture was cooled down to room temperature, and quenched with 1 M HCl until the pH was below 2. After extraction with pentane (2 times 30 mL), the aqueous layer was basified using solid sodium hydroxide pellets (pH > 12). Then, the product was extracted with dichloromethane (twice 30 mL). evaporation of the solvent yielded the crude product that was purified by column chromatography (silica, dichloromethane/methanol 99/1- 90-10. The pure product was obtained in a yield of 3% (7 mg, 0.033 mmol).



**Scheme AV.1.** Reaction procedure of the synthesis of HCC-dpa.

<sup>1</sup>H NMR (300 MHz, chloroform-*d*, 298 K)  $\delta$  8.38 (ddd,  $J = 5.0, 2.0, 0.9$  Hz, 2H, 6), 7.55 (ddd,  $J = 8.4, 7.2, 2.0$  Hz, 2H, 4), 7.20 (dt,  $J = 8.4, 0.9$  Hz, 2H, 3), 6.90 (ddd,  $J = 7.2, 4.9, 1.0$  Hz, 2H, 5), 4.99 (d,  $J = 2.4$  Hz, 2H, N-CH<sub>2</sub>), 2.13 (t,  $J = 2.4$  Hz, 1H, CCH). <sup>13</sup>C NMR (75 MHz, chloroform-*d*, 298 K)  $\delta$  156.3 (2), 148.5 (6), 137.5 (4), 117.7 (5), 114.6 (3), 81.2 (CCH), 70.5 (CCH), 37.7 (N-CH<sub>2</sub>). ES MS  $m/z$  (calc.): 210.2 (210.1, [M + H]<sup>+</sup>).

After several days in solution, new peaks of a decomposition product appeared in the <sup>1</sup>H NMR spectrum. The number of these new peaks and integration indicated that the new product is not symmetric. Literature research led to the conclusion that an intramolecular rearrangement took place (Scheme AV.3).<sup>2,3</sup> In addition, examples were found of the same rearrangement for non-terminal alkynes. A protecting group would therefore not prevent the formation of the new product.



**Scheme AV.2.** Intramolecular rearrangement of alkyne-functionalized Hdpa ligand.

<sup>1</sup>H NMR (300 MHz, chloroform-*d*, 298 K)  $\delta$  9.43 (s, 1H, C1), 8.99 (dt,  $J = 9.3, 1.1$  Hz, 1H, B3), 8.81 (dt,  $J = 6.8, 1.1$  Hz, 1H, B6), 8.58 (ddd,  $J = 4.9, 1.9, 0.8$  Hz, 1H, A6), 8.42 (d,  $J = 8.3$  Hz, 1H, A3), 8.11 (td,  $J = 8.0, 1.9$  Hz, 1H, A4), 8.04 (ddd,  $J = 9.3, 7.1, 1.2$  Hz, 1H, B4), 7.68 (td,  $J = 6.9, 1.1$  Hz, 1H, B5), 7.44 (ddd,  $J = 7.5, 4.9, 0.8$  Hz, 1H, A5), 2.85 (d,  $J = 1.1$  Hz, 3H, C3). <sup>13</sup>C NMR (75 MHz, chloroform-*d*, 298 K)  $\delta$  148.7 (A6), 140.9 (A4), 134.9 (B4), 127.3 (B6), 124.2 (A5), 122.2 (C1), 119.2 (B5), 117.2 (A3), 115.3 (B3), 9.5 (C3), all three quaternary peaks are not reported.

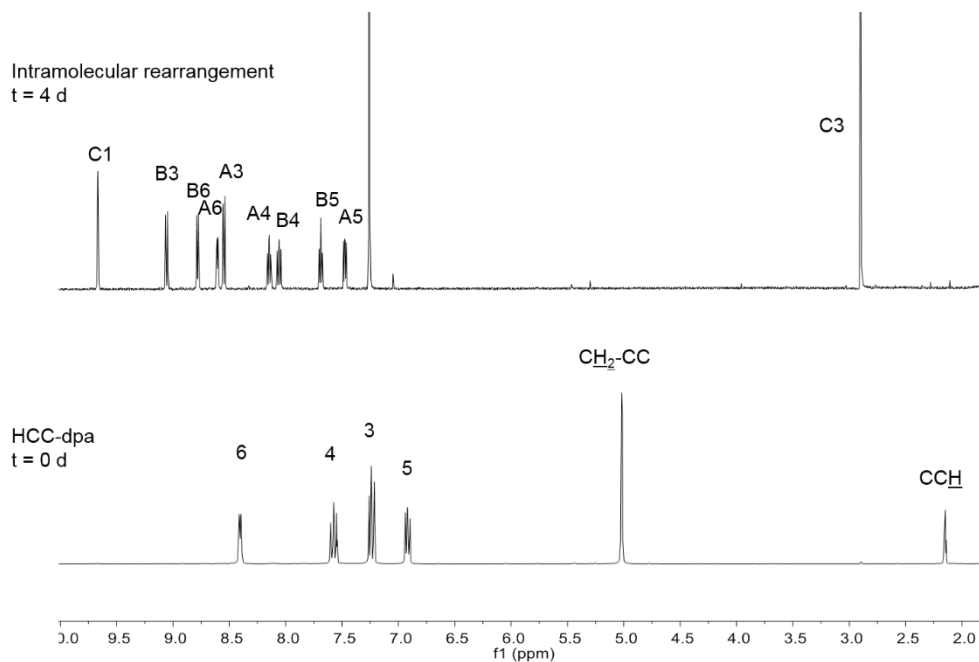
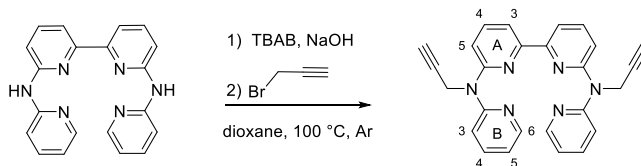


**Figure AV.4.**  $^1\text{H}$  NMR spectra of a solution of the alkyne-functionalized HCC-dpa ligand in chloroform- $d$  over time at room temperature.

#### AV.4 Synthesis and reaction with HCC-babppy



**Scheme AV.3.** Reaction procedure of the synthesis of HCC-babppy.

The reaction was performed under dry, degassed conditions.  $\text{H}_2\text{babppy}$  (300 mg, 0.880 mmol, 1 eq), tetrabutyl ammonium bromide (TBAB, 284 mg, 0.880 mmol, 1 eq), and NaOH powder (176 mg, 4.40 mmol, 5 eq) were dissolved in fresh, dry dioxane (40 mL). The reaction mixture was heated up to 100 °C (reflux) and stirred. After 1 h, a solution of propargyl bromide (0.2 mL, 1.76 mmol, 2 eq) was added dropwise *via* a syringe to the reaction mixture. The reaction continued for another 4 h. Then, the reaction mixture was cooled down to room temperature, and quenched with 1 M HCl to decrease the pH below 2. This mixture was extracted with pentane ( $2 \times 60$  mL), the aqueous layer was basified using solid sodium hydroxide to pH > 12, and the aqueous layer was extracted twice with dichloromethane ( $2 \times 60$  mL). The combined dichloromethane layers were concentrated *in vacuo* to yield the crude product which was purified by column chromatography using silica gel and dichloromethane/methanol (99:1) as eluent. Yield: 110 mg (0.265 mmol, 31%).

$^1\text{H}$  NMR (300 MHz,  $\text{DMSO-}d_6$ , 298 K)  $\delta$  8.39 (ddd,  $J = 4.9, 2.0, 0.9$  Hz, 2H, B6), 7.93 (dd,  $J = 7.6, 0.9$  Hz, 2H, A3), 7.84 (t,  $J = 7.9$  Hz, 2H, A4), 7.76 (ddd,  $J = 8.4, 7.2, 2.0$  Hz, 2H, B4), 7.38 (dt,  $J = 8.4, 0.9$  Hz, 2H, B3), 7.29 (dd,  $J = 8.2, 0.9$  Hz, 2H, A5), 7.06 (ddd,  $J = 7.3, 4.9, 0.9$  Hz, 2H, B5), 5.05 (d,  $J = 2.4$  Hz, 4H, N- $\underline{\text{CH}_2}$ -), 3.06 (t,  $J = 2.3$  Hz, 2H, - $\underline{\text{CCH}}$ ).  $^{13}\text{C}$  NMR (75 MHz,  $\text{DMSO-}d_6$ , 298 K)  $\delta$  155.6 + 155.0 + 153.5 (A2 + A6 + B2), 148.0 (B6), 148.8 (A4), 137.9 (B4), 118.1 (B5), 114.8 (B3), 114.2 (A5), 114.0 (A3), 101.3 (- $\underline{\text{CCH}}$ ), 73.2 (- $\underline{\text{CCH}}$ ), 37.1 (N- $\underline{\text{CH}_2}$ -). ES MS  $m/z$  (calc.): 417.3 (417.2,  $[\text{M} + \text{H}]^+$ ).

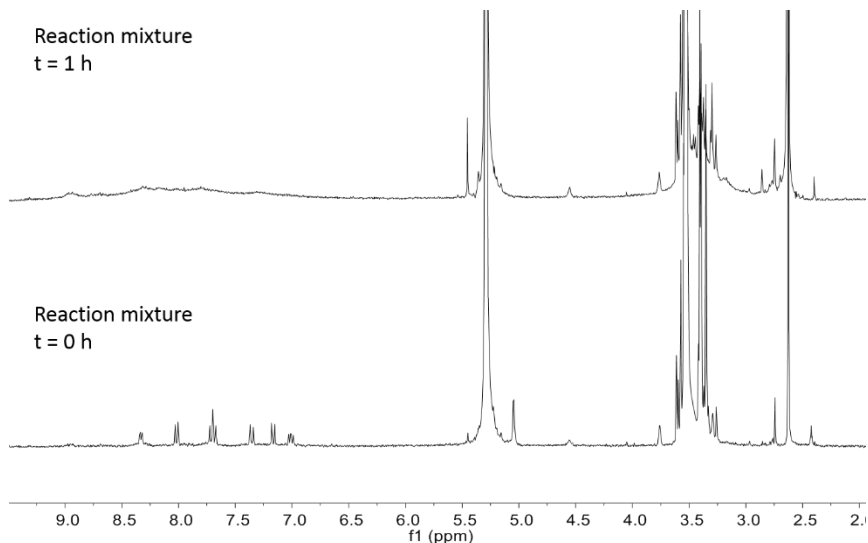


**Figure AV.5.**  $^1\text{H}$  NMR evolution during the reaction of  $[\text{Ru}(\text{DMSO})_4(\text{Cl})_2]$  and HCC-bapby in ethanol- $d_6$  at 60 °C.

### AV.5. Enol ester formation on RCC-bapby

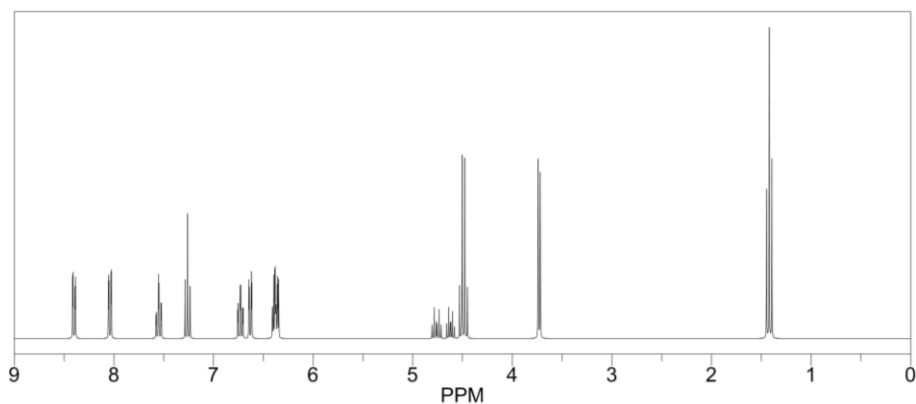


**Figure AV.6.** Predicted  $^1\text{H}$  NMR spectrum for enol ester on HCC-bapby ligand.

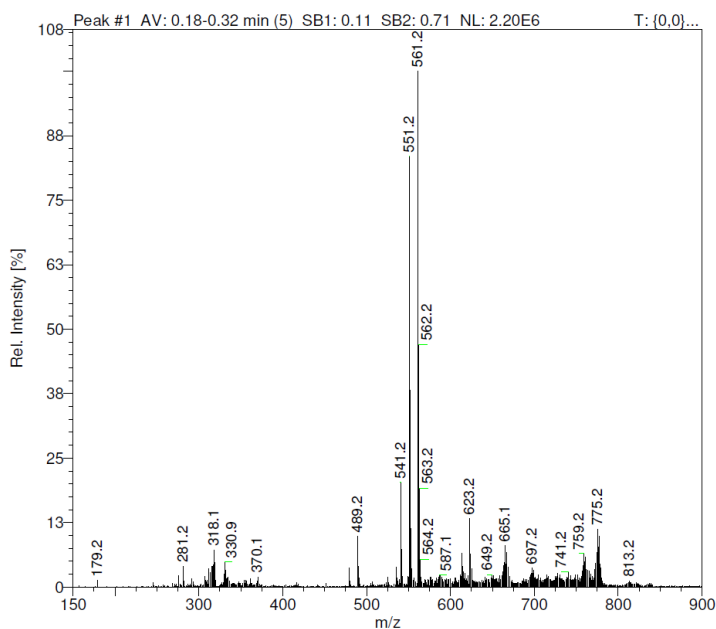


**Figure AV.7.** MS spectrum of the reaction mixture after reaction of  $[\text{Ru}(\text{DMSO})_4(\text{Cl})_2]$  and RCC-bapby in ethanol at 60 °C for 18.5 h.

## AV.6 References

- 1 S. Ogawa, N. Kishii, and S. Shiraishi, *J. Chem. Soc., Perkin Trans. 1* **1984**, (0), 2023-2025.
- 2 M. Chioua, E. Soriano, L. Infantes, M. L. Jimeno, J. Marco-Contelles, and A. Samadi, *Eur. J. Org. Chem.* **2013**, 2013 (1), 35-39.
- 3 D. Chandra Mohan, S. Nageswara Rao, and S. Adimurthy, *J. Org. Chem.* **2013**, 78 (3), 1266-1272.

# SAMENVATTING

---

## **PACT als selectieve behandeling tegen kankercellen**

Chemotherapie gaat vaak gepaard met bijwerkingen die worden veroorzaakt door de slechte selectiviteit van het medicijn: naast de kankercellen worden ook gezonde cellen aangevallen. Om deze bijwerkingen tegen te gaan is het belangrijk om de toxiciteit van het medicijn specifiek op het tumorweefsel te richten. Dat kan bijvoorbeeld door het medicijn aan een eiwit te laten binden dat alleen in de kankercellen voorkomt. In een andere aanpak wordt het medicijn in inactieve vorm (de zogenoemde *prodrug*) toegediend. Het verspreidt zich door het hele lichaam en vervolgens wordt het alleen rond de tumor geactiveerd. Activatie kan onder andere met zichtbaar licht. Van deze zogenoemde fotherapie bestaan twee varianten. Bij fotodynamische therapie (*photodynamic therapy*, PDT) resulteert de bestraling van de *prodrug* in de vorming van reactieve zuurstofdeeltjes (*reactive oxygen species*) die toxisch zijn voor cellen. Bij de zuurstofafhankelijke foto-actieve chemotherapie (*photoactivated chemotherapy*, PACT) leidt de interactie met licht tot het verbreken van een binding in de *prodrug* wat leidt tot de vorming van het actieve medicijn. Deze actieve stof bindt aan specifieke onderdelen van de cel waardoor verschillende mechanismen in werking gezet worden die uiteindelijk tot de dood van de cel leiden. Voor dit proefschrift zijn verschillende foto-actieve metaalcomplexen op basis van ruthenium onderzocht om erachter te komen of ze geschikt zijn als PACT-medicijn.

## **Het gedrag van metaalcomplexen in de cel**

Wanneer de biologische werkwijze van een metaalcomplex in de cel bekend is kan ook het ontwerp van de verbinding worden aangepast om bijvoorbeeld de interacties met de *targets* in de cel te verbeteren. Verschillende methoden kunnen informatie opleveren over de interacties van het metaalcomplex in de cel. De interactie met geïsoleerde biomoleculen wordt bestudeerd met massaspectrometrie, UV/VIS-spectroscopie of röntgendiffractie. Proteomica helpt om het effect van het medicijn op de expressie van eiwitten in cellen te bepalen. Om uiteindelijk een goed beeld te krijgen van het effect van een medicijn moeten verschillende methoden gecombineerd worden. Bovendien zijn er nieuwe methoden nodig waarmee een medicijn onder fysiologisch-relevante omstandigheden bestudeerd wordt. Voor dit proefschrift is de intracellulaire verspreiding van een ruthenium-gebaseerd

PACT-medicijn onderzocht met behulp van een fluorofoorlabeling. Dit label is gekoppeld aan de rutheniumverbinding via een door koper gekatalyseerde azide-alkynycycloadditie (CuAAC).

### **Alkynfunctionalisering van foto-activeerbare rutheniumcomplexen**

Om een label zoals een fluorofoor door middel van CuAAC aan een rutheniumcomplex te koppelen is het noodzakelijk om aan het complex eerst een zogenoemde “klikgroep” aan te brengen, waaraan later het label gekoppeld kan worden. Wij hebben besloten om het kleinst mogelijke handvat te gebruiken, een alkyngroep. Het aanbrengen van een alkyn blijkt doorgaans een lage opbrengst te hebben vanwege nevenreacties. Bovendien vindt de reactie plaats in aanwezigheid van zilverionen. Echter, zelfs zeer lage concentraties zilverionen in een medicijn kunnen dodelijk zijn voor de mens, waardoor deze vermeden moeten worden bij het synthetiseren van stoffen die bedoeld zijn voor therapeutisch doeleinden. Zoals beschreven in **hoofdstuk 2** hebben wij een nieuwe syntheseroute ontwikkeld om metaalcomplexen met een alkyngroep te functionaliseren. We hebben de alkynbeschermgroep tert-butyldimetylsilyl (TBDMS) geïntroduceerd. Deze is zowel bestand tegen de eventuele nevenreacties van het alkyn met het rutheniumion als ook tegen de reactiecondities gedurende het syntheseproces. Terwijl het dus wel een sterke beschermgroep is, is TBDMS makkelijk van het alkyn te splitsen door middel van een reactie met fluorideionen. Het gebruik van zilverionen is in deze nieuwe syntheseroute niet nodig.

### **Verbeterde PACT-medicijnen gebaseerd op ruthenium**

Om als PACT-medicijn in aanmerking te komen moet een verbinding stabiel zijn in het donker, geactiveerd worden door bestraling met licht en op dat moment cytotoxisch worden. Van het complex  $[\text{Ru}(\text{tpy})(\text{bpy})(\text{Hmte})](\text{PF}_6)_2$  is bekend dat het lichtactiveerbaar is, maar het wordt slecht opgenomen door de cel waardoor het niet giftig kan zijn. In **hoofdstuk 3** beschrijven we de ontwikkeling van rutheniumcomplexen die beter door de cel worden opgenomen. Dat lukt door het aromatische oppervlak van het bidentaat ligand te vergroten waardoor het complex een verhoogde lipofiliciteit krijgt. Dit zorgt voor verbeterde opname van de verbinding door de cel en dus voor een hogere cytotoxiciteit na lichtactivatie, terwijl het complex nog steeds stabiel is in het donker. Het toevoegen van een niet-coördinerende secundaire amine aan het bidentaat ligand resulteert in een rutheniumcomplex met een verbeterde lichtactivatie. Dit laat zien dat PACT-



eigenschappen van het complex kunnen worden afgesteld door de liganden aan te passen.

### **Het effect van de klikgroep op het rutheniumcomplex**

Via de alkyngroep kunnen labels aan het rutheniumcomplex gebonden worden die het complex bijvoorbeeld zichtbaar maken in de cel, of waarmee het complex geïsoleerd kan worden. Om de werking van het originele rutheniumcomplex te onderzoeken via een complex mét een alkyngroep moeten de fotofysische en biologische eigenschappen van de complexen met elkaar vergeleken worden (**hoofdstuk 2 en 4**). De vergelijking van de kristalstructuren, de mate van lichtactivatie en de vorming van singletzuurstof laten zien dat de klikgroep geen significant effect heeft op de geometrie en de eigenschappen van het complex. Alle complexen zijn zeer slechte kandidaten voor fotodynamische therapie omdat ze maar in beperkte mate zorgen voor de vorming van singletzuurstof. Toch resulteert de aanwezigheid van de alkyngroep in een verdubbeling van de rutheniumconcentratie in de cel wat kan worden toegeschreven aan de verhoogde lipofiliciteit van het complex. Het kan geconcludeerd worden dat het toevoegen van een alkyngroep maar een minimale invloed heeft op de eigenschappen van het complex.

### **Het zichtbaar maken van niet-lichtuitzende PACT-medicijnen**

Doorgaans zijn PACT-medicijnen niet emissief door het doven van de thermisch gegenereerde  $^3\text{MC}$ -toestand. Daardoor is het niet mogelijk deze complexen in de cel te volgen met behulp van een microscoop. Dat kan echter wel door een fluorofoor te koppelen aan de verbindingen. Via de functionalisatie van het complex met een alkyngroep kan binnen de gefixeerde cel een fluorofoor aan het rutheniumcomplex gebonden worden. Op deze manier waren we in staat om het complex zichtbaar te maken nadat het aan het eiwit BSA gebonden was (**hoofdstuk 2**). Pas na lichtactivatie verliest het complex zijn beschermgroep en komt er een coördinatieplek vrij waar het eiwit kan binden. Wanneer het complex in het donker in de niet-actieve toestand werd gehouden was er geen fluorescentiesignaal zichtbaar. De interactie tussen actief medicijn en BSA kon niet worden waargenomen met traditionele technieken zoals massaspectrometrie en UV/VIS-spectroscopie, technieken die geschikt zijn om sterkere covalente interacties te volgen. Dat betekent dat de interactie tussen het rutheniumcomplex en het eiwit relatief zwak is en dat deze zwakke binding tijdens het gebruik van de genoemde traditionele technieken verbroken wordt. Labeling met een fluorofoor in combinatie

met gelelektroforese daarentegen is zacht genoeg om de zwakke interactie tussen het metaal gebaseerde medicijn en het eiwit intact te houden.

Nadat de interactie tussen het rutheniumcomplex met geïsoleerde eiwitten was bestudeerd (hoofdstuk 2) gingen we de interactie met kankercellen onderzoeken (**hoofdstuk 4**). Het labelen van het complex werd wederom via CuAAC gedaan, deze keer in gefixeerde cellen. Door het fluorofoor pas in de cel aan het complex met alkyngroep te koppelen, en niet al daarvoor, kan de biologische activiteit van het complex behouden worden: de opname, verspreiding en interactie in de cellen wordt niet door de fluorofoorgroep beïnvloed waardoor het gedrag van het complex zonder alkyngroep zoveel mogelijk wordt benaderd.

Na het binden van de fluorofoor werd een fluorescentiesignaal in de gefixeerde cellen waargenomen, maar alleen als het complex voor de koppeling met licht was geactiveerd. Zonder activatie kan het complex niet binden aan eiwitten of andere celonderdelen en wordt het na de koppeling uit de cel gewassen. Dit experiment vormt opnieuw bewijs dat de interactie van het complex met eiwitten via licht kan worden aangestuurd. De resultaten laten bovendien zien dat de complexen de kern van de cel niet binnengaan. De complexen blijven in het cytoplasma in de buurt van de kern. Kleuring van de celonderdelen buiten de kern laat zien dat de complexen niet in de mitochondria of het endoplasmatisch reticulum terechtkomen. De verdeling van fluorescentiesignalen geeft aan dat de complexen zich 24 uur na activering in het Golgicomplex bevinden.

### **Algemene toepassing van de methode met klikgroep**

In **hoofdstuk 5** beschrijven wij de koppeling van een alkyngroep aan drie verschillende polypyridyl-rutheniumcomplexen. De synthese is uitdagend omdat de alkyngroep kan reageren met het centrale rutheniumion dat vrije bindingsplekken heeft, zelfs in de aanwezigheid van een TBDMS-beschermgroep. Wanneer het gebruikte complex twee vrije bindingsplekken heeft is de kans op bijproducten groter bij het koppelen van de alkyngroep. In het algemeen vinden deze ongewenste reacties plaats als de reactiecondities niet worden aangepast. Het optimaliseren van de condities is niet eenvoudig en tijdrovend, maar is wel mogelijk. Ook andere metaalcomplexen kunnen daardoor uitgerust worden met een klikgroep.

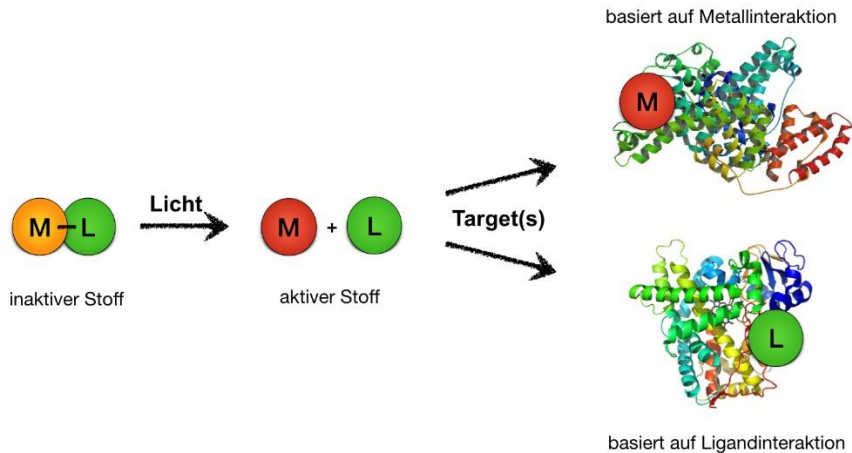
# ZUSAMMENFASSUNG

---

## **PACT als selektive Krebsbehandlung**

Krebs wird mit drei verschiedenen Methoden behandelt: der operative Entfernung des Tumorgewebes, der Strahlungs-therapie und einer Chemokur. Die traditionelle Chemokur beinhaltet giftige chemische Substanzen, die die Zellteilung der Zellen angreift und dadurch zu deren Tod führt. Dabei wird kein Unterschied zwischen gesunden Zellen und Krebszellen gemacht, wodurch Nebenwirkungen, wie Übelkeit und Haarausfall, auftreten. Um die Krebsbehandlung für den Patienten erträglicher zu machen, muss daher ein Medikament entwickelt werden, das hauptsächlich Krebszellen angreift und keine Wirkung auf gesunde Zellen hat. Diese Selektivität kann auf unterschiedliche Weise erreicht werden: entweder ist der wirksame Stoff auf einen Bestandteil in den Zellen gerichtet, der nur in Krebszellen vorkommt (biologische Selektivität) oder das Medikament wird nur in der Nähe der Krebszellen aktiviert und wirkt daher nur lokal (physische Selektivität).

Unserer Arbeitsgruppe hat sich auf Letzteres spezialisiert, die physische Selektivität. Unsere Chemotherapeutika beinhalten das Metall Ruthenium und verschiedene organische Seitengruppen (Liganden genannt), die an das Metall gebunden sind. Die resultierenden Stoffe zeigen keinerlei giftige Eigenschaften solange sie in Dunkelheit gehalten werden. Erst nach Lichtbestrahlung wird eine der Verbindungen zwischen Metall und Ligand zerbrochen. Diese chemische Umwandlung führt zur Bildung des aktiven Chemotherapeutikums. Jetzt erst ist der Stoff im Stande um in den Zellen eine Bindung mit Zellbestandteilen (Proteinen) anzugehen. Die Verbindung zwischen aktiviertem Stoff und Protein führt zu einer Behinderung des natürlichen Zellmechanismus und letztendlich zum kontrollierten Zelltod. Auf diese Weise kann man mit Hilfe von Licht lokal die Krebszellen bekämpfen, und gesunde Zellen von der Behandlung ausschließen. Diese Methode der Krebsbehandlung nennt man lichtaktivierbare Chemotherapie (*photoactivated chemotherapy, PACT*).



**Figur 1.** Licht verursacht die Spaltung einer Bindung im inaktive Chemotherapeutikum zwischen Metall (M) und Ligand (L). Dadurch kommt es zur Umwandlung in die aktive Form des Chemotherapeutikums. Erst im aktivem Zustand kann es an Zellbestandteile binden und damit den Zellmechanismus stören und zum Zelltod führen.

### Die Wirkungsweise eines Chemotherapeutikums untersuchen

Abhängig vom Chemotherapeutikum und der Krebsart kann ein anderes Protein den zellulären Bindungspartner (Target genannt) des aktivierte Medikaments darstellen und einen spezifischen Wirkungsmechanismus einleiten. Je mehr man über die Wirkungsweise und das Target des Medikamentes weiß, desto besser. Diese Informationen ermöglichen es nämlich um den wirksamen Stoff noch effizienter zu machen und eventuell auftretende Nebenwirkungen frühzeitig zu beseitigen. Es gibt bereits verschiedene Methoden, die Wirkungsweise eines Medikamentes zu erforschen. So kann man zum Beispiel untersuchen, welchen Effekt das Medikament auf die Zellen hat. Je nachdem welche Proteine in einer erhöhten, niedrigen, oder gleichbleibenden Anzahl in den Zellen zu finden sind, lässt sich schlussfolgern auf welchen Zellmechanismus der Stoff Einfluss hat. Außerdem kann das Targetprotein identifiziert werden. So werden oft vorkommende Proteine aus der Zelle isoliert und die Bindung derer mit dem Medikament untersucht. Allerdings beinhaltet eine Zelle zu viele Proteine um sie alle nacheinander ausprobieren zu können. Daher ist es sinnvoll um die Auswahl möglicher Proteintargets im Vorherein zu begrenzen. Mit Hilfe der Lokalisierung des Chemotherapeutikums in der Zelle ist eine Eingrenzung vielversprechender Proteine möglich. Abhängig von der Stelle in der Zelle (in der Nähe von Zellorganellen) sind bestimmte Proteine wahrscheinlicher als andere.

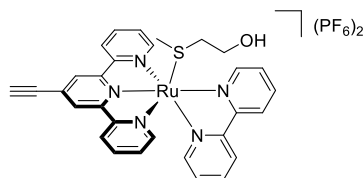
## Lokalisierung eines unsichtbaren Stoffes

Die von uns hergestellten Rutheniumstoffe haben jedoch keine fluoreszierten Eigenschaften und sind daher unter einem Mikroskop nicht sichtbar. Darum ist es notwendig um einen Fluorophor, also ein lichtaussendenden Stoff, an unser Chemotherapeutikum zu koppeln, um dieses in den Zellen zu sehen. So ein Fluorophor kann aber die Eigenschaften des Medikaments verändern: Die Aufnahme des Stoffes durch die Zelle, die Verteilung in der Zelle und die Interaktion mit dem Target können durch die lichtgebende Gruppe stark beeinflusst werden.

Meine Aufgabe war es eine Methode zu entwickeln, die es uns ermöglicht die unsichtbaren Chemotherapeutika in den Zellen zu lokalisieren und zu erfahren mit welchen Zellorganellen sie interagieren, um Rückschlüsse auf ihre Wirkungsweise ziehen zu können. Anstelle den Fluorophor vor der Behandlung an das Medikament zu koppeln und damit eine Beeinflussung der Stoffeigenschaften zu riskieren, wollten wir den Fluorophor erst dann an das Chemotherapeutikum koppeln, wenn es bereits von der Zelle aufgenommen wurde und an sein Target gebunden ist. Die Kopplung erfolgt also in der Zelle.

## Die Herstellung des alkynierten Chemotherapeutikums

Um den Fluorophor in der Zelle an das Chemotherapeutikum koppeln zu können, muss der wirksame Stoff mit einem minimalen „Griff“ versehen werden, an den die Kopplung erfolgen kann. Dieser „Griff“ war in unserem Falle ein Alkyn ( $C\equiv C$ ), das erst an das Chemotherapeutikum befestigt werden musste. Alle Anleitungen, die in der Literatur zur Herstellung vergleichbarer Stoffe zu finden sind, waren mit niedriger Ausbeute und vielen Nebenprodukten verbunden. Wir haben es geschafft um eine neue Herstellungsrouten zu entwickeln, die durch gezielten Einsatz von chemischen Schutzgruppen zu einer höheren Ausbeute für das alkynierte Produkt führte.

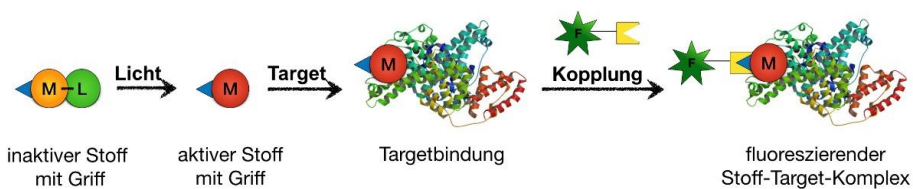


**Figur 2.** Das Chemotherapeutikum, basiert auf dem Metall Ruthenium. An der linken Seite wurde das Alkyn als Griff für die Kopplungsreaktion angebracht.

Nach der Herstellung haben wir überprüft, ob das Chemotherapeutikum mit Alkyn die gleichen Eigenschaften hat wie das Medikament ohne. Dies ist notwendig um feststellen zu können ob das kleine Alkyn allein nicht bereits einen Einfluss auf die Stoffeigenschaften hat. Verschiedene Analysetechniken wurden von uns verwendet, die uns Aufschluss über die Struktur des Stoffes lieferten, seine Zusammensetzung zeigte und seine Fähigkeit mit Hilfe von Licht aktiviert zu werden bestätigten. Die Experimente ergaben, dass das Alkyn keinen maßgeblichen Einfluss auf diese Eigenschaften hat und man davon ausgehen kann, dass sich das alkynierte Chemotherapeutikum genauso verhält wie das ursprüngliche ohne Alkyn.

### Das Unsichtbare sichtbar machen

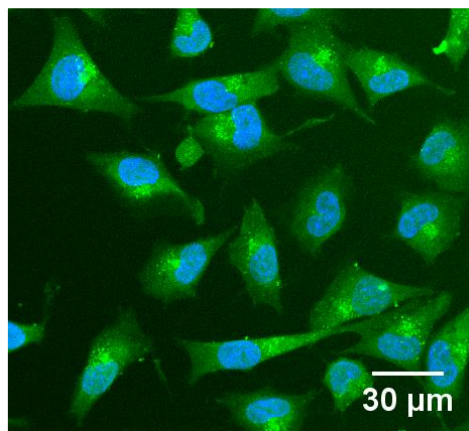
Danach wollten wir die Kopplung von Fluorophor und alkynierten Chemotherapeutikum testen. Dies taten wir unter Benutzung des Transporterprotein *bovine serum albumin* (BSA). BSA dient in diesem Falle als Modeltarget an das das Chemotherapeutikum nach Lichtaktivierung binden kann. Nach dieser Bindung wurde der Fluorophor zum Versuch hinzugeben und konnte die Kopplungsreaktion stattfinden. Wir kamen zu zwei wichtigen Erkenntnissen: 1) die Kopplung war erfolgreich. Wir sahen ein fluoreszentes Signal, das dem Fluorophore-Chemotherapeutikum-BSA Komplexes zuzuschreiben war. Und 2) ohne Lichtaktivierung war keine Bindung zwischen dem Chemotherapeutikum und BSA möglich. Dementsprechend erfüllt unser Stoff die Kriterien eines lichtaktivierbaren Chemotherapiestoffes (kein Effekt im Dunkeln, aber Wirkung nach Lichtaktivierung).



**Figur 3.** Nach Lichtaktivierung des Chemotherapeutikums kann die Bindung an das zelluläre Target stattfinden. Danach erfolgt die Kopplung des Fluorophores über den Griff an den Stoff-Target-Komplex.

Nachdem das Experiment erfolgreich an isoliertem BSA ausgeführt wurde, wurde der Versuch in Zellen wiederholt. Hierfür wurden Krebszellen gezüchtet und mit dem inaktiven Stoff gefüttert. Nach der Inkubationszeit im Dunkeln wurde die Zellen mit Licht beschienen. Die Zellen wurden danach fixiert (konserviert) und der

Fluorophor wurde hinzugeben. Nach der Kopplungsreaktion des Fluorophors an das Chemotherapeutikum in den Zellen konnte wieder festgestellt werden, dass nur der aktivierte Stoff bindet, während der inaktive Stoff keine Interaktion innerhalb der Zelle eingehen kann und daher auch keine Wirkung zeigt. Mit Hilfe von Mikroskopie konnte das Signal des fluoreszenten Chemotherapeutikums in der Zelle lokalisiert werden. Entgegen der allgemeinen Auffassung, dass die wirksamen Stoffe einer Chemokur mit dem Zellkern interagieren, wurde unser Stoff außerhalb des Zellkerns gefunden. Nach der Einfärbung der verschiedenen Zellorganellen konnte nach dem Ausschlussprinzip ein Zellorganell, der Golgi Apparat, als möglicher Zielort des Chemotherapeutikums identifiziert werden.



**Figur 4.** Unser Chemotherapeutikum (grün) in Krebszellen. Wie man sieht befindet sich der Stoff nicht im Zellkern (blau).

Zusammenfassend lässt sich sagen, dass wir lichtaktivierbare rutheniumhaltige Chemotherapeutika erfolgreich mit einem Alkyn herstellen konnten, an das ein Fluorophor gekoppelt werden kann. Diese Kopplung ist auch in Zellen erfolgreich und hilft damit die chemische Substanz zu lokalisieren. Weitere Experimente sind nötig um die ersten Resultate zu bestätigen und das genaue Target des Stoffes zu erforschen.





# LIST OF PUBLICATIONS

---

## Articles

V.H.S. van Rixel, **A. Busemann**, A.J. Göttle, and S. Bonnet, "Preparation, stability, and photoreactivity of thiolato ruthenium polypyridyl complexes: Can cysteine derivatives protect ruthenium-based anticancer complexes?", *J. Inorg. Biochem.*, **2015**, *150*, 174-181.

V. H. S. van Rixel, B. Siewert, S. L. Hopkins, S. H. C. Askes, **A. Busemann**, M. A. Siegler and S. Bonnet, "Green light-induced apoptosis in cancer cells by a tetrapyrindyl ruthenium prodrug offering two trans coordination sites", *Chem. Sci.* **2016**, *7* (8), 4922-4929.

X-Q. Zhou, **A. Busemann**, M.S. Meijer, M.A. Siegler, and S. Bonnet, "The two isomers of a cyclometalated palladium sensitizer show distinct photodynamic properties in cancer cells", *Chem. Comm* **2019**, *55*, 4695-4698.

V. H. S. van Rixel, **A. Busemann**, M.F. Wissingh, S.L. Hopkins, B. Siewert, C. van de Griend, M. A. Siegler, T. Marzo, F. Papi, M. Ferraroni, P. Gratteri, C. Bazzicalupi, L. Messori, and S. Bonnet, "Induction of a four-way junction-like structure in the DNA palindromic hexanucleotide 5'-d(CGTACG)-3' by a mononuclear platinum complex", *Angew. Chem. Int. Ed.* **2019**, Accepted Author Manuscript. doi:10.1002/ange.201814532

**A. Busemann**, M.C. Araman, I. Flashpohler, A. Pratesi, X-Q. Zhou, V.H.S. van Rixel, M. Siegler, S.I. van Kasteren, L. Messori, and S. Bonnet, "Alkyne functionalization of photoactivated ruthenium complex [Ru(tpy)(bpy)(Hmte)](PF<sub>6</sub>)<sub>2</sub> for protein interaction studies", *manuscript in preparation*.

## Poster Presentations

**A. Busemann**, T. van Teijlingen, S.I. van Kasteren, and S. Bonnet, "Preparation of alkyne-modified ruthenium complexes for pull-down experiments", *Reedijk Symposium 2016* in Leiden, The Netherlands.

**A. Busemann**, T. van Teijlingen, S.I. van Kasteren, and S. Bonnet, "Preparation of alkyne-modified ruthenium complexes for pull-down experiments", *Chemistry as Innovating Science (CHAINS) 2016* in Veldhoven, The Netherlands.

**A. Busemann**, S.I. van Kasteren, and S. Bonnet, "Interaction of ruthenium-based anticancer compounds with biomolecules" *Figon Dutch Medicine Days 2017* in Ede, The Netherlands.

**A. Busemann**, P. Del Bufalo, S.I. van Kasteren, and S. Bonnet, "Alkyne-modified ruthenium complexes for pull-down experiments" *Chemistry as Innovating Science (CHAINS) 2017* in Veldhoven, The Netherlands.

**A. Busemann**, M.C. Araman, I. Flaspohler, S.I. van Kasteren, and S. Bonnet, "Investigation of the interaction of ruthenium-based anticancer compounds with biomolecules", *Gordon Research Conference "Metals in Medicine" 2018* in Andover, NH, USA (**poster award**).

**A. Busemann**, S. Le Dévédec, V. DeRose, S. Bonnet, "Cell imaging of click-enabled ruthenium complexes for photoactivated chemotherapy", *Holland Research School of Molecular Chemistry (HRSMC) Symposium 2018* in Leiden, The Netherlands (**poster award**).

## Oral Presentations

**A. Busemann**, S. Le Dévédec, V. DeRose, S. Bonnet, "Cell imaging of click-enabled ruthenium complexes for photoactivated chemotherapy" *Figon Dutch Medicine Days 2018* in Ede, The Netherlands.

**A. Busemann**, S. Le Dévédec, V. DeRose, S. Bonnet, "Cell imaging of click-enabled ruthenium complexes for photoactivated chemotherapy" *Chemistry as Innovating Science (CHAINS) 2018* in Veldhoven, The Netherlands.

# CURRICULUM VITAE

---

Anja Busemann was born in Naumburg (Saale), Germany, on 20th December 1988. In 2007, she graduated from Landesschule Pforta. In 2012, she received her Bachelor of Science degree in Chemistry from the Radboud University in Nijmegen. She moved to Leiden and in 2014, she obtained her Master of Science degree in Chemistry at Leiden University. Her MSc thesis was entitled: *"Synthesis of [Ru(tpy)(bpy)(SR)]<sup>+</sup> complexes and photoreactivity studies"*. During her MSc studies she visited the University of Nottingham for six months within the Erasmus Exchange Program for a Minor MSc Thesis, entitled: *"Transition metal macrocyclic complexes"*.

In 2014, she started her PhD studies under the supervision of Dr. Sylvestre Bonnet and Prof. Elisabeth Bouwman in the research group 'Metals in Catalysis, Biomimetics, and Inorganic Materials' (MCBIM) of the Leiden Institute of Chemistry, Leiden University. During her PhD studies she collaborated with Dr. Sander van Kasteren (Leiden University), Dr. Sylvia Le Dévédec (Leiden University), Prof. Ingo Ott (TU Braunschweig), Prof. Ben Giepmans (UMC Groningen), and Prof. Luigi Messori (University of Florence). In addition, she went on a two-month study trip to the University of Oregon, Eugene, OR, USA, where she worked with Prof. Vickie DeRose on fluorescent microscopy imaging. During her PhD studies, she assisted at a number of first year chemistry lab courses, and supervised eleven 2nd year BSc students, three 3rd year BSc students and three MSc students.

# ACKNOWLEDGEMENTS

---

The European Research Council is acknowledged for financially supporting this work. The Kroese-Duijsters Fonds of the Leids Universiteits Fonds is acknowledged for financial support of the short-term scientific project at the University of Oregon, USA, and the “Metals in Medicine” Gordon conference in Andover, USA. Dr. Can Araman (Leiden University) is gratefully acknowledged for gel electrophoresis experiments and scientific support (Chapter 2). Dr. Sander van Kasteren (Leiden University) is acknowledged for scientific discussions (Chapter 2). Dr. Alessandro Pratesi and Prof. Luigi Messori (University of Florence) are kindly acknowledged for ESI-MS measurements and scientific discussions (Chapter 2). Xuequan Zhou and Dr. Michael Meijer are kindly acknowledged for singlet oxygen emission experiments (Chapter 2, 3, and 4) and scientific discussions. Dr. Sylvia Le Dévédec (LACDR, Leiden University) is gratefully acknowledged for fluorescent microscopy imaging and scientific discussions (Chapter 4). Dr. Rachael Cunningham and Prof. Victoria DeRose (University of Oregon) are gratefully acknowledged for their hospitality, scientific support, and supply of chemicals during the short-term scientific project at the University of Oregon, USA (Chapter 4). Dr. Claudia Schmidt and Prof. Ingo Ott (TU Braunschweig) are acknowledged for AAS measurements (Chapter 4). Jeroen Kuipers and Dr. Ben Giepmans (UMC Groningen) are acknowledged for EDX measurements (Chapter 6). Crystallographer Dr. Maxime Sieglar (Johns Hopkins University) is kindly acknowledged for solving X-ray crystal structures presented in Chapter 2, 3, and 4. John van Dijk, Jos van Brussel, and Dr. Anne-Geert Volbeda are acknowledged for MS measurements. Dr. Sipeng Zheng (Leiden University) is kindly acknowledged for MS measurements and his contribution to Chapter 5. Dr. Karthick Sai Sankar Gupta and Fons Lefeber (Leiden University) are gratefully acknowledged for their assistance with NMR measurements. Hans van der Elst (Leiden University) is acknowledged for HR-MS measurements. Dr. Bianka Siewert and Dr. Samantha Hopkins are acknowledged for designing the (photo)cytotoxicity assay. Dr. Vincent van Rixel, Dr. Jordi-Amat Cuello-Garibo, and Bob de Vis (Leiden University) are gratefully acknowledged for scientific discussions and support. Supervised students, notably Tess van Teijlingen, Paolo Del Bufalo, Anna Levering, Maarten van Ginkel, Ingrid Flashpohler, and Emma Cleary are all acknowledged for their contributions to this thesis.